Contact electrodes for heterojunction silicon solar cells: Evaluations and optimizations of the electron contact

Léo Basset

FACULTÉ DES SCIENCES ET TECHNOLOGIES

Université de Lille

iemn

THESE DE DOCTORAT

liten cea tech

ines NATIONAL INSTITUTE OF SOLAR ENERGY

Réalisée au

Laboratoire des cellules à hétérojonctions (LHET) du CEA Liten et à l'institut d'électronique, de microélectronique et de nanotechnologie (IEMN)

Ecole Doctorale Régionale Sciences Pour l'Ingénieur Lille Nord de France

Pour l'obtention du grade de

DOCTEUR de l'Université de Lille

Spécialité: Micro et Nanotechnologies, Acoustique et Télécommunications

Par

Léo BASSET

Électrodes de contact pour cellules à hétérojonctions de silicium: Evaluations et optimisations du contact de type N

Contact electrodes for heterojunction silicon solar cells: Evaluations and optimizations of the electron contact

Thèse soutenue le 10 Novembre 2020 au Bourget-du-Lac

Mustapha LEMITI *Professeur, Université de Lyon (INSA)*	Président
Marie GUEUNIER-FARRET *Maître de Conférences HDR, Université Paris Saclay (GeePs, Gif sur Yvette)*	Rapportrice
Jan SCHMIDT *Professeur, Université Leibniz (ISFH)*	Rapporteur
Mathieu BOCCARD *Chercheur, Ecole Polytechnique Fédérale de Lausanne (PV LAB)*	Examinateur
Wilfried FAVRE *Ingénieur, Commissariat à l'Energie Atomique et aux Energies Alternatives (INES, Chambéry)*	Encadrant
Jean-Pierre VILCOT *Directeur de Recherche, CNRS (IEMN, Villeneuve d'Ascq)*	Directeur de thèse
Marina FOTI *Ingénieure, Enel Green Power (Catania)*	Invitée

Acknowledgment:

En premier lieu, je tiens à remercier le CEA pour le financement de ma thèse ainsi que mon laboratoire d'accueil, le LHET. J'ai pu passer un peu plus de trois ans sur mon sujet de recherche de caractérisation avancée sur des dispositifs à l'état de l'art, et avec l'appui d'infrastructures de très haut niveau, le tout dans un cadre alpin très agréable à vivre. Merci donc à toute l'équipe du LHET, et de manière plus globale à tous ceux avec qui j'ai pu interagir à INES.

Ensuite, j'aimerais remercier les membres du jury pour leur implication dans ce travail de thèse. Je remercie Mustapha Lemiti pour avoir présidé ce jury, les deux rapporteurs du manuscrit, Marie Geunier-Farret et Jan Schmidt, ainsi que Mathieu Boccard et Marina Foti. De plus, je voudrais remercier mon directeur de thèse, Jean-Pierre Vilcot, pour son aide et sa bonne humeur. Enfin, je remercie Wilfried Favre pour son encadrement tout au long de cette thèse, pour toutes les heures passées à discuter en profondeur de toute sorte de sujets techniques, ainsi que pour les blagues fréquentes et de qualité discutable.

Je me dois aussi de remercier SunsChemical, qui nous a gracieusement fourni des cires organiques hot-melt pour les applications de patterning Inkjet.

Merci à toutes les équipes qui font tourner les plateformes Restaure et Labfab: la maintenance, les responsables équipement, les ateliers, la team planning. J'ai eu l'occasion d'embêter chacune avec mes problèmes sur les équipements, mes demandes de réalisation de lots exotiques et mes soucis de planification des différentes étapes de fabrication d'échantillons. Merci pour votre temps et votre compétence.

Merci Olivier pour toute l'aide que tu apportée sur la thématique Rcontact, on en a passé des heures en réu avec Wilfried à se tordre les neurones sur la compréhension de tout ça. Merci Valentin et Renaud pour votre aide sur Silvaco, et pour les discussions autour de la physique des contacts et des cellules. Merci aussi Martin pour ton expertise sur les sujets polissage et patterning. Merci Julien (Diaz) et Florent pour votre aide pour les sérigraphies avec alignement et sur le design des masques. Merci Julien (Eymard), mon pendant côté module, pour les échanges sur les pertes résistives. Et merci à un troisième Julien (Sudre) pour ton aide pour les manips de patterning.

Je suis également très reconnaissant envers les chapeauteurs de projets du LHET (Jean-François, Delfina, Wilfried et Jordi) de m'avoir donné l'occasion de participer à des Workshop chez nos voisins suisses et siciliens, ça a toujours été des moments enrichissants.

J'ai eu la chance d'encadrer deux stagiaires au top au cours de ma thèse, qui ont fait avancer la thématique Rcontact avec une belle quantité de manips effectuées. Merci à Gilles et à Antonin pour les avancées dans la thématique, bonne chance à vous dans la suite de votre parcours. Bonne chance aussi à Pia et Senami qui démarrent leur thèse cette fin d'année 2020 dans un contexte un peu particulier !

Merci aux thésards du bureau 238 qui m'ont réservé un chaleureux accueil à INES pour mes débuts en stage au LHMJ : Audrey, Elise et Antoine, j'ai passé un superbe premier été à Chambéry en grande partie grâce à vous trois. Merci aussi à Rafael pour ton encadrement lors

de ce stage, et pour les intermèdes musicaux, a capela en salle ou accompagné d'un piano ou d'un micro de karaoké. Merci aussi à tous les voisins du LHMJ Nicolas, Marc, Christine, Hélène, Florent, Lionel, Remi, Sebastien, Adeline, Thibaut, Armand, Mylène, Sarra, Coralie…

Je remercie aussi les montagnards savoyards aguerris : Jordi et Felix pour la randonnée bivouac inoubliable dans le Dévoluy, et pour les sorties rando à ski ; et Adrien pour les sessions grimpe dans les environs après le boulot.

Merci à tous ceux que je n'ai pas encore cité avec qui j'ai pu discuter, rire et festoyer à INES, Ravi, Camille, Maxim, Thibault, Son, Daniel, Baptiste, Joël, Mylène, Charles, Elénore, Médéric, Aurélie …

Pour tous mes amis, pensées pour les super moments que j'ai pu avoir avec vous pendant cette période : perdu dans la forêt, en montagne, à la Morte, dans le Diois, à Venon, à Toulouse, à Grenoble, à Chambéry… et sur Skype/Discord, pandémie oblige.

Je remercie également mes parents, vos deux blondinets ont un peu grandi, en pas trop mal, même si on a plus les mêmes gueules d'ange et nos coupes au bol, non ? Merci à vous, à Christophe et à Alexane pour les bols d'air frais à Saint-Martin le week-end après des semaines chargées. Et merci Syl, c'est toujours cool de râler sur tous les sujets avec toi.

Enfin, merci beaucoup Apo pour ton soutien constant, pour m'avoir supporté pendant ma rédaction quand j'arrivais plus trop à décrocher, et pour tous ces moments partagés.

Abstract

Silicon heterojunction solar cells (SHJ) combining hydrogenated amorphous and crystalline silicon have demonstrated very high efficiencies in both laboratory and production environments. Further efficiency improvement is still possible with the main efforts to be focused on electronic transport properties, and on enhanced optical confinement at the various interfaces of the device.

Transport mechanisms inside such devices are still not fully understood yet, in particular the electron and hole contacts are complex hetero-interfaces with several transport phenomena at play. Lateral transport has also to be fully considered, as a substantial amount of the current can spread laterally in the silicon wafer, in parallel to the transparent conductive oxide (TCO) layers.

This work focuses on developing methods to evaluate the resistive losses in SHJ cells under dark and illumination conditions, to assess their possible origin, and proposing strategies for their reduction. For this purpose, experimental characterization procedures of the total series resistance as well as contact resistance of different contacts and interfaces are proposed and evaluated considering various sample designs and properties (wafer doping, effective lifetime, TCO conductivity, etc.). Confrontation of the results to existing analytical models showed the need for modification mainly related to the SHJ device design, while 2D TCAD simulations were used to give additional insights on the local transport mechanisms. The impact of illumination and temperature variations on those quantities is also studied.

We show that extracting accurately TCO sheet resistance and Ag/TCO contact resistivity from TLM samples that are representative of the SHJ device (i.e. including amorphous / crystalline silicon materials underneath), requires for c-Si insulation to limit current flow through interfaces and in the bulk c-Si which leads to underestimate $R_{\square}$ of the TCO and overestimate ρ_C of the Ag/TCO contact. Emitter insulation and thick (i) a-Si:H layer strategies give satisfying results as the experimental data are not affected by bulk c-Si properties. Values as low as $\rho_C\,(Ag/ITO) = 0.11 \pm 0.03 m\Omega.cm^2$ have been extracted from the studied samples.

We report values of contact resistivities for the electron and hole contacts of respectively $75 \pm 13\ m\Omega.cm^2$ and $292 \pm 54\ m\Omega.cm^2$. We found that they feature large temperature dependence indicative of thermionic emission, and can be influenced by illumination intensity in some instances, meaning that the values determined in the dark may not be representative of MPP conditions.

In the final device, lateral transport is found to be highly influenced by local carrier concentrations, in particular when high resistivity / high lifetime c-Si wafers are used. For a 22.3% efficiency M2 area SHJ cell with a 5-busbars design produced at CEA (INES), the series resistance is estimated to account for approximately $4.3\%\ abs$. Fill Factor (FF) and $1\%\ abs$. efficiency reduction. In this example, the electron and hole contacts are identified as being the main source of losses, accounting for $1.9\%\ abs$. FF, while lateral transport reduces FF by approximately $1.2\%\ abs$.

Résumé

Les cellules photovoltaïques (PV) à hétérojonction de silicium (SHJ) combinant du silicium amorphe hydrogéné (a-Si :H) et cristallin (c-Si) ont démontré de très hauts rendements à la fois en laboratoire et en environnement de production. De nouvelles améliorations sont toujours possibles, avec un effort consacré à l'amélioration des propriétés de transport électronique, et à un meilleur confinement optique aux différentes interfaces du dispositif.

Les mécanismes de transport dans ces cellules ne sont toujours pas complètement compris, notamment au niveau des couches de contact pour la collecte des électrons et des trous, qui sont de complexes hétéro-interfaces où plusieurs phénomènes de transport sont impliqués. Le transport latéral doit aussi être considéré totalement, puisqu'une partie importante du courant latéral circule dans le silicium cristallin, en parallèle de la couche d'oxyde transparent conducteur (OTC).

Ces travaux de thèse portent sur l'évaluation des pertes résistives dans les cellules SHJ à l'obscurité et sous éclairement, sur celle de leur possible origine, et proposer ainsi des stratégies pour les réduire. Pour ce faire, des procédures expérimentales de caractérisation de la résistances série, ainsi que des résistances de contact des différents contacts et interfaces de la cellule sont proposés et évalués en considérant des échantillons de conception et propriétés variés (dopage du wafer, durée de vie, conductivité de l'OTC etc.). La confrontation de ces résultats à ceux des modèles analytiques classiques du PV montrent la nécessité de prendre en compte les spécificités de la cellule SHJ dans ces modèles, tandis que des simulations TCAD en 2D sont utilisées pour donner davantage d'indices sur les mécanismes de transport. L'impact de la variation de l'illumination et de la température sur ces valeurs est aussi étudié.

Il est montré que pour extraire avec précision la résistance carrée de l'OTC et la résistivité de contact du contact Ag/OTC par des mesures sur des échantillons TLM représentatifs de la cellule SHJ, c'est-à-dire où l'OTC est déposé sur du silicium amorphe sur substrat cristallin, il faut isoler électriquement le c-Si pour limiter le passage du courant à travers les interfaces et le volume du silicium cristallin, qui entraine une sous-estimation de la mesure du $R_{\square}$ de l'OTC et une surestimation de la mesure de ρ_C pour le contact Ag/OTC. Des stratégies d'isolation par l'émetteur ou par une couche épaisse d'a-Si :H donnent des résultats satisfaisants puisque les données mesurées ne dépendent pas des propriétés du c-Si bulk. Des valeurs de l'ordre de $\rho_C\,(Ag/ITO) = 0{,}11 \pm 0{,}03 m\Omega.cm^2$ sont extraites des échantillons étudiés (l'OTC étant de l'oxyde d'indium étain ou ITO dans cet exemple).

De plus, les résistivités de contact des contacts électrons et trous sont mesurées respectivement à $75 \pm 13\, m\Omega.cm^2$ et $292 \pm 54\, m\Omega.cm^2$, avec une forte sensibilité à la température indicative de l'effet thermo-ionique. Ces valeurs peuvent être dans certains cas influencées par l'illumination incidente, ce qui montre l'importance de les mesurer dans des conditions représentatives de fonctionnement de ces cellules.

Dans le dispositif final, le transport latéral est fortement influencé par la densité de porteurs de charge locale, en particulier lorsque des wafers à haute résistivité ou à haute durée de vie sont utilisés. Pour une cellule SHJ de 22,3% de rendement sur une surface M2 utilisant une

conception à 5 busbars fabriquée au CEA, la résistance série est estimée impacter d'environ $4{,}3\%\ abs$. le facteur de forme (FF) et d'$1\%\ abs$. le rendement. Dans cet exemple, les contacts électrons et trous sont identifiés comme étant les principales sources de pertes, correspondant à $1{,}9\%\ abs$. FF, tandis que le transport latéral réduit le FF d'approximativement $1{,}2\%\ abs$.

Table of Contents

Chapter 1

General introduction

In this chapter, we introduce the field of photovoltaic solar cells. We first address why it is important for the decarbonization of the electricity production. Secondly, we study the operating principles of solar cells, and discuss their figures of merits. Thirdly, we examine the main factors limiting their efficiency; we address recombination, parasitic resistance and optical losses. Subsequently, we review the main technologies of silicon solar cells dominating the market today, and examine the emerging technologies that are forecasted to take on a significant part of the market shares in the near future. Finally, we introduce the objectives of this work.

1.1 Photovoltaics in the energy production

It is now a very strongly established fact that the Earth's climate is affected by a global warming due to anthropogenic greenhouse gas emission [1]. Figure 1 illustrates the global temperature anomaly of the Earth as a function of time, as well as the CO_2 levels in the atmosphere.

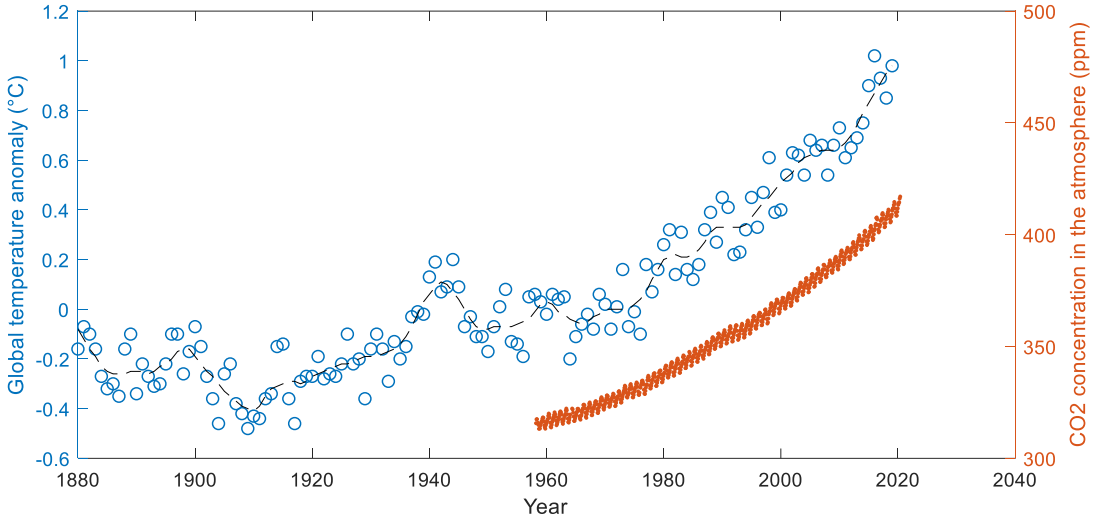

Figure 1: Temperature anomaly relative to the 1951-1980 average temperatures [2] and direct measurement of CO_2 concentration in the atmosphere [3] as a function of time

Since 1950, the CO_2 level in the atmosphere is unprecedented in all the accessible historical data (inferred from ice cores) [3], and this has led to a temperature anomaly beyond 1°C recorded in 2016, the warmest year ever registered. This affects, and will affect even more in the future, humans, lands and biodiversity, with for instance massive species extinction, sea level rise, diminished crop yields etc.

This now very widespread knowledge, as well as the fact that fossil energy is by essence a finite resource, has led to the recent boom of low-carbon renewable energy sources. Strategies for future energy mixes to mitigate climate change include large amount of wind and solar energy [4]. In particular, most scenarios include very large shares of photovoltaic energy (PV) in the worldwide electricity supply [5].

The PV industry is already growing at a very high rate: since 2017 more than 100 GWp are installed every year, and as of 2019 the cumulated installed capacity of solar PV has surpassed 600 GWp [6]. This has been made possible by the drop of the average price of the modules over the last years, with an average value in 2019 at 0.23 $USD/Wp (see Figure 2).

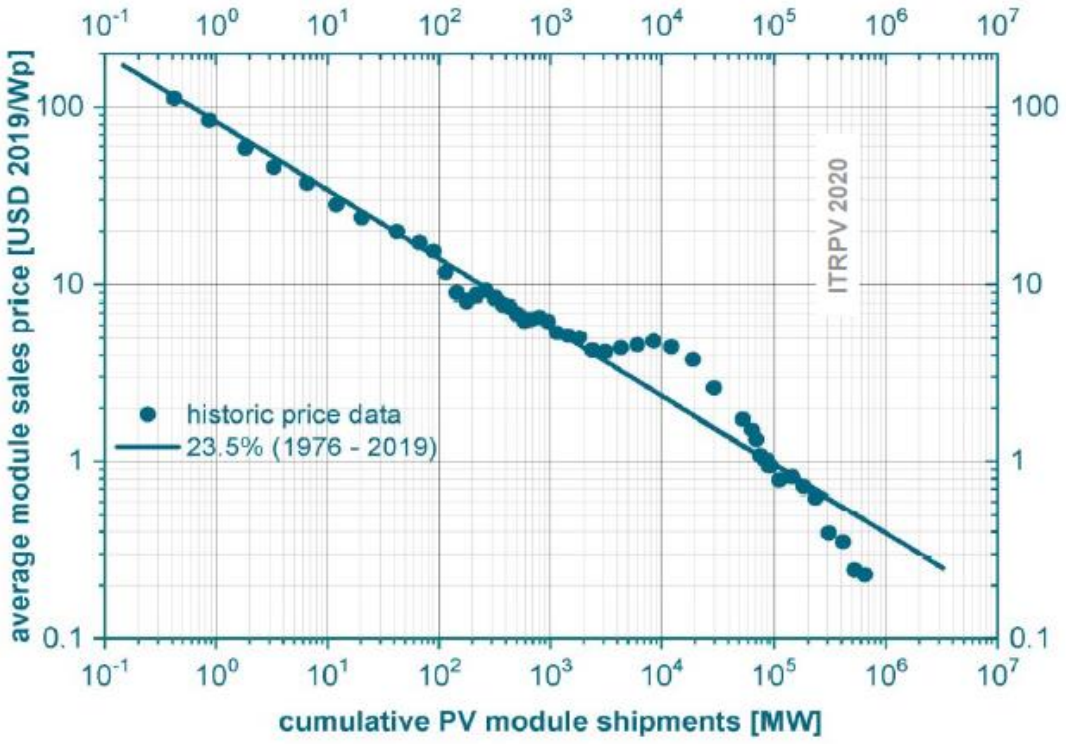

Figure 2: Learning curve for module price as a function of cumulative shipments. Taken from [7]

Of course the problematic is more complex than price alone, and a lot of other issues need to be tackled to make solar energy a real substitutive to fossil energy. PV produces energy with intermittence (capacity factor around 15% [8]): this implies that either some storage is needed [9], or that some load management is needed to match energy production with its consumption [10]. Other important problematics include mineral material consumption [11] and integration in electricity grid [12], but all of this is well beyond the scope of this work. Overall, solar PV is an important player in the incredibly complex problem that the future energy mix represents.

Now, to further improve the relevance of solar PV, the price per produced power needs to diminish, which can be achieved by reducing the price of the system, and/or by increasing its electric yield. At the PV cell level - building block of the PV systems - the research focuses on efficiency improvement, and tremendous improvement has been demonstrated over the last decades [13]. Industry is now switching towards more efficient cell technologies due to system price being less and less governed by PV cell price, therefore accommodating for more pricy cells. In 2019, the module cost was about 41% of the total price for a large PV installation, with 58% of the module cost due to the PV cell [7]. In particular for silicon technologies, more advanced cell concepts are rapidly replacing the more basic ones, and we assist to the fast rise of passivating contacts technologies fabricated with high quality wafers [7]. Other important trends include the use of larger wafer formats, cut cells and bifaciality (e.g. [14], [15]).

1.2 Photovoltaic solar cells

This work focuses on silicon PV solar cells. In the following, we will address the functioning of a solar cell and its basic features. We will then discuss on the different factors limiting their efficiency and on the main existing silicon solar cells technologies.

1.2.1 Photovoltaic cells' working principle

Any semi-conductor absorbing light generates electron-hole pairs in excess compared to thermal equilibrium. However, there is no current nor potential difference that is generated simply by illuminating such a material, as there is no driving force allowing the extraction of power. Generated carriers therefore randomly diffuse and recombine through the semi-conductor.

The concept of a solar cell is to generate charge carriers inside a semi-conductor material under illumination, and to use an induced driving force to separate electrons and holes to collect them at the two terminals of the cell, thus generating power through a load. In a classical silicon based solar cell (see Figure 3), the thick bulk material allowing the generation of carriers is referred to as the absorber, while the electron and hole contacts are the layers allowing the preferential collection of one type of carrier or the other.

The driving force in a solar cell can originate either from an electric field (Conduction current of electrons and holes, expressed by Eq. 1) or from a diffusion gradient (Diffusion current of electrons and holes, expressed by Eq. 2).

$$\begin{aligned}\overrightarrow{J_{n,cond}} &= qn\mu_n\overrightarrow{\nabla\varphi} \\ \overrightarrow{J_{p,cond}} &= qp\mu_p\overrightarrow{\nabla\varphi}\end{aligned} \qquad \text{Eq. 1}$$

Where q is the elementary charge, n and p are the electron and hole densities, μ_n and μ_p are electron and hole mobilities, and φ is the electric potential.

$$\begin{aligned}\overrightarrow{J_{n,diff}} &= qD_n\overrightarrow{\nabla \mathrm{n}} = k_BT\mu_n\overrightarrow{\nabla \mathrm{n}} \\ \overrightarrow{J_{p,diff}} &= -qD_p\overrightarrow{\nabla \mathrm{p}} = -k_BT\mu_p\overrightarrow{\nabla \mathrm{p}}\end{aligned} \qquad \text{Eq. 2}$$

Where D_n and D_p are the diffusion coefficient for electrons and holes, k_B is Boltzman's constant, and T is the temperature.

The hole and electron currents are each the sum of their field and diffusion components [16]:

$$\begin{aligned}\overrightarrow{J_n} &= \overrightarrow{J_{n,cond}} + \overrightarrow{J_{n,diff}} = qn\mu_n\overrightarrow{\nabla\varphi} + k_BT\mu_n\overrightarrow{\nabla \mathrm{n}} \\ \overrightarrow{J_p} &= \overrightarrow{J_{p,cond}} + \overrightarrow{J_{p,diff}} = qp\mu_p\overrightarrow{\nabla\varphi} - k_BT\mu_P\overrightarrow{\nabla \mathrm{p}}\end{aligned} \qquad \text{Eq. 3}$$

Another convenient expression of these equations involves the quasi-Fermi levels of electrons and holes, respectively $E_{F,n}$ and $E_{F,p}$, and their conductivities σ_n and σ_p:

$$\begin{aligned}\overrightarrow{J_n} &= \frac{\sigma_n}{q}\overrightarrow{\nabla E_{F,n}} \\ \overrightarrow{J_p} &= \frac{\sigma_p}{q}\overrightarrow{\nabla E_{F,p}}\end{aligned} \qquad \text{Eq. 4}$$

Note that the electron flow is in opposite direction to $\overrightarrow{J_n}$ as electrons are of negative charge. J_n and J_p add up even though charges flow in opposite directions:

$$\overrightarrow{J_{tot}} = \overrightarrow{J_n} + \overrightarrow{J_p} \qquad \text{Eq. 5}$$

To get a current, electrons and holes need to flow in opposite directions towards their respective contacts, meaning that a so-called "selectivity" is needed. The field component is always selective as it drives electrons and holes oppositely due to their opposite charge (i.e. $\overrightarrow{J_{n,cond}}$ and $\overrightarrow{J_{p,cond}}$ are of same direction). However, this is not necessarily the case for the diffusion component. To make it selective, spatial variations of the mobility or the charge

density across the cell are necessary. As $np = ni^2$, a local increase of n induces a decrease of p, and vice versa, making $\overrightarrow{\nabla n}$ and $\overrightarrow{\nabla p}$ of opposite directions, creating selectivity. Selectivity can also be achieved if $\overrightarrow{\nabla E_{F,n}}$ and $\overrightarrow{\nabla E_{F,p}}$ are not selective, by asymmetries in σ_n and σ_p at the vicinity of each contact (i.e. $\sigma_n \gg \sigma_p$ at the electron contact, so that $J_n \gg J_p$, and vice versa at the hole contact [17]). For most solar cells, selectivity mostly stems from this latter effect. Figure 3 illustrates a simple solar cell structure:

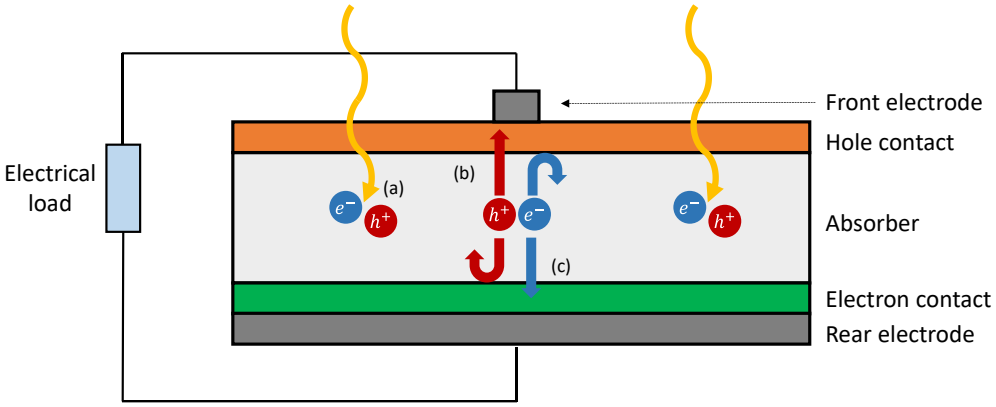

Figure 3 : Drawing of a basic cell structure. (a) Electron-hole pairs are generated upon absorption of light in the absorber, (b) at the hole contact, holes are selectively attracted while electrons are repelled, and (c) at the electron contact the reverse phenomenon appears

The difference in potential between the two terminals of the solar cells is expressed:

$$V_{ext} = \frac{1}{q} * \left(E_{F,n}(electron\ contact) - E_{F,p}(hole\ contact)\right) \qquad \text{Eq. 6}$$

An ideal cell therefore generates a strong difference in Fermi energy under illumination in its bulk, and has sufficiently selective contacts to ensure collection with negligible voltage losses (see Figure 4).

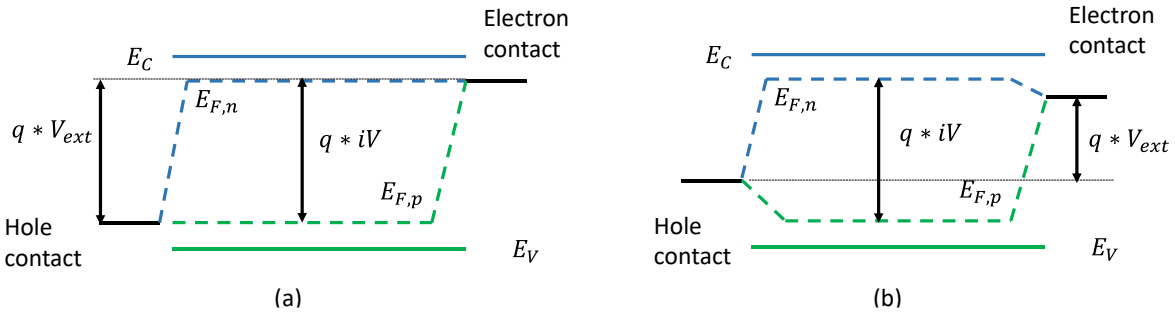

Figure 4: Band diagrams of simple cells featuring an undoped bulk with (a) ideal electron and hole contacts and (b) with non-ideal contacts

Keep in mind that saying that holes are "collected" at the p-contact is a bit erroneous: in fact, electrons collected at the n-contact cross the external circuit and are reinjected at the p-contact where they recombine with holes accumulated there. It is essential for cell functioning that all charges recombine at the collection terminal. Electrons are not consumed in the load, what is important is electron flow through the load. As pointed out by Cuevas et al. [18] an ideal cell nearly has all its charges recombining at one contact. In fact, he states, "localized recombination is the ultimate cause for carrier flow". It is less pointed at in single-junction devices, but is well

known as the principle of multi-junctions functioning, where sub-cells are separated with recombination junctions [19].

1.2.2 Basics of PV solar cells

1.2.2.1 Current-voltage characteristic of a solar cell

The main characteristic of a solar cell is its current/voltage curve (I-V), or alternatively current-density/voltage curve (J-V) when current is normalized over the surface area. Under dark conditions, the J-V characteristic of the solar cell is very similar to that of a diode. The current is very close to zero up to a "threshold voltage" where current increases exponentially. A simple diode characteristic is modelled using:

$$J_D = J_0 * \left(exp\left(\frac{qV}{nk_BT}\right) - 1 \right) \quad \text{Eq. 7}$$

Where J_0 is the saturation current of the diode [mA/cm²] and n is the ideality factor.

Considering a solar cell acts as a diode in the dark, under illumination, a photogeneration term is added, and the current is shifted downwards:

$$J_D = J_0 * \left(exp\left(\frac{qV}{nk_BT}\right) - 1 \right) - J_L \quad \text{Eq. 8}$$

Where J_L is the photogenerated current [mA/cm²].

Figure 5 illustrates an experimental cell's J-V characteristic, both under dark conditions and under illumination (1Sun intensity, corresponding to the Air Mass 1.5 (AM1.5) sun irradiation, in standardized conditions). We find that the J-V curve under illumination is not only shifted downwards due to J_L but has also a different shape, meaning that the solar cell's physics is a bit more complicated than a simple diode model

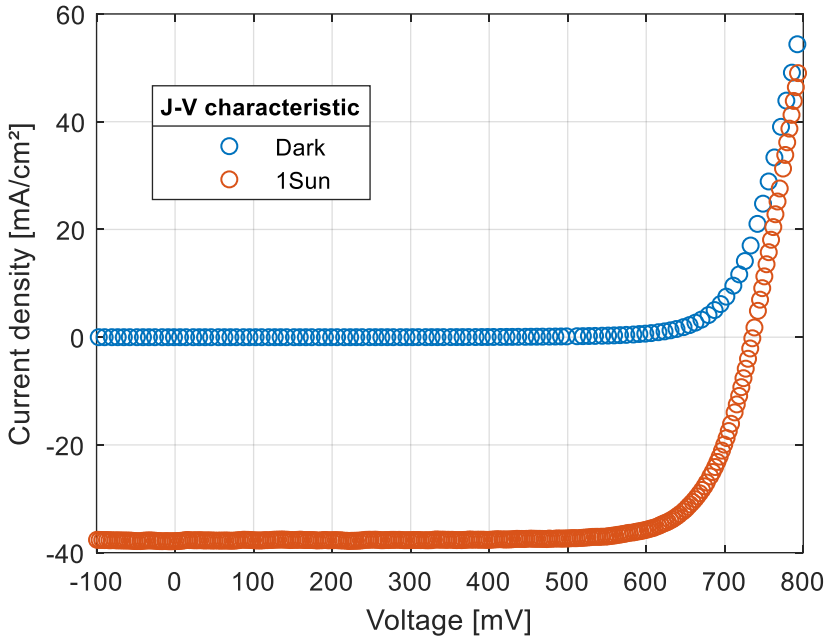

Figure 5: J-V characteristic of an SHJ solar cell measured in the dark (blue) and under 1Sun illumination intensity (orange)

Note that I-V curves of solar cells are often represented in the active sign convention, as they are generator devices.

1.2.2.2 Figures of merits of a solar cell

For a better readability, the J-V curves are usually represented upside-down, with a positive current. Figure 6 represents a typical cell's J-V curve, as well as its power/voltage curve.

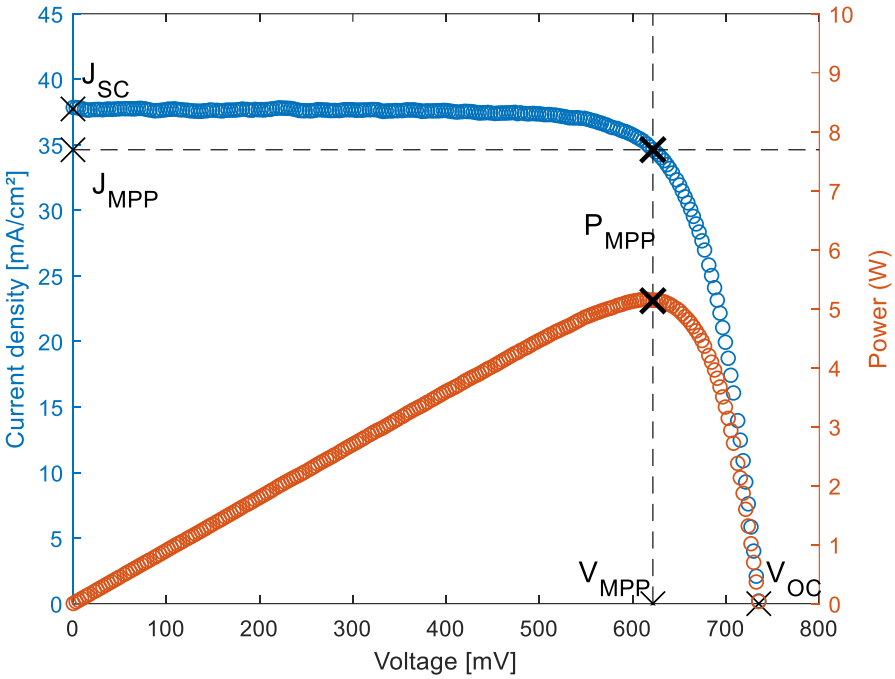

Figure 6 : Current density/voltage (blue) and power/voltage (orange) characteristics of an SHJ solar cell. Black crosses represent the main device parameters

Several figures of merit in this curve need to be introduced:

- The short-circuit current-density, J_{SC}, represents the maximum current that the cell can generate, occurring when the cell's voltage is zero (load in short-circuit)
- The open-circuit voltage, V_{OC}, represents the maximum voltage that can be drawn, occurring when current is zero (load in open circuit).
- The maximum power point is where the power is maximum in the curve. We can define the power, current-density and voltage at maximum power point, respectively P_{MPP}, J_{MPP} and V_{MPP}.
- The Fill Factor, FF, is the ratio defined such as:

$$FF = \frac{P_{MPP}}{V_{OC}J_{SC}} = \frac{V_{MPP} * J_{MPP}}{V_{OC}J_{SC}} \qquad \text{Eq. 9}$$

  It quantifies the "squareness" of the J-V curve, or how close to ideality the cell operates.

- Finally, the efficiency of the solar cell, η, can be defined as:

$$\eta = \frac{P_{MPP}}{P_{in}} = \frac{FF * J_{SC} * V_{OC}}{P_{in}} \qquad \text{Eq. 10}$$

Where P_{in} is the incident irradiation power on the cell, and:

$$P_{in} = E * S \qquad \text{Eq. 11}$$

Where E is the irradiation power-density expressed in [W/m^2], and S is the area of the cell. Usually E is controlled to a standard value of 1Sun (1kW/m^2).

1.2.2.3 Equivalent circuit of a solar cell

Previously we referred to a diode model for modelling a solar cell's J-V curve (Eq. 8). A more detailed model of the equivalent circuit of a solar cell adds terms for parasitic resistances such as depicted in Figure 7:

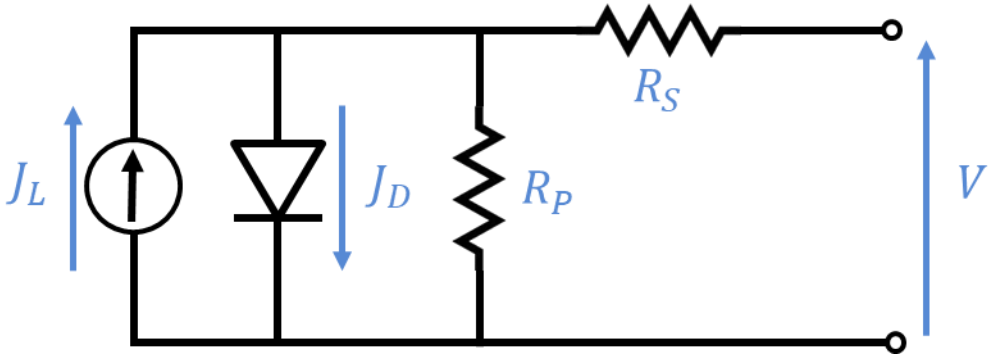

Figure 7 : The 1-diode model of equivalent circuit of a solar cell, where J_D is the diode dark-current

This is referred to as the "1-diode model". Eq. 8 becomes:

$$J = -J_L + J_0 * \left(exp\left(\frac{V - R_S J}{n \frac{k_B T}{q}} \right) - 1 \right) + \frac{V - R_S J}{R_P} \qquad \text{Eq. 12}$$

Where R_S is the series resistance of the cell, and R_P the shunt resistance (or parallel resistance), both expressed here in terms of [$\Omega . cm^2$].

Using a single diode model is based on the assumption that transport takes place with a single process, but usually this is not verified. A real solar cell will feature several transport mechanisms characterized by different sets of the parameters J_0 and n. Typically, in the case of pure diffusion mechanisms n should equal 1, and recombination mechanisms imply $n \leq 2$ ($n \sim 2$ for space charge recombination, and $n < 1$ for Auger recombination) [20].

Therefore, in numerous cases, the single-diode model does not adequately describe a solar cell, and a second diode is added, hence the 2-diodes equivalent model described in Figure 8 is more commonly used:

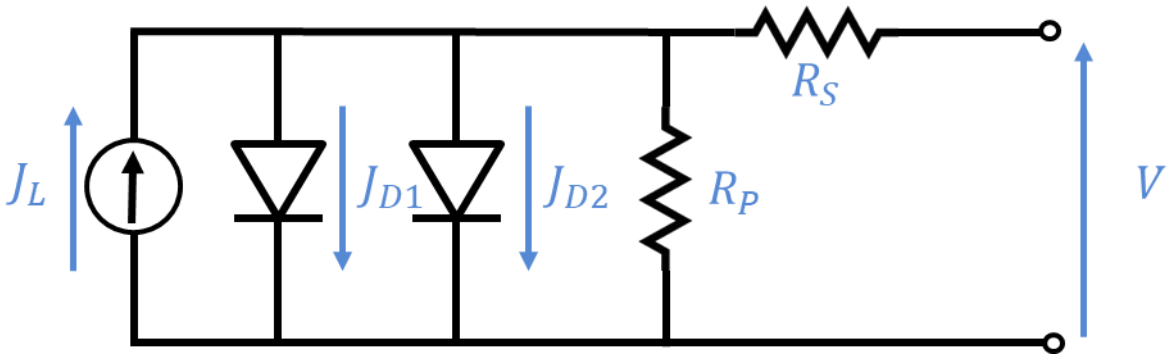

Figure 8 : The 2-diodes model equivalent circuit of a solar cell, where J_{D1} and J_{D2} are the diode dark-currents

It reads:

$$J = -J_L + J_{01} * \left(exp\left(\frac{V - R_S J}{n_1 \frac{k_B T}{q}} \right) - 1 \right) + J_{02} * \left(exp\left(\frac{V - R_S J}{n_2 \frac{k_B T}{q}} \right) - 1 \right) + \frac{V - R_S J}{R_P} \qquad \text{Eq. 13}$$

Where J_{01} & J_{02} and n_1 & n_2 are the saturation currents and ideality factors of both diodes.

Assuming that all the model's parameters do not vary with illumination, diode models can be used for modelling a cell under both illuminated and dark (with $J_L = 0$) conditions.

Note that for good efficiency solar cells, J_{SC} is very close to J_L as recombination and resistive effects have low impact at low voltages for silicon cells of medium to high efficiencies. In this work all modelling using the 1 or 2-diodes models will make the approximation that $J_L = J_{SC}$.

1.2.3 Efficiency limiting factors

The objective of a solar cell is to absorb as many photons from the incoming solar power as possible, and to allow the collection of the maximum amount of photo-generated electron-hole pairs at each of its terminals. The maximum theoretical efficiency for a single junction solar cell based on a semiconductor absorber material of bandgap energy E_g is mainly limited by photons of too low energy to be absorbed ($h\nu < E_g$) and thermalization of photons with too high energy ($h\nu > E_g$). Advanced concepts [21] are needed to tackle those limitations, and the maximum theoretical efficiency has been estimated to be 29.43% for conventional silicon solar cells [22].

The remaining "non-ideal" losses ruling the efficiency of a solar cell include electrical losses (recombination, shunt and series resistances), and optical losses (parasitic absorption or unabsorbed photons due to transmission or reflection).

The higher the excess density of charge, the stronger the separation of the quasi-Fermi energy levels (QFL) will be. The voltage resulting from the QFL splitting is referred to as the implied-voltage iV:

$$iV = \frac{kT}{q} * \ln\left(\frac{(\Delta n + n_0)(\Delta p + p_0)}{n_i^2} + 1 \right) \qquad \text{Eq. 14}$$

When charge collection is ideal, the implied voltage is the external voltage. However, when non-ideal charge collection occurs at the electron or hole contacts, i.e. when contacts are highly recombining or resistive, the QFL splitting is reduced near the contacts, and from Eq. 6 the external voltage diminishes [16].

- In open circuit conditions, considering perfect charge collection, the open-circuit implied-Voltage iV_{OC} corresponds to V_{OC}. **Therefore the main limiting factor of V_{OC} in solar cells is recombination.**
- In short circuit conditions, for high to moderate cell efficiencies where $J_{SC} = J_L$, the current is not affected by resistive effects nor recombination. **J_{SC} is then only limited by optical effects.**
- At maximum power point, both effective lifetime and charge collection are of importance, so resistive effects will intervene. **FF is affected by series resistance, shunt resistance, and recombination losses.**

1.2.3.1 Recombination

Generation and recombination refer to the processes in which free electron-hole pairs are created and annihilated: respectively, an electron in the valence band is either excited to the conduction band, or transfers back energy to transition back to the valence band. This can happen through different channels, through the absorption and emission of phonons and photons.

At thermal equilibrium the generation rate (G_0) is equal to the recombination rate (R_0), leading to constant charge density of holes and electrons. Once excited, an electron is in an unstable state, where it will rapidly transfer back its energy through the emission of other particles. This happens through two channels:

1- Thermalization: Intra-band multiple emissions of low-energy phonons. This is the fastest process, occurring in time scales of the order of 10^{-12} seconds [23].
2- Recombination. This is a much slower process, occurring in time scales of the order of several milliseconds in high quality crystalline silicon.

In metals, where the energy states form a continuum, the excess energy of an excited electron is predominantly transferred through thermalization, leading to the quick de-excitation of said electron and production of heat, whereas in semi-conductors, both processes are of importance. When a photon of energy higher than E_g is absorbed, thermalization will occur first, decreasing the electron energy to the bottom of E_C : as thermalization can only induce low energy steps, it cannot overcome E_g. In a second time, recombination takes place and the electron is de-excited to the valence band.

Instead of recombination rates, the usual metric chosen to quantify recombination is the minority carrier lifetime (τ), assuming $\Delta n = \Delta p$[1] it can be simplified to [24]:

[1] $\Delta n = \Delta p$ is true in most practical cases : in the absence of trapping and band bending effects where charge neutrality is locally not true

$$\tau = \frac{\Delta n_{av}}{G_{ph,av} - \frac{\partial \Delta n_{av}}{\partial t}} \quad \text{Eq. 15}$$

Where Δn_{av} is the average minority carrier density in bulk of the sample, and $G_{ph,av}$ is the average photogeneration rate.

There are several mechanisms that lead to the recombination of charge carriers. Among them, we can distinguish between intrinsic and extrinsic recombination. Intrinsic recombination is related to inherent bulk material properties, meaning it cannot be avoided whatever the optimization, whereas extrinsic recombination is related to the impact of defects. When several recombination processes are in competition, the effective lifetime is the reciprocal sum of all given phenomena limited lifetimes:

$$\frac{1}{\tau} = \sum \frac{1}{\tau_i} \quad \text{Eq. 16}$$

In principle, any extrinsic recombination is avoidable and can be tackled either by removing defects or by passivating them. Passivation is the process of reducing recombination through the reduction of the activity of these defects. The most common example is the hydrogenation of surface defects, where through the incorporation of hydrogen, dangling bonds will form links with hydrogen, strongly reducing their recombination rate. Passivation can be applied to the bulk of a material, notably through hydrogenation, but most processes involve high temperatures usually not compatible with low-temperature processed cells, such as SHJ cells [25].

1.2.3.1.1 Radiative recombination

Radiative recombination is the direct recombination of an electron-hole pair through the emission of a photon. In indirect semi-conductors such as silicon, radiative recombination is mediated by phonons, which makes it fare less likely to happen. The conduction band electron transits to the valence band by emitting a photon of energy very close to E_g.

The radiative-limited lifetime (τ_{rad}) only varies as a function of carrier density and can be expressed such as :

$$\tau_{rad} = \frac{1}{B(n_0 + p_0) + B\Delta n} \quad \text{Eq. 17}$$

Where B is a constant, which depends on the band structure of the material. For silicon $B = 4.73 * 10^{-15} cm^3/s$ at room temperature [26].

1.2.3.1.2 Auger recombination

Auger recombination is based on a three-particle interaction: the energy from an electron-hole pair recombining is transferred to another free charge carrier through collision; or additionally through Coulomb interaction of free charge carriers in said Coulomb-enhanced Auger recombination. The process either involves two electrons and a hole (eeh process) or two holes and an electron (ehh process).

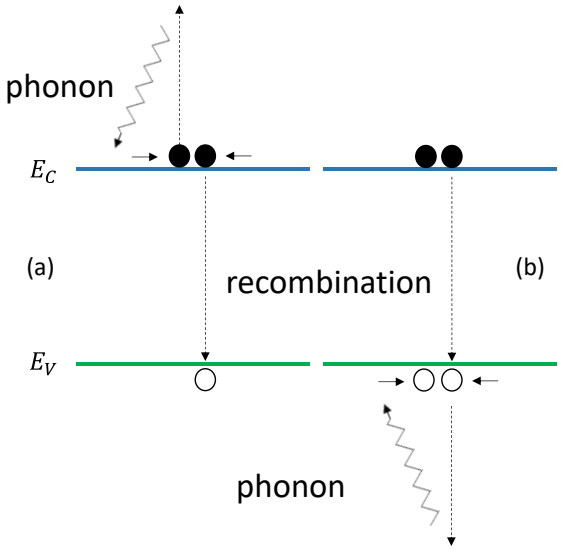

Figure 9 : (a) eeh and (b) ehh Auger processes

At high injection levels ($\Delta n\ or \Delta p\ \gg N_{D,A}$), Auger recombination becomes very important, and it is one of the major effects limiting the maximum theoretical efficiency of solar cells [22].

Richter et al. proposed a general parametrization of intrinsic recombination (Auger and radiative) of both n and p-type c-Si in 2012 [27]. Recently a more accurate model for n-type c-Si was proposed by Veith-Wolf et al. [28], while for p-type Richter's model is still considered as the state-of-the-art.

1.2.3.1.3 SRH recombination

Defects introduced in a semi-conductor lattice, such as metallic impurities or crystallographic defects, induce parasitic energy states in the band structure. Electrons and holes can transit to these energy levels, and recombine or be generated in them. The formalism proposed by Shockley, Read and Hall [29], [30] to describe this phenomenon is referred to as SRH recombination. In usual cases of no trapping ($\Delta n = \Delta p$) and single defect level, the SRH-limited lifetime reads:

$$\tau_{SRH} = \tau_{n_0} * \frac{p_0 + p_1 + \Delta n}{n_0 + p_0 + \Delta n} + \tau_{p_0} * \frac{n_0 + n_1 + \Delta n}{n_0 + p_0 + \Delta n} \qquad \text{Eq. 18}$$

Where:

n_1, p_1 are the SRH densities defined such as:

$$n_1 = N_C * \exp\left(-\frac{E_C - E_t}{k_B T}\right), \quad p_1 = N_V * \exp\left(-\frac{E_t - E_V}{k_B T}\right) \qquad \text{Eq. 19}$$

With E_t the energy level of the defect in the bandgap of the material.

τ_{n_0}, τ_{p_0} are the capture time constants of electrons and holes such as:

$$\tau_{n_0} = (N_t \sigma_n v_{th})^{-1}, \tau_{p_0} = \left(N_t \sigma_p v_{th}\right)^{-1} \qquad \text{Eq. 20}$$

With:

N_t the defect density at energy level E_t [cm^{-3}], σ_n and σ_p the capture coefficients of electrons and holes of the defect [cm^2], v_{th} the thermal velocity of the material – defined

as the average velocity of minority carrier by Brownian motion – approximately equal to $1 * 10^7$cm/s for Silicon at 300K [31].

1.2.3.1.4 Surface recombination

An extended SRH-recombination formalism is usually used to express surface recombination rate [32]:

$$U_{surf} = \frac{(n_0 + \Delta n_S)(p_0 + \Delta p_S)}{\frac{p_0 + p_1 + \Delta n_S}{S_{n0}} + \frac{n_0 + n_1 + \Delta n_S}{S_{p0}}} \quad \text{Eq. 21}$$

Where Δn_S and Δp_S are the excess carrier electron and hole densities near the surface, n_1 and p_1 are the SRH densities of the surface defect, S_{n0} and S_{p0} are the surface recombination velocities of electron and holes defined such as:

$$S_{n0} = N_{t,surf}\sigma_n v_{th} \quad , \quad S_{p0} = N_{t,surf}\sigma_p v_{th} \quad \text{Eq. 22}$$

Where $N_{t,surf}$ is the density of traps at the surface, and σ_n & σ_p are the capture coefficient of electrons and holes of this surface defect.

However the expression for the lifetime limited by surface recombination is not straightforward as band-bending close to the surface implies that $\Delta n_S \neq \Delta p_S$ [32]. Thorough calculations need to be assessed from numerical modelling [33]–[35].

1.2.3.2 Optical losses

In the energy range where photons can be absorbed by the absorber, i.e. when their energy is higher than the bandgap energy of the absorber material, there is still some non-ideal optical losses that affect efficiency, mostly through a J_{SC} diminution. Mechanisms for optical losses are (see Figure 10):

(a) Reflected light at the front electrodes, at the front surface or at interfaces
(b) Un-absorbed photons due to the finite absorbance and thickness of the absorber material, which lead to non-ideal optical confinement.
(c) Parasitic absorption, or absorption that does not participate to the current flow, such as free carrier absorption where photons are absorbed by already excited electrons, or generation of electron-hole pairs in locations where they very quickly recombine (e.g. antireflective coatings).

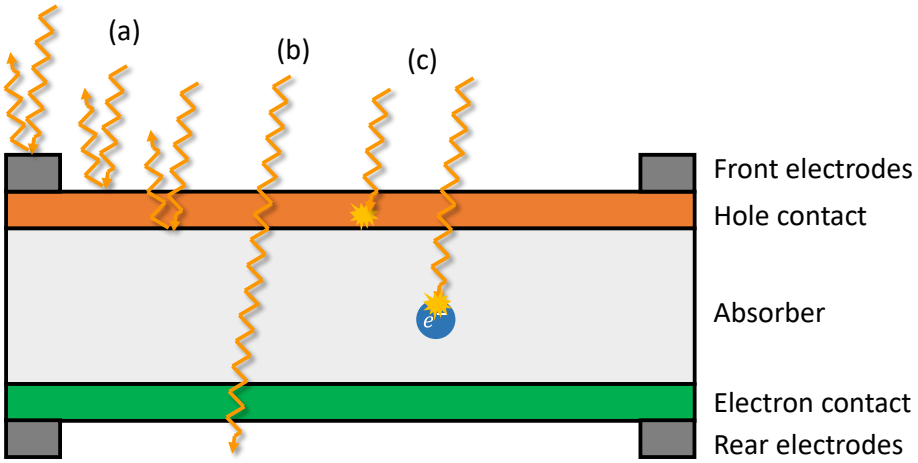

Figure 10: Drawing of a bifacial solar cell illustrating different mechanisms of optical losses: (a) reflection, (b) transmission, and (c) parasitic absorption (same considerations apply to monofacial solar cell)

1.2.3.3 Resistive losses

1.2.3.3.1 Series resistance

From their generation in the absorber to their collection in the external circuit, charge carriers experience resistive effects as they cross materials with finite resistivity, interfaces and contacts. Indeed, this generates power losses due to Joule effect. Figure 11 illustrates the path of an electron hole pair across the cell.

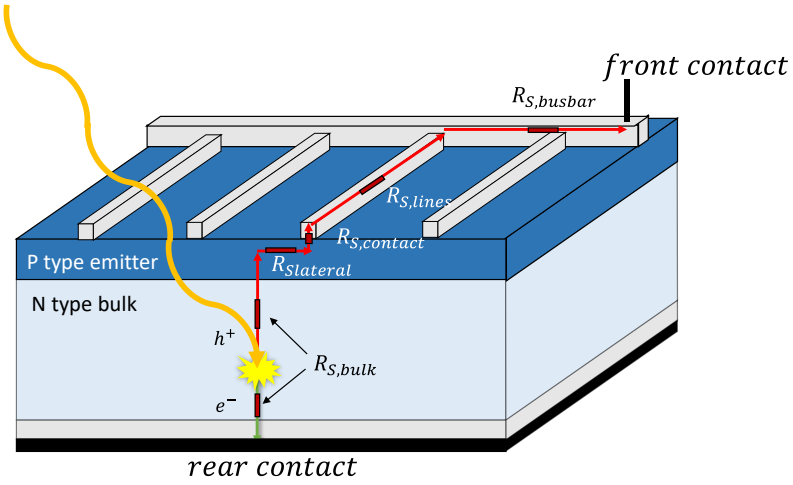

Figure 11: Drawing of the current path of electrons (green) and holes (red) from generation in the bulk to collection at the contacts

In the frame of the diode(s) model, the series resistance, denoted as R_S represents the lumped effect of all resistive effects through the cell, i.e. the conduction through all layers, interfaces, contacts and metallizations.

R_S typically has a very low impact on J_{SC} for solar cells of decent efficiencies, but can have a significant effect on FF.

A single value of R_S would only exist if the cell was homogeneous, however due to spatial heterogeneity, R_S is a function of the voltage [36]. For this reason R_S is mostly reported at maximum power point to be representative of the functioning point of the cell.

1.2.3.3.2 Shunt resistance

Shunt resistance stems from photo-generated current flowing through an alternate path than the external load, lowering the built-in potential through the device. For example, shunts can arise from edge leakage current if no proper edge isolation is carried out [37].

Shunt resistance is usually high (i.e. low current flow through the shunt paths) in high efficiency silicon solar cells [38] and we will mostly overlook it in this work.

1.2.4 Photovoltaic solar cell technologies

1.2.4.1 Mainstream silicon PV cells

The vast majority of the solar cells produced up to 2020 are based on silicon material [39]. Among the silicon cells, two technologies form the mainstream with more than 95% combined market share as of 2018 [40], the Aluminum-Back Surface Field (Al-BSF) and Passivated Emitter Rear Contact (PERC) cells.

The Al-BSF structure (see Figure 12) is the most-simple one, based on a P-type absorber. The front surface consists of a highly n-doped emitter, formed using phosphorous diffusion on the front side with an upper layer of anti-reflection coating, and fire-through metallization. The rear side features a full area aluminum contact, which upon annealing at high temperatures, enables the formation of an AlSi alloy which acts as back surface field (BSF). It allows efficiencies of 19-20 % in production as of 2018 [40].

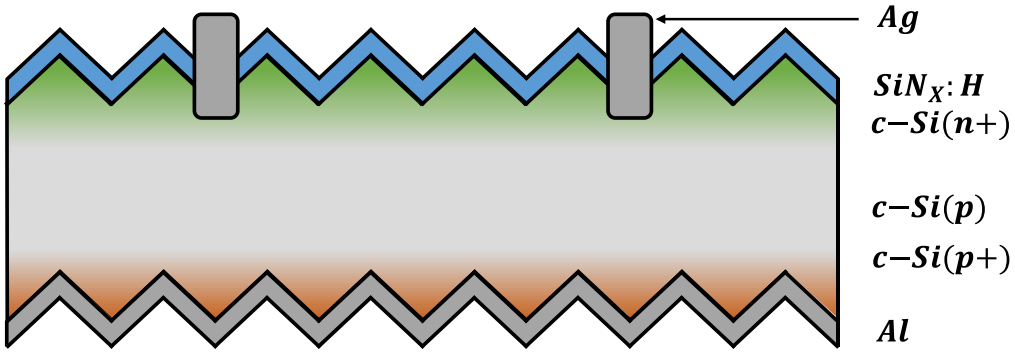

Figure 12 : the Al-BSF structure

The more limiting factor of the structure is its back contact, which is, despite the BSF, the major source of losses due to recombination. The PERC structure (see Figure 13) proposed in 1989 [41] is an evolution of the Al-BSF, which features the same front side, but a more complex rear side. To decrease recombination at the rear, a passivation stack is deposited on the c-Si at the rear contact, typically aluminum oxide and silicon nitride. However theses stacks cannot be directly used as contacts as they are insulating materials, so the contact is made through the passivation oxides, and there is still a direct c-Si(p+)/Al direct local contact. This structure enables higher efficiencies than the Al-BSF, at 20-22% in production lines [40].

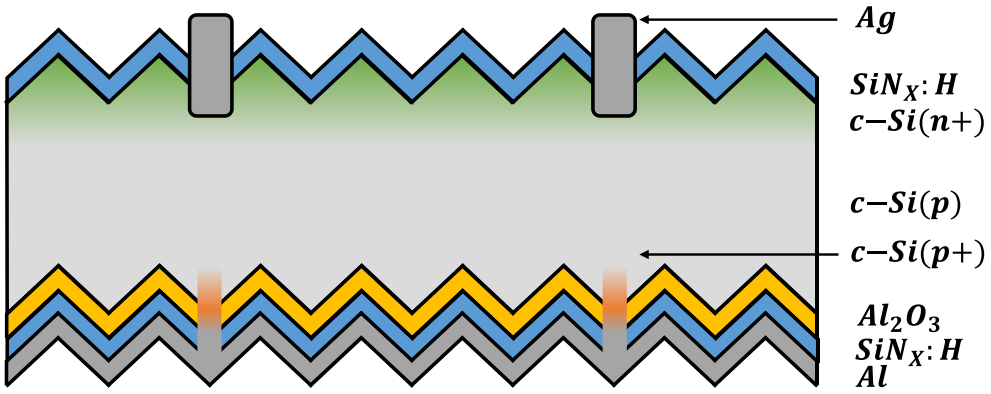

Figure 13 : the PERC structure

Due to manufacturing costs reduction [42], and monocrystalline wafer price drop [43], the total cost of PV systems has dropped over the last decade (~-66% in 6 years [40]). This makes high-efficiency devices more and more cost-efficient. For these reasons, forecasts predict that the less efficient solar cell concepts such as the Al-BSF technology may soon disappear for the profit of PERC and more evolved efficient architectures.

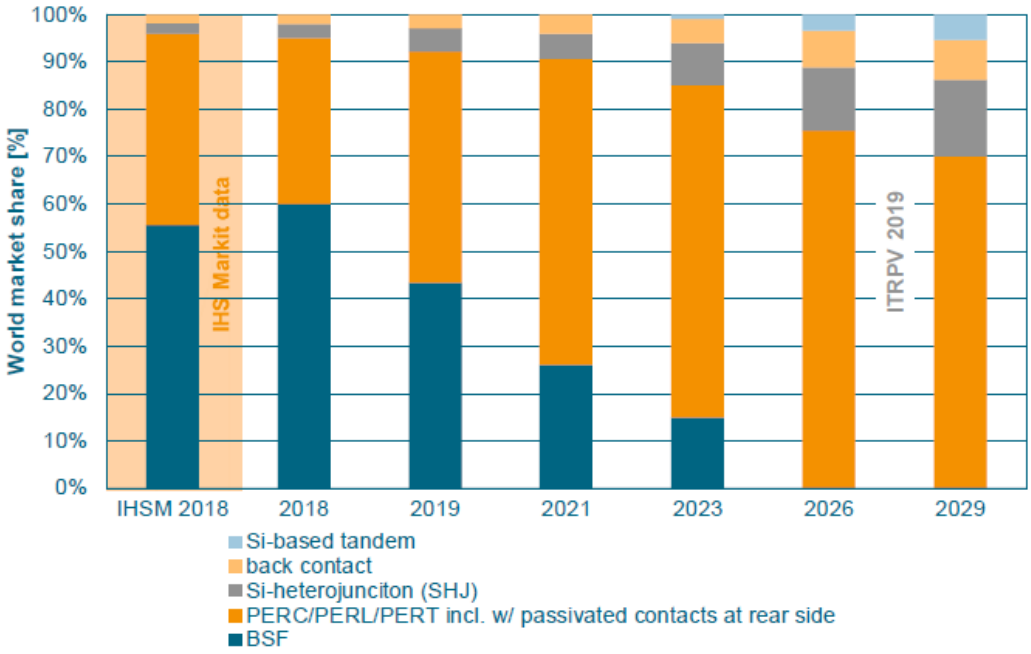

Figure 14: World market share of different silicon solar cell technologies, confirmed data and projected evolution until 2029. Taken from [7]

1.2.4.2 High efficiency silicon solar cells

The main problem with standard PV cell technology is their highly recombinative metal contact [44], thus new approaches to increase the efficiency of single junction silicon cells rely on so-called "passivating contacts". Passivating contact solar cells employ thin passivating layers in between the c-Si absorber and the metal contacts to play simultaneously contacting and passivating roles. The two predominant technologies for passivating contacts are the poly-silicon based approaches (e.g. TOPCon [45], POLO [46]) and the silicon heterojunction solar cell (SHJ).

The TOPCon structure employs a diffused emitter at the front surface, and a very thin (<20 Å) tunnel oxide combined with a poly-Si layer at the rear surface [47] (see Figure 15). The tunnel oxide passivates very effectively dangling bonds at the c-Si surface, and if thin enough, allows for efficient transport (either by tunneling or through "pinholes" conduction [48]) and therefore generates no important transport losses. The poly-Si, which is typically highly doped, is a very good selective contact thanks to its high conductivity and to the band bending it induces in the absorber. It however leads to substantial free carrier absorption, reason why it is usually put at the rear surface, and complicates its integration in both side poly-Si based contacts devices [49].

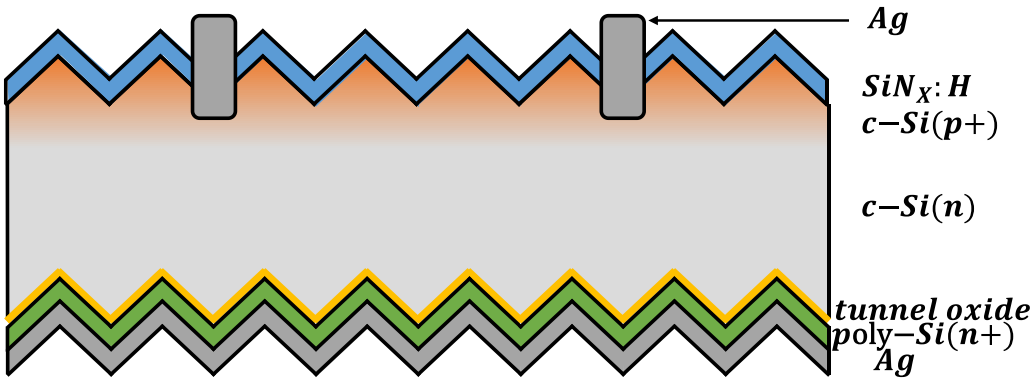

Figure 15: TOPCon solar cell

Historically, the first passivating contact structure that reached high efficiencies was the SHJ cell, but we will discuss it in the next chapter.

Additionally, both the TOPCon and the SHJ concepts have been derived in back-contact architectures, which enables better J_{SC} due to the absence of shading at the front surface and have reached very high efficiencies [46], [50].

To achieve even higher efficiencies in the near-future, beyond that of the theoretical limit of single-junction c-Si cells, silicon-based tandem solar cells are a very promising approach which still needs to be demonstrated at the production scale [49].

1.3 Objectives of this work

In this chapter, we have seen that PV energy is forecasted to be a very important source of electricity at the global scale in the near future as it provides low-carbon non-fossil energy. We have then discussed the working principles of solar cells, their main figures of merit, and the main factors limiting the efficiency of solar cells. Finally, we have discussed the main PV cell technologies in the market today, and the emerging trend for passivating contact designs enabling to reach high efficiencies that are expected to dominate the market in the near future.

This work addresses the resistive losses in silicon heterojunction solar cells. In particular, it focuses on current transport through the interfaces and contacts of the SHJ cell and how we can characterize, model, and improve it.

In Chapter 2, State-of-the-art, we will review the literature on resistive losses in silicon heterojunction solar cells. First, we will discuss the SHJ device and its pros and cons. Then we will address the measurement methods for series and contact resistances. Subsequently, we

will break down the different contributions of the series resistance and see how it can be calculated from these various inputs. Finally, we will examine charge transport in SHJ cells.

In Chapter 3, Characterization & fabrication processes, we will describe the fabrication of various samples and the main characterization methods employed during this work. We will also discuss the details of our numerical simulations.

In Chapter 4, Development of methods to measure contact resistance in SHJ cells, we will discuss our approach for the fabrication of samples to measure accurately the contact resistance of the Ag/ITO contact and the electron and hole contact stacks.

In Chapter 5, Impact of varying the fabrication process on SHJ cells and on the electron contact, we will review the various studies that we conducted to understand the influence of fabrication settings on the series and contact resistances in the device.

In Chapter 6, Impact of varying measurement conditions on SHJ cells and contacts, we will discuss how temperature and illumination influence efficiency, series and contact resistances. We will also discuss what can be learned from those regarding the transport mechanisms in SHJ cells.

In Chapter 7, Resistive power loss analysis for bifacial SHJ cells, we will derive a model to break down the series resistance of SHJ cells such as produced at CEA into different contributions, and identify the main resistive losses. We will then propose pathways for loss mitigation in such devices.

Chapter 2

State-of-the-art

In this chapter we review the state-of-the-art regarding silicon heterojunction solar cell (SHJ) cells, and their resistive losses. First, we describe the SHJ cell and examine its main advantages and weaknesses. We then discuss methods for the measurements of the series resistance of solar cells, as well as contact resistance in the device, introducing the transfer length method (TLM). We then discuss models that estimate power losses due to series resistance of classical cells, and break it down into contributions mainly in the metallization lines, in the emitter and in the contacts. Finally, we discuss carrier transport phenomena involved in SHJ cells, and examine the contact resistance between the TCO and silver metallization and the contact resistance of the c-Si(n)/a-Si:H(i)/a-Si:H(n)/ITO and c-Si(n)/a-Si:H(i)/a-Si:H(p)/ITO contact stacks.

2.1 Silicon heterojunction solar cells

The silicon heterojunction solar cell, or SHJ, is one of the most common type of passivating contact device: it allowed for record efficiencies of up to 26.7% in a back-contact design [51], and 25.1% in a more conventional industrial process with both side contacts on full area industrial wafers (>244cm^2) [52]. The CEA heterojunction lab at INES is well positioned among the competition with a certified efficiency of 25% announced recently for a both-side contacted device [53]. Figure 16 illustrates a typical n-type bifacial rear-emitter SHJ solar cell, such as produced at CEA and discussed throughout this work.

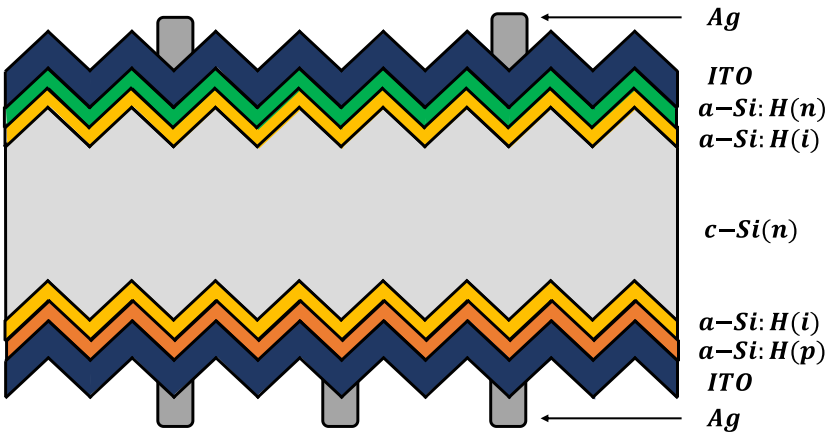

Figure 16: Bifacial rear emitter SHJ cell structure

The technology is based on the introduction of a few nanometers thin bilayers of doped and undoped hydrogenated amorphous silicon (a-Si:H) at the front and rear surface, usually using Plasma Enhanced Chemical Vapor Deposition (PECVD) technique. In most cases, the structure is based on an n-type substrate, and features a rear emitter, so the front interface will be c-Si(n)/a-Si:H(i)/a-Si:H(n) and the rear c-Si(n)/a-Si:H(i)/a-Si:H(p). These double layers act as highly selective and passivating contacts, providing high levels of both field effect and chemical passivation. Historically, the first SHJ devices only featured doped a-Si:H, the introduction by Sanyo of a second buffer layer of undoped a-Si:H in between the c-Si and doped a-Si:H was found to be necessary to reach high levels of passivation, and thus efficiency [54].

An approximately 70nm thick Transparent Conductive Oxide (or TCO), in most cases Indium Tin Oxide (ITO), is subsequently deposited on top of the a-Si:H layers. This deposition is usually carried out using Physical Vapor Deposition (PVD) but alternative techniques such as Reactive Plasma Deposition have demonstrated low ion bombardment damages [55]. The TCO serves several functions. First it facilitates lateral charge transport towards the metal electrodes thanks to its high conductivity oppositely to a-Si:H layers which are very resistive. Additionally, it plays a role in contact formation of the electron and hole selective contact stacks, and lastly it acts as an antireflective coating. It therefore requires adequate electrical properties, good contact properties with both the a-Si:H layer and the metallization, and proper optical properties. The ITO properties can be tuned by varying the Indium/Tin ratio, the oxygen content, or by introducing hydrogen or other compounds such as Cerium [56].

Finally, low-temperature Ag pastes are deposited using screen-printing, and the cell is annealed at approximately 200°C. This anneal both cures the pastes and improves the electrical

properties of the ITO [57] and its contact with a-Si:H layers [58]. At the CEA heterojunction lab we work on bifacial devices, with both front and rear metallization grids.

The front a-Si:H(i)/a-Si:H(n)/ITO and rear a-Si:H(i)/a-Si:H(p)/ITO stacks form what are commonly called the electron and hole contacts. They need to provide excellent levels of chemical and field effect passivation, low light absorption, and good contact properties with the metallization and the c-Si.

The main advantage of the SHJ cell is the outstanding level of passivation reached thanks to a-Si:H layers, allowing very high V_{OC} values above $750\ mV$ [59]. The main weak-point is a lower current density than conventional structures due to parasitic absorption in a-Si:H and ITO layers [60].

From an industrial point of view, other aspects are of importance. The low-temperature processing does not permit the gettering process that is performed for homojunction devices fabrication and allows to improve bulk quality [25], therefore high bulk lifetime materials are needed. In addition, low-temperature pastes have higher silver contents, making them more expensive, and usually exhibiting lower electric properties [60]. The use of indium is also problematic, as it is a rare material, which price is unstable [61]. At the module level, there are also some issues: SHJ interconnection cannot be done by standard soldering (too high temperature or too large quantities of silver paste requested), but two alternatives are proposed based on the SmartWire Connection Technology (from Meyer Burger) or ribbons gluing with Electrical Conductive Adhesive [62]. Finally, the capital expenditure for an SHJ fabrication line is much higher than for PERC or Al-BSF cells, because it is not yet a mainstream technology.

However, the price of high quality n-type wafers has dropped over the last decade with a material quality that keeps on improving [43]. Alternatives to the ITO such as indium-free TCOs (e.g. ZnO [63]) or completely new contact materials such as transition metal oxides [64] have been proposed. Alternative metallization technologies such as copper plating may also reduce costs and risks of material price volatility in the future as copper is cheaper and less scarce [61]. Additionally the capital expenditure of standard SHJ fabrication tools may decrease over time as happened for the PERC technology [42], allowing better competitiveness to standard devices. Finally, the nearly symmetrical structure of the SHJ cell simplifies its adaption in bifacial devices, which allows for better productivity in outdoor conditions due to the additional light from the backside [65].

Several companies have already started producing SHJ cells, pioneering the mass production of such devices, for instance Panasonic, Hevel, REC, Enel Green Power, Ecosolifer and Risen [66].

2.2 Measuring series resistance

There exists a variety of proposed methods to measure solar cell series resistance. However, there is still no consensus on the preferred method, and each one may result in slightly different R_S values [67], [68]. We will discuss what methods are preferred in this work in §3.6.

The most practical methods to determine R_S only rely on examining a single J-V curve. Some methods rely on fitting the solar cell J-V curves, under dark or illuminated conditions, with a

one or several diode(s) model. Other proposed methods are based on integration [69] or derivation [70] of the J-V curve.

However, treating R_S as a constant in the diode(s) model leads to errors: due to spatial variations of R_S (cut lines, inhomogeneous layer etc.), the global R_S often is a function of the voltage [36], [71]. All these methods determine a single value of R_S, which in addition is representative of the average R_S and not that at MPP conditions. A more accurate procedure would allow extracting R_S at the maximum power point, or for a more detailed analysis as a function of voltage. Moreover, all these methods rely on several assumptions that make them less accurate theoretically than methods that use several J-V curves measured at different illuminations [72].

The J-V curves of a solar cell measured under varying illumination hold the information of the series resistance (expressed in $\Omega.cm^2$). Indeed, current is proportional to illumination, and Joule power losses (in $W.cm^{-2}$) are such as:

$$P_{loss} = R_S J^2 \qquad \text{Eq. 23}$$

Therefore, as illumination intensity increases, the J-V characteristic is more impacted by R_S. Figure 17 shows different J-V curves following a two-diodes model (see Eq. 13) generated with the same parameters ($n_1, n_2, J_{01}, J_{02}, R_S, R_{Sh}$). Each curves measured at an illumination of x Suns is shifted by a current ΔJ so that all curves are superposed at $J = J_{SC1}$:

$$\Delta J = J_{SC1} - J_{SCx} \qquad \text{Eq. 24}$$

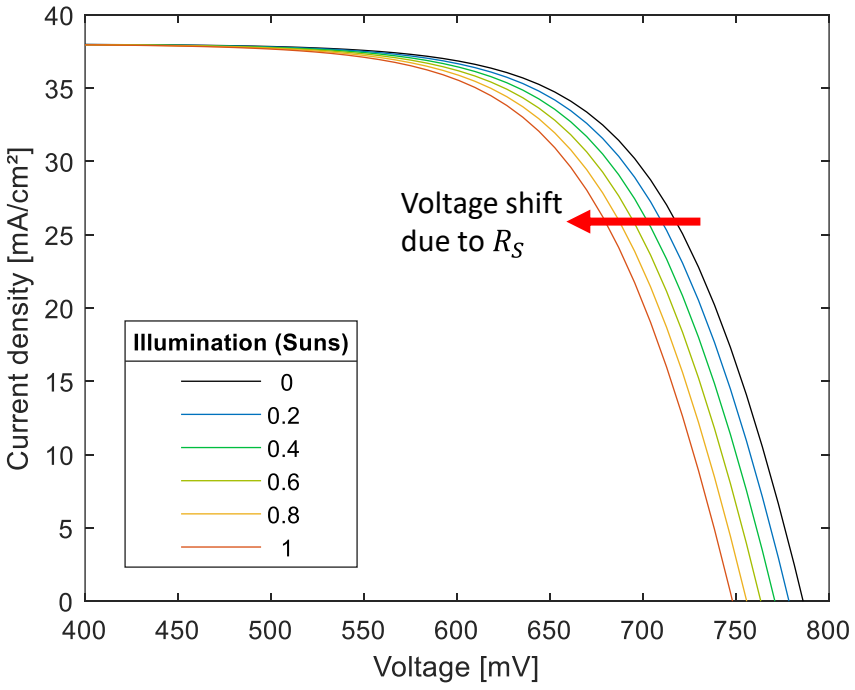

Figure 17: J-V curves generated for the same cell parameters shifted so that their J_{SC} match

In the simple description of a solar cell as a diode characteristic shifted by a photogenerated current (see Eq. 8), J-V curves at different illuminations should superimpose when shifted this way (i.e. all curves should equal the shifted dark J-V in Figure 17). However, when considering

R_S (Eq. 12), a voltage difference occurs due to different Joule power losses as currents differ (i.e. shifted J-V curves do not match the dark J-V one in Figure 17). From this potential difference, R_S can be extracted. Of course this relies on the hypothesis that the only parameter responsible for this variation with illumination level is R_S, otherwise this introduces error. However, it is well known that lifetime and therefore J_0 and n parameters, are functions of the injection level (e.g. [24]). This means a certain bias is unavoidable.

- The dual-light method (DLM) [67] uses two J-V curves at illumination intensities E_1 and E_2. By shifting vertically the J-V curves by respectively $+\Delta J/2$ and $-\Delta J/2$ in order to make the curves representative of an intermediate illumination E, and match at $V = 0$ (see Eq. 24), R_S reads:

$$R_{S_{DLM}}(\Delta J) = \frac{V_2(\Delta J) - V_1(\Delta J)}{J_{SC1} - J_{SC2}} \qquad \text{Eq. 25}$$

  Where V_1 and V_2 are the voltages of each curve at a given ΔJ, and J_{SC1} and J_{SC2} are the short circuit current of both curves. Now, this can be plotted as a function of voltage by stating $V(\Delta J) = \frac{V_1+V_2}{2}$.
  Typically, E_1 is chosen slightly above 1Sun (e.g. 1.1 Sun) and E_2 slightly below (e.g. 0.9 Suns) in order to be centered around 1 Sun with low variations of injection level in the functioning cells. The derivation of Eq. 25 from the 1-diode model is proposed in Appendix 3 (a).

- The multi-light method (MLM) uses the same approach but averages over multiple illumination intensities (E_i). For the mean illumination level, R_S reads [36]:

$$R_{S_{MLM}}(J) = \left| \frac{\sum_{i=1}^{i=N} \left(V_i(\Delta J) - \overline{V(\Delta J)}\right)^2}{\sum_{i=1}^{i=N} \left(V_i(\Delta J) - \overline{V(\Delta J)}\right)\left(J_i(\Delta J) - \overline{J(\Delta J)}\right)} \right| \qquad \text{Eq. 26}$$

  Where V_i and J_i are the voltages of each involved J-V curve, and $\bar{V}$ and $\bar{J}$ are the average voltage and current density, all for a given ΔJ.
  Again, illumination levels are typically chosen centered on and close to 1Sun illumination. See Appendix 3 (b) for more details.

- The dark/light method (LIV-DIV) uses an J-V curve at a given illumination, typically 1Sun, and the dark J-V. Similarly to the DLM method, the dark J-V curve is shifted such as in Figure 17 and the R_S is mostly calculated from the voltage difference:

$$R_{S_{LIV-DIV}}(J) = \frac{V(J) - V_{dark}(J) + J_{dark}(J)R_{S,dark}}{J_{dark}(J) - J_{SC}} \qquad \text{Eq. 27}$$

  Where V_{dark} and J_{dark} are the voltage and shifted current density of the dark J-V curve, $R_{S,dark}$ is the R_S in the dark, and can be calculated at V_{OC} (corresponding to $J_{dark} = -J_{SC}$) from:

$$R_{S,dark} = \frac{V_{OC} - V_{dark}(J_{dark} = -J_{SC})}{J_{SC}} \qquad \text{Eq. 28}$$

  The assumption of equal R_S in the dark and under illumination is usually not verified: current paths in the dark differ significantly from the illuminated case, as current is

injected from the contacts and not photo-generated across the absorber, which leads to a different value of $R_{S_{dark}}$ and R_S [36].
Derivation of Eq. 27 and Eq. 28 from the 1-diode model is proposed in Appendix 3 (c).

- Another method consists in V_{OC} and J_{SC} measurements as a function of the illumination intensity. Indeed, at V_{OC}, there is no current, so the voltage is unaffected by R_S. At J_{SC}, as long as the cell is of decent quality so that the approximation $J_{SC} = J_L$ holds, R_S has no impact either. Varying light intensity varies J_{SC} and V_{OC} and allows to plot each couple of $J_{SC} - V_{OC}$ values in a J-V plot. When shifted by J_{SC} it is representative of a solar cell as unaffected by R_S, and is alternatively called the pseudo J-V curve (see example in Figure 18 below).

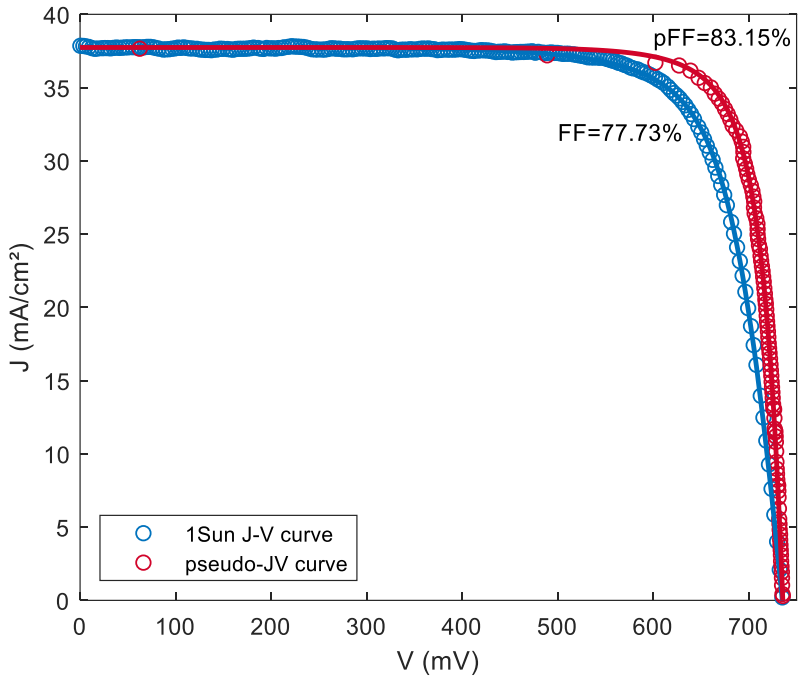

Figure 18: J-V curve and pseudo J-V curve of an SHJ solar cell strongly affected by R_s

At a given current, R_S can be determined from the potential difference between the J-V and pseudo J-V curves (see derivation in Appendix 3(d)):

$$R_{S,JscVoc-JV}(J) = \frac{V(J) - V_{OC,shifted}(J)}{J} \qquad \text{Eq. 29}$$

- A convenient alternative is to measure the fill factor of the pseudo J-V curve, also called pseudo-fill factor (pFF), and to compare it to FF such as [73]:

$$R_S(V_{mpp}) = (pFF - FF) * \frac{J_{SC}V_{OC}}{J_{mpp}^2} \qquad \text{Eq. 30}$$

This can only yield a result at MPP, but is a fast way to obtain a value of series resistance from the easily obtained J-V and pseudo J-V parameters without the necessity of any graphic calculations.

Alternatively Eq. 30 can be used to calculate the FF loss due to R_S:

$$\Delta FF_{R_S} = R_S * \frac{J_{mpp}^2}{J_{SC}V_{OC}} \quad \text{Eq. 31}$$

And in turn, efficiency loss due to R_S:

$$\Delta\eta_{R_S} = \frac{J_{SC}V_{OC}\Delta FF_{R_S}}{P_{in}} \quad \text{Eq. 32}$$

Where P_{in} is the power of the incident light.

In theoretical grounds, the method that uses the less assumption and that should therefore be more precise is the $J_{SC} - V_{OC}$ method, followed by the LIV/DIV and DLM/MLM methods [72]. Experimentally, the $J_{SC} - V_{OC}$ and LIV/DIV methods have been shown to yield very close results while being more reproducible than the DLM method [68]. We will discuss which methods were chosen in this work in §3.6.

2.3 Measuring contact resistance

2.3.1 The transfer length method (TLM)

The most common approach to measure contact resistances is the Transfer Length Method (TLM). The method was first proposed [74] by Shockley in 1964, and formalized in 1969 by Berger [75].

Let us consider planar contacts of length L and width W on a layer of sheet resistance R_{Sh} deposited on an insulating substrate (see Figure 19 (a)).

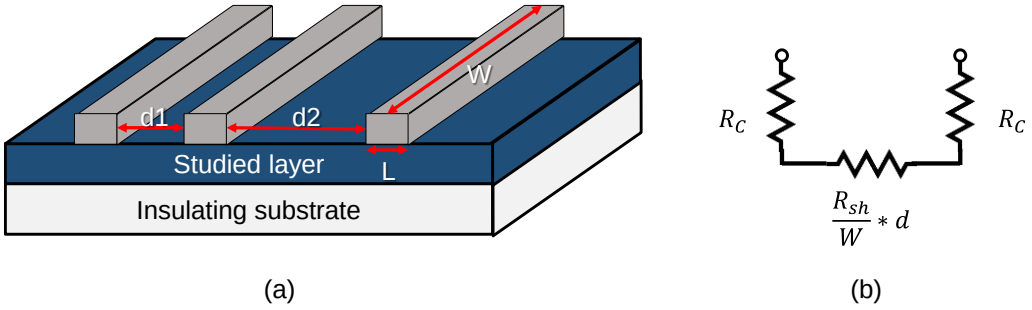

Figure 19 : (a) planar contact structure (b) simple equivalent circuit of a measurement in between two consecutive electrodes

If the contact is ohmic, the IV characteristic between two consecutive electrodes will be linear and symmetric for both polarities. The inverse slope of the IV curve allows to determine a resistance, and as can be seen on the equivalent circuit of the measurement (Figure 19 (b)), it can be expressed such as:

$$R_{TLM}(d) = 2R_C + \frac{R_{Sh}}{W} * d \quad \text{Eq. 33}$$

By varying the inter-electrode spacing d one can plot $R_{TLM} = f(d)$, and extract from the slope and y-intercept the sheet resistance of the layer and the contact resistance between the electrode and the studied layer, respectively.

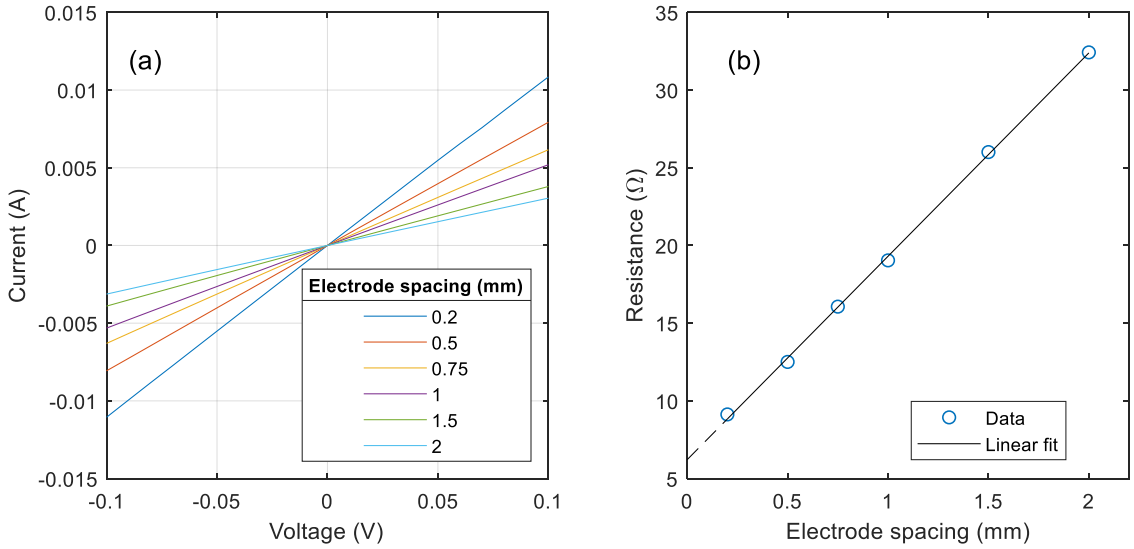

Figure 20 : **(a)** I-V curves measured at different inter-electrode distances in a TLM structure and **(b)** measured resistance as function of electrode spacing (TLM curve)

However, R_C is not a representative metric for a contact, as it depends on contact geometry (L and W). A more representative metric is the contact resistivity, ρ_C [$m\Omega.cm^2$], defined such as :

$$\rho_C = \lim_{\Delta A_C \to 0} Rc\, A_C \qquad \text{Eq. 34}$$

Where A_C is the contact area ($A_C = LW$).

In the case of perfectly homogeneous current below the contact, a simple expression of $\rho_C = R_C * A_C$ could be achieved. However, this is usually not the case as the current will tend to accumulate below the inner edge of the contact.

The concept of transfer length (L_t) was first proposed by Shockley in 1964 [74], to take into account the effective distance over which the electric contact spreads. L_t is defined such as:

$$L_t = \sqrt{\frac{\rho_C}{R_{Sh}}} \qquad \text{Eq. 35}$$

By using the transmission line model, on can demonstrate Eq. 36 [75]. A thorough demonstration of the TLM model is found in Appendix 1.

$$R_C = R_{Sh} * \frac{L_t}{W} * \coth\left(\frac{L}{L_t}\right) \qquad \text{Eq. 36}$$

L_t can be determined by solving Eq. 36 for L_t. Note that the equation can be solved easily only in two boundary cases:

- When $L \gg L_t$ where the hyperbolic cotangent tends to unity ; which is known as the "**long contact**" approximation:

$$R_C = R_{Sh} * \frac{L_t}{W} = \frac{\rho_C}{L_t W} \qquad \text{Eq. 37}$$

- When $L_t \gg L$, where the hyperbolic cotangent term tends to L_t/L ; which is known as the "**short contact**" approximation:

$$R_C = R_{Sh} * \frac{L_t^2}{LW} = \frac{\rho_C}{LW} \qquad \text{Eq. 38}$$

For the intermediate cases, Eq. 36 needs to be solved numerically for L_t. Once L_t is determined contact resistivity can be assessed from Eq. 35:

$$\rho_C = R_{Sh} L_t^2 \qquad \text{Eq. 39}$$

2.3.2 Transfer length model for a two-layer system

The TLM model is only valid in the hypothesis of current conduction in a single layer. However, there is a model in the literature allowing to consider the TLM model in a two-layer configuration separated with an interface, detailed by Huang et al. [76]. This model is more representative of the front side of a rear-emitter SHJ cell, with the ITO and c-Si layers separated by an ohmic interface characterized by a contact resistivity (see Figure 21).

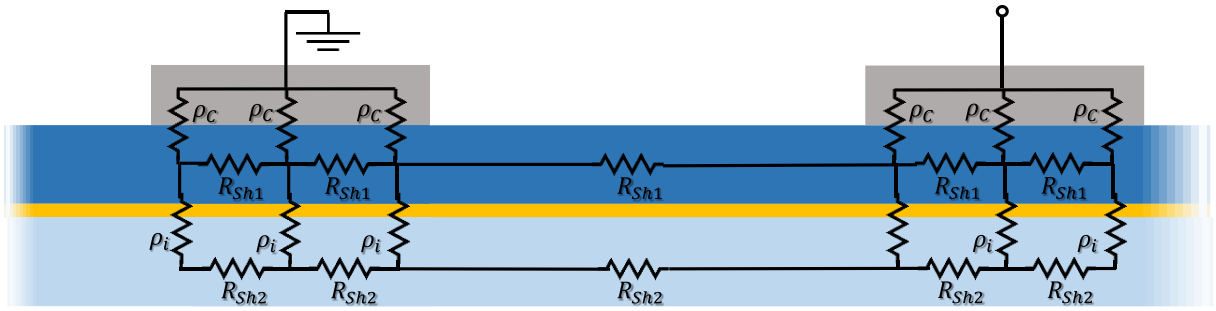

Figure 21: Two-layer TLM model depiction

Where R_{Sh1} and R_{Sh2} are the sheet resistances of each layer, ρ_C is the contact resistivity between the first layer and the electrode, and ρ_i is the contact resistivity of the interface between the two layers. d, W and L are defined such as in the one-layer model in previous paragraph.

The methodology for the demonstration of the model is very similar to the demonstration of the one-layer TLM, however its resolution is more complicated as it implies solving matrix problems. For more details on the demonstration see [76].

Total resistance can still be split into two contributions, from layer and contact subparts:

$$R_{tot}(d) = 2 * R_C(d) + R_{layer}(d) \qquad \text{Eq. 40}$$

Huang's model then gives a simple expression for R_{layer}:

$$R_{layer}(d) = \left(\frac{1}{R_{Sh1}} + \frac{1}{R_{Sh2}}\right)^{-1} * \frac{d}{W} \qquad \text{Eq. 41}$$

However, for R_C the expression is quite cumbersome and reads:

$$R_C = \frac{1}{(\lambda_p - K) * G_p + (\lambda_n - K) * G_n} * \frac{R_{Sh1} - K R_{Sh2}}{R_{Sh1} + R_{Sh2}} \qquad \text{Eq. 42}$$

Where K, $\lambda_{p,n}$, $G_{p,n}$ are defined such as:

$$K = \frac{(\lambda_p F_p + \lambda_n F_n) * \tanh\left(\frac{\xi d}{2}\right) + 1}{(F_p + F_n) * \tanh\left(\frac{\xi d}{2}\right) - 1} \qquad \text{Eq. 43}$$

$$\lambda_{p,n} = -\frac{\xi^2 \frac{R_{Sh1}}{R_{Sh1}+R_{Sh2}}}{\eta_{p,n}^2 - \xi^2 * \frac{R_{Sh2}}{R_{Sh1}+R_{Sh2}}} \quad \text{Eq. 44}$$

$$G_{p,n} = \frac{W\eta_{p,n}}{R_{Sh2}} * \frac{1}{\lambda_{p,n}-\lambda_{n,p}} * \left(1 - \lambda_{n,p} * \frac{R_{Sh2}}{R_{Sh1}}\right) \tanh(\eta_{p,n}L) \quad \text{Eq. 45}$$

With ξ, $\eta_{p,n}$ and $F_{p,n}$ reading:

$$\xi = \sqrt{\frac{R_{Sh1}+R_{Sh2}}{\rho_i}} \quad \text{Eq. 46}$$

$$\eta_{p,n} = \frac{1}{\sqrt{2}} * \left(\frac{R_{Sh1}}{\rho_C} + \xi^2 \pm \sqrt{\left(\frac{R_{Sh1}}{\rho_C} + \xi^2\right)^2 - 4 * \frac{R_{Sh1}R_{Sh2}}{R_{Sh1}+R_{Sh2}} * \frac{\xi^2}{\rho_C}}\right)^{\frac{1}{2}} \quad \text{Eq. 47}$$

$$F_{p,n} = \frac{\eta_{p,n}}{\xi} * \frac{1}{\lambda_{p,n}-\lambda_{n,p}} * (1+\lambda_{n,p}) * \tanh(\eta_{p,n}L) \quad \text{Eq. 48}$$

Note that here the R_C term is also a function of d. Experimental implementation of the model cannot be done graphically such as in standard TLM, and requires fitting procedures.

2.4 Resistive power loss analysis

Contact resistance or sheet resistance are useful metrics to qualify materials or interfaces, however they do not directly give quantitative indications on how detrimental they are to solar cell efficiency. A common tool for solar cell characterization is to use "resistive power loss analysis": based on several experimental inputs such as contact resistance, sheet resistance of layers, metallization grid resistivity and geometry etc., it assesses the impact on the power loss due to R_S. Well known models have been proposed as early as 1984 by Meier et al [77]. Refinements of their approach have been proposed more recently [78], [79].

For the sake of simplicity, let us consider a basic solar cell such as depicted in Figure 22 (we will address specificities for the SHJ cell later on (Chapter 7)):

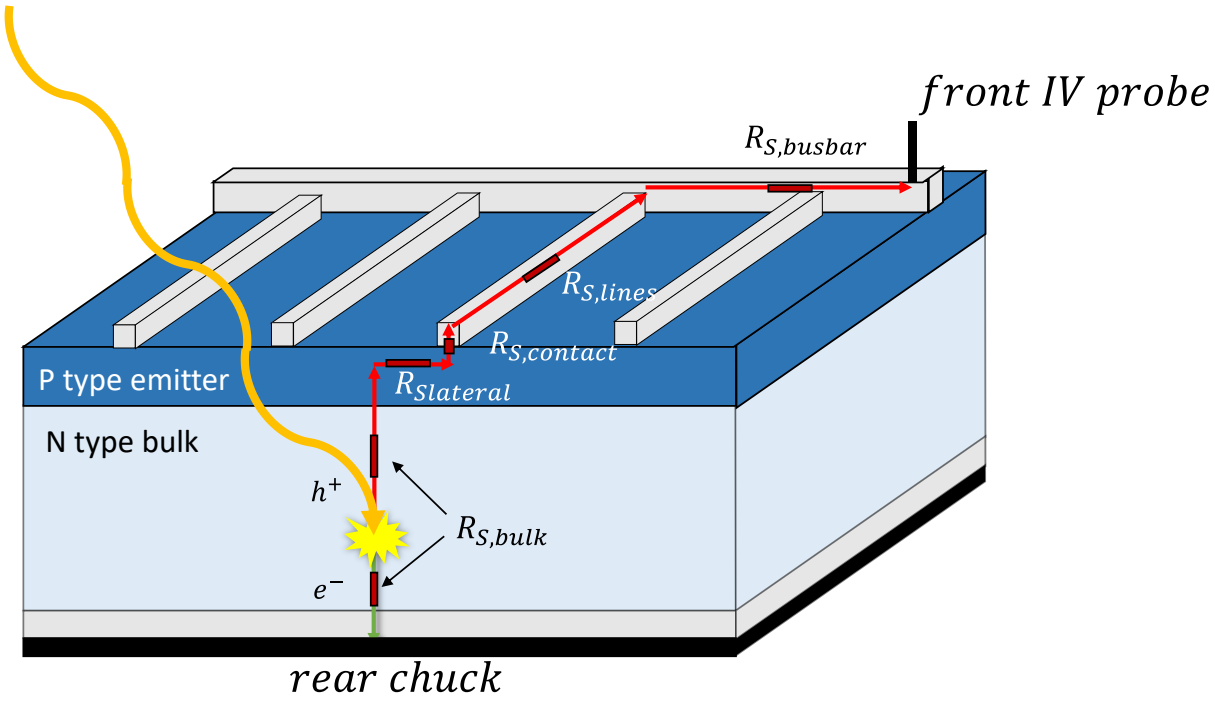

Figure 22: Drawing of the charge transport of electrons and holes from generation to collection respectively in rear and front metallizations for a simple cell structure

Once an electron-hole pair is generated, carriers will flow throughout the cell to the IV probes at the front or at the rear. The series resistance R_S is the addition of the individual contributions of resistance along the current path: bulk, contact, lines, busbars, and lateral current. We will label each contribution $R_{S,x}$, where x is the said contribution.

The most common approach to estimate losses in cells is to hypothesize that the cell can be separated into identical "unit cells" [77], [78], [80], consisting of divisible symmetry elements such as depicted in Figure 23.

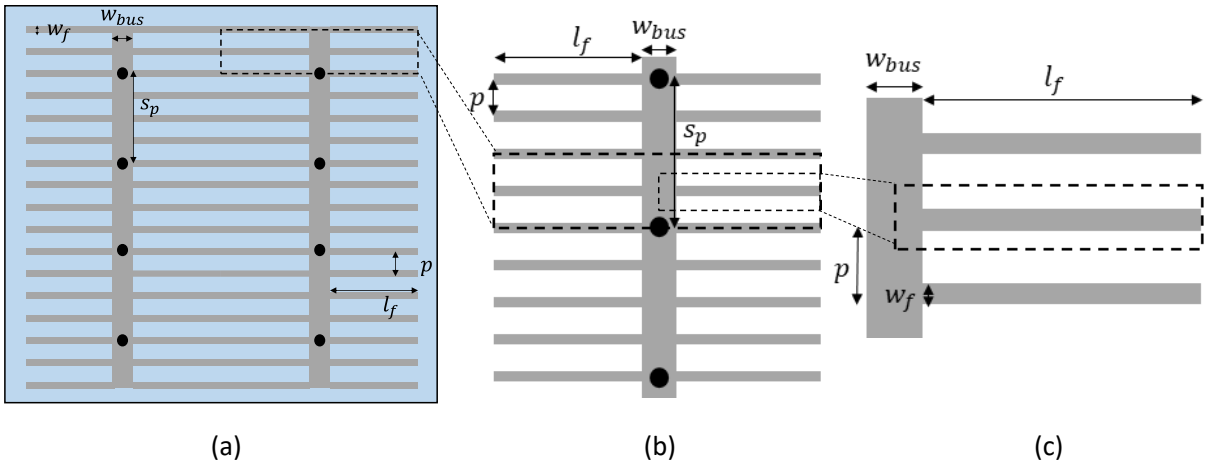

Figure 23 : Unit cells (a) unit cell #3: full cell area ; (b) unit cell #2: lines joining a busbar in between tester's IV probes; (c) unit cell #1: lines joining a busbar

The expression for the series resistance (in $\Omega.cm^2$) reads:

$$R_S = \frac{P_{loss,UC}}{I_{UC}^2} * A_{UC} \quad \text{Eq. 49}$$

Where $P_{loss,UC}$ is the power loss and I_{UC} is the current photo-generated in the unit-cell of interest of area A_{UC}.

The methodology therefore consists in calculating:

- The expression for power loss due to series resistance in each part of interest (emitter, lines, busbars etc.)
- The generated current in each unit cell
- The area of each unit cell

The total R_S calculated is then the sum of each contribution. In our example, neglecting the back contact, the total R_S can be expressed as:

$$R_S = R_{S,bulk} + R_{S,lateral} + R_{S,contact} + R_{S,fingers} + R_{Sbusbars} \quad \text{Eq. 50}$$

A few assumptions are also needed:

- No current goes directly from the emitter to the busbar, all current is directed in a straight line towards fingers, then to the busbars through the fingers, and finally to the IV tester probes.
- No current is generated under shaded areas, and generated homogeneously in non-shaded areas[2]
- Current follows a vertical path in the absorber towards the emitter

Table 1 summarizes the expressions for each of contributions to R_S. Grid parameters are represented in Figure 23, t is the wafer thickness and ρ the wafer resistivity.

Contribution to resistive power loss	**Labels**	**Expression [$\Omega.cm^2$]**
Lateral conduction in the emitter	$R_{S,lateral}$	$\frac{1}{12} * R_{Sh} * p^2$ Eq. 51
Emitter/grid contact	$R_{S,contact}$	$\frac{1}{2}\frac{\rho_C}{L_t} * p * \coth\left(\frac{w_f}{2L_t}\right)$ Eq. 52
Conduction through fingers	$R_{S,fingers}$	$\frac{1}{3} * R_{line} * p * l_f^2$ Eq. 53
Conduction through busbars	$R_{Sbusbars}$	$\frac{1}{6} * l_f * R_{bus} * s_p^2$ Eq. 54
Transverse conduction in c-Si	$R_{S,bulk}$	$\rho * t$ Eq. 55

Table 1 : Expressions for classical contributions to resistive power losses

For derivation of these expressions, see Appendix 2.

[2] Note that this hypothesis is not completely true, and another hypothesis of uniform generation over the whole cell is sometimes preferred [81]. The best hypothesis is debatable, and is discussed in the Appendix 2 (f).

However, this model is not satisfactory for power loss analysis of SHJ cells, notably due to some particularities of transport phenomena that will be addressed in the next section. We will discuss in depth how we can derive these models to our SHJ structure in Chapter 7.

2.5 Charge transport in SHJ cells

In bulk semi-conductors, charge transport mostly stems from drift-diffusion mechanisms[3]. However when considering potential barriers due to perturbations in the band structure of the system, such as a P-N junction, a heterojunction or a contact with a metal, some additional transport mechanisms are crucial.

The SHJ cell structure uses several layers in between the absorber and the metallic electrodes at both sides, with radically different properties, creating hetero-interfaces involving complex transport mechanisms in the transverse direction. These mechanisms are not yet fully understood but are generally described as a combination of phenomena such as tunneling (intra-band tunneling, band-to-band tunneling, trap-assisted tunneling), thermionic emission and hopping [82]. In addition, one has to consider lateral transport of charges (enhanced by the TCO), and device inhomogeneities (process, handling, etc.) which will affect the charge carrier transport.

In this paragraph, we will address contact formation and mechanisms for charge transport over potential barriers at contacts and interfaces. Then we will examine the different contacts and interfaces of the SHJ cell, how they can be experimentally characterized, and what is known about the phenomena at play. We will also give insights on lateral transport, and inhomogeneities.

2.5.1 TCO/Ag contact

The most common metallization technique for SHJ cell is the used of low-temperature screen-printed silver pastes contacted with the TCO at both surfaces of the cell. This forms a metal/semi-conductor contact which may significantly reduce the fill factor if not optimized properly. In this section we will address the physics of metal to semi-conductor contacts, then the specificities of the Ag/TCO contact, and finally we will talk about its characterization with the TLM technique.

2.5.1.1 Metal/Semi-conductor contacts

An ideal metal/n-type semi-conductor contact can be modelled using the so-called Schottky model [83]. When both materials are put into contact, the band alignment depends on the metal work function and on the electron affinity of the semi-conductor. We define an ideal electron barrier height for this contact such as:

$$\phi_{Bn,e^-} = \phi_M - \chi_{SC} \qquad \text{Eq. 56}$$

Depending on the position of the Fermi level, the semi-conductor experiences a band bending of varying intensity. Figure 24 illustrates different regimes of contact according to the Schottky model.

[3] Hopping transport can also take place in disordered semi-conductors at low temperatures but is not discussed in the following

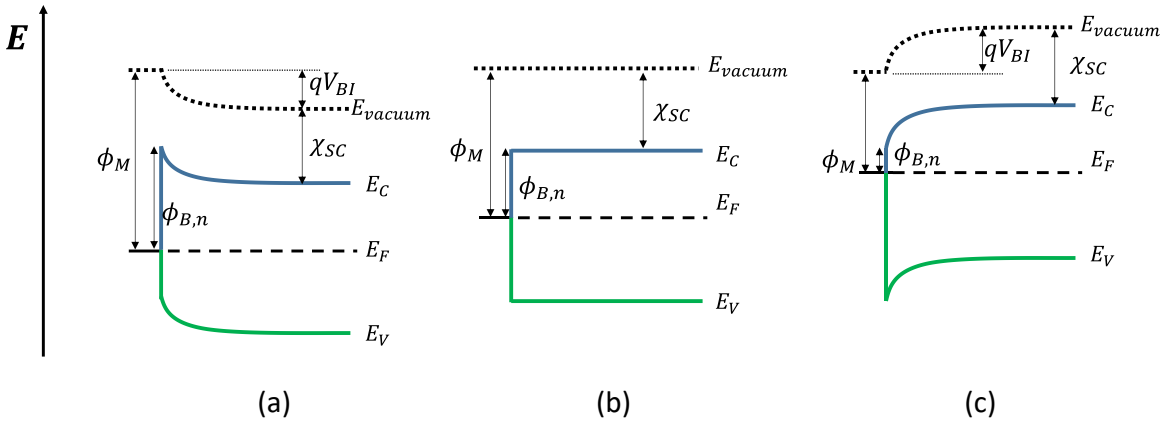

Figure 24: n-type semi-conductor contact to metals of various work function leading to (a) depletion, (b) neutral and (c) accumulation regimes

Therefore, it appears convenient to select metals that have work functions leading to an accumulation regime, as it presents the lesser barrier for electrons. However, for non-ideal contacts, charged surface states present at the interface have an impact on the band alignment, referred to as *Fermi level pinning*. An equilibrium potential can be calculated from the charge neutrality principle, and when this is the driving mechanism [84] the barrier height becomes:

$$\phi_{B,n} = \phi_{CNL} - \chi_{SC} \qquad \text{Eq. 57}$$

For all contacts, the barrier height is a combination of both phenomena:

$$\phi_{B,n} = S * (\phi_M - \phi_{CNL}) + (\phi_{CNL} - \chi_{SC}) \qquad \text{Eq. 58}$$

Where S is the "pinning factor", between 0 and 1, expressing how much the material is pinned to a given metal [85].

Additionally, the presence of a metal or good conductor near the surface of a semi-conductor induces modifications in the electric field at the interface. In electrostatics, this is usually solved using a method of image charges. The electric field at the metal semi-conductor contact reads:

$$\xi = \sqrt{2q\frac{N_D}{\epsilon_r\epsilon_0}\left(V_{BI} - V - \frac{k_B T}{q}\right)} \qquad \text{Eq. 59}$$

Where ϵ_r is the dielectric constant of the material and $\epsilon_0 \sim 8.85 * 10^{-10} F.cm^{-1}$ the vacuum permittivity, and V_{BI} the built-in potential, express in the case of depletion such as:

$$qV_{BI} = \phi_{B,n} - (E_C - E_F)$$

This results in what is commonly referred to as *image force lowering*. The effective barrier height is reduced by a factor $\Delta\phi$ that can be expressed as [86]:

$$\Delta\phi = \sqrt{\frac{q\xi}{4\pi\epsilon_r\epsilon_0}} \qquad \text{Eq. 60}$$

The barrier height considering this effect is therefore:

$$\phi_B = \phi_{B,n} - \Delta\phi \qquad \text{Eq. 61}$$

To overcome such potential barriers, two important transport mechanisms take place at a metal/semi-conductor contact in addition to the drift-diffusion mechanisms: thermionic emission and tunneling. Thermionic emission is a process in which electrons overcome a potential barrier through thermal excitation while tunneling refers to quantum tunneling over the barrier. Thermionic emission typically is the main transport mechanisms for low doping (Figure 25 (a)), and tunneling becomes dominant for high doping (Figure 25 (b)).

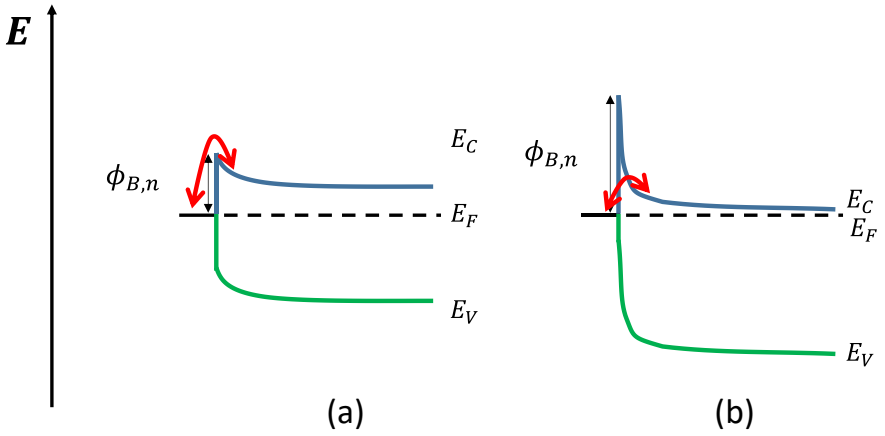

Figure 25: Thermionic emission (a) and tunneling (b) transport mechanisms at a metal/semi-conductor contact

First considering only thermionic emission (TE), electrons can overcome the barrier when their energy is over $E_F + \phi_{Bn,e^-}$. Current densities from the semi-conductor to the metal and vice-versa can be expressed such as:

$$J_{SC\to M}(TE) = A^*T^2 * \exp\left(-\frac{\phi_B}{k_BT}\right)\exp\left(\frac{qV}{k_BT}\right) \quad \text{Eq. 62}$$

$$J_{M\to SC}(TE) = A^*T^2 * \exp\left(-\frac{\phi_B}{k_BT}\right) \quad \text{Eq. 63}$$

The total electron current density is therefore:

$$J_{e^-}(TE) = A^*T^2 * \exp\left(-\frac{\phi_B}{k_BT}\right)\exp\left(\frac{qV}{k_BT} - 1\right) \quad \text{Eq. 64}$$

And the contact resistivity can then be defined as:

$$\rho_C = \lim_{\Delta A_C\to 0}\left(\frac{\delta V}{\delta J}\right)_{V=0} \quad \text{Eq. 65}$$

This leads to an expression of contact resistivity in the case of thermionic emission [87]:

$$\rho_C(TE) = \frac{1}{A_n^*} * \frac{k_B}{qT} * \exp\left(q\frac{\phi_B}{k_BT}\right) \quad \text{Eq. 66}$$

Where A_n^* is the effective electron Richardson's constant, defined as:

$$A_n^* = 4 * \pi q k_B^2 * \frac{m_e^*}{h^3} \quad \text{Eq. 67}$$

Where m_e^* is the effective mass of the electron in the semi-conductor, and h is Planck's constant (h~$6.626 * 10^{-34} J.s$).

In the opposite case of purely tunneling transport, also referred to as *field emission* (FE), ρ_C can be expressed as [17]:

$$\rho_C(FE) = C_{FE} * \frac{1}{A_n^*} * \frac{k_B}{qT} * \exp\left(q\frac{\phi_B}{E_{00}}\right) \quad \text{Eq. 68}$$

Where E_{00} is the characteristic energy for tunneling defined as:

$$E_{00} = \frac{qh}{4\pi}\sqrt{\frac{N_D}{\epsilon_r \epsilon_0 m_{e^-}^*}} \quad \text{Eq. 69}$$

And C_{FE} is a coefficient such as [18]:

$$C_{FE} = \left[\frac{\pi}{\sin\left(\frac{\pi k_B T}{2E_{00}} ln\left(-\frac{4\phi_B}{(E_C - E_F)}\right)\right)} - \frac{2E_{00}}{k_B T ln\left(-\frac{4\phi_B}{(E_C - E_F)}\right)} \exp\left(-\frac{E_F\, ln\left(-\frac{4\phi_B}{(E_C - E_F)}\right)}{2E_{00}}\right)\right]^{-1} \quad \text{Eq. 70}$$

Where E_F is the Fermi level (with respect to the conduction band edge)

Finally, for mixed cases, *thermionic field emission* (TFE), ρ_C reads [87]:

$$\rho_C(TFE) = C_{TFE} * \frac{1}{A_n^*} * \frac{k_B}{qT} * \exp\left(q\frac{\phi_B}{E_0}\right) \quad \text{Eq. 71}$$

Where E_0 is:

$$E_0 = E_{00} \coth\left(\frac{E_{00}}{k_B T}\right) \quad \text{Eq. 72}$$

And [88]:

$$C_{TFE} = \frac{k_B T \cosh\left(\frac{E_{00}}{k_B T}\right)\sqrt{\coth\left(\frac{E_{00}}{k_B T}\right)}}{\sqrt{\pi(\phi_B - (E_C - E_F))E_{00}}} \exp\left(-E_F\left(\frac{1}{E_0} - \frac{1}{k_B T}\right)\right) \quad \text{Eq. 73}$$

2.5.1.2 Transport mechanisms at the metal/TCO contact

The mechanisms of transport at metal/ITO contacts seem to be dominated by Field-Emission and Thermionic-Field-Emission, as TCO doping are on the order of $N_D > 10^{19} cm^{-3}$. The metal/semi-conductor contact theory predicts that ρ_C should decrease with increasing TCO carrier density, but it is not always the case experimentally [65], [67]. Barraud et al. reported that hydrogenated indium oxides (IO:H) feature very different contact resistivities when water partial pressure is varied, while the charge density stays quite constant, and hypothesized that this may be due to silver oxides forming at the TCO/metal contact [90]. Schube et al. also observed deviations from the expected trend when high temperatures are used for the curing (T=350°C), and they attribute this to cavities forming at the TCO/metal contact due to differing surface energies between the ITO and the silver particles [89].

2.5.1.3 Measuring the Ag/ITO contact resistance

The easiest way to extract the contact resistance between a layer and a metal is to deposit this layer on an insulating substrate, prior to the TLM electrodes deposition. This method has often been used to measure the Ag/ITO contact by depositing ITO on glass substrates e.g. in [91]. This allows a straight-forward measurement as all the current goes only into the ITO, however

it lacks representativeness to the final device, as ITO may grow differently on a glass substrate and a textured c-Si surface [57].

For classical solar cells, contact resistance measurements are carried out at the front emitter side, by screen-printing TLM electrodes instead of a conventional solar cell design. As the PN junction confines the current in the thin emitter, the emitter/electrode contact resistance as well as the emitter sheet resistance can be extracted by TLM [87]. Similarly, in rear emitter SHJ cells, the Ag/TCO at the rear emitter side can be measured by TLM [89]. The c-Si(n)/a-Si:H(p) heterojunction confines the current in the TCO layer- as the a-Si:H(p) emitter has a very large resistivity it does not participate in lateral transport- (see Figure 26). In the following, we label these samples such as "**p-side ITO/Ag TLM samples**".

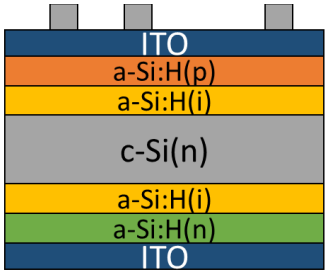

Figure 26: p-side ITO TLM samples' drawing

Optimized screen-printed Ag/ITO contact resistivity values are reported on the order of 0.1-2.5 $m\Omega.cm^2$ [89][92][90].

2.5.2 Transport through the interfaces of SHJ cells

2.5.2.1 Transport mechanisms at heterojunctions

Similarly to metal/semi-conductor contacts, in ideal cases, the band alignment is driven by the affinity of each contacted material [93]:

$$\Delta E_C = \chi_1 - \chi_2 \qquad \text{Eq. 74}$$

However, charged interface states at heterojunctions are playing a role in band lineup [94], alike Fermi level pinning for contacts with metals, which invalidates Eq. 74 in non-ideal cases.

The band offsets in between two materials create potential barriers, which can be overcome by thermionic emission (TE), or by intra-band tunneling (FE). Additionally, some band-to-band tunneling (B2B) can take place, especially at locations were valence and conduction bands are close to each other, such as highly doped P/N junctions: electrons (holes) tunnel from CB (VB) to the VB (CB) where they quickly recombine due to the high density of oppositely charged carriers (see Figure 27). This can happen on either side of the junction or from one side to the other. Due to the presence of defects in the bandgap or at the interface of the materials in contact, charges can tunnel through these states and recombine, leading to trap-assisted tunneling (TAT).

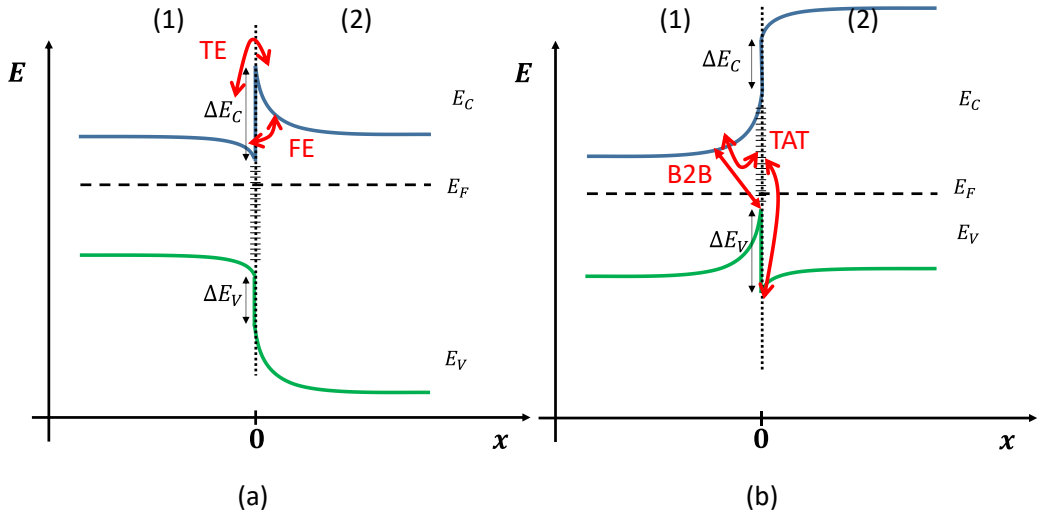

Figure 27: n/n (a) and n/p (b) heterojunctions

Several authors have proposed expressions to model such transport mechanisms, which have been implemented in commercial TCAD simulation software such as Silvaco Atlas [21] or Sentaurus [22] (their respective instruction notes propose thorough discussions of these models). Some are based on so called "local approaches" allowing to express them in terms of variables at the interface [95], [96] which allows easy implementations, while some other models account for the spatial distribution of every variable, but cannot be simply expressed in terms of analytical expressions and are harder to implement in TCAD simulations. For qualitative discussion later on, we will detail two models based on a local approach.

2.5.2.1.1 Yang's model for thermionic-field emission at heterojunctions

Yang et al. [96] proposed a model for the current across an heterojunction taking into account both thermionic and tunnel transport mechanisms. The expression for the electron current going from one side of the heterojunction (material (1)) to the other (material (2)) over a conduction band offset ΔE_C can be expressed such as [97]:

$$J_n = A^*_{n,min} T^2 (1+\delta) \left(\frac{n^{(2)}(0)}{N_C^{(2)}} - \frac{n^{(1)}(0)}{N_C^{(1)}} \exp\left(-\frac{\Delta E_C}{k_B T}\right) \right) \qquad \text{Eq. 75}$$

Where $N_C^{(1,2)}$ are the conduction band density of states for each contacted material, $n^{(1,2)}(0)$ are the electron density at the interface in each material, and $A^*_{n,min}$ is the smallest effective Richardson constant in between both materials. δ is a parameter accounting for the thermionic field mechanism, set to zero when only thermionic emission occurs, and of the form:

$$\delta = \frac{1}{k_B T} \exp\left(\frac{E_C^{(2)}(0)}{k_B T}\right) * \int_{E_{\min}}^{E_C^{(2)}(0)} \exp\left(-\frac{E}{k_B T}\right) * T(E) dE \qquad \text{Eq. 76}$$

Where $E_C^{(2)}(0)$ is the conduction band energy at the interface in material (2), $E_{\min}$ is the minimum energy required for tunneling, and $T(E)$ is the tunneling probability. For more details on the expressions of these terms refer to [96], [98].

2.5.2.1.2 Danielsson's model for band-to-band and trap-assisted tunneling

Danielsson et al. [99] proposed a model for trap-assisted tunneling in abrupt PN heterojunctions. The recombination current at the interface can be expressed such as:

$$J_{TAT} = q\frac{n_{i,n}n_{i,p}\exp\left(-\frac{q}{k_BT}\Delta\psi\right)\left(\exp\left(\frac{qV}{k_BT}\right)-1\right)}{\frac{1}{S_n}\left(p_p + n_{i,p}\exp\left(\frac{E_F-E_t}{k_BT}\right)\right)+\frac{1}{S_p}\left(n_n + n_{i,n}\exp\left(\frac{E_t-E_F}{k_BT}\right)\right)} \quad \text{Eq. 77}$$

Where all quantities are considered exactly at the interface, at the n-side or p-side depending on the subscripts. $n_{i,n}$ and $n_{i,p}$ are the intrinsic carrier densities, p_p the hole density at the p side and n_n the electron density at the n side. S_n and S_p are the surface recombination velocities, $(E_F - E_t)$ is the trap position with respect to the Fermi level, and $\Delta\psi$ is the difference in potential across the junction which can be expressed such as:

$$\Delta\psi = \Delta E_C + \frac{k_BT}{q}\ln\left(\frac{N_{C,p}n_{i,n}}{n_{i,p}N_{C,n}}\right) \quad \text{Eq. 78}$$

Where $N_{C,p}$ and $N_{C,n}$ are the conduction band densities for the p and n materials.

2.5.2.2 *Mechanisms for current transport at the electron and hole contacts of SHJ cells*

The SHJ cell band diagram at equilibrium is illustrated in Figure 28. Several band offsets are present and will lead to different transport mechanisms at the contacts and interfaces.

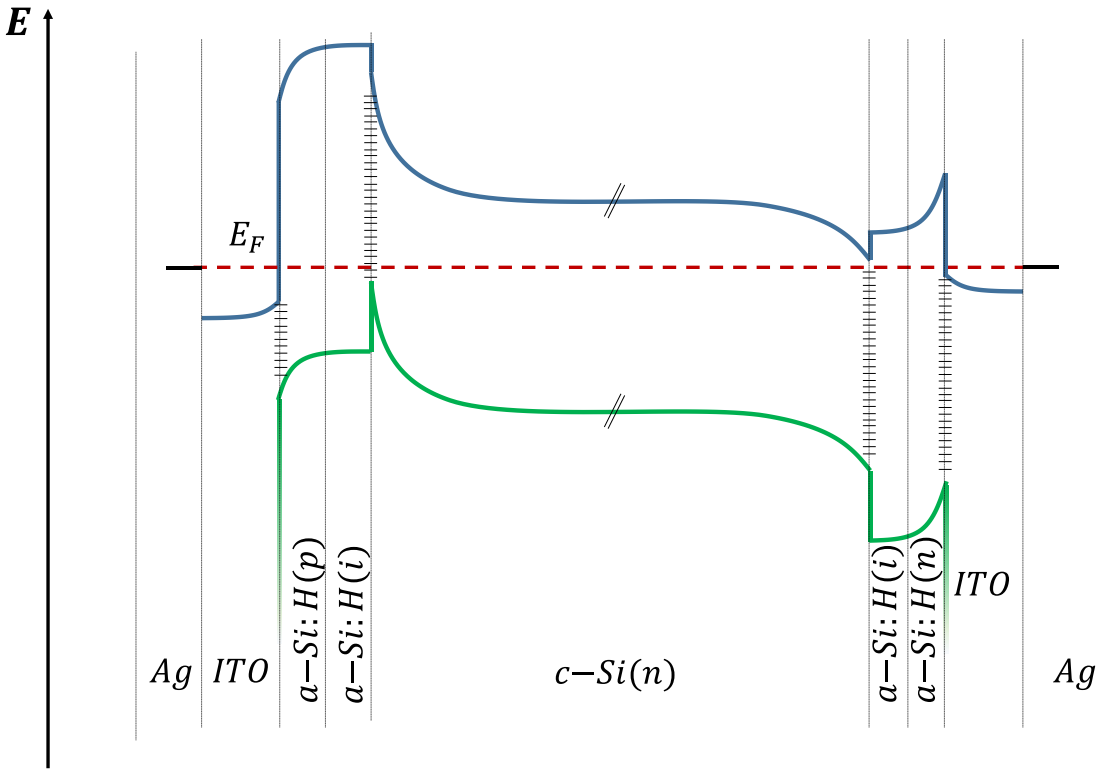

Figure 28: Band diagram of a typical SHJ cell at equilibrium. Depending on the electronic affinities and bandgaps of each layer, it is susceptible to change. As ITO is degenerated and has a very large bandgap (~4eV) the bottom of its valence band is not represented for convenience

First, we focus on the c-Si(n)/a-Si:H(i+n)/ITO interface, illustrated in Figure 29.

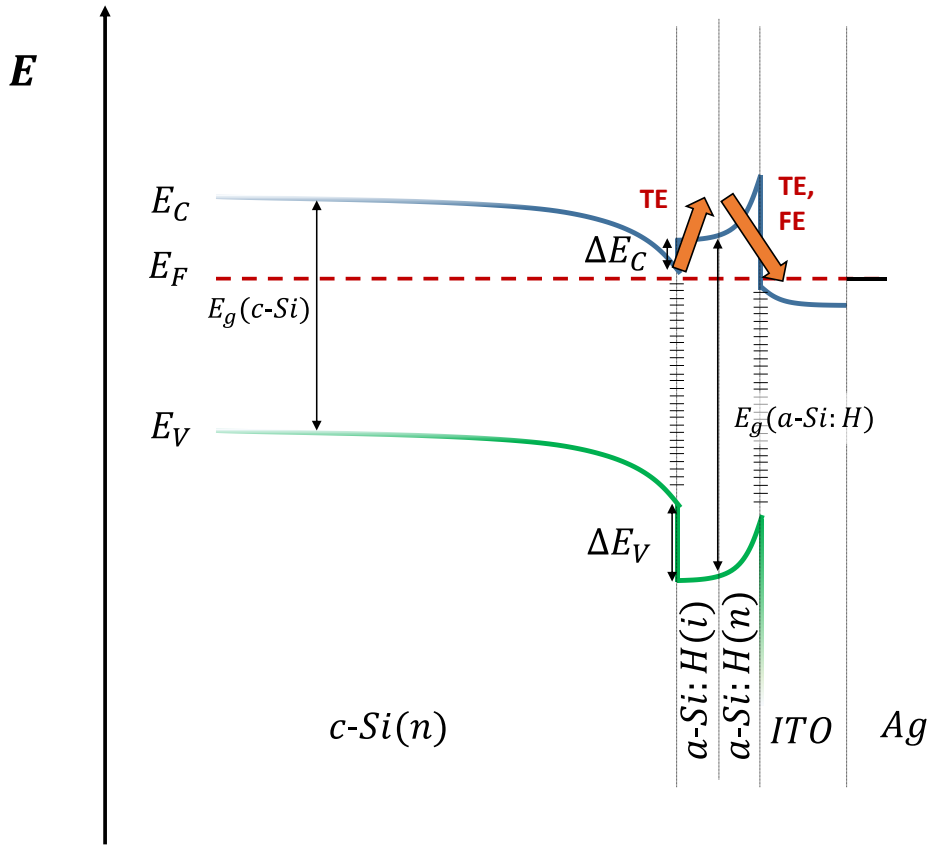

Figure 29: Band diagram illustrating transport mechanisms at the electron contact. Orange arrows representpossible transport mechanisms for electrons, where TE stands for thermionic emission and FE for field emission (i.e. intra-band tunneling)

The selectivity of this contact is very good as hole transport is blocked by the built-in potential in c-Si and by both large valence band offsets at the c-Si/a-Si ($\Delta E_V \sim 0.36eV$ [100]) and a-Si/ITO ($\Delta E_V > 2eV$) interfaces, while electron transport is enabled by relatively low potential barriers.

The quite low conduction band offset at the a-Si:H(n)/c-Si(n) interface ($\Delta E_C \sim 0.15eV$ [100]) should allow for substantial thermionic emission at room temperature, but this does not rule out tunneling. Especially in some cases strong band bending inside the a-Si:H layers may create spikes in the conduction band which make it easier for tunneling to occur, both at the a-Si/c-Si and at the a-Si/ITO interfaces [101]. Nogay et al. showed that electron contact resistance features a large temperature dependent variation in their devices, indicative that thermionic emission is the predominant phenomenon at play [102]. Engineering the electron affinity of the front a-Si:H layers in order to obtain lower barriers could be one way to improve transport at this contact.

At the c-Si(n)/a-Si:H(i+p)/ITO interface, there are two potential barriers for holes to overcome: the valence band offset between c-Si(n) and a-Si:H(p) valence bands ($\Delta E_V \sim 0.36eV$ [100]), and the huge valence band offset due to the a-Si:H(p)/ITO(n+) interface: in fact, it is an N/P/N structure as presented in Figure 30.

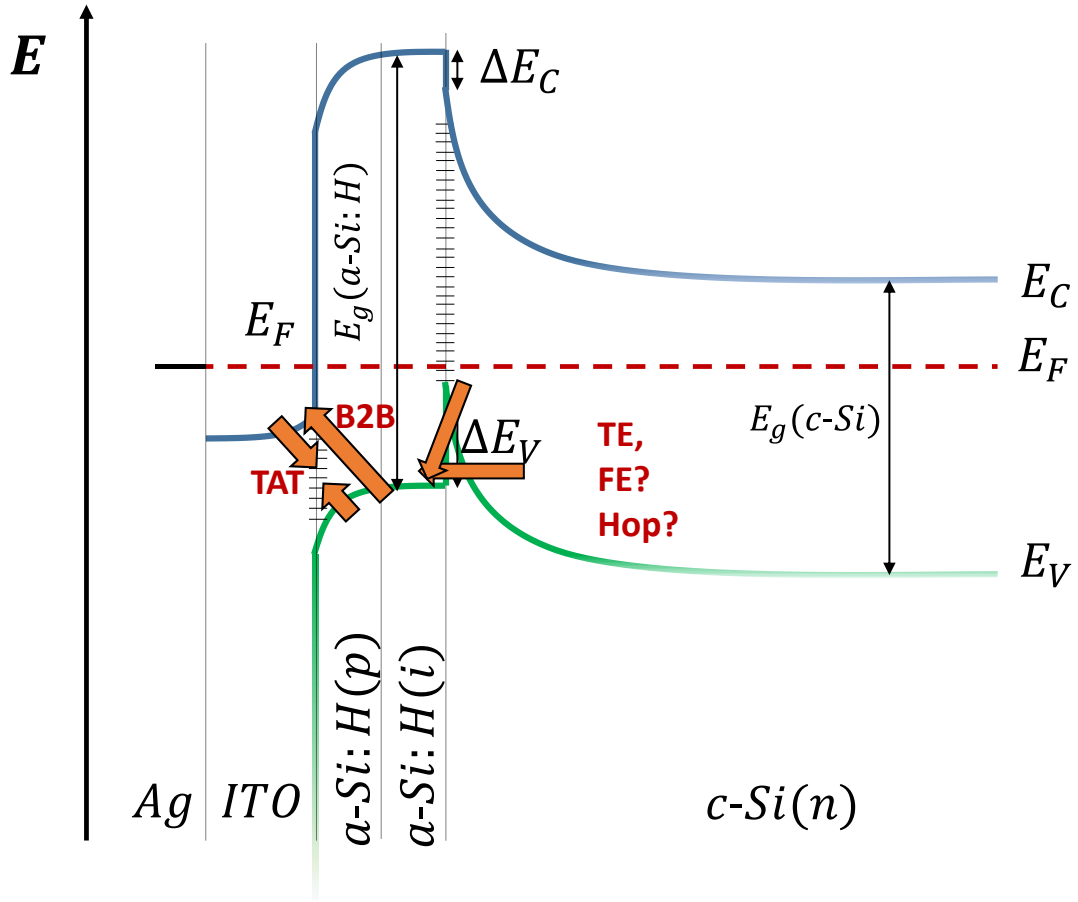

Figure 30: Band diagram illustrating possible transport mechanisms at the hole contact. Orange arrows represent transport mechanisms, where TAT stands for "trap-assisted tunneling", B2B for "band-to-band" tunneling, TE for thermionic emission, FE for field emission and Hop for hopping

Kanevce et al. [103] showed that if only thermionic transport is considered, abnormal IV characteristics are obtained, because transport at the a-Si:H(p)/ITO(n+) interface is impeded. Lowering the valence band offset at the c-Si(n)/a-Si:H(p) interface leads to slightly increased performances, but cannot explain alone transport at the hole contact. Band-to-band tunneling (direct or trap-assisted [95]) is the crucial mechanism at play, allowing holes to recombine at the a-Si:H(p)/ITO(n+) interface. Recombination junctions are also widely studied in multi-junction cell architectures (e.g. [19]).

Additional transport phenomena may be at play at the c-Si(n)/a-Si:H(p) interface, including intra-band tunneling and hopping. Nogay et al. confirmed with temperature dependent I-V measurements that thermionic emission is also important at the hole contacts [102]. Crandall et al. [104] suggested that hopping through defects is an important transport mechanism through the a-Si:H(i) at the hole contact.

The thickness of layers play an important role on the band lineup: both the doped a-Si:H layers must be thick enough not to be too strongly depleted by the ITO layers, otherwise leading to weakened band bending at the c-Si/a-Si:H interface and resistive losses [101], [105], [106].

2.5.2.3 *Measuring electron and hole contact resistances in SHJ cells*

Due to the presence of transport barriers, both the a-Si:H(i)/ a-Si:H(n)/ITO & a-Si:H(i)/ a-Si:H(p)/ITO interfaces are expected to induce resistive effects. Following the notation introduced in §1.2.1, we will denote the a-Si:H(i)/a-Si:H(n)/ITO stack as the "electron contact", and the a-Si:H(i)/a-Si:H(p)/ITO stack as the "hole contact". These encompass all contributions stemming from vertical conduction through each layer and interface.

Gogolin et al. proposed in 2014 a method to evaluate the electron and hole contact resistances of a SHJ cell from measurements on cell-like structures without junction [107]. However, their method is indirect and requires several test structures and modelling of the expected contribution on R_S from lateral currents in the ITO. They found optimized contact resistivities of $100\ m\Omega.cm^2$ and $420\ m\Omega.cm^2$ for the electron and hole contacts respectively, concluding on a high impact on R_S and efficiency. Lee et al. followed a similar approach and reported values of 370 and 380 $m\Omega.cm^2$ for the electron and hole contacts respectively [91].

Lachenal et al. [58] proposed a more direct approach in 2016, using TLM measurements on dedicated test structures. These structures consist of electron and hole contacts deposited respectively on n or p-type c-Si substrates, on which the ITO and silver have been etched away using wet etching. Because the conductivity of the a-Si:H layers is very low and that they are only nanometers thick, they do not participate in any significant lateral conduction. Therefore, when making an I-V measurement in between two consecutive contacts the current will go vertically through each layer of the electron or hole contact (ITO, doped a-Si:H and a-Si:H(i)), then laterally through the c-Si(n or p). For the measurement of the hole contact, a p-doped c-Si substrate is used to keep the same polarity through the whole sample and avoid the presence of a PN junction. In the following, we label this kind of samples **n or p-stack TLM samples**.

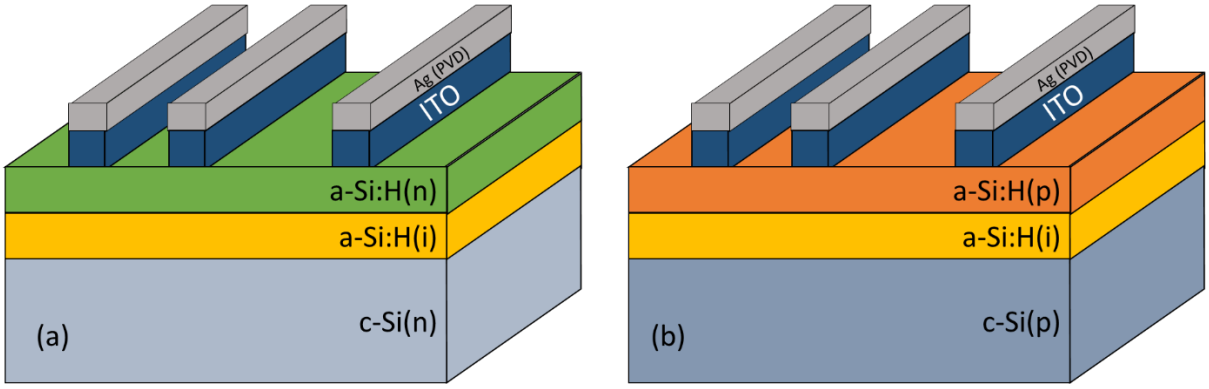

Figure 31 : n and p stack TLM samples such as proposed by Lachenal et al. for measuring **(a)** electron contact and **(b)** hole contact

Note that the contacts are similar to that of SHJ cell, except silver is deposited by PVD and not screen-printing, and that a p-type substrate is used for the hole contact structure. They report values of electron and hole contact resistivities of respectively $140\ m\Omega.cm^2$ and $240\ m\Omega.cm^2$, concluding they are the major factor of losses in their 22.4% efficiency cell.

2.5.3 Lateral transport in SHJ cells

2.5.3.1 Parallel lateral transport in bulk c-Si and ITO

In conventional silicon solar cells, most of the lateral transport towards the metallization grids occurs in the highly doped emitter. However, SHJ solar cells have very thin and highly resistive emitters, but feature TCOs enabling lateral transports in them. Also, the transport in the c-Si is often overlooked but has an impact in lateral losses.

Bivour et al. showed that lateral transport at the front side differs in front and rear emitter configurations: in front emitter configuration, the lateral transport inside the c-Si absorber is low, while in rear emitter configuration it is substantial [108]. They showed that in the case of a rear emitter configuration the effective sheet resistance of the front surface $R_{Sh}(eff)$ is quite accurately expressed with a simple parallel connection of both layers:

$$R_{Sh}(eff) = \left(\frac{1}{R_{Sh}(ITO)} + \frac{1}{R_{Sh}(c-Si)}\right)^{-1} \qquad \text{Eq. 79}$$

Rear emitter solar cells have the advantage that they allow more transparent and less conductive front TCOs, as they benefit from lateral conduction in the base. This lowers resistive power losses due to lateral transport at the front side.

It may seem straightforward but it is worth mentioning that ITO is too n-doped to conduct holes: the p-contact ITO does not conduct holes but electrons. Therefore the lateral transport in n-type SHJ cells is mainly stemming from electrons, holes only have a low lateral component from c-Si lateral conduction, as their mobility is lesser.

In Chapter 7, we will derive a more complete model for this lateral transport, taking into account the contact resistance in between the TCO and c-Si layers. Our approach will be confronted to a new model that was recently proposed [64].

2.5.3.2 Lateral transport in the inversion layer

Several authors (e.g. [110], [111]) showed that in SHJ cells, there is an inversion layer inside the n-type crystalline silicon where it is locally p-type due to the high band bending induced by the a-Si:H(p) layer (see Figure 28). Therefore the P/N junction is not located at the c-Si(n)/a-Si:H(i)/a-Si:H(p) interface, but is de-located inside the c-Si. This inversion layer has a quite large resistivity (~10-100 $k\Omega.cm$ [111]), but allows some current to be transported inside it. However, this current cannot be enough to ensure lateral current without the use of an ITO for high performance cells [111].

2.5.4 Cell inhomogeneity and impact on transport

Solar cells are not fully homogeneous, and any local variation of a property may impede charge transport. Inhomogeneities such as cell edges or punctual defects have a significant impact on cell performance. Edges for instance are highly active recombination areas and can induce strong FF losses [112]. Any other defect such as physical scratches or unpassivated areas can alter efficiency. A metric of the "defectivity" has been proposed, to quantify from photoluminescence (PL) images the quality of a solar cell, and was found to correlate very well with FF in SHJ cells [113].

R_S may also be inhomogeneous, due to metallization paste asperities, cut lines, inhomogeneous properties of the ITO layer etc. A localized R_S increase can influence significantly the global R_S. It also introduces bias in characterization: Bowden et al. showed that strong inhomogeneities in R_S can easily be mistaken for shunt or high recombination effects when examining the IV curve of the device [71].

2.6 Chapter outlook

We have presented the SHJ cell technology. This device, with the interdigitated back contact design, holds the record for conversion efficiency of silicon solar cells, while the both sides contacted design holds large silicon area devices record efficiency, and is on the path to industrialization. We studied the TLM method for measuring contact resistance, and addressed a two-layer TLM model. We also saw that there exists a variety of measurement methods to determine R_S, but that some are considered more precise from theoretical considerations. We addressed the power loss analysis, and found that there exists some simple analytical expressions to break down R_S into its different components, but noted that these expressions apply only to conventional simple cell structures. We then saw that several mechanisms of charge transport are at play at the contacts and interfaces of the SHJ cell, and are still not completely well known. Finally, we showed that structures compatible with TLM measurement to determine both the Ag/TCO contact and the electron and hole contacts were proposed in the literature.

Chapter 3

Characterization & fabrication processes

This chapter presents the fabrication process of samples at the CEA SHJ lab, and the different characterization techniques that were used within the frame of this work, mainly for measurement of carrier effective lifetime, sample homogeneity, layer thicknesses, and I-V curves. Then we review the different series resistance measurement methods and conclude on the preferred method that we will use in the rest of this work. We also present the numerical simulation employed in the frame of this work to use for cell or TLM sample modelling, as well as the parameters used for each layer composing the modelled device. Experimental precautions taken for the TLM sample fabrication and measurement in order to avoid a certain amount of biases are also examined.

3.1 Fabrication of SHJ cells at CEA industrial pilot line

The LabFab platform of CEA at INES is a pilot line dedicated to SHJ solar cells fabrication with industrial tools at a nominal capacity of up to 2400 wafers per hour (M2 size) [114]. The line allows researchers to perform R&D in a semi-industrial environment. The current process enables to produce cells with a baseline efficiency around 23.4%, for devices with busbarless screen-printing design. Paths for further efficiency increase have been identified and a best cell was recently certified at 24.63% on full M2 area using screen-printing metallization.

The standard fabrication procedure is described in the following. Commercial (100) "as-cut" Czochralski (Cz) silicon wafers are generally used. As-cut wafers go through a wafer inspection system performing in-line measurements of thickness via laser interferometry, and of resistivity using eddy-current technique.

Once wafers are loaded into carriers, they are moved to an automatic wet bench where they are plunged into a KOH-based solution for saw-damage removal and surface texturing. They are then cleaned using a $O_3 - HF$ solution [114] followed by an HF-last step to remove remaining surface contaminants.

After cleaning and texturing, wafers are loaded into a Meyer Burger PECVD tool to perform the deposition of the a-Si:H layers. Cells are made in a rear-emitter design, so an a-Si:H(i)/a-Si:H(n) stack is deposited at the front surface and an a-Si:H(i)/a-Si:H(p) at the rear surface. The PVD step is also carried out using a Meyer Burger tool, depositing ITO on both surfaces of the cells, the tray being specially designed to allow edge exclusion on one side and avoid possible shunts.

Finally, the cells are screen-printed, and cured at approximately 200°C for up to 30 minutes. Several metallization schemes are possible ranging from busbar technologies (BB4, BB5, BB6) to busbar-less designs (BB0) (BBX where X represents the number of busbars). Two IV sorters are available, a PASAN tool for Grid-Touch measurements [115] on busbarless cells and a Chroma tool for busbar cells. The devices being bifacial, IV sorter design and calibration are optimized to avoid any light contribution (and thus efficiency gain) from the rear side (dark background).

During this PhD thesis, I had the opportunity to use these facilities to fabricate and characterize industry-relevant SHJ samples. We favored busbar designs for commodity, as some characterizations cannot be carried out easily on busbarless cells, and we mostly used 5-busbars (BB5) screen-printing designs as they are more conveniently contacted at the chuck of IV testers as they have a rear busbar located at the center. Within the duration of this work, the process of reference (POR) for each step has evolved, and so did our samples, batch to batch direct comparison is sometimes not possible with every data in this document.

3.2 Effective lifetime measurements

There are several methods to determine the effective carrier lifetime of a semi-conductor material, but the most commonly implemented for solar grade silicon devices is the photo-conductance decay measurement [116], with the most widely used tool being a Sinton Instruments WCT-120. Contactless measurement of the conductance are carried out at the center of a sample under a flash of light, while simultaneously monitoring the flash intensity,

allowing the determination of the effective lifetime as a function of the minority carrier density. Note that the measurement averages over a defined surface area (40mm diameter) and is not representative of a whole device (e.g. does not take into account device edge effects).

Under illumination, the conductivity of a semi-conductor can increase by $\Delta\sigma$. In silicon, in the hypothesis of no trapping, this photo-conductivity can be linked to the average excess minority carrier density (Δn_{av} in cm^{-3})[4]:

$$\Delta\sigma(\Delta n_{av}) = q * \Delta n_{av} * (\mu_n + \mu_p) \quad \text{Eq. 80}$$

Photo-generation rate ($G_{ph,av}$) and illumination intensity (E_{av}) can also be linked through [31]:

$$G_{ph,av} = \frac{E_{av} * f_{abs} * N_{ph}^{1sun}}{t} \quad \text{Eq. 81}$$

Where f_{abs} is the fraction of absorbed incidents photons, N_{ph}^{1sun} is the photon flux under 1Sun illumination and t the wafer thickness.

Finally, the average lifetime can be expressed as a function of Δn_{av} with Eq. 15 (see §1.2.3.1). Knowing the thickness of the sample and its resistivity, from the measured $E_{av}(t)$ and $\Delta\sigma(t)$ one can derive $\tau(\Delta n_{av})$ from Eq. 80, Eq. 81 and Eq. 15.

If the flash of light is long compared to the effective carrier lifetime, the regime is quasi-steady-state (QSS). In this case:

$$\frac{\partial \Delta n_{av}}{\partial t} = 0 \quad \text{Eq. 82}$$

And Eq. 15 simplifies to:

$$\tau_{eff} = \frac{\Delta n_{av}}{G_{ph,av}} \quad \text{Eq. 83}$$

Oppositely, in the case of a very brief flash, generation is negligible compared to the time-derived term. The regime is said to be transient and:

$$\tau_{eff} = \frac{\Delta n_{av}}{-\frac{\partial \Delta n_{av}}{\partial t}} \quad \text{Eq. 84}$$

Depending on the lifetime range expected in the samples a technique or the other will be used. As SHJ cell precursors (i.e. cells before metallization) usually feature very high carrier lifetimes (above 1ms), the transient technique is used most of the time.

3.3 Luminescence techniques for imaging

Luminescence is the process of light emission under excitation from different interactions. It can be employed as a tool for semi-conductor characterization, as it is linked to carrier density. The intensity of emitted light close to the bandgap energy can be written:

$$R_{rad} - R_0 = B(np - n_0 p_0) \quad \text{Eq. 85}$$

Where R_{rad} is the recombination rate due to radiative recombination, R_0 is the equilibrium recombination rate, and B is a constant characteristic of each material. For silicon $B = 4.73 *$

[4] Writing Δn as the minority carrier assumes the samples is p-type, but under the assumption of no trapping $n_{av} = p_{av}$, so the equations of this paragraph are valid for both sample types.

$10^{-15} cm^3/s$ at room temperature [26]. Under a given input excitation, the more emission there is the higher the carrier density will be.

Various luminescence techniques exist, differentiated by the excitation mode. In photovoltaics, mostly photoluminescence and electroluminescence are commonly used, typically for imaging:

- Photoluminescence (PL) is a photon-induced luminescence. Carriers are photo-generated using a laser of single wavelength. By illuminating homogeneously a sample, one can image the emitted PL signal across the sample, linked to the local carrier density of each elementary zone (linked to the pixel size of the detection system). Zones where passivation is good appear brightly (high PL intensity), and oppositely zones where the passivation is harmed will appear darker (low PL intensity).
- Electroluminescence (EL) is an electron-induced luminescence: electrons are injected locally using contact probes. It is complementary to the photoluminescence technique as carrier injection is not homogeneous. Therefore, it allows to examine the pathway of current injected in the cell, and to visualize zones of impeded transport.

Other techniques include time-resolved PL for effective lifetime measurements [117], spatial resistivity variations imaging of bare wafers with PL [118], determination of series resistance through PL and EL [119] etc.

In this work, we mostly used a tool from BTImaging that allows both PL and EL imaging. Figure 32 shows PL and EL images of a same SHJ cell. PL only detects local passivation defects, such as marks due to the belts rubs during processing of the cell, or local defective areas. EL also detects zones where carrier transport is impeded, such as badly printed or cut lines during the electrode screen print design processing step (blackish zones in the upper and lower left side of the cell) in this example.

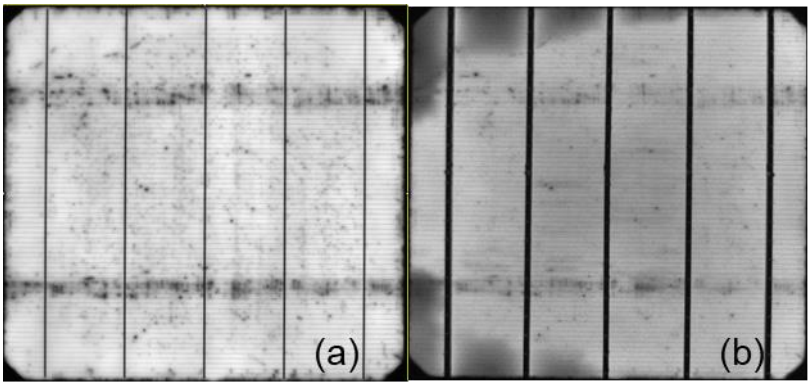

Figure 32 : (a) PL and (b) EL images of a 19.7% efficiency BB5 inverted emitter N-type SHJ cell with screen-print defects

3.4 Ellipsometry

Ellipsometry is a technique that allows to measure the complex dielectric function of thin films. It can characterize several material properties, mainly thickness and optical parameters, but a variety of other properties can also be determined [120]. It is based on the measurement of the change of polarization of linearly polarized light reflected from a sample surface (i.e. change

in phase shift (Δ) and amplitude ratio upon reflection ($\tan(\psi)$). Spectroscopic ellipsometry uses light with varying wavelength (λ) in order to obtain information over a wide spectral range:

$$\varepsilon(\lambda) = sin^2\phi_0 + sin^2\phi_0 tan^2\phi_0 * \left(\frac{1 - \tan(\psi(\lambda))\, e^{i\Delta(\lambda)}}{1 + \tan(\psi(\lambda))\, e^{i\Delta(\lambda)}}\right)^2 \quad \text{Eq. 86}$$

Where ϕ_0 is the angle between the incident light and the vector normal to the sample surface. Material properties are inferred indirectly from data analysis (e.g. [121]).

3.5 I-V measurements

In this work, we used several kinds of IV testers depending on the aim of the measurement, all being in the 4-probes / force-sense configuration.

- When measuring SHJ cells after production, we used an in-line IV tester for bifacial solar cells IV measurement, from Chroma. Measurements are made automatically with arrays of pins contacting the busbars on both sides of the cell.
- When measuring devices under varying light intensity or under varying temperature, we used a solar simulator from NeonSee. This tool allows to vary the temperature from 15 to 80°C, and to tune the illumination intensity from 0 to 1000 W/m² (1Sun). To measure solar cells, we contact the cells with arrays of pins at the front and to the chuck at the rear. To perform TLM measurements we used contact probes to contact the electrodes of our samples, while isolating the device from the chuck with an insulating layer to ensure right thermal contact but avoid any parasitic conduction.
- When measuring TLM samples in the dark at ambient temperature, we used a Keithley 4200-SCS with a 4210A pre-amplifier unit tool combined with a dedicated manual probing platform.
- To obtain Jsc-Voc curves fast, we used a SunsVoc tool from Sinton Instrument.
- To obtain the sheet resistance at the surface of a sample, we use four-point probe measurements (4PP) on a Napson equipment.
- TLM measurements on cut strips of finished cells can also be done using a GP solar "GP4 test" tester

If not stated otherwise, all TLM measurements are conducted under dark conditions and ambient temperature.

3.6 Review of the different R_S measurement methods

We have discussed several methods proposed in the literature to determine the series resistance of a solar cell in §2.2. In this paragraph, we compare these different approaches and argument which techniques were selected for this work.

All methods reviewed have been implemented into a Matlab code. Note that the NeonSee solar simulator is limited to a maximum light intensity of 1000 W/m², so we chose a center illumination at 950 W/m² instead. I-V curves of a rear-emitter SHJ solar cell from CEA-INES featuring 5 busbars were measured under various light intensity (dark, 100, 900, 950, and 1000 W/m²), and a SunsVoc curve was also measured with reference J_{SC} measured at 950W/m².

As IV curves can be noisy, all curves were fitted with a 2-diode model, and the results of the fits were used in the calculations to smooth results and avoid interpolations issues[5].

The DLM method was applied in between curves at 900 and 1000W/m², the MLM using the 3 curves centered on 950W/m² and the DIV/LIV between the curve at 950W/m² and the dark-IV. The R_S from fitting is that of the 950W/m² J-V curve (see Figure 33).

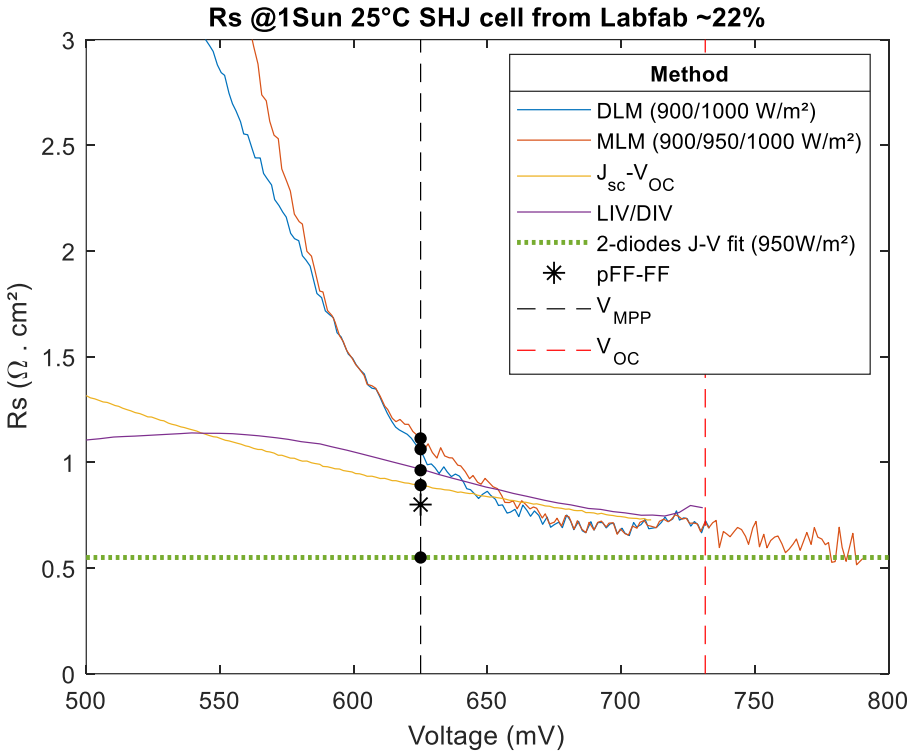

Figure 33: R_S at an illumination of 950W/m² as a function of voltage, as measured on a solar cell with different methods from the literature. Black dots indicate the values at MPP

All methods differ significantly at low voltages but are very close at high voltages: this is because R_S does not affect strongly the cell characteristics at low voltages. As all measurement methods are based voltage drop due to the effect of R_S, the uncertainty in the measurement is higher at low voltages. At MPP, the difference is still quite marked between all methods (Table 2).

Table 2: R_S at MPP as measured with different methods

Method	Value ($\Omega.cm^2$)
DLM (900/1000 W/m²)	1.06
MLM (900/950/1000 W/m²)	1.11
Jsc-Voc /J-V	0.89
LIV/DIV	0.96
pFF-FF	0.80
J-V fitting	0.55

[5] Due to the discrete nature of experimental data, extrapolations are needed to compare curves at a given ΔJ (see §2.2)

The DLM and MLM methods yield very similar results, and converge at high voltages. Averaging more IV curves does not seem to change significantly the precision of the measurement [36]. Both Jsc-Voc/J-V comparison and LIV/DIV comparison methods yield similar curve dynamic but different values at MPP. The pFF-FF method also gives a comparable value at MPP. Finally, the fitting methods gives a lower R_S value in this example, and it has been shown before (e.g. [36], [71]) that it systematically yields underestimated value of R_S . Excluding the fitting method we get values of R_S for the studied cell ranging from 0.80 to 1.11 $\Omega.cm^2$.

Over the course of this work, results of Jsc-Voc and pFF-FF methods are similar most of the time. The pFF-FF technique is also very handy because it is faster to implement than the other methods, as it only requires SunsVoc measurements after the in-line J-V measurements. Both measurements and analyses are quite quick, which allows to make large quantities of measurements, and to get statistically significant trends when varying conditions.

Overall, in this work we chose the pFF-FF method to determine R_S values.

3.7 Numerical simulation on Silvaco Atlas

To simulate solar cells accurately and accounting for both transverse and lateral transport, 2D simulation is required. In this work we used Silvaco Atlas: a technology computer-aided design (TCAD) software that performs simulations of 2D and 3D electronic devices such as solar cells. The cell model that we used is the fruit of a continuous effort at the heterojunction lab of CEA at INES to produce an accurate model for SHJ cell modelling [112], [122], [123].

Note that the numerical model used for this purpose was originally developed to model SHJ cells representative of the devices produced at CEA-INES in STC conditions, but it is not fine-tuned to model accurately the contacts of the cell. Further refinement of the model would be necessary to fit both a good contact behavior and IV performances matching the experimental results.

On this software, we developed several models, for simulation of TLM samples and solar cells.

3.7.1 Simulation parameters

The simulation parameters used in our simulation model are described in this section. Table 3 describes the parameters for the c-Si wafer, Table 4 for the a-Si:H layers. Here we model ITO as a semi-conductor, and not as a metal (see Table 5).

Table 3: Simulation parameters for the c-Si layer

Quantity	c-Si
Band gap (eV)	1.124
Relative permittivity	11.9
Electron affinity (eV)	4.05
Thickness (µm)	160
Doping (cm^{-3})	$4.95 * 10^{15}$
Conduction band density of states (cm^{-3})	$2.857 * 10^{19}$
Valence band density of states (cm^{-3})	$2.514 * 10^{19}$

Table 4: Simulation parameters for a-Si:H layers

Quantity	a-Si:H(n)	a-Si:H(i) n side	a-Si:H(p)	a-Si:H(i) p side
Band gap (eV)	1.75	1.65	1.65	1.75
Relative permittivity	11.9			
Electron affinity (eV)	3.9	3.9	3.874	3.774
Thickness (nm)	3.5	3.5	12	5
Activation energy (eV)	0.20	0.55	0.24	0.87

Table 5: Simulation parameters for ITOs

Quantity	ITO (front)	ITO (rear)
Band gap (eV)	3.65	3.65
Relative permittivity	20	20
Electron affinity (eV)	4.2	5.1
Thickness (nm)	70	70
Doping (cm^{-3})	$1.25 * 10^{20}$	$1.5 * 10^{20}$
Conduction band density of states (cm^{-3})	$1 * 10^{19}$	$1 * 10^{19}$
Electron mobility (cm^2/Vs)	25	25

A single mid-gap defect is added in the c-Si with $\tau_{p0} = 10\,\tau_{n0} = 5.785 * 10^{-3} s$. To model surface defects at the c-Si/a-Si:H interface, a highly defective 1nm thick c-Si layer was introduced, equivalent to a D_{it} of $10^9 cm^{-2}$ [123]. To model the defects inside the a-Si:H layers, realistic values based on [124] were used and the doping of the layers were adapted to fit experimental values of activation energies [100].

Silvaco Atlas features many different transport models that can be enabled. In our simulation, we use Yang's model for thermionic emission over heterojunctions at the a-Si:H/ITO and c-Si/a-Si:H interfaces (see §2.5.2.1.1). In addition, at the rear a-Si:H(p)/ITO interface, Danielsson's model (see §2.5.2.1.2) is implemented to model the trap-assisted recombination necessary for current flow. All other transport mechanisms are the automatically implemented models.

Optical parameters for the a-Si:H and ITO layers are based on characterization of the optical indexes of experimental layers. Reduced reflections are considered at the front surface due to the textured surface.

3.7.2 Simulating solar cell performance

We model a rear emitter n-type SHJ cell in Silvaco Atlas using the layers previously described. We use a cylindrical boundary condition at the sides of the cell to model. Infinitely thin ideal electrodes of 50µm width are added at both sides with a front pitch (p_f) of 1.8mm and a rear pitch (p_r) of 0.6mm. A periodic boundary condition is added at the edges of the cell so that we measure bulk quantities without the influence of the edges (see [112]). The default width of the sample (in the direction perpendicular to the drawing) is $W = 1\mu m$.

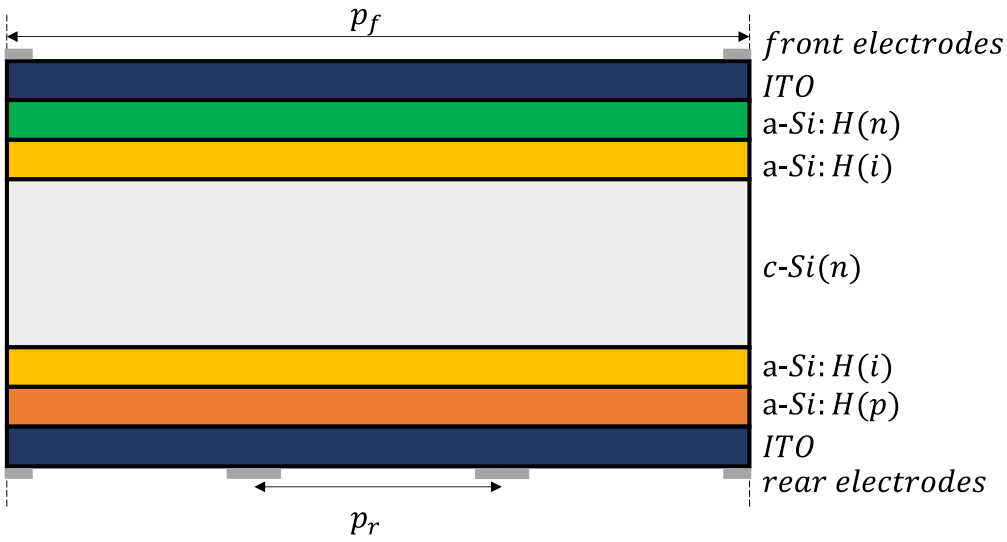

Figure 34: Simulated SHJ structure on Silvaco Atlas

For each bias point, the current flow is simulated and we can extract the J-V curve (in the dark or illuminated cases).

3.7.3 Simulating TLM samples

To simulate TLM samples, we use the same layer parameters, but we adapt the design to model a TLM structure such as p-side ITO/Ag or n or p stack samples. The rear and the edges of the structures are left bare and do not recombine charge carriers. The electrodes are put at the front surface and we measure current from anode to cathode, varying the spacing in between the electrodes. The TLM curve is then analyzed such as an experimental curve to extract R_C, R_{Sh}, L_t and ρ_C (see §2.3.1). If not stated otherwise, we define electrode length of 500µm, and spacing distances between 300 and 2200 µm.

At the electrode/TCO contact, we can tune the contact by considering an ohmic contact with a given contact resistivity. At the electron and hole contacts, the parameters ruling the contact according to Yang's and Danielsson's models need to be adjusted to tune contact properties (electron affinities, doping densities, trap density at the interfaces etc.).

3.8 Contact resistance measurement

TLM is a very simple method to implement: it is based on simple structure architecture, and uses a very simple way to extract contact and layer contributions to the total resistance. However, a severe drawback of TLM is its susceptibility to all sort of bias and uncertainties. In this part, we will discuss the methodology implemented to measure contacts in SHJ cells during the PhD.

3.8.1 Improving the measurement precision of contact resistivity

3.8.1.1 Calculation of uncertainties

Ueng et al. have demonstrated analytical formulas to calculate uncertainties in the measurement of ρ_C and R_{Sh} due to systematic and random errors [125]. Their approach however considers the TLM equations only in the "Long-contact" approximation, so their equations are valid only in this case.

Random error on ρ_C ($\frac{\sigma_{\rho_C}}{\rho_C}$) and on R_{Sh} ($\frac{\sigma_{R_{Sh}}}{R_{Sh}}$) can be written such as:

$$\frac{\sigma_{\rho_C}}{\rho_C} = \frac{1}{\sqrt{N}}\left(\left(\frac{2W}{\sqrt{\rho_C R_{Sh}}} + \frac{2\sqrt{3}}{R_{Sh} d_{\max}}\right) * \sqrt{\left(\frac{R_{Sh}}{W}\right)^2 \sigma_d^2 + \sigma_R^2} + \left(\frac{4}{W}\right)\sigma_W\right) \quad \text{Eq. 87}$$

$$\frac{\sigma_{R_{Sh}}}{R_{Sh}} = \frac{1}{\sqrt{N}}\left(\left(\frac{2\sqrt{3}}{R_{Sh} d_{\max}}\right)\sqrt{\left(\frac{R_{Sh}}{W}\right)^2 \sigma_d^2 + \sigma_R^2} + \left(\frac{2}{W}\right)\sigma_W\right) \quad \text{Eq. 88}$$

Where N is the number of IV curves used in the TLM measurement, $d_{\max}$ is the maximum spacing distance in the TLM design, and σ_d, σ_R and σ_W are the standard deviations in the measurement of d, R and W. The latter values can be obtained experimentally by repeating independent measurements of said quantities.

Systematic error on ρ_C ($\frac{\delta\rho_C}{\rho_C}$) and on R_{Sh} ($\frac{\delta R_{Sh}}{R_{Sh}}$) can be written such as:

$$\frac{\delta\rho_C}{\rho_C} = \left(\frac{W}{\sqrt{\rho_C R_{Sh}}}\right)\delta R + \sqrt{\frac{R_{Sh}}{\rho_C}}\delta d + \frac{4}{W}\delta W \quad \text{Eq. 89}$$

$$\frac{\delta R_{Sh}}{R_{Sh}} = \frac{2}{W}\delta W \quad \text{Eq. 90}$$

Where δR, δd and δW are the systematic errors on R, d and W. They can be determined from the sensibility specifications of the tools used for each measurements.

Total error for ρ_C ($\frac{\Delta\rho_C}{\rho_C}$) and R_{Sh} ($\frac{\Delta R_{Sh}}{R_{Sh}}$) are the sum of these two quantities and reads:

$$\frac{\Delta\rho_C}{\rho_C} = \frac{\sigma_{\rho_C}}{\rho_C} + \frac{\delta\rho_C}{\rho_C} \quad \text{Eq. 91}$$

$$\frac{\Delta R_{Sh}}{R_{Sh}} = \frac{\sigma_{R_{Sh}}}{R_{Sh}} + \frac{\delta R_{Sh}}{R_{Sh}} \quad \text{Eq. 92}$$

The error bars in the TLM plots can be assessed from the total errors on d and R, $\frac{\Delta d}{d}$ and $\frac{\Delta R}{R}$.

3.8.1.2 Measuring the TLM dimensions

When depositing TLM electrodes on a sample, whatever the technique used, there is usually spreading effects. When using evaporation, there will be a thickness gradient towards the edge of the mask, and some deposition occur under the mask if it is not stuck strongly enough against the sample. When using screen-printing the paste does not exactly transfer through the mesh, it spreads further than the defined stencil due to the viscosity of the paste and to the pressure applied: lines and busbars are always wider than defined on the stencil. Changing the design of the mesh, or the type of paste used, or even the texturing of the wafer results in different spreading.

It is important to know with precision the geometrical features of the design for a good evaluation of the TLM results. **Therefore, in this work we always used measured dimensions of the TLM design, and not its specifications**. When printing TLM designs, the spreading is of the order of 15-30µm for our metallization patterns. Spreading leads to larger electrodes, and smaller spacing distances. This leads to a horizontal shift towards the left in the TLM curve, which does not change the slope of the TLM curve, and therefore does not change the determined R_{Sh}, but does change the y-intercept, leading to an underestimated value of R_C and ρ_C. This effect is known to lead to wrong evaluations of ρ_C, and even to negative values of R_C [126].

3.8.1.3 Evaluation of uncertainty in TLM geometry parameters

The profile of the metallization is not homogeneous along its length (see Figure 35). We measure σ_d by repeating measurements of d along the electrode for a spacing designed at 200µm.

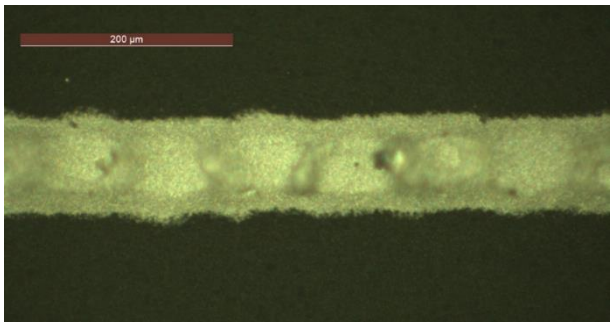

Figure 35: Optical microscope image of a thick metallization line

We find $\sigma_d = 10\mu m$. The systematic error on the measurement of d, δd, is estimated to 20µm, leading to a total uncertainty of $\Delta d = 30\mu m$. For the width of the electrode, $\sigma_W = 10\mu m$ is also estimated The systematic error is also estimated to 20µm, leading to $\Delta W = 30\mu m$. Here we consider that σ_d and σ_W are independent of d and W as the variations of the print parameters have no reason to change with d and W.

From repeated measurements of resistance using the same spacing distance, we estimate a statistical error of the resistance $\sigma R = 0.11\Omega$. The systematic error is estimated at $\delta R = 0.2\Omega$.

Throughout this work, calculations of uncertainties will be made using the expressions from §3.8.1.1 and these parameters.

3.8.1.4 Signal to noise ratio

TLM measurements are based on the discrimination of two terms in the total resistance measured, as already seen in §2.3.1 (Eq. 33):

$$R_{tot}(d) = 2R_C + \frac{R_{Sh}}{W} * d \qquad \text{Eq. 93}$$

- Contact resistance, R_C, highlighted by the y-intercept of the TLM curve, which can be expressed as (variant of Eq. 36):

$$R_C = \frac{\rho_C}{W L_t} * \coth\left(\frac{L}{L_t}\right) \qquad \text{Eq. 94}$$

- Layer resistance, R_{layer}, a direct function of the width of the TLM electrode (W), sheet resistance of the studied layer (R_{Sh}), and inter-distance electrode (d):

$$R_{layer} = \frac{R_{Sh}}{W} * d \qquad \text{Eq. 95}$$

For TLM to be carried out with precision, the signal of both terms needs to be significant: this means that the TLM pattern dimensions need to be selected wisely to reduce uncertainty. Note that from Eq. 94 and Eq. 95, it is straightforward that the electrode width W has no impact on the ratio R_C/R_{layer}. Parameters of importance are thus mostly electrode spacing d and electrode length L.

TLM was originally developed in micro-electronics, where some contact resistivities are commonly reported below $10^{-6}\ \Omega.cm^2$ [127]. The spacing distances used in the TLM patterns are thus micrometric. Low distances therefore minimize the R_{layer} contribution and allow good R_C signal. Additionally the use of high precision alignment and patterning techniques such as lithography is common in the microelectronics domain, but is not common in the PV domain, as the latter aims at low manufacturing costs.

When studying high efficiency solar cells, contact resistance can also be very low [92]. However, we are dealing with more macroscopic objects and usual characterization techniques. TLM patterns are thus usually of millimeter to centimeter scale. This can generate impractical situations, where the R_C signal is completely drowned under the R_{layer} signal. This prevents from extracting the y-intercept of the TLM curve with a decent precision. This can even lead to negative R_C values (e.g. [80]).

This effect is more pronounced when contact resistance is low, and is notably encountered when measuring Ag/TCO contacts. As the electron and hole contact resistances are quite high, this problem does not significantly affect them. For instance, consider the TLM plot in Figure 36 (a), which corresponds to such a problematic measurement on a p-side ITO/Ag TLM sample (see §2.5.1.3). A wide range of inter-electrode distances has been used, varying from 0.3 mm to 14.4 mm (distances are slightly different for the second sample in Figure 36 (b)).

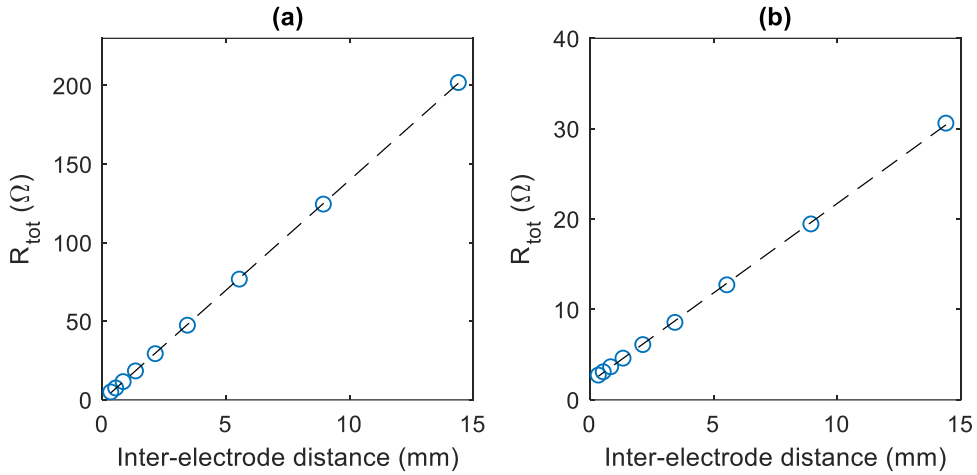

Figure 36: TLM curves for different samples: (a) for a p-side ITO/Ag sample and (b) for a n-stack sample

In this example, both curves are remarkably well fitted with a line, with an $R^2 = 0.99996$, but it is noticeable that the y-intercept of curve (a) is very close to 0, oppositely to curve (b). In fact the y-intercept of curve (a) is negative, with an uncertainty higher than its value: $y\ intercept = -0.2\Omega \pm 0.53\Omega$. This indicates that refinement of the measurement method is needed.

Refinement could be made based on the calculation of uncertainty, but the error in measurement may vary for all measurements within a data set, as highlighted in [125]. Typically, when a parameter increases, its uncertainty also increases. Here we use a broad range of spacing distances, which makes it likely that the uncertainty in each TLM point should vary, and be independently determined, which is unpractical.

A way to get more precise results is to select lower inter-electrode distances, in order to increase the R_C/R_{tot} ratio. This ratio cannot be calculated for each point as at least two points are needed to measure R_C and R_{Sh}, because we need a slope and a y-intercept. In Figure 37 (a) and (c) R_C and R_{Sh} are measured for three consecutive pads (i.e. two spacing distances) for both curves, and in Figure 37 (b) and (d) the ratio $\frac{2R_C}{R_{tot}}$ and $\frac{R_{layer}}{R_{tot}}$ are also shown (R_{tot} is the one measured for the lowest distance among each pair of distances).

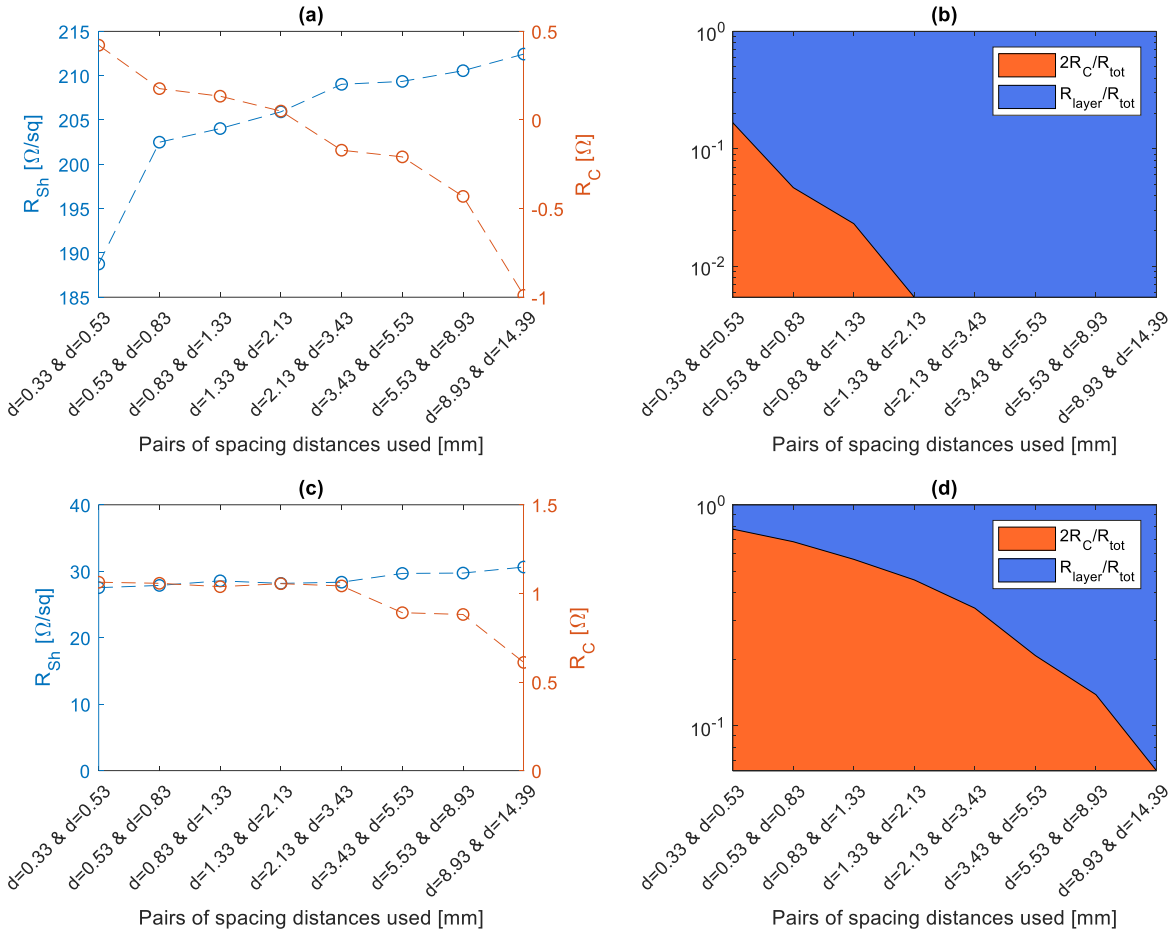

Figure 37: TLM results with each pair of consecutive electrodes for (a) and (b) the p-side ITO/Ag sample and (c) and (d) n-stack sample

We decided to set the criterion that for a TLM measurement to be valid, $\frac{2R_C}{R_{tot}}$ is to be above 1% in order to have a significant signal. In this example, for the p-side ITO/Ag sample, it means removing data with $d > 1.33\,mm$, while all data points can be used for the n-stack sample. Figure 38 illustrates the TLM curve of the p-side ITO/Ag sample with only the selected data.

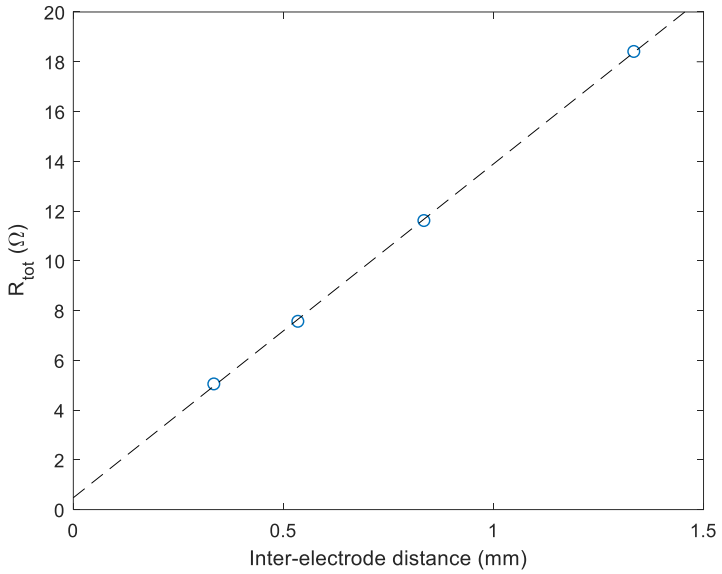

Figure 38: TLM curve with only low spacing distances and new fit on restricted data range

The contact resistance extracted this way is measurable: $R_C = 0.24 \pm 0.52\ \Omega$, which leads to ρ_C $0.64 \pm 1.14\ m\Omega.cm^2$. Even though it is slightly lower than before, the uncertainty is still very high but we get positive values of R_C. Of course, with even lower electrode spacing, we could obtain a more precise measurement but it would also require improved electrode definition to keep the uncertainty $\frac{\Delta d}{d}$ value small enough to avoid measurement uncertainty increase.

3.8.2 Technical implementation of the TLM

The TLM equations are based on a model of the contact that depends on some hypotheses that need to be respected for the characterization of real devices. Here we will discuss several points, sometimes neglected, that can lead to wrong assessment of the sheet resistance and contact resistivity values.

3.8.2.1 Lateral shunt currents

Classically, a TLM structure is represented such as (Figure 39):

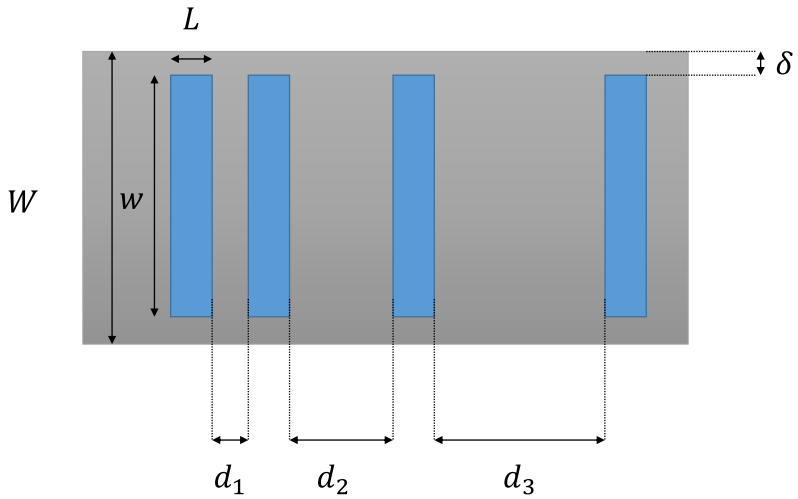

Figure 39 : TLM structure

The distance in between the edge of a TLM electrode and the edge of the sample, δ, should be kept minimal using long electrode so that $w \to W$ [128]. If this is not the case, 2D current flow takes place as current will use the additional space, giving rise to non-straight current lines near the electrode edges when a voltage is applied (see Figure 40).

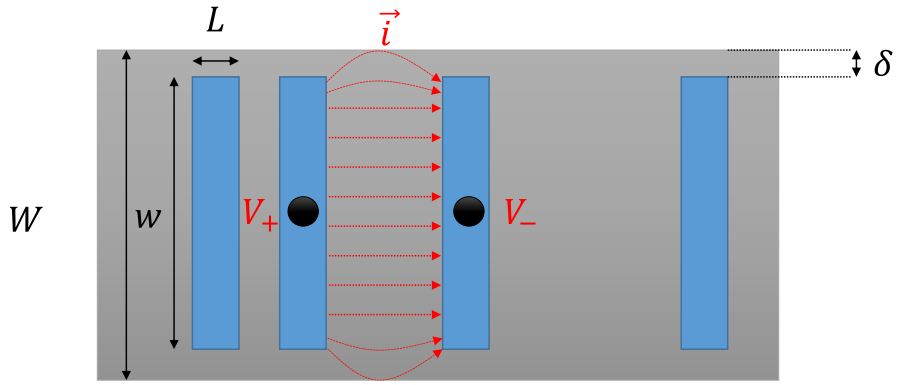

Figure 40: TLM structure with "edge current". Red lines represent qualitatively current lines and their curvature near the electrodes edge

A simple way to get rid of these “edge currents” is to cut the sample up to the electrode edge, to simply get $W = w$. This represents an additional step so we decided to test its necessity.

We used microelectronics grade P-type wafers of very high resistivity ($\rho > 1000\ \Omega.cm$), that we cleaned and textured, and on which we deposited the SHJ front stack a-Si:H(i)/a-Si:H(n) and ITO. TLM patterns of various geometries were screen-printed, varying the length and width of the electrodes, then samples were cured (Figure 41). Due to very high resistivity c-Si and the presence of a PN junction, very low current is expected to flow in the bulk c-Si wafer and we should thus be sensitive mainly to the conduction in the ITO layer.

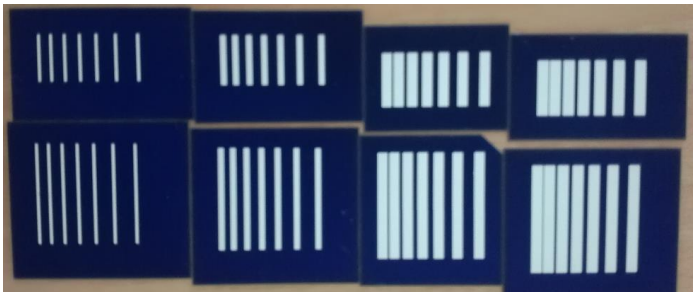

Figure 41 : Picture of TLM samples used for this experiment

These 8 samples were then measured with TLM, and a reference sample without electrodes was measured with 4PP measurement.

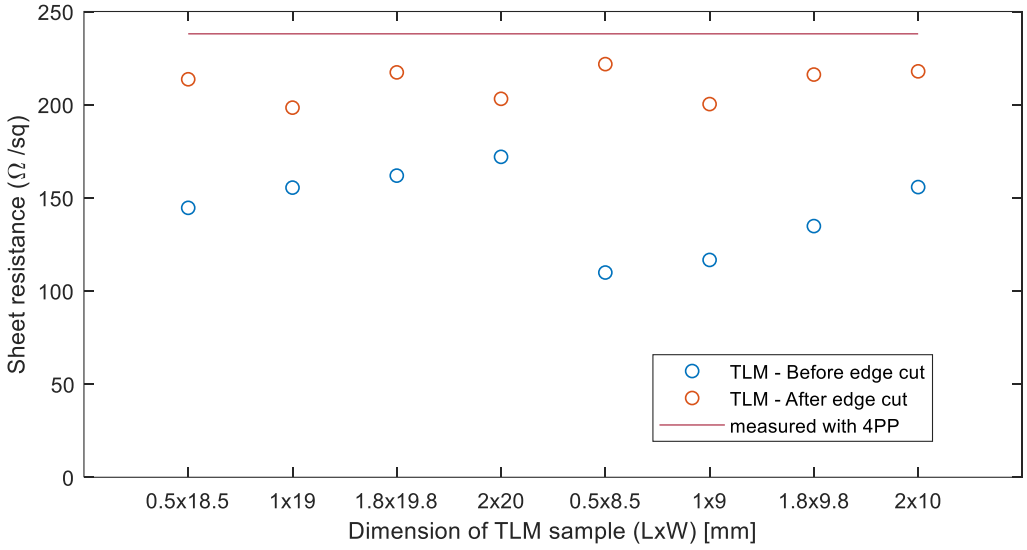

Figure 42 : TLM results as a function of the geometry of the TLM samples: before (blue dots) and after (red dots) cleavage to the electrodes edges

The blue dots in Figure 42 represent the R_{Sh} extracted with these measurements. We can see that the measurement varies with electrode geometry: increasing the length and widths of the electrodes increases the R_{Sh} determined. All blue dots are well below the value measured using 4PP technique. ρ_C also varies a lot with electrode geometry. The lower is the measured sheet resistance, the higher ρ_C is measured: for the 2x20mm sample $\rho_C = 4.6\ m\Omega.cm^2$ while for the 0.5x0.85mm sample $\rho_C = 85.0\ m\Omega.cm^2$.

These samples were then cleaved to the electrode edges and measurements performed again after this operation. The data are represented in the same figure with the orange dots. We can see that the R_{Sh} determined no longer varies with geometry (or only randomly), and is much closer to the value obtained with 4PP measurement. Due to measurement precision, ρ_C values were then unmeasurably small, showing that underestimating R_{Sh} leads to overestimated values of ρ_C. Note that there is a remaining unexplained difference in R_{Sh} between 4PP and TLM after edge cutting.

From now on, all presented results will be "electrode edge cut".

3.8.2.2 Insufficiently conducting electrodes

Another assumption of the classical TLM approach is that the electrodes are infinitely conducting. This allows considering equal potential across the electrodes, and therefore homogeneous current in between the electrodes. It also allows to consider that the electrode itself has no resistance, only its contact with the studied layer impacts the total measured resistance. As real electrodes have a finite conductivity, this has two main drawbacks:

- If the electrode itself has a resistance, it may be non-negligible with respect to the contact [129]. In this work we consider this negligible.
- Electrode resistance from the probe contact to the edge of the sample may induce potential drops, making the assumption of equipotential electrode non-exact. This leads to non straight current lines and to a wrong determinations of both ρ_C and R_{Sh} [130][131]. Similar problems arise for precise FF measurement of solar cells [132].

Often in the literature, metallic TLM electrodes are deposited using PVD, e.g. [58], [91], [133]. These electrodes are then very thin, a few hundred nanometers maximum, and therefore are poorly conducting - even though the metal conductivities are very high -, leading to potential drops in the electrodes and bias in the TLM results. Another occurrence of this phenomenon is when too narrow electrodes are used, for example when using finished cut strips of cells [131].

Screen-printed Ag electrodes typically are much thicker than PVD ones (usually over 10µm VS ~200-400nm), and feature conductivities close to pure Ag, which leads to a better R_{Sh} determination and should diminish the impact of this problem.

Using screen-printed electrodes, we prepared samples of various electrode lengths (0.25 to 2mm) and widths (5 to 30mm), with constant inter-electrode distances. These samples are p-type, in order to measure the hole contacts of the SHJ cell (see §2.5.2.3), but any TLM sample could have been selected. They were chosen for convenience as they have high contact resistance that emphasizes what we want to show in the next section.

To test how the measurements are impacted by the electrode conductivity, we carried out TLM measurements for all these samples with varied length (L) and width (W) (Figure 43).

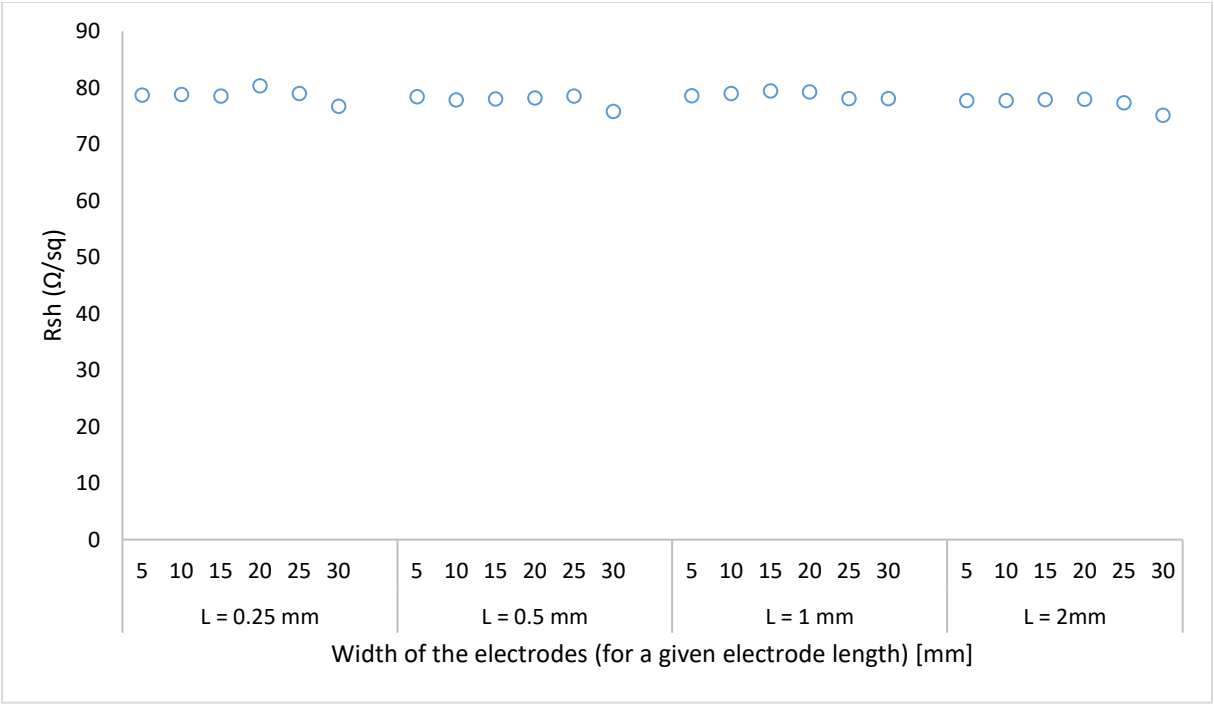

Figure 43: Determination of R_{Sh} on the same kind of samples with various electrode widths and lengths

We found that the extracted R_{Sh} values vary only slightly with the dimensions of the electrodes. A variation may appear for too large widths as most samples exhibit a decrease of R_{Sh} for $W = 30mm$, but it is not very significant. This indicates that our choice for screen-printed electrodes is appropriate, as they are sufficiently conductive for voltage drops to be negligible.

In this work, we exclusively used screen-printed electrodes to avoid such effects and be the most representative of the real device.

3.8.2.3 Use of the "long contact" approximation

The long contact approximation is very handy as it significantly simplifies the model of the TLM by getting rid of the hyperbolic tangent term. It is also valid for a wide range of measurements, as long as $L \gg L_t$. Nevertheless, it is sometimes used abusively (e.g.[58], [125]), even though the full formula is well known. It yields some errors that we will discuss in this section.

From the TLM determination of R_C and R_{Sh}, and three analyses are possible, using either the full TLM formula or some approximations, namely:

(1) Long contact approximation: L_t is determined with Eq. 37, and it yields:

$$\rho_C = R_C^2 * \frac{W^2}{R_{Sh}} \qquad \text{Eq. 96}$$

(2) Short-contact approximation: L_t is not necessary in the calculation from Eq. 38, and it yields:

$$\rho_C = R_C * W * L \qquad \text{Eq. 97}$$

(3) General formula: solving Eq. 36 for L_t:

$$\rho_C = \frac{R_C * W * L_t}{\coth\left(\frac{L}{L_t}\right)} \qquad \text{Eq. 98}$$

We tested all three formulas with the TLM samples of varied W and L depicted in §3.8.2.2, and reported calculated values of ρ_C in Figure 44.

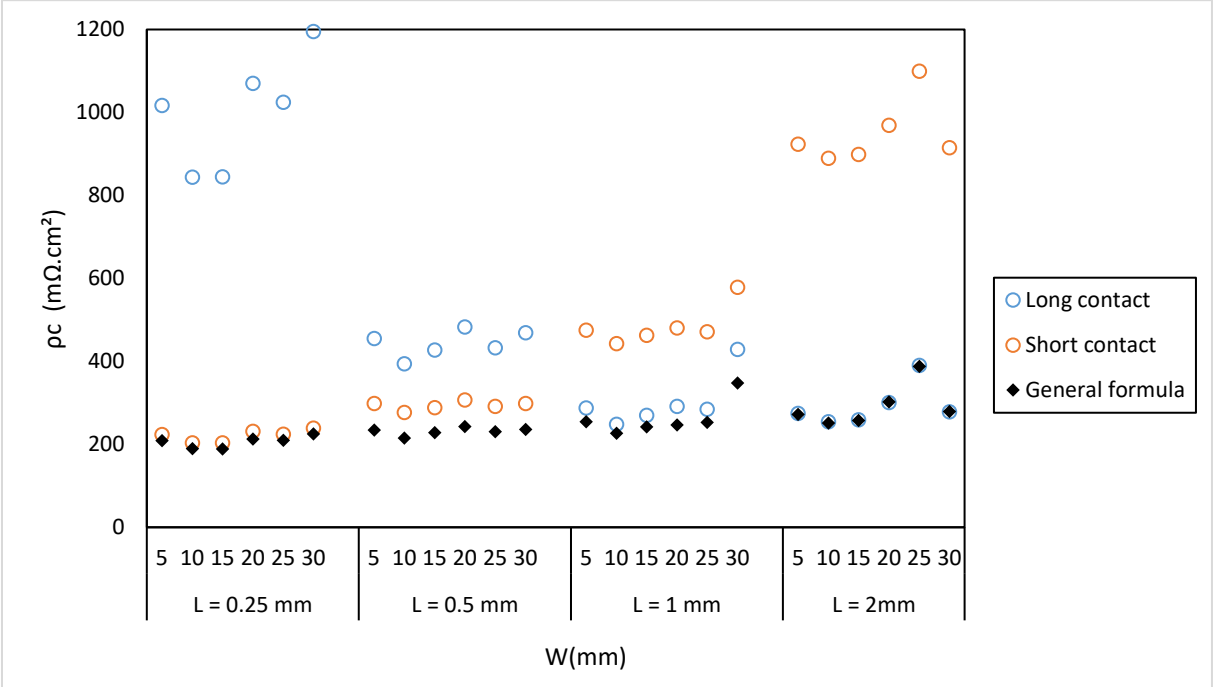

Figure 44 : Contact resistivities of the samples extracted using the three models

Figure 44 shows that using the full formula, the extracted ρ_C only varies slightly with the geometry of the samples, despite a slight unexplained drift and some outliers. However, using both long contact and short contact approximation can yield very inexact results: long contact approximation gives erroneous results of up to 5 times the "full formula" value for the shortest electrodes (L=0.25mm). Oppositely, the short contact formula gives wrong results for too long electrodes, close to 4 times the value obtained with the full formula.

We conclude that the use of the full formula is recommended, especially when studying highly resistive contacts, which are susceptible to yield long transfer lengths. It will be used throughout this work.

3.8.2.4 TLM measurements on cut strips from finished cells

TLM is sometimes carried out using finished cell cut strips. In this configuration, we only have one distance available, so in order to obtain several ones, the measurements are made on non-consecutive fingers leaving un-contacted fingers in between. Then the assumption that no current circulates in the intermediate fingers is made. This assumption has already been questioned in the literature, where it was shown that it could lead to an overestimated value of R_C [131].

Using this kind of measurements on a GP solar "GP 4 test" tool, we saw significant differences in results for both R_{Sh} and ρ_C extracted as compared to conventional TLM samples. Therefore verifying if the hypothesis of no current in intermediate fingers holds is important to conclude on the validity of this kind of measurement.

If the approximation of no current in intermediate fingers holds, then the equivalent circuit of the TLM can be depicted such as in Figure 45 (a). In the contrary, if some current flows in intermediate fingers Figure 45 (b) is more adapted.

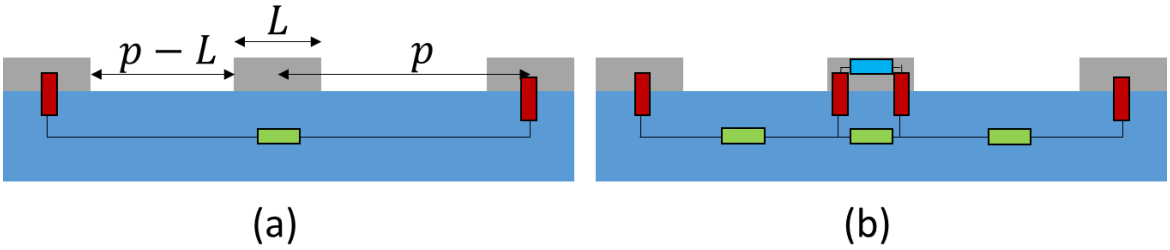

Figure 45: Equivalent circuits for the TLM samples on cut strips of finished cells

In the first case, the measured TLM resistance can be expressed:

$$R_{TLM(a)} = 2 * R_C + R_{Sh} * \frac{(N_i * p) - L}{W} \qquad \text{Eq. 99}$$

Where N_i is the number of inter-finger spacing distances. R_C can be calculated according to the standard TLM model following Eq. 103.

Oppositely, in case (b), including current flow in un-contacted intermediate fingers, we consider the model from Schroder et al [77] and obtain:

$$R_{TLM(b)} = 2 * R_C + N_i * \frac{p - L}{W} + (N_i - 1) * \frac{2R_{Sh}}{R_{Sh} + R_{Sh,Ag}} * \left(\frac{R_{Sh,Ag} L}{2W} + \frac{R_{Sh}\sqrt{\frac{\rho_C}{R_{Sh} + R_{Sh,Ag}}}}{W} * \tanh\left(\frac{L}{2\sqrt{\frac{\rho_C}{R_{Sh} + R_{Sh,Ag}}}} \right) \right) \qquad \text{Eq. 100}$$

Using these formulas, we can simulate what to expect from TLM results on such samples following both models. We take the example of a design with $L = 50\mu m$, $p = 1.8mm$ and strips cut at $W = 1cm$, a metallization thickness of 10µm, and a silver paste resistivity of 5 $\mu\Omega.cm$. We consider $N_i = 6$, agreeing with the sample design for the GP solar tester at CEA.

Varying input R_{Sh} and ρ_C, we simulate TLM curves with Eq. 99 and Eq. 100 and extract results by TLM analysis. Of course, with Eq. 99 we extract the very same input parameters as no current goes in the intermediate fingers. However, when we use Eq. 100, our results differ due to current in intermediate fingers (Figure 46).

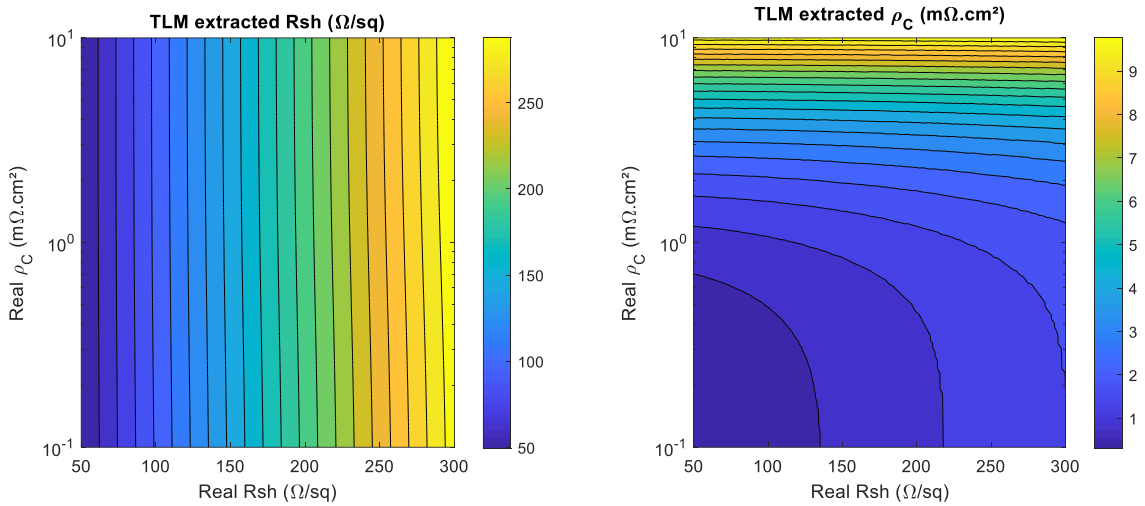

Figure 46: Contour plots of the extracted ρ_C and R_{Sh} by TLM as a function of input parameters, following modelling with Eq. 100

We observe that the R_{Sh} measured is slightly underestimated, especially when sheet resistance is high and contact resistivity is low. We also observe that this can lead to errors in the determined ρ_C, which tends to be overestimated, especially when ρ_C is low and R_{Sh} is high.

For $R_{Sh} = 200\Omega/sq$ and $\rho_C = 1m\Omega.cm^2$, it can lead to $-1.5\Omega/sq$ and $0.5m\Omega.cm^2$ errors. As fingers are thin, they are also more susceptible to the problem of insufficiently conducting electrodes. **For these reasons, in this work we preferred the use of samples with printed TLM patterns.**

3.8.2.5 TLM on thick layers

Another limit of the TLM model is the assumption of a "sheet conduction" regime. In other words, the studied layer should be so that the current density in this layer can be considered homogeneous. This is well verified for thin layers, but can cause significant errors when studying thick layers, such as the samples for electron and hole contacts determination presented in §2.5.2.3.

This is likely to pose no threats for the study of the Ag/ITO contact, as the ITO thickness is low (t ~70nm) compared to the spacing distances used in our TLM designs ($d > 100\mu m$). However this is not the case for n and p-stack TLM samples, were the current spreads laterally in the approximately 160µm thick c-Si wafer. In this case, caution should be taken to restrict the use of too low inter-electrode spacing.

To test that we are not affected by too low inter-electrode spacing, we simulated n-stack TLM samples in Silvaco Atlas, and varied the electrodes spacing from 10 to 5000 µm. The resistivity of the substrate was set to $1\Omega.cm$, so we expect a sheet resistance for our 160µm thick wafer of $R_{Sh,c\text{-}Si} = 62.5\Omega/sq$. To perform a TLM measurement, only two I-V measurements at two

different spacing distances are needed. Here we carried out TLM analyses with each pair of consecutive spacing (10 and 20µm, 20 and 50µm, etc.), and extracted R_{Sh} and R_C for each.

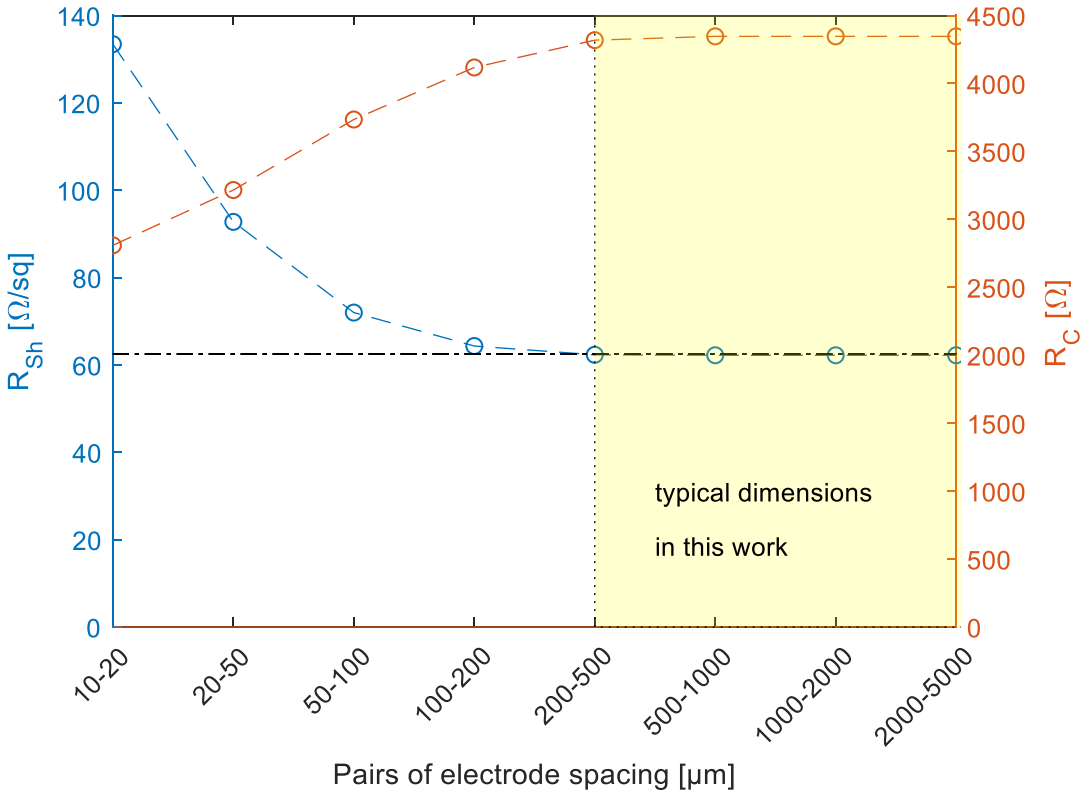

Figure 47: TCAD simulation of the sheet resistance and contact resistance extracted by TLM with varying pairs of electrode spacing

We can see in Figure 47 that varying the electrode spacing used in the TLM design leads to varying results when using spacing distances below approximately 200µm. Using spacing distances above this ensures constant results, matching the expected value of $R_{Sh,c\text{-}Si}$, showing that above 200µm the approximation of $t \ll d$ is valid. **The minimum value for the electrode spacing should not be below 200µm for a c-Si thickness of 160µm.**

Additionally, the TLM method was developed for thin layers, and yields non-physical results when 2D transport phenomena occur, for instance when the thickness of the layer becomes non-negligible compared to the contact length (i.e. contact resistivity is a function of the thickness of the studied layer). Eidelloth and Brendel [134] proposed a model to consider such cases. They define a resistance parameter γ such that:

$$\gamma = \frac{L^2 \rho}{\rho_C t} \qquad \text{Eq. 101}$$

Which allows to calculate the geometry factor in the case of the classical "1D" TLM model:

$$G_{1D} = \sqrt{\gamma} * \coth\left(\sqrt{\gamma}\right) \qquad \text{Eq. 102}$$

Contact resistivity can then be derived from:

$$\rho_C = \frac{R_{C,TLM} W L \rho}{G * R_{Sh,TLM} t} \quad \text{Eq. 103}$$

Where $R_{C,TLM}$ and $R_{Sh,TLM}$ are the experimental values of R_C and R_{Sh} extracted with the y-intercept and slope of the TLM curve, and G is the geometrical factor.

In the case where thickness and resistivity of the layer are unknown, $R_{Sh,TLM}$ is estimated to be equal to ρ/t, and using $G = G_{1D}$, Eq. 103 becomes equivalent to the classical TLM model. It is solved iteratively directly for ρ_C.

Now in the case of a thick layer, to account for 2D current flow, a more complex expression of G is needed, G_{2D} such that:

$$G_{2D} = 1 + \sqrt{(G_{1D} - 1)^2 + (G_{CM} - 1)^2} \quad \text{Eq. 104}$$

Where G_{CM} is the geometrical factor obtained from conformal mapping:

$$G_{CM} = 1 + \gamma + \frac{\gamma\delta}{\pi} * \left[\ln(4) - \ln\left(e^{\frac{\pi}{\delta}} - 1\right)\right] \quad \text{Eq. 105}$$

And δ is the height parameter:

$$\delta = \frac{t}{L} \quad \text{Eq. 106}$$

Solving Eq. 103 with $G = G_{2D}$ gives the results accounting for 2D effects and allows determining contact resistivity independently of the thickness of the layers. Later on in this work, we will discuss this model regarding the characterization of electron and hole contacts in SHJ cells (§4.2.2).

3.9 Chapter outlook

In this chapter, we have discussed the fabrication process of SHJ cells at CEA, and presented the principal means of characterization that we carried out in this work. We also described our approach for modelling solar cells and TLM samples with 2D TCAD, and detailed the parameters used for simulations. Finally, we addressed the experimental measurement of series and contact resistances: we chose the pFF-FF method to measure R_S as it offers the best compromise between precision and handiness. For ρ_C measurements, we detailed some precautions that we take to ensure the measurement is valid. We use samples with screen-printed TLM patterns, cutting the outer edge of the samples, using the general formula of the TLM, and with a minimal spacing of 200µm.

Chapter 4

Development of methods to measure contact resistance in SHJ cells

We have discussed that interfaces at the electron and hole contacts of the SHJ cell have been identified as high contributors to resistive losses. As such they are extensively studied by different research groups [58], [133], [135]. Reducing transport losses across these contacts without affecting passivation would lead to increased performance of the device.

The Ag/TCO contact is also important: its contact resistivity is lower, but as the contact is more localized due to low area coverage, it also supports higher currents. As values reported in the literature vary a lot, it is hard to know if it has any significant impact on device efficiency.

We have also discussed that TLM measurements are prone to different biases and that a precise determination of these quantities requires a thorough measurement and precautions.

The objective of this chapter is to validate procedures to fabricate samples and measure them in a way that avoids most of the biases, in order to get reliable values of electron and hole contact resistivities, as well as Ag/TCO contact resistivity and sheet resistance of the TCO.

4.1 Measuring the ITO sheet resistance and ITO/Ag contact with high fidelity to SHJ structure

4.1.1 4-point probe measurement of ITO sheet resistance

The sheet resistance of the TCO is an important figure of merit to quantify its electrical properties, and is an important input for models to assess the series resistance of a SHJ cell (§2.3.2). It is easily measured using 4-point probe (4PP) or transfer length method (TLM). However, some aspects of the measurement are often overlooked, and can lead to a wrong determination of its value, mostly:

(1) In rear-emitter cells, a measurement on the front surface of the cell does not probe only the TCO, as current is not confined in the TCO layer and can cross the electron contact and flow in the c-Si [108].
(2) Growth of the TCO can differ depending on the substrate and lead to different crystalline structure. Techniques that use TCO deposited on insulator substrates thus may not be representative to the TCO in an SHJ cell [57].
(3) PVD deposition of a material on a flat surface as opposed to a textured surface leads to different layer thickness. Using same deposition parameters, film deposited on a flat surface is usually of higher thickness than deposited on a textured surface. Not accounting for this effect can cause an underestimation of the TCO sheet resistance [136].

We used TEM pictures to measure the thickness of ITO on a-Si:H passivated textured c-Si wafers (Figure 48) and measured approximately 70nm. As a comparison, the standard ITO thickness on polished substrate is measured by ellipsometry and SEM to be approximately 100nm. We consider a polished to textured surface thickness ratio of 1.39 ± 0.05.

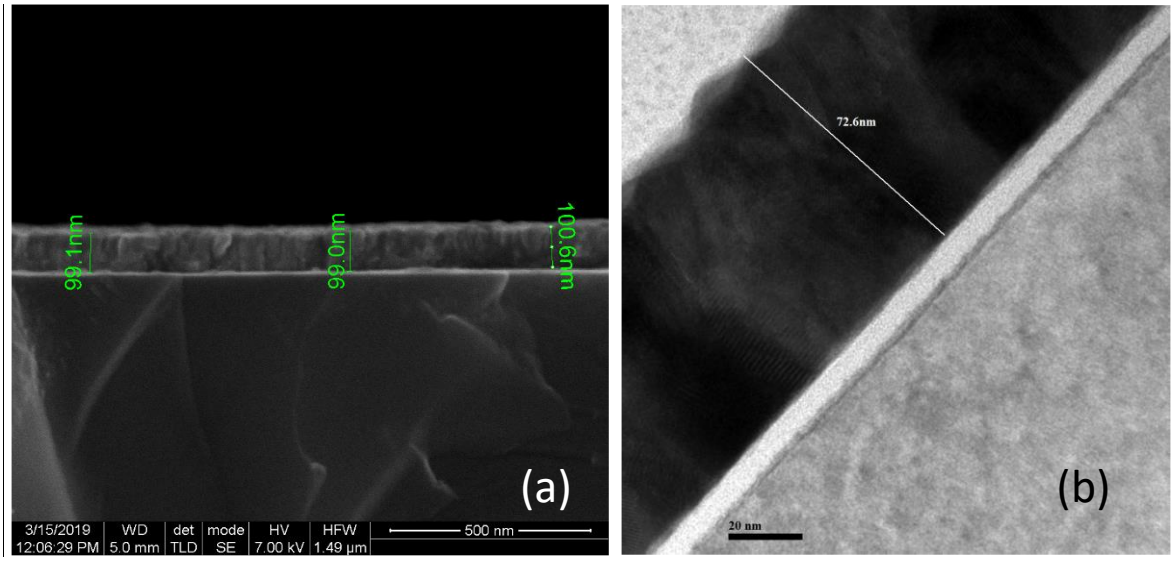

Figure 48: Cross section of an SHJ cell precursor after ITO deposition, (a) on polished substrate, (SEM picture and measurement) and (b) on textured surface at a pyramid side (TEM picture and measurement)

To account for the difference in thickness, the expected $R_{Sh}(ITO)$ of a layer deposited with the same deposition parameters on textured substrate is thus the raw measurement on that flat surface multiplied by the textured to flat thickness ratio.

We prepared samples of ITO deposited directly on bare glass, and on glass with an a-Si:H(i)/a-Si:H(n) stack interlayer to be closer to the SHJ structure, with similar seed layer. The samples were then annealed with the standard curing process of SHJ cells (Figure 49).

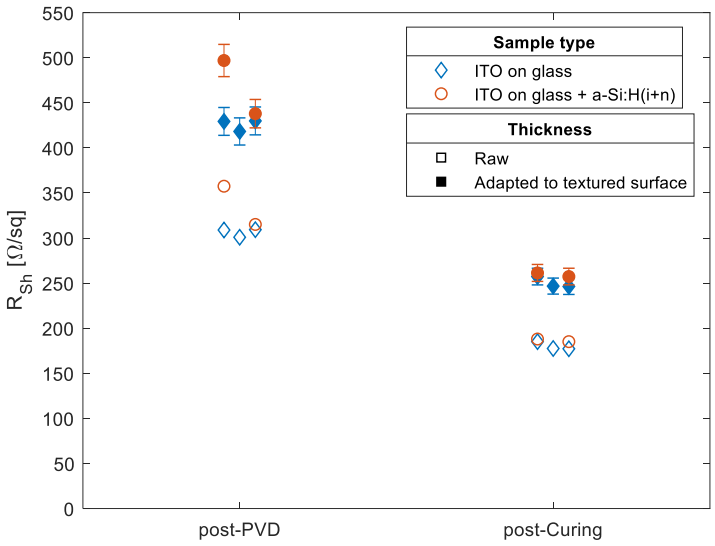

Figure 49: Sheet resistance of ITO layers deposited directly on glass substrates (blue diamonds) and on glass with a a-Si:H(i)/a-Si:H(n) buffer layer (orange circles) before and after curing. Empty symbols are raw measurements, filled symbols are values corrected for textured/flat surface ratio (see text). Error-bars account for the uncertainty in the textured to flat surface ratio

Prior to curing, the ITO sheet resistance is very high (>300 Ω/sq), and decreases significantly after curing where the average value is $183\,\Omega/sq$. For the deposition process we use, the deposition on a a-Si:H(i)/a-Si:H(n) buffer stack layer does not impact significantly the results compared to that obtained on bare glass, and even more after curing, contrary to [109], [137].

Accounting for the texturing and the effect of the ITO curing on a finished SHJ cell stack, $R_{Sh}(ITO)$ is expected to yield $256\,\Omega/sq$.

4.1.2 Insulating the TCO layer from the c-Si to measure Ag/TCO contact resistance and sheet resistance of the TCO

In this section we will test the ability of several sample preparations to allow the precise measurement of the sheet resistance of the ITO layer, $R_{Sh}(ITO)$, in a complete SHJ cell structure using both TLM and 4PP methods and to extract the contact resistivity between the ITO and silver screen-printed contact $\rho_C(Ag/ITO)$.

We fabricated three kinds of samples, with free space for 4PP measurements and deposited TLM electrodes (see Figure 50):

(a) Samples with no insulation scheme – standard SHJ cell with TLM screen-printed pattern at the front surface field (a-Si:H(i)/a-Si:H(n) stack), that we label "n-side ITO/Ag TLM samples"
(b) Samples with junction insulation scheme – SHJ cells with TLM screen-printed pattern at the emitter side (a-Si:H(i)/a-Si:H(p) stack), or called "p-side ITO/Ag TLM samples"

(c) Samples with dielectric layer insulation scheme – samples with a-Si:H(i)/a-Si:H(n) stack at the rear and thick intrinsic a-Si:H(i) layer at the front (~50nm). "thick-(i) ITO/Ag TLM samples"

As a way to determine if the current is indeed confined in the ITO, all of these samples were fabricated using wafers of varying bulk resistivity, from 0.49 to 14.12 $\Omega.cm$. Electrode measured dimensions are 14.65mm x 1.97mm and electrodes spacing varies between 0.33 and 2.13mm.

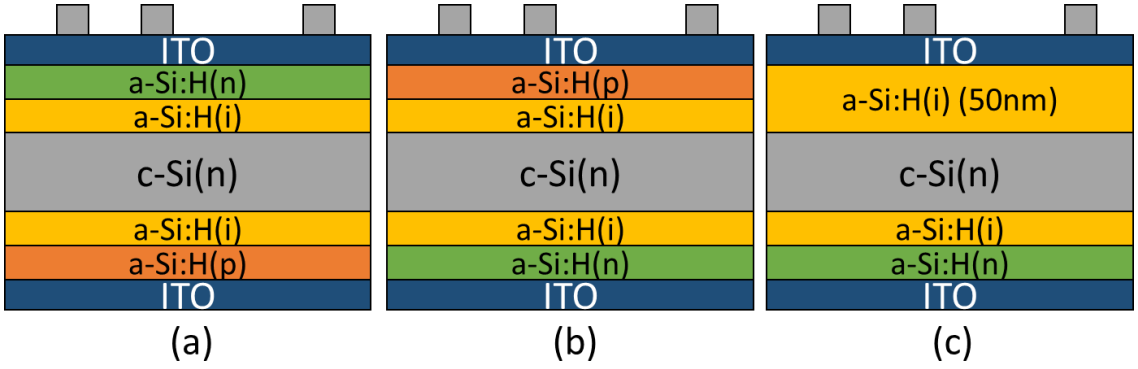

Figure 50: TLM samples (a) n-side ITO/Ag, (b) p-side ITO/Ag and (c) thick-(i) ITO/Ag

Note that the ITO on glass samples from the last section were fabricated during the same PVD activity as these samples, therefore, no drift of the deposition parameters is expected, and ITO layers are supposed to be homogeneous from sample to sample.

All these samples were then measured using both 4PP and TLM methods. For the n-side ITO/Ag TLM samples, we expect a sheet resistance that is not representative of only the ITO layer, but of the whole front stack: we will then label it as $R_{Sh}(eff)$. Results for these samples are represented in Figure 51:

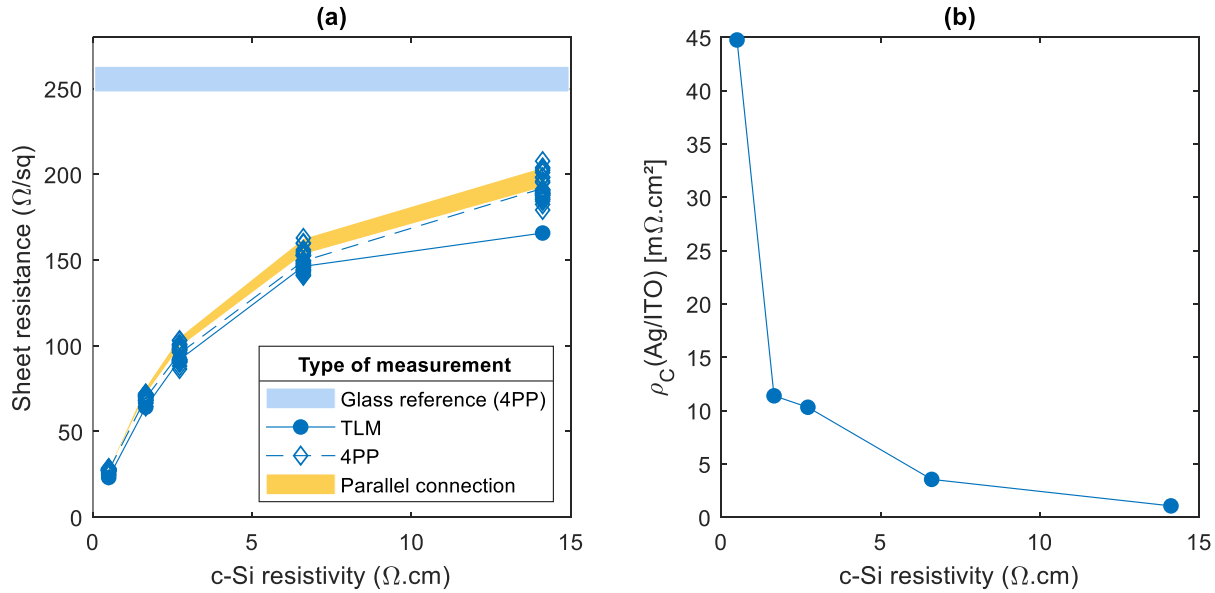

Figure 51: n-side ITO/Ag TLM samples: (a) sheet resistance versus c-Si resistivity as obtained with different methods: filled blue area is the expected range of $R_{Sh}(ITO)$ as deduced in §4.1.1, empty blue diamonds represent $R_{Sh}(eff)$ as measured with 4PP, and filled blue dots correspond to $R_{Sh}(eff)$ as measured with TLM. Finally the yellow line is $R_{Sh}(eff)$ as calculated from measurements on glass (b) contact resistivity of the Ag/ITO contact determined from TLM results

The measured $R_{Sh}(eff)$ with both TLM and 4PP is varying with the c-Si wafer resistivity, clearly indicating that an important part of the current is going through the c-Si wafer. Values obtained with both methods agree to a certain degree, demonstrating a good agreement with the model proposed by Bivour et al. [108] (see §2.5.3) involving parallel conduction in c-Si and ITO.

$$R_{Sh}(eff) = \left(\frac{1}{R_{Sh}(c-Si)} + \frac{1}{R_{Sh}(ITO)}\right)^{-1} \quad \text{Eq. 107}$$

In Figure 51 (a), the yellow line corresponds to $R_{Sh}(eff)$ calculated with $R_{Sh}(ITO)$ =256 Ω/sq, corresponding to the measurement on glass adapted to textured surface, and $R_{Sh}(c-Si) = \frac{\rho_{c-Si}}{t}$. It fits very well with the 4PP measurements, indicating that Eq. 107 and the measuring approach presented in the previous paragraph (§4.1.1) concur.

Shown in Figure 51 (b) is the corresponding contact resistivity determined from TLM measurements. We can see that the more current spreads in the underlying c-Si base (i.e. $R_{Sh}(eff)$ is low), the more the contact resistivity increases. This contact resistivity is not representative of the Ag/ITO contact, as the c-Si/a-Si:H(i)/a-Si:H(n)/ITO interface is crossed by a part of the current. The TLM model, based on 1-layer conduction, does not hold anymore, and the determined value corresponds to an "effective contact" resistivity, which is not rigorously defined, but includes a contribution from the very resistive electron contact.

Even for the most resistive c-Si wafers, a significant amount of current spreads in the base, as the difference between $R_{Sh}(eff)$ and $R_{Sh}(ITO)$ is still over 50 Ω/sq. This kind of samples thus does not allow to measure the Ag/ITO contact resistivity but allows to demonstrate the parallel conduction of the ITO and c-Si layers.

Figure 52 illustrates the results of the TLM and 4PP measurements obtained with different insulation schemes: p-side ITO/Ag TLM samples and thick-(i) ITO/Ag TLM samples

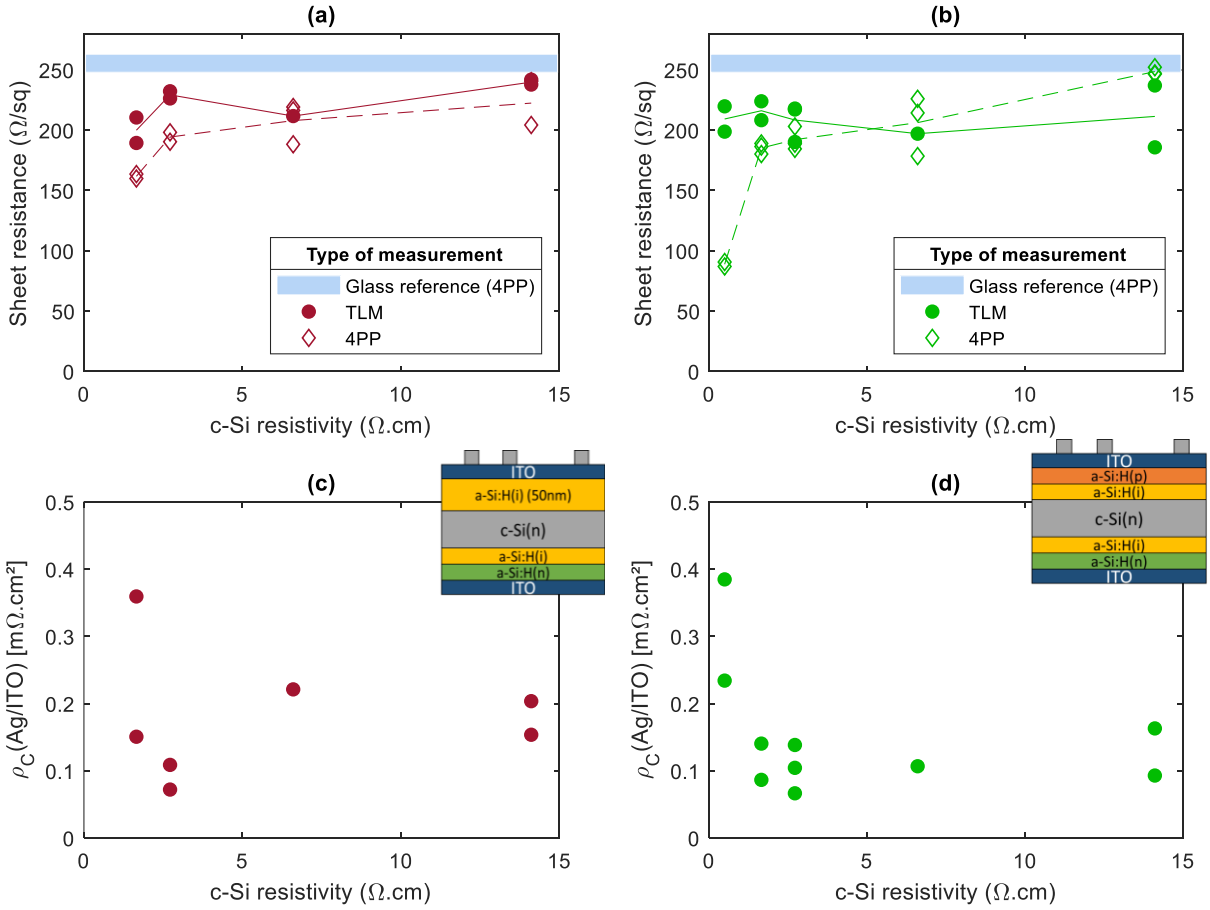

Figure 52: Results of TLM and 4PP measurements for: left hand side ((a) and (c) curves): thick-(i) ITO/Ag samples and right hand side side ((b) and (d) curves): p-side ITO/Ag samples. (a) and (b) show Rsh values versus c-Si resistivity extracted from each method (as well as the reference value obtained on glass). Lines show average values. (c) and (d) curves show extracted contact resistivity of the Ag/ITO contact as a function of c-Si resistivity

- Figure 52 (a) & (b) demonstrate that for both insulation strategies, R_{Sh} values extracted with TLM vary little with c-Si resistivity with no obvious trend, indicating that the measurement is valid, with a R_{Sh} measured between 185 and 241 Ω/sq with an average value of 214 Ω/sq. Measurements on thick-(i) ITO/Ag samples have a slightly higher average value of 221 Ω/sq than p-side ITO/Ag samples with an average value of 210 Ω/sq. However, these values are quite lower than those determined for the "reference" sample (see §4.1.1). This indicates that either the insulation is not complete or, maybe more likely, that the conclusions of the measurements on glass must be revised towards those proposed in [57], [109] when the starting substrate is c-Si and not glass.

  Unfortunately the samples from the 0.49 $\Omega.cm$ class with thick a-Si:H(i) insulation were broken during fabrication. This is particularly regrettable as R_{Sh} at 1.66 $\Omega.cm$ with this type of sample was slightly lower, suggesting a possible incomplete insulation. More statistics would also be helpful to strengthen this result.

- 4PP measurements do not allow to extract the R_{Sh} of the ITO, as they show a clear trend with c-Si resistivity, indicating that part of the current goes through the c-Si wafer. As

TLM results are not affected the same way, we interpret this as probes from the 4PP tool piercing through the ITO and the insulating layer (a-Si:H(p) or thick a-Si:H(i)), probing both ITO and the c-Si and measuring some form of parallel conduction in the ITO and c-Si layers. The TLM measurements do not suffer from this effect as the thin layers are protected from the probes by the thick screen-printed electrodes. Note that, at least for the junction insulation samples, another hypothesis has been proposed in the literature, accounting for "stress induced junction leakage" [138]. Also note that we are using "soft" probes which should prevent junction leakage [138].

- Figure 52 (c) & (d) illustrate that $\rho_C(Ag/ITO)$ measured with insulation schemes is below $0.4\ m\Omega.cm^2$ for all samples. Discarding the value obtained for the lower c-Si resistivity, samples with junction insulation show remarkably constant Ag/ITO contact resistivity value at $0.11 \pm 0.03\ m\Omega.cm^2$.

The preferred method for measuring contacts is chosen as the junction insulation: it is simpler to fabricate samples, as it only requires to flip the samples in between the PECVD and PVD steps, without the need of different deposition conditions, as opposed to the thick a-Si:H(i) layer. Also, the latter seem to be more ambiguous on whether there is a trend with bulk resistivity or not. Additionally, junction insulation is already documented in the literature, and its results can be more directly compared to values from e.g. [89]. Therefore, we report a value of $R_{Sh}(ITO) = 210\ \Omega/sq$ for the ITO layer under study and of $\rho_C(Ag/ITO) = 0.11 \pm 0.03\ m\Omega.cm^2$.

This method may also be more appropriate than 4PP measurements to assess the sheet resistance of the ITO, both on the emitter side of a cell precursor, or on a glass substrate, because it ensures that the probes do not pierce the layers, and that growth of the ITO is representative of the cell.

4.1.3 Simulation of Ag/ITO TLM samples

To verify that, theoretically, current is indeed confined in the ITO layer, we performed TCAD simulations on Silvaco Atlas (see §3.7) of the different samples structures. We did not adapt parameters of the ITO to match our experimental results, and kept the standard parameters for the simulation (detailed in § 3.7.1): with the given electron mobility and electron density, the 70nm thick ITO is expected to yield a sheet resistance of $289.48\ \Omega/sq$.

We simulated n-side ITO/Ag and p-side ITO/Ag TLM structures for details).

When studying the simulated p-side ITO/Ag structure, we can notice that there is a gradient in the electron concentration close to the junction, due to the presence of the a-Si:H(p) layer which produces a field effect that induces band bending inside the ITO.

To calculate the R_{Sh} of the layer when n is inhomogeneous, we use the integral expression (in the case of a highly n-doped material such as ITO):

$$R_{Sh} = \frac{1}{q * \mu_n * \int_0^t n(t)dt} \qquad \text{Eq. 108}$$

In this case, as data from TCAD simulations are discrete:

$$R_{Sh} = \frac{1}{q * \mu_n * \sum_{i=0}^{i=n-1}(x_{i+1} - x_i) * \frac{(n_{i+1} + n_i)}{2}} \quad \text{Eq. 109}$$

The new value from the discrete numerical integration reads $R_{Sh,ITO} = 295.2\Omega/sq$.

Simulations were ran with varying electrode spacing, and IV curves were extracted, and treated just as experimental ones with the TLM model. Note that physical parameters of the contact and interface are not optimized to match experimental data, and therefore in the following section we are only interested in the R_{Sh} values extracted with the TLM. The simulation values are compared to the theoretical parallel conduction expected from Eq. 107.

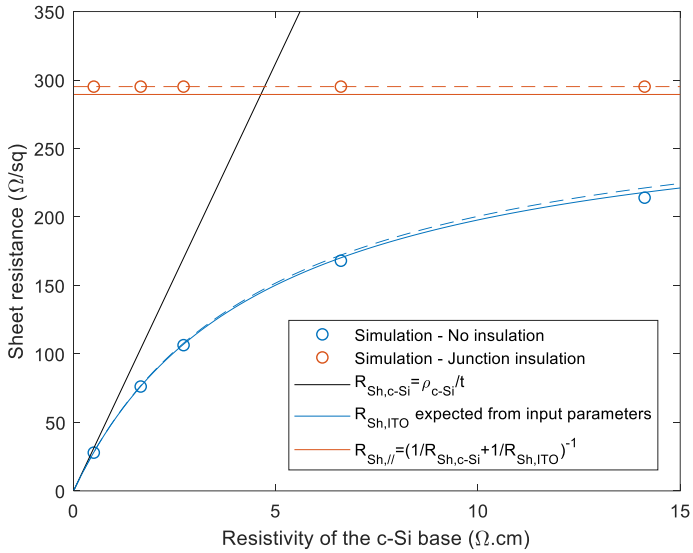

Figure 53: Simulation results of the sheet resistance extracted with TLM as a function of the resistivity of the c-Si base for non-insulated (n-side ITO/Ag) and junction insulated samples (p-side ITO/Ag). Solid lines represent data with $R_{Sh}(ITO)$ determined from the input properties of the ITO while dashed lines are the value for $R_{Sh}(ITO)$ determined from Eq. 109

In Figure 53, we can see that when there is no insulation (blue dots), the measured R_{Sh} follows quite closely the expected parallel resistance from Eq. 107 (blue dashed curve). As c-Si resistivity increases, the slight deviation between simulated and expected R_{Sh} increases a bit but stays below 2% error. Note that this is likely explained by the impact of the contact resistance which may impede parallel conduction but that we neglected here. This is also quite similar to what was observed experimentally in §4.1.2 (see Figure 51(a)). Note that the error is slightly higher when using the value from integration as the band bending from the a-Si:H(p) layer is absent in this case and should not be considered.

When using junction insulation (orange dots), the R_{Sh} extracted from our TLM simulation is independent of the c-Si resistivity, and equals 295.2 Ω/sq matching the value of $R_{Sh}(ITO)$ determined from integration, showing that indeed the junction does insulate the base from the ITO.

Therefore, **we confirmed using TCAD simulations that the junction does insulate the ITO layer from the substrate.** We also show that the method slightly overestimates $R_{Sh}(ITO)$ due to band bending of the a-Si:H(p) that depletes the ITO layer close to the interface.

4.2 Measuring the electron and hole contact layers in SHJ structures

4.2.1 Development of a process for the fabrication of structures for electron and hole contact resistivity measurement

We have seen previously that Lachenal et al. [58] proposed a method to extract the contact resistivity of the electron and hole contacts of the SHJ cell.

Their approach may be affected by several biases:

- They hypothesize "long contact" approximation instead of the complete model so they may be affected by the geometry of their electrodes (see §3.8.2.3)
- They use PVD deposited metal electrodes, so they may be subjected to potential drops along the electrodes (see §3.8.2.2)
- They do not account for the effect of a thick bulk material (see §3.8.2.5), and use low electrode spacing which may lead to bias
- They do not have a rear passivation, and they do not verify that their samples are not degraded during the process, which will be important in the following of this work (§6.2.3)

In this section, we will discuss the development of our approach to avoid these biases, and demonstrate that our samples can be fabricated without significantly harming passivation.

4.2.1.1 Process flow

Our approach to fabricate samples is to use a process that is as close as possible to that of a real SHJ solar cell: we use textured wafers, we want our electrodes to be screen-printed, both front and rear passivation layers are made, and we want these layers unharmed during the fabrication process. We also want an as close to design as possible definition of the electrodes.

First, we prepare SHJ cells precursors, i.e. up to the end of the PVD step. Secondly, we use inkjet printing to deposit a hot-melt organic compound to pattern a TLM design. Thirdly, we realize the etching of the ITO of the unmasked region using concentrated HCl. Fourthly, we remove the hot-melt using a KOH free wet recipe. We then perform the screen-printing step aligned to the ITO patterns. Finally, we cut the sample edges (see Figure 54).

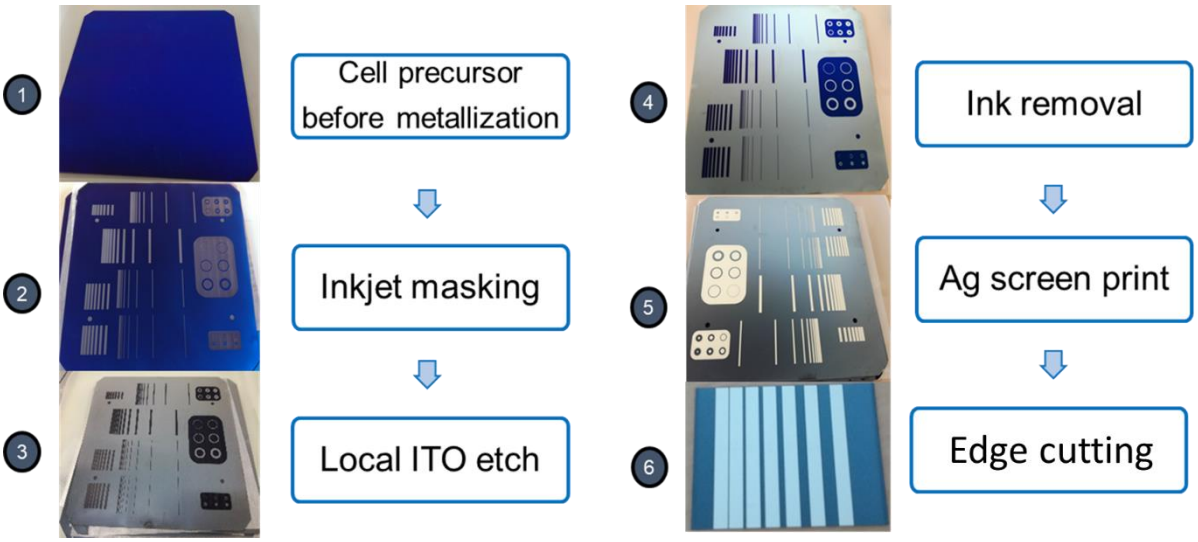

Figure 54: Process flow for electron/hole contact resistivity measurement samples

In the end our samples are slightly different than those from Lachenal et al. [58] (see Figure 55). They differ by the rear side, which is passivated in our samples, and by the silver electrodes, which are screen-printed and not sputtered.

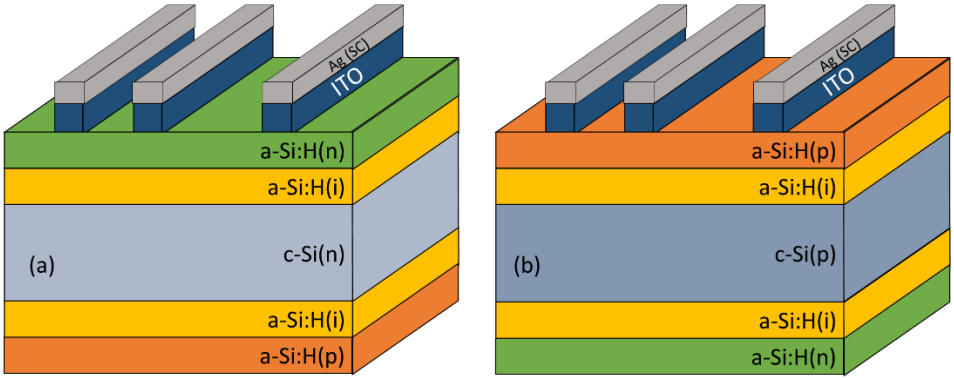

Figure 55: (a) n and (b) p type stack TLM samples for extraction of the electron and hole contact parameters, respectively (texturing is not illustrated)

To measure the hole contact, P-type wafers are used for the fabrication of the cell precursors. Then the masking and subsequent steps are done on the rear side of the wafer, at the c-Si(p)/a-Si:H(i)/a-Si:H(p)/ITO contact.

4.2.1.2 Inkjet masking

To realize the masking step, we use an inkjet printer from Ceraprint to deposit organic hot-melt waxes from SunsChemical. The patterns are first defined in the built-in software, then the wafer is set in the machine and aligned. The hot-melt is heated above its melting point, and then the deposition starts. Temperature is kept below 150°C so we expect no damages to the a-Si:H layers due to thermal degradation.

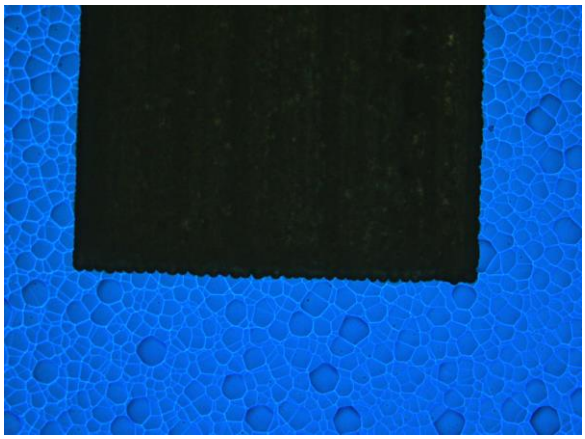

Figure 56: Hot-melt deposited on a cell precursor with polished substrate (c-Si(n)/a-Si:H(i+n)/ITO). For reference, the width of the hot-melt design is approximately 2mm

As can be seen on Figure 56, the droplets do not always completely regroup at the edges of the design and they form a not completely straight edge. The effect is more pronounced in the direction the print head is moving: the design must be made so that the most critical edge is parallel to the print head course during printing. With our TLM samples, as we cut the outer edges of the samples (bottom edge in Figure 56), the definition of the pattern is satisfying.

4.2.1.3 ITO removal

ITO can be etched with the use of strong acids [139]. For this purpose, we chose HCl for commodity as it is slightly less dangerous and polluting than HF. The hot-melt specifications ensure that it resists strong acids, and that was verified experimentally. To estimate the time needed to etch the ITO, we designed a study to measure the etch rate of the ITO layers deposited on our samples in HCl. A second experiment to ensure that passivation was unharmed by this etch step was also realized.

4.2.1.3.1 ITO etch rate

We measured layer thickness as a function of etch time in HCl using ellipsometry. Ideally, ellipsometry requires single side polished (SSP) surfaces to avoid parasitic reflection at the rear side, mainly for n and k determination. However, to measure the thickness of a layer double side polished (DSP) are sufficient. Mostly, SSP and DSP samples are available on microelectronics grade wafers which is not convenient for our equipment tools adapted to M2 size wafers. For easier integration into our fabrication line, we used a wet polishing recipe to obtain flat surfaces with our M2 Cz c-Si. These wafers then received the reference process of fabrication for our SHJ samples, as described in §3.1, except for the ITO which was deposited thinner to account for the textured to flat surface thickness ratio (§4.1.1) and aim for an approximately 70nm thick ITO layer on flat surface.

After fabrication of the samples, they were immersed in concentrated HCl for various durations, and then rinsed in deionized water and dried. We then used ellipsometry to obtain the real and imaginary parts of the dielectric contacts of the layers. The raw signal is first analyzed, then a model is applied to infer the thickness of the ITO layer as a function of time in HCl and deduce the corresponding etch rate of ITO.

Raw results of ellipsometry, and more specifically the imaginary part of the dielectric constant, are given in Figure 57 for etching times between 0 and 360 s, with a 30s step.

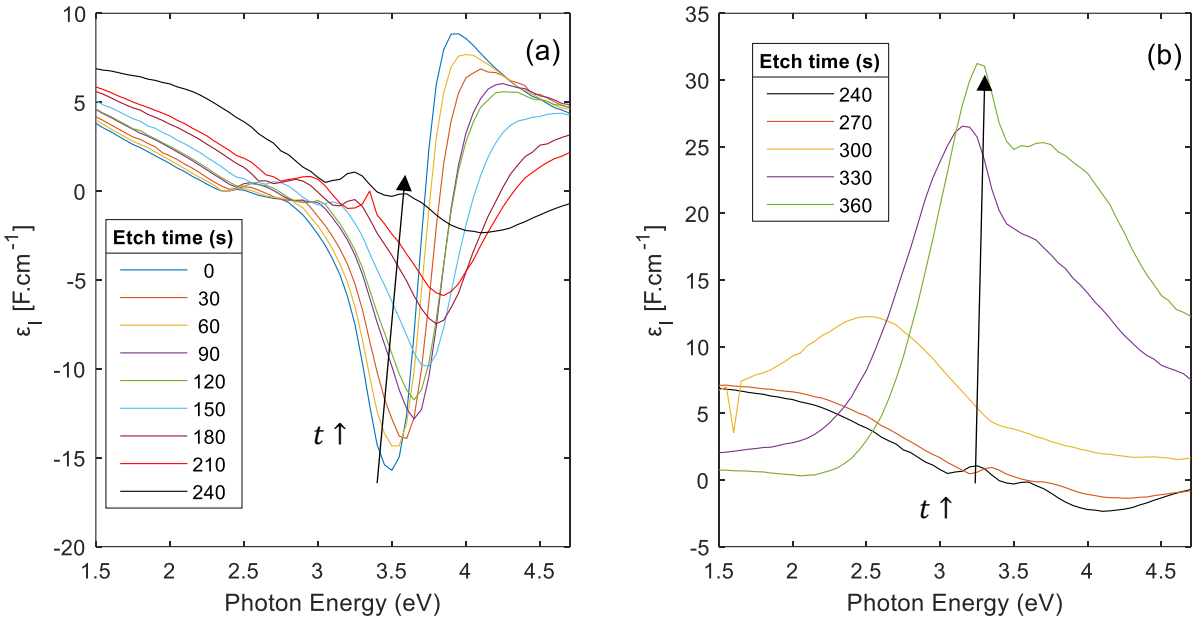

Figure 57: Imaginary part of the dielectric constant measured with ellipsometry for samples that were drowned in HCl for times between (a) 0 and 240s and (b) 240 and 360s. Arrows are just guides to the eye

To serve as references, a bare c-Si wafer, a-Si:H(i+n) layers deposited on c-Si substrate, and finally a 70nm thick ITO layer deposited on a-Si:H(i+n) layers on a c-Si substrate were measured. In Figure 58 we observe that the raw signal for the imaginary part of the dielectric constant is quite different for these 3 samples. The sample after 360s etch time is also represented.

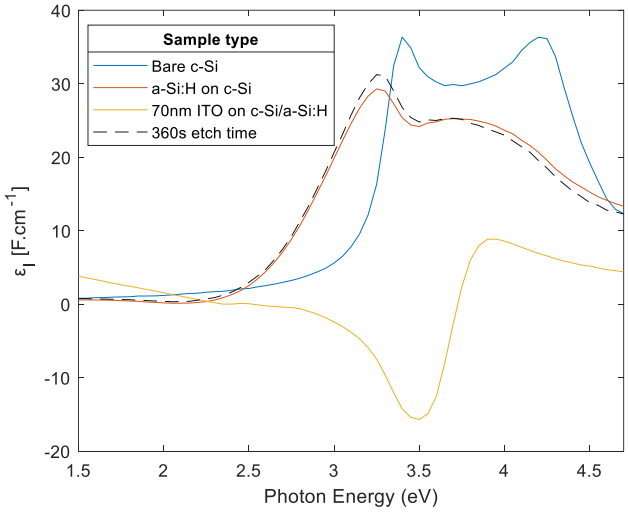

Figure 58 : Imaginary part of the dielectric constant measured with ellipsometry for different sample types

The initial signal, i.e. without any etching, is represented by the "70nm ITO on c-Si/a-Si:H" curve in Figure 58 (yellow continuous line). Up to 150 seconds of etching time (see Figure 57 (a)) the signal is qualitatively similar. However, after 180s (see Figure 57 (a) and (b)) a second peak appears, and at 240s (see Figure 57 (b)) the signal is not representative of an ITO layer anymore. Finally the signal after 360s (see Figure 58) corresponds to that of a-Si:H(i+n) layers deposited on c-Si (orange and black dashed lines in Figure 58 match closely): the ITO layer is completely removed.

For reference samples (70nm ITO on c-Si/a-Si:H), the thickness was measured at 4 different spots on a wafer, and at the center of 4 different samples. The uniformity was very good: thickness varied from 76.9 to 77.4 nm intra-wafer, and from 77.1 to 80.3 nm from wafer to wafer.

A fitting model was applied using these raw ellipsometry data. The model takes into account an infinite c-Si wafer, with a 10nm a-Si(i+n) layer on top with fixed parameters, and ITO layer over it, with a rugosity layer at the surface (50% ITO and 50% voids). The a-Si:H layer is parameterized with a Tauc-Lorentz function and the ITO layer is fitted using a parameterized equation combining a double Lorentzian oscillator with the Drude model [121].

Thicknesses determined with this model confirm that **the ITO layer is completely removed after 360s in HCl** with our recipe (see Figure 59). We find that two etch rates can be defined, until 210 seconds the etch rate is approximately -0.12nm/s, then it increases to about -0.39nm/s.

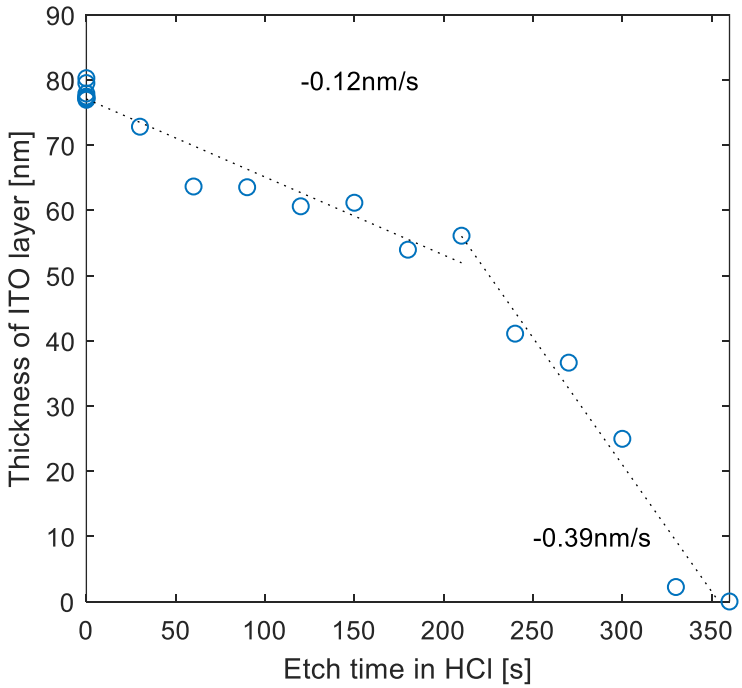

Figure 59 : ITO layer thickness as a function of etching time in HCl

4.2.1.3.2 Passivation quality before and after ITO etching with HCl

Now that we have determined that the ITO film is completely etched after 6 minutes in HCl, we want to verify that HCl does not degrade the a-Si:H layers once the ITO is removed. To check this assumption we fabricated test samples with:

- ITO/a-Si:H(n)/a-Si:H(i)/c-Si(n)/ a-Si:H(i)/a-Si:H(n)/ITO, labelled IN/IN samples
- ITO/a-Si:H(p)/a-Si:H(i)/c-Si(n)/ a-Si:H(i)/a-Si:H(p)/ITO, labelled IP/IP samples
- ITO/ a-Si:H(i)/c-Si(n)/ a-Si:H(i)/ITO, labelled I/I samples
- ITO/a-Si:H(n)/a-Si:H(i)/c-Si(n)/a-Si:H(i)/a-Si:H(p)/ITO labelled INIP samples

The effective lifetime was measured using transient PCD (see §3.2) for each sample before and after ITO etching in HCl, and for various durations above the one corresponding to the total removal of ITO layer, i.e. 6, 8, 10 and 15 minutes.

During the ITO etching, as it acts as an anti-reflective coating, the sample reflectivity may change, introducing a bias in a PCD measurement. However, in transient measurements, the result is not influenced to a significant extent by optics [140].

Figure 60 illustrates the evolution of the lifetime at $\Delta p = 10^{15} cm^{-3}$ for the different samples and for various HCl etching durations.

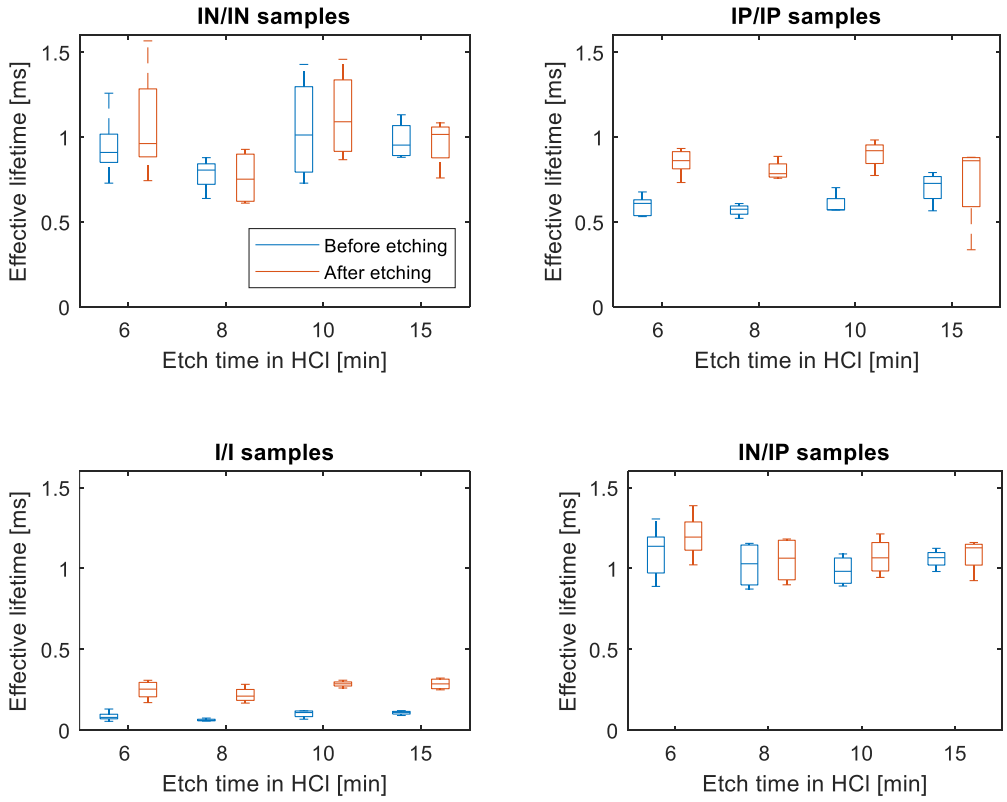

Figure 60 : Evolution of the effective lifetime (at $\Delta p = 10\text{^}15 cm^{-3}$) of the samples before and after the ITO etching with HCl. The blue boxplots show the effective lifetime of samples before the etching step, and the orange boxplot the lifetime of the same samples after the etching step. At least 4 samples were measured by condition

- For IN/IN samples, the difference in lifetime is almost null before and after the HCl etching. The duration of the HCl etching does not have an effect on the passivation, which stays quite constant even after 15 minutes. The dynamic of the curve also stays quite similar (see left side of Figure 61).
- For IP/IP samples, passivation improves when the ITO layer is removed. This is well known that the ITO increases recombination at the emitter side in SHJ cells [141] due to a Schottky diode behavior [142] that is detrimental to field effect passivation. This can be seen with the improvement at low injection in Figure 61 (right side). Note that one sample sees an important degradation after 15 min, we attribute this to a manipulation issue.
- The I/I samples confirm that the doped a-Si:H layers are not affected by the HCl, because when they are absent passivation is quite low (below 350 µs at $\Delta n = 1e15cm^{-3}$). It also shows that the passivation is improved when ITO is etched even for a-Si:H(i) layers, which seems to indicate that the band bending induced by the ITO layer creates a field effect which is detrimental to surface passivation.
- Finally the IN/IP samples show a slight improvement, mostly due to the p-side passivation removal as observed on the IP/IP samples, and indicated by the low injection behavior in Figure 61

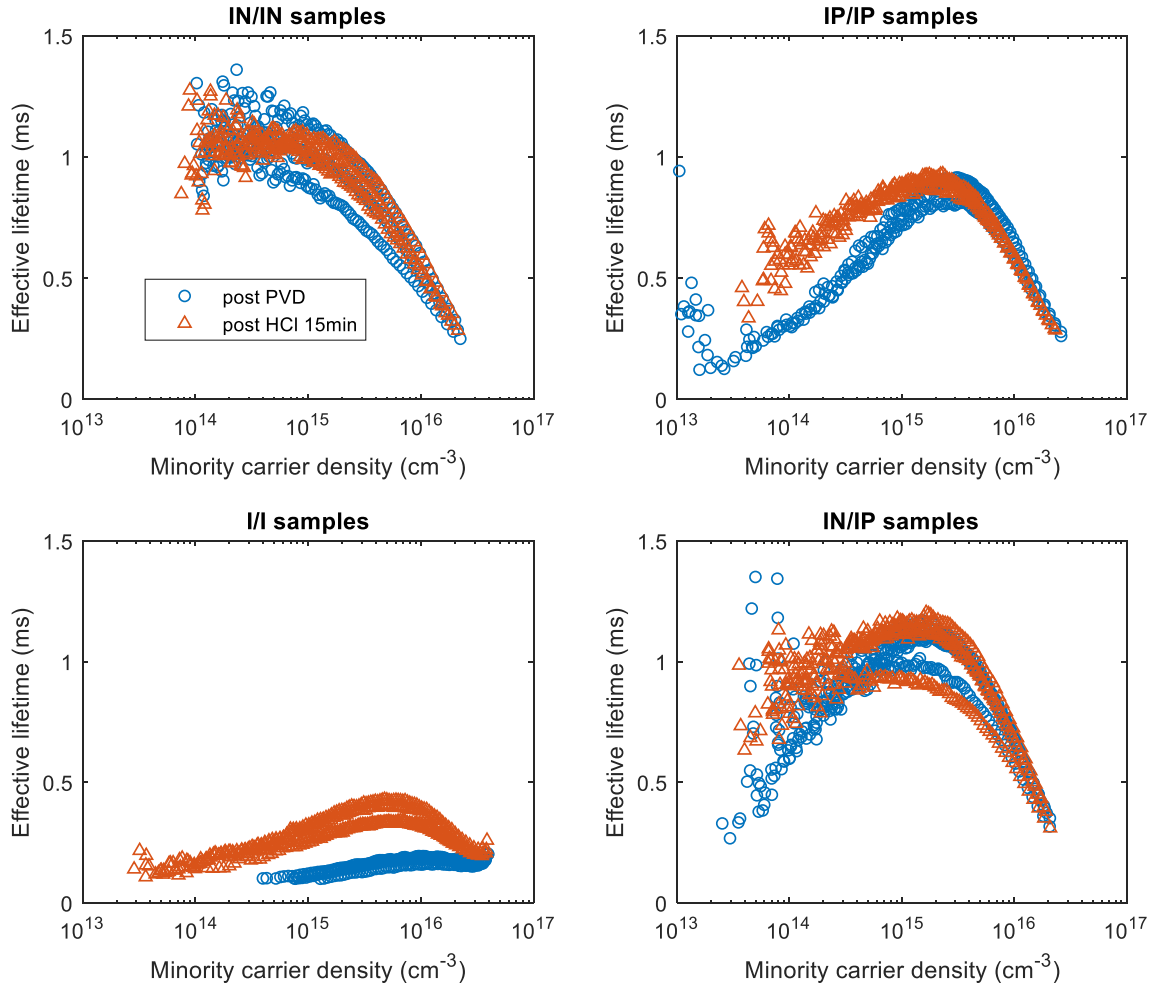

Figure 61: Effective lifetime evolution before and after ITO removal (15min HCl wet etching) for all samples. The data for the only degraded sample in the IPIP condition has been removed for clarity

We can conclude that a-Si:H layers are not affected by the HCl treatment in a way that would change significantly the effective lifetime for these samples: we thus validate this step for TLM samples fabrication.

Figure 62 illustrates samples before and after HCl etching.

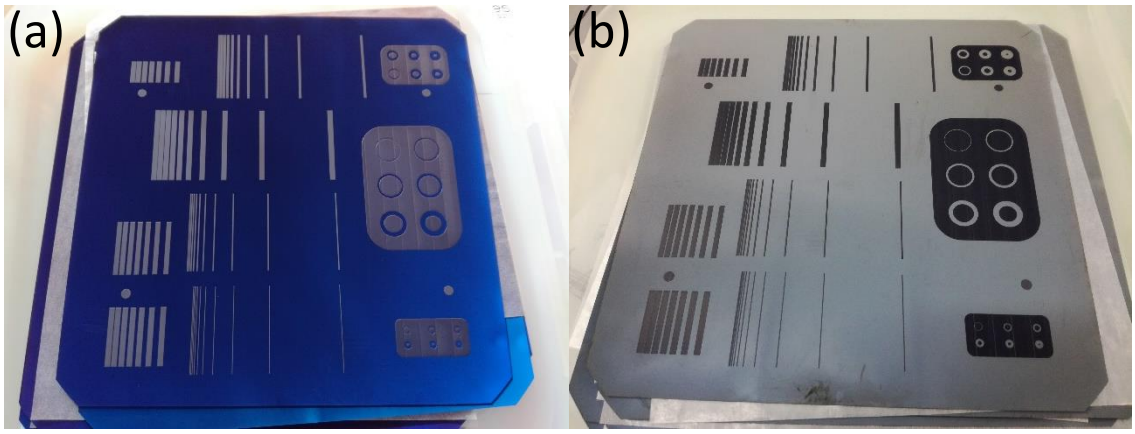

Figure 62: Pictures of samples (a) after hot-melt deposition and (b) after ITO etching for 6 minutes in HCl

4.2.1.4 Hot-melt removal

4.2.1.4.1 KOH removal of hot-melt

The samples used in the previous section were then used to examine the removal of the hot-melt in KOH.

A solution of KOH was prepared according to the supplier specifications for hot-melt removal, and several durations were tested. The hot-melt was found to be completely removed (by visual inspection, see Figure 63) after approximately 90 seconds. However, KOH has also been reported to etch a-Si:H layers [143], so a good etch selectivity of the a-Si:H layers and the hot-melt is not guaranteed.

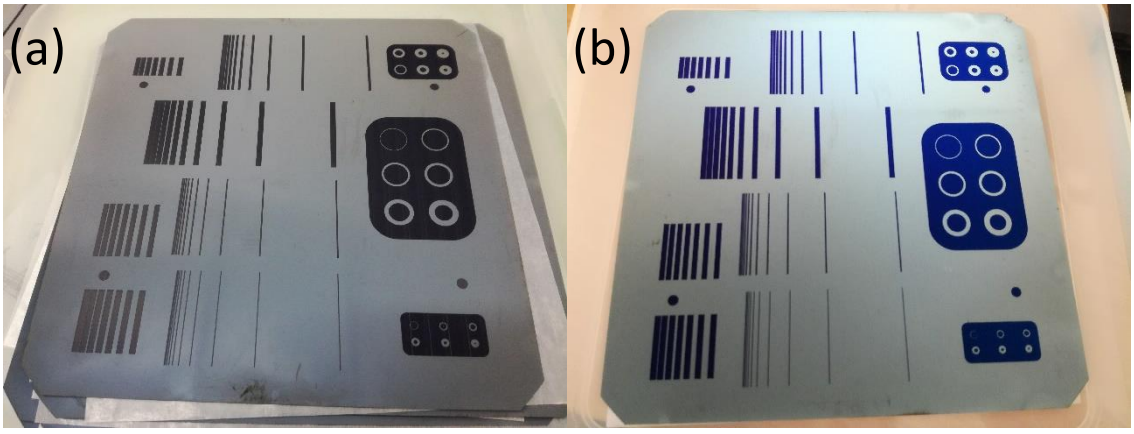

Figure 63: Pictures of a sample with hot-melt (a) (same as Figure 62(b)) after ITO etching and (b) after hot-melt removal

PCD measurements were carried out on each sample to follow the level of passivation (see Figure 64):

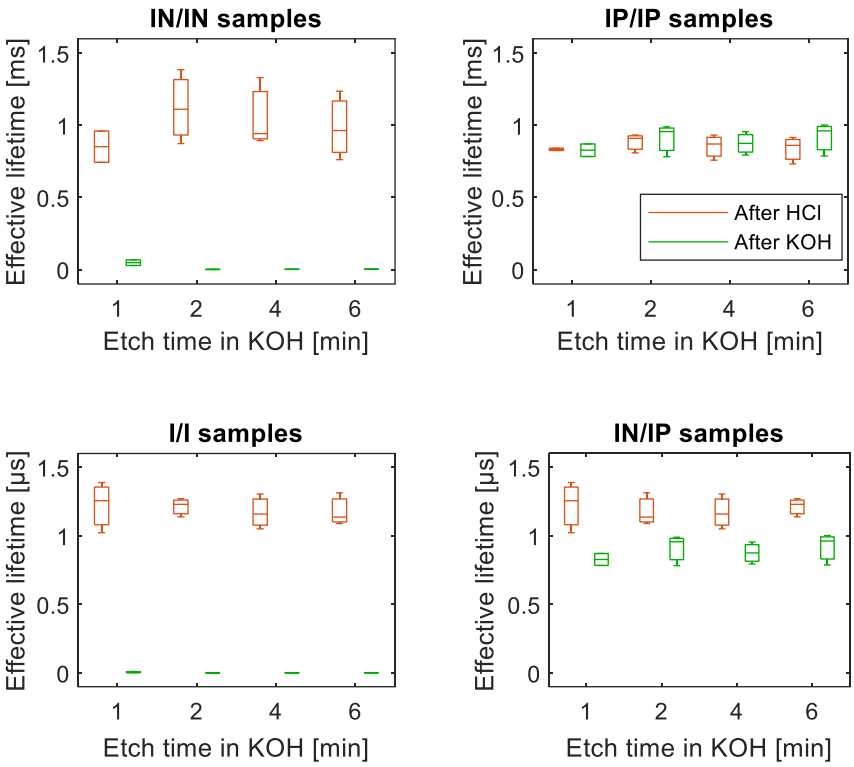

Figure 64: Evolution of the effective lifetime (at $\Delta p = 10\text{^}15cm^{-3}$) for the samples before and after the hot-melt removal with KOH. The orange boxplots show the effective lifetime of samples before the removal (post HCl step), and the green boxplot the lifetime of the same samples after the removal

The IN/IN samples show very low levels of passivation after just 1 minute, and passivation levels too low to be measured after 2 minutes. The same effect is observed with I/I samples. However the IP/IP samples experience no degradation even after 6 min. In fact, this can very well be seen with visual inspection (see Figure 65). This demonstrates that KOH wet etching can be very selective to the a-Si:H doping as opposed to what was claimed in [143]. Surprisingly the IN/IP samples seem to keep a decent effective lifetime.

Figure 65: Picture with two samples after KOH etching, with IN side (top-right half) appearing visibly degraded with white dots, and IP sample (bottom-left) appearing unaffected

KOH etches both hot-melt and a-Si:H(n) and a-Si:H(i) layers away, but could allow to selectively remove the hot-melt without degradation of an a-Si:H(p) layer. It is not adapted in our case as it deteriorates too much the passivation.

4.2.1.4.2 KOH free removal of hot-melt

To get samples with intact passivation, chemistries with better selectivity to the a-Si:H layers need to be implemented. A KOH free recipe was therefore tested, but was found to be mildly effective: the hot-melt is partially removed, but leftovers are still present even after very long exposure (>20min). However, it was found not to degrade significantly the passivation.

Combining this KOH free recipe and ultra-sounds was found to be very effective, with complete removal of the hot-melt in a little more than 1 minute. Note that some stains appear on the wafer, which are probably due to tiny amounts of ink redepositing on the wafer (Figure 66). Using proper rinsing techniques this could probably be avoided, but such wet processing equipment was not made available during this work.

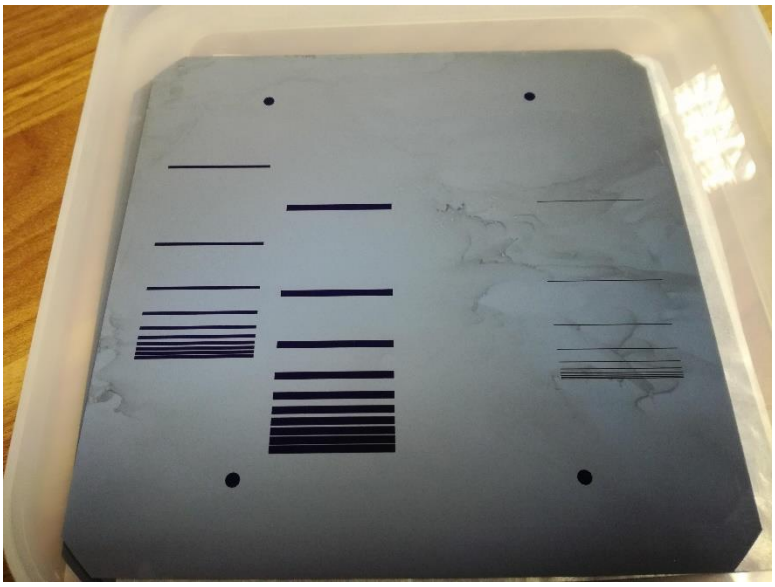

Figure 66: Picture of a sample with completely removed hot-melt after 1.5 minute in KOH free etchant with ultrasounds (35kHz)

Using some post PECVD IN/IP test samples, we monitored the effective lifetime prior and after different times in the KOH-free solution with ultrasounds, and found that the passivation was only slightly degraded (Figure 67).

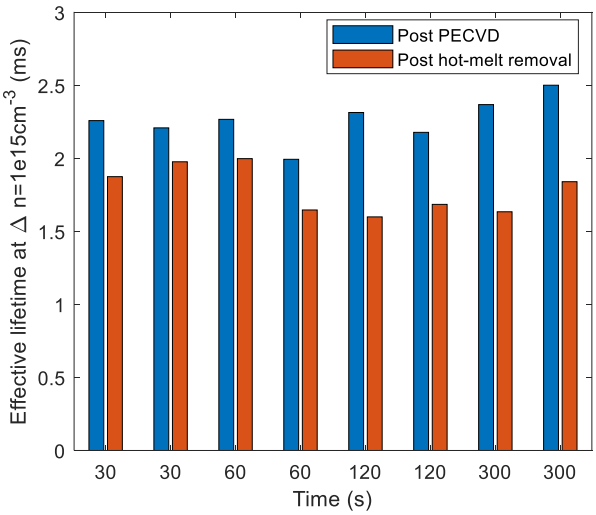

Figure 67: Effective lifetime before and after hot-melt removal with KOH free solution and ultrasounds for different times in the solution

We could identify that most of this degradation comes from the sample rubbing an asperity in the tank, causing a very distinctive mark at the center of PL images (Figure 68). This could easily be avoided with a slightly more adapted setup.

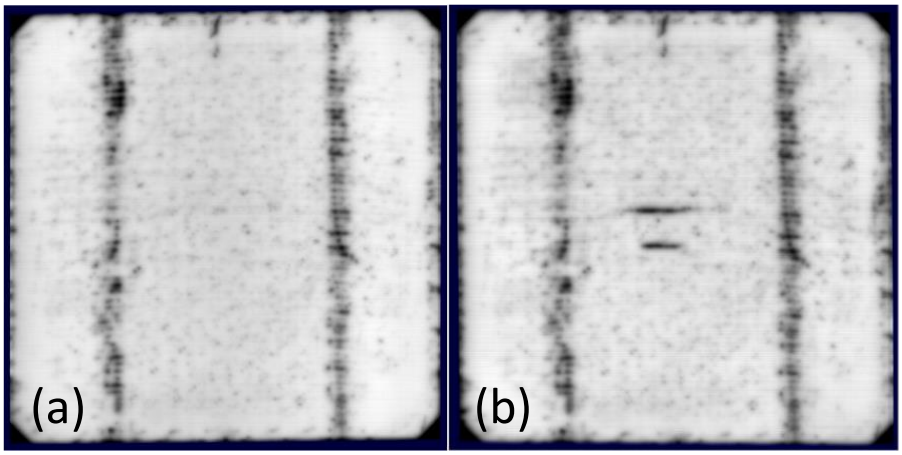

Figure 68: PL signal (a) before and (b) after KOH-free hot-melt removal

4.2.1.5 Metallization and cutting of the samples

The metallic TLM electrodes are screen-printed using standard metallization process of SHJ cells, with the addition of an alignment step, using a mesh corresponding to the inkjet-printed pattern used for above described ITO layer etching step. During the latter step, alignment marks are printed at precise points on the wafer: the screen-print tool is then able to align on them and to print precisely on top of the ITO patterns.

The alignment is precise to about 10 µm. The design of the ITO layer etching mask for the inkjet printing is then made slightly larger than the screen-print mask, so that the silver paste spreading does not lead to Ag/a-Si:H direct contact in the case of a slight misalignment.

Figure 69: Picture of TLM samples (a) after hot-melt removal (same as Figure 63(b)) and (b) after aligned screen-print. The dots are used as alignment marks

The samples are then cured with the standard process, and the last step consists of cutting the samples along the outer edge to avoid lateral shunt currents, such as discussed in §3.8.2.1.

4.2.2 Measurement of the electron and hole contact resistivities

We fabricated n and p stack TLM samples: IV measurements were then carried out from -0.1V to 0.1V for each spacing. The design was 1x20 mm electrodes with spacing of 0.2 to 25.6mm for both samples. Subsequently, we applied the TLM equations to infer R_{Sh} and ρ_C for each sample (Figure 70).

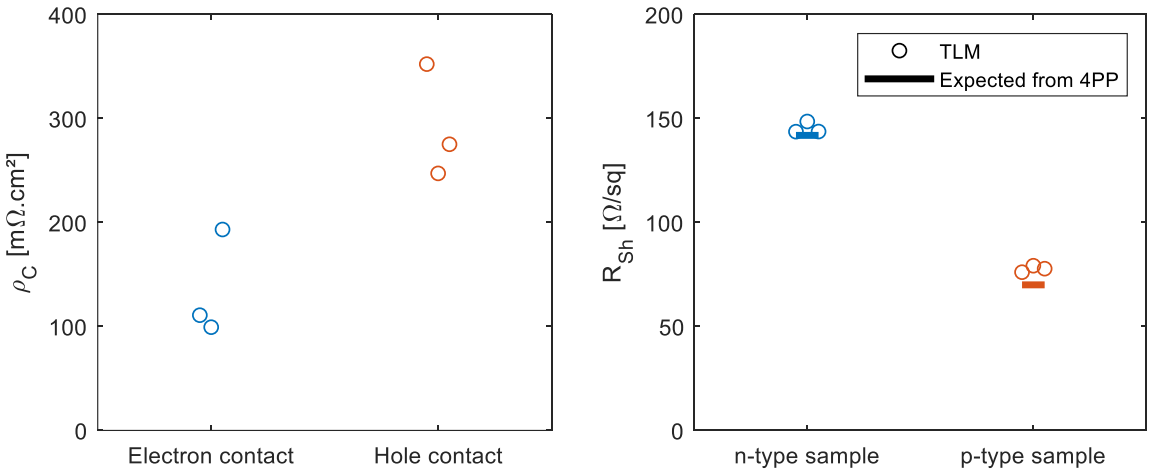

Figure 70: Measured values of (a) contact resistivity and (b) sheet resistance for n and p type samples. Values expected from 4PP measurement before processing are also displayed

The measured sheet resistance allows calculating the resistivity of each sample. We found $\rho_{n-type} = 2.25\ \Omega.cm$ and $\rho_{p-type} = 1.21\ \Omega.cm$, which are very close to the values of the average resistivity of each sample groups measured with 4PP before their processing i.e. $\rho_{n-type} = 2.27\ \Omega.cm$ and $\rho_{p-type} = 1.12\ \Omega.cm$, validating the quality of the measurements.

The average values of measured contact resistivity are also in good agreement with that reported by other authors, $\rho_C(e^-) = 133.8\ m\Omega.cm^2$ ($140\ m\Omega.cm^2$ in [58]) and $\rho_C(h^+) =$

$291.1\ m\Omega.cm^2$ ($240\ m\Omega.cm^2$ in [58]), with a hole contact more resistive than its electron counterpart.

Using Eidelloth model to correct for the thickness of the substrate (see [134] and §3.8.2.5) does not lead to significantly different results: solving iteratively equation Eq. 103 for ρ_C we found average values of $\rho_C(e^-) = 134.5\ m\Omega.cm^2$ and $\rho_C(h^+) = 291.6\ m\Omega.cm^2$.

4.2.3 Discussion of the approach

4.2.3.1 Patterning VS masking

An alternative approach for the fabrication of samples to measure ρ_{C,e^-} and ρ_{C,h^+} would be to use masking during the PVD step. This would be easier to implement as the patterning approach involves several masking and etching steps. We fabricated samples following the two approaches, and compared the edges of the samples. For the masking approach, we used a metallic mask patched on top of a post PECVD sample, and realized the PVD deposition step with the mask on. First, with visual inspection (Figure 71), we observe that the edges of the sample with the masking method have a blur brownish zone, likely due to a thickness gradient, which is not observed with the sample fabricated with the patterning method.

Figure 71: Pattern edges: sharp aspect using patterning technique (top) and blurred aspect using masking technique (bottom). Both lengths measure approximately 2cm

This suggests that some deposition takes place under the edge of the mask. This is confirmed using SEM imaging: the thickness of the ITO layer in a direction perpendicular to its edge was measured on both patterned and masked fabricated ITO samples. Very sharp delimitation between patterned and un-patterned zones of approximately 10µm was obtained on the patterned samples, while it extended over one millimeter for the masked samples (Figure 72). This ensures the aSi/ITO/Ag interface is homogeneous over the contact with the patterning approach.

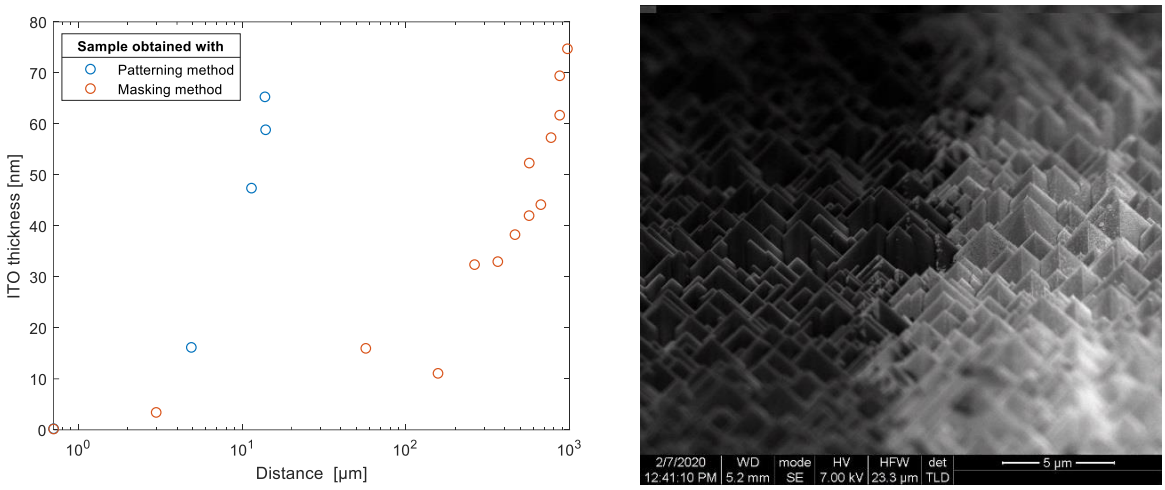

Figure 72: left - profiles of ITO thickness perpendicular to the pattern edge; right – SEM image at the proximity of the edge of the ITO pattern (with patterning method)

The patterning approach therefore allows better edge definition of the patterns than the masking approach.

4.2.3.2 Aligning screen-printing to the ITO patterns VS etching both Ag and ITO

Another point to discuss in our process is the alignment of the screen-print to the pattern. This step is not so easy, and could be avoided: for instance by depositing Ag on the full sample, depositing the hot-melt, and to etch both silver and ITO. This is the approach described by Lachenal et al. [58].

Etching silver is easily feasible, for instance using a solution containing a mix of ammonium hydroxide and hydrogen peroxide. We prepared a 400nm thick evaporated Ag layer deposited on a post PVD precursor, and found that it is removed in less than 1 minute in a solution of NH_4OH / H_2O_2 / H_2O in 1/1/10 proportions.

Nevertheless, this kind of sample could hardly be fabricated with screen-printing, otherwise it would imply a large waste of silver paste, which is quite expensive. Also, silver pastes contain large amounts of organic solvents and binders, remaining even after the curing step [89], which may also be degraded by the KOH free stripping of the hot-melt. Finally, screen-printed electrodes would be more than 10 microns thick, which is unlikely to be etched without severe under etch below the resist.

Alternatively, if Ag can resist to the HCl etching, it may be used directly as an etching mask layer without the use of an etch resist. In this case, the removal of the hot-melt would be non-necessary. However, both sputtered and screen-printed silver, were found to be at least partially removed in HCl; this led us to abandon this method.

Finally, any method using PVD deposited electrodes instead of screen-printed ones would lack representativeness to the finished device.

4.2.3.3 Range of voltage for I-V measurements

An ohmic contact is defined by its linear I-V characteristic. However, most contacts exhibit ohmic behavior over a limited range of voltage or current. We measured the IV curve for a

spacing $d \sim 3.2mm$ for both n and p-stack TLM samples on a broad range of voltages, from -2V to 2V.

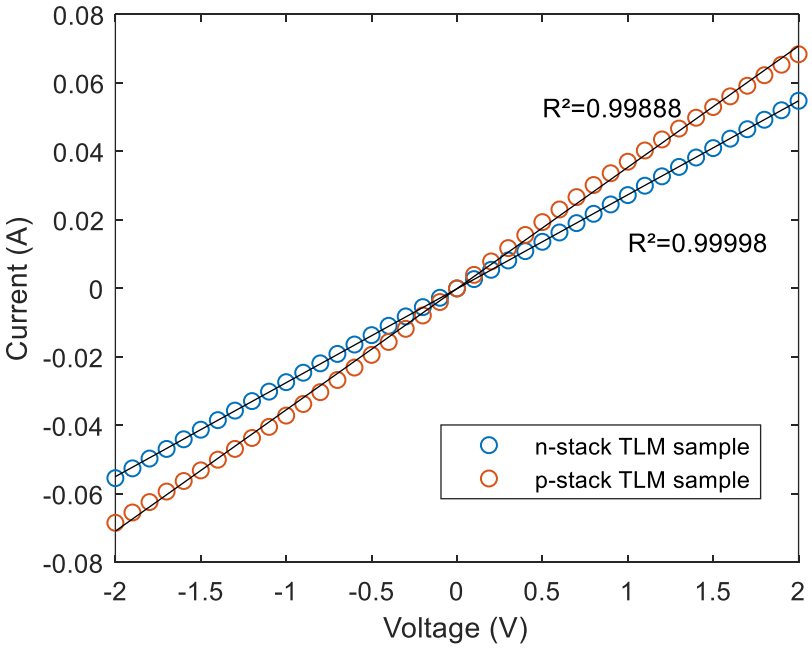

Figure 73: n and p-stack TLM samples measured from -2V to 2V (d=3.2mm)

We observe that the curve stays quite ohmic for the n-stack sample (R^2=0.99998), while the p-stack samples exhibits a slight rectifying behavior and is less accurately described by a line (R^2=0.99888).

When using the full range, we extract a lower resistance than when we restrict the range to [-0.1V 0.1V]. When contacts are not completely ohmic, it is arguable which value of the slope is most accurately describing the device: slope close to zero, slope over the whole range, tangent at a chosen operating point etc. We did not investigate this effect into more depth, we just ensured that the non-linearities stay small, then restricted the range of voltages to [-0.1V 0.1V] and extracted the slope.

4.2.3.4 On the use of p-type wafers for measurement of the hole contact resistance

The preferred approach in this work is proposed in §4.2.1, where we use p-type c-Si samples to study the hole contact. This is not completely representative of the cell which uses n-type c-Si absorber.

An argument for the validity of this approach relies on the existence of the inversion layer (see §2.5.3.2). At the proximity of the c-Si(n)/a-Si:H(i)/a-Si:H(p) interface, the c-Si wafer is in fact p-doped due to the inversion layer; thus using directly c-Si(p) wafers may not represent a strong bias. However, the doping of the p-type sample should be very high to mimic the inversion.

Later on in this work we will discuss that we need to preserve a good passivation on these samples to carry out certain characterization methods (§6.2.3). The bulk lifetime of monocrystalline p-doped c-Si wafers tends to be lower than that of n-doped, as most metallic impurities have bigger capture cross section for electrons than for holes [144]. Additionally, the

sensitivity of homojunction devices to as-cut bulk lifetime is lower than for SHJ cells. This is due to the high temperature steps and gettering effects that occur during homojunction devices fabrication, where bulk impurities are mostly neutralized. Also, due to the very good passivation of a-Si:H layers leading to lower surface recombination, the effective lifetime is comparatively much more bulk-limited with SHJ cells [145]. With the additional deterioration due to the fabrication process of the samples, the final lifetime of the p-type TLM samples to study the hole contact is usually very low, and therefore cannot sustain a large photo-generated current.

Nevertheless, some very good efficiencies were recently reached on p-type Cz samples on SHJ cells [146][147], using gettering or high quality Cz p-type materials could solve this problem.

4.2.3.5 An alternative approach for measuring the hole contact

Another approach to measure the hole contact is proposed, relying on the use of the inversion layer (see §2.5.3.2). If the resistance is too high to support current without substantial ohmic losses, it still can support a lateral transport in a TLM sample. Inversion layers have indeed already been used to perform TLM measurements, e.g. in the Transition Metal Oxides (TMO) community [126], but to our knowledge not for measuring the electron/hole contact of an SHJ cell. We propose a sample structure with etched ITO on top of an a-Si:H(i)/a-Si:H(p) stack at the front surface, with a rear side passivated with an a-Si:H(i)/a-Si:H(n) stack, such as depicted below in Figure 74:

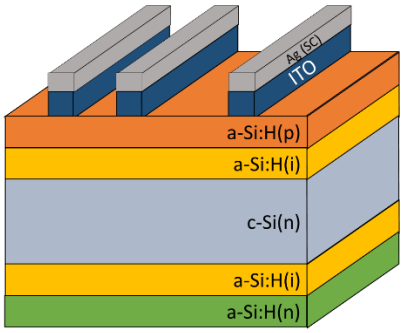

Figure 74: Drawing of a TLM structure for $\rho_C(h^+)$ assessment using the inversion channel

We fabricated such samples within the same batch than the ones presented in §4.2.2: only some of the n-type samples were patterned on the rear side. Performing IV measurements on them gave good ohmic behaviors for spacing distances below 2mm (Figure 75):

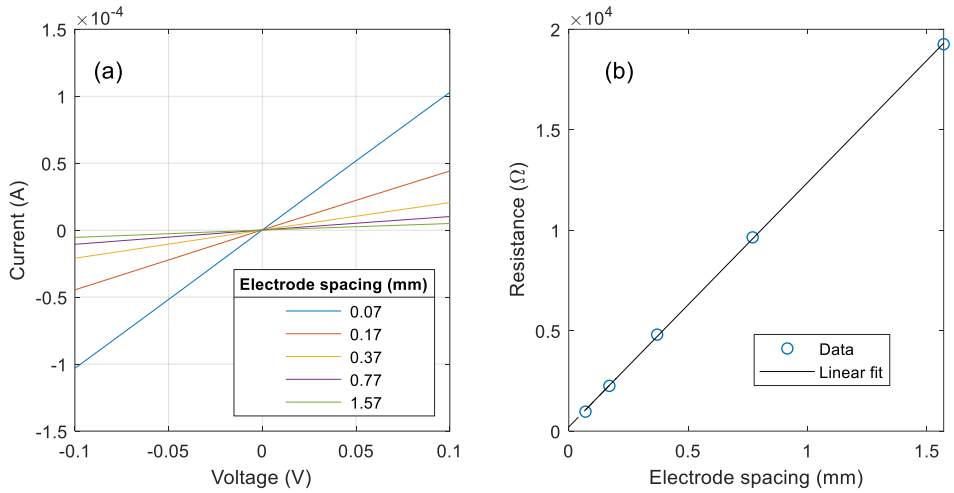

Figure 75: (a) IV curves for TLM patterns with inter-electrode spacing below 2mm and (b) deduced resistance versus spacing curve

The resulting TLM curve is a line of R^2>0.9998, showing very good measurement precision. Measurements above 2mm spacing however showed non-ohmic behavior (Figure 76), and were not included in calculations. A hypothesis for this could be leakage current through the junction: because the sheet resistance of the inversion layer is very high, when high spacing of electrodes are measured, current may see a better path through the junction to flow laterally in the c-Si.

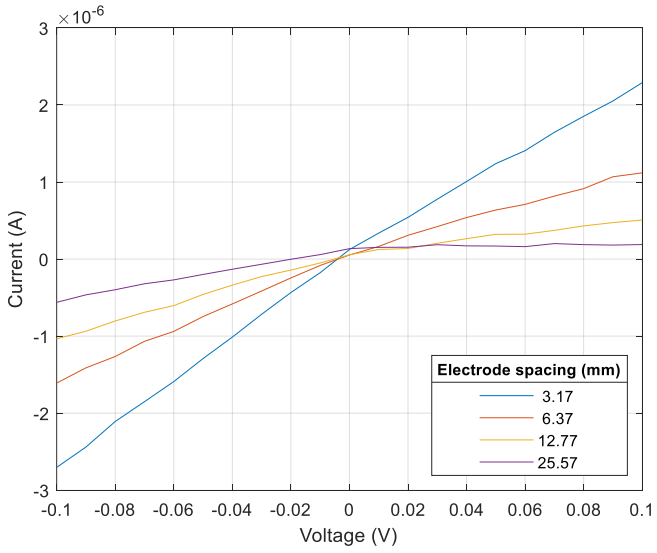

Figure 76: IV curves for inter-electrode spacing above 2mm

Using the low distance data, the method allows the extraction of $\rho_C(h^+) = 178\ m\Omega.cm^2$ and $R_{Sh}(inversion\ layer) = 243\ 000\ \Omega/sq$. We repeated this measurement over a range of 24 samples fabricated with different electrode length and width, removing all non-linear data at high electrode spacing. We measured an average $R_{Sh}(inversion\ layer) = 2.2 \pm 0.22\ 10^5\ \Omega/sq$, and an average $\rho_C(h^+) = 214 \pm 342\ m\Omega.cm^2$.

The value for the inversion layer is coherent with the values reported in the literature [111]. However, similarly than with the Ag/ITO contact, because the contact resistance signal is low compared to the layer resistance, the uncertainty of the measurement is very high. Here the uncertainty in the measurement of the electrode spacing is also very detrimental to the measurement as very small variations induce large changes in the determined ρ_C. Lower inter-electrode distances and better-defined electrodes would be required to improve the signal-to-noise ratio and yield meaningful results for this sample configuration.

In any case, this method allows a direct measurement of the sheet resistance of the inversion layer with satisfying precision.

4.3 Chapter outlook

On this chapter we have discussed the methodology used in the frame of this thesis to measure different quantities that are required for the diagnostic of resistive losses in SHJ cells: the sheet resistance of the ITO, the metal to ITO contact resistivity, and the contact resistivity of both electron and hole contacts of the SHJ cell.

We have discussed problems with contact measurements using the TLM technique in SHJ cells.

- TLM samples for accurate measurement of the sheet resistance of the ITO and the contact resistivity between silver and ITO should be prepared in order to be as most representative of the finished device as it can be. When studying the front side of the cell, electrical insulation of the ITO is necessary to ensure that no current crosses the electron contact to the c-Si bulk, which was shown to lead to erroneous results of both contact resistance and sheet resistance of the ITO. We show that depositing ITO on the emitter side (p-side ITO/Ag TLM samples) allows to efficiently confine current in the ITO, and to perform accurate TLM analysis. We report values of ITO sheet resistance of $210\ \Omega/sq$ and Ag/ITO contact of $0.11 \pm 0.03\ m\Omega.cm^2$.
- We discussed our methodology for the fabrication of samples to accurately extract the electron and hole contact resistivity, and the sheet resistance of the c-Si substrates used. We also showed that we can fabricate this kind of samples preserving the passivation. We report values of $\rho_C(e^-) = 133.8\ m\Omega.cm^2$ and $\rho_C(h^+) = 291.1\ m\Omega.cm^2$.

In the two following chapters, we are going to use these methodologies to study the contacts after various fabrication process variations, and under varying conditions of measurements, in order to study the device performance and contacts.

Chapter 5

Impact of varying the fabrication process on SHJ cells and on the electron contact

The goal of this chapter is to study the impact of some process steps on the efficiency of SHJ solar cells in terms of resistive power losses, by studying their series resistance, electron and hole contact resistance, Ag/ITO contact resistance and passivation properties.

For this purpose, several batches of samples were fabricated for which specific process steps and conditions were tuned: (i) substrate doping, (ii) alternative TCO and (iii) front side layers thicknesses. All characterization techniques are performed in their standard conditions: TLM measurements are carried out at 25°C in the dark, and J-V measurements under STC conditions. We measure contacts using the approaches developed in Chapter 4.

5.1 Influence of the c-Si substrate doping

In order to assess the effect of the c-Si wafer resistivity on the performance of SHJ cells, we chose as-cut wafers of different resistivity specifications. Using inline measurement of the thickness via laser interferometry, and 4PP measurements, we determined the resistivity for these as-cut wafers ranging from 0.49 to 14.12 $\Omega.cm$.

The corresponding doping densities were determined with state-of-the-art models using the PV-Lighthouse online calculator [148] and range from $1.06 * 10^{16}$ to $3.18 * 10^{14}$ cm^{-3}. These wafers were cleaned and textured, then standard PECVD and PVD layers were deposited. After PVD, most samples continued the standard fabrication process 5 busbars bifacial SHJ cells, but some samples were put aside. Some of them were put through the curing step with no metallization, in order to get cell precursors representative of the finished cells (including thermal budget), and some were put through the patterning and screen-printing processes in order to fabricate TLM samples to extract the electron contact properties.

5.1.1 Influence of c-Si doping on J-V parameters

The J-V parameters of the finished cells were measured in line using the Chroma tester, and are shown in Figure 77.

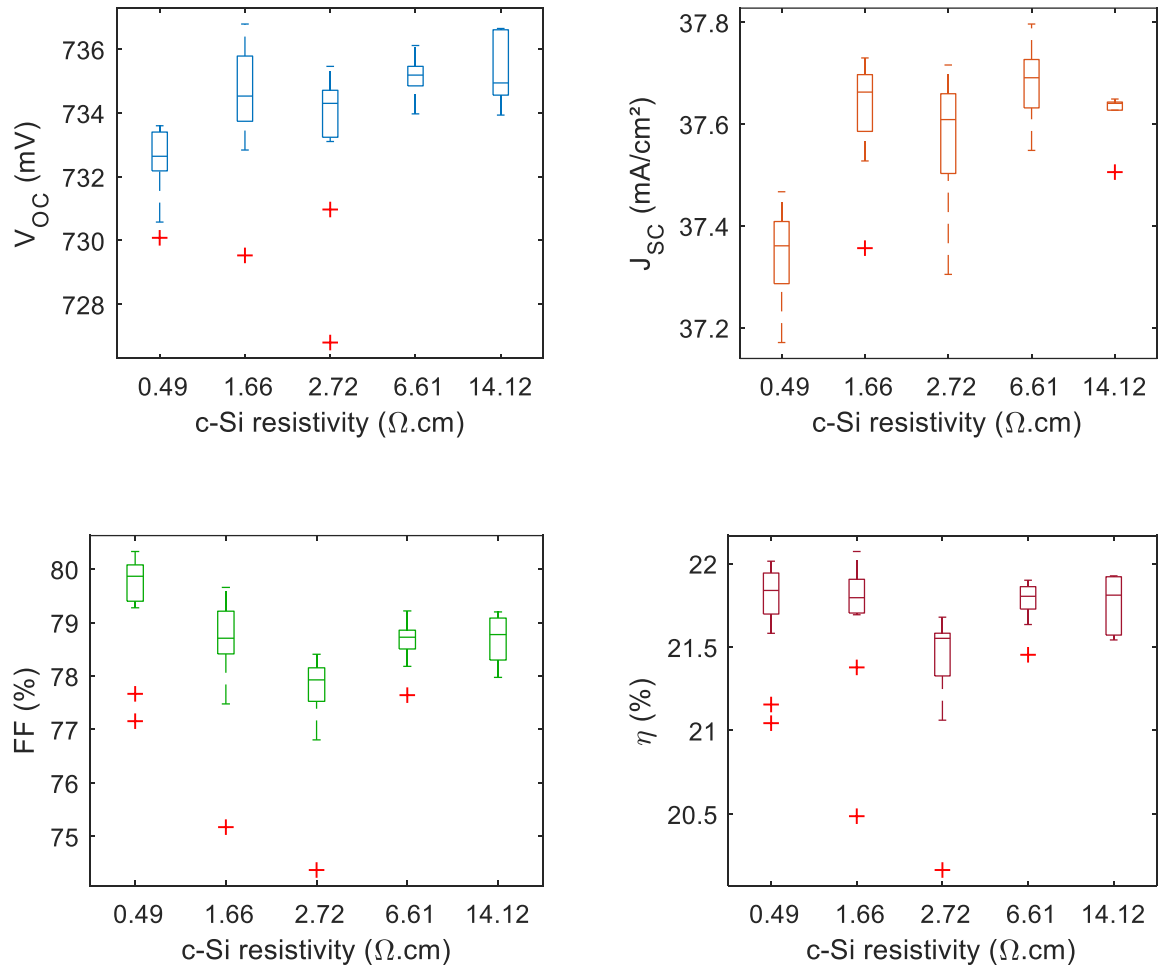

Figure 77: J-V cell parameters as a function of the resistivity of the c-Si wafer (red crosses are outliers)

We can see that the efficiencies obtained with the lower and higher classes of c-Si resistivity are very similar. Cells made using wafers with low dark resistivity suffer from V_{OC} and J_{SC} drops compensated by higher FF while the cells with high dark resistivity wafers show higher $V_{OC}$and J_{SC} but reduced FF. Overall, the worst batch is the one with medium range resistivity. We also examined the series resistance of each batch (Figure 78).

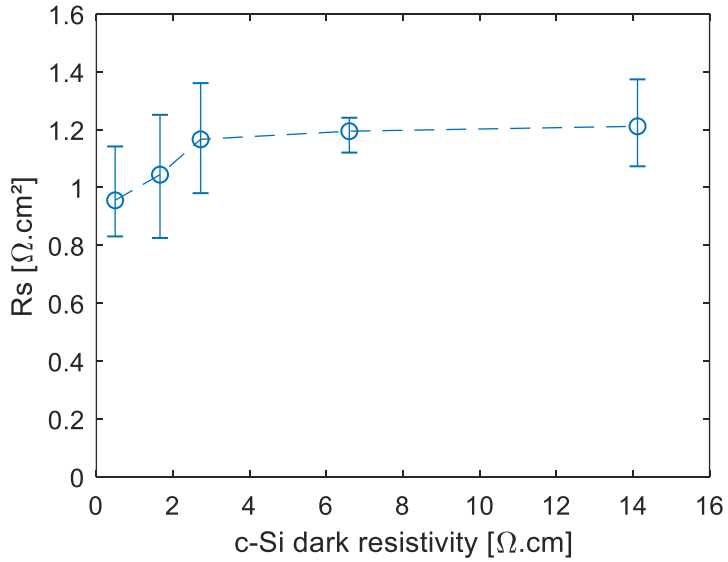

Figure 78: Measured series resistance as a function of the c-Si wafer resistivity. The blue dots represent the median values and error bars represent the first and third quartiles

We observe that R_S increases with wafer resistivity. It increases much more in the low range of wafer resistivity, then stabilizes after the 2.72 $\Omega.cm$ class reaching 1.21 $\Omega.cm^2$ for the $14.12\Omega.cm$ class.

5.1.2 Influence of c-Si doping on effective lifetime

Minority carrier effective lifetimes as a function of the injection level was determined from the PCD technique for samples cured without metallization (Figure 79).

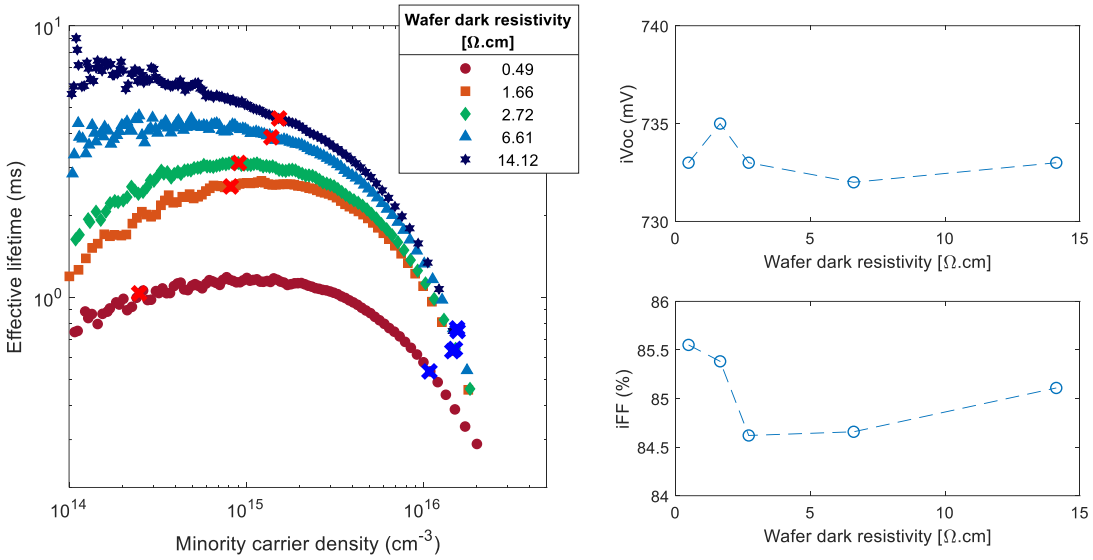

Figure 79: (left) Effective lifetime as a function of minority carrier density. Red crosses indicate the value closest to MPP and blue crosses closest to V_{OC}. (right) corresponding iV_{OC} and iFF

In Figure 79, we also pointed out the minority carrier density at maximum power point (MPP) and open-circuit voltage (OC) for the different cells. They were calculated from the doping level and voltages on the J-V curve at MPP and OC following Eq. 110:

$$\Delta p(V) \cong \frac{-N_D \pm \sqrt{N_D^2 + 4n_i^2 \exp\left(\frac{q}{nkT} * V\right)}}{2} \qquad \text{Eq. 110}$$

We find that the effective lifetime increases over the full injection range with increasing wafer dark resistivity. We also clearly observe a large change of behavior at low injection levels when modifying the wafer dark resistivity. This could be due to surface recombination having less impact on lowly doped wafers. The increased lifetime however does not correspond to better iV_{OC} and iFF: the determined iV_{OC} is quite constant and the iFF is actually better for the lowest resistivity class.

We can then estimate the resistivity of the wafers under working conditions (1Sun MPP, 25°C) using [6]:

$$\frac{1}{\rho_{1Sun,MPP}} = q\left((N_D + \Delta p) * \mu_n + \Delta p * \mu_p\right) \qquad \text{Eq. 111}$$

Figure 80 depicts the charge density in the bulk c-Si and its resistivity under functioning conditions.

[6] Again, we hypothesize that $\Delta n = \Delta p$

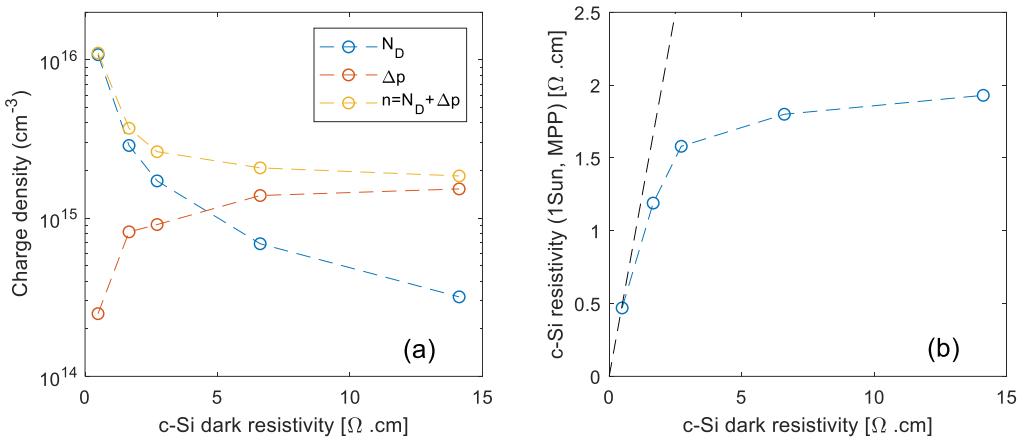

Figure 80: (a) Doping and minority carrier densities (at MPP under 1 Sun) as a function of wafer dark resistivity; (b) resistivity in working conditions as a function of c-Si dark resistivity (blue), black dotted line represents a slope of 1

In Figure 80 (a), we can see that Δp_{MPP} increases rapidly for low dark c-Si resistivity values, and saturates for high values where it lowly depends on N_D. Devices made using relatively low resistivity wafers (0.49 to 2.72 $\Omega.cm$) stay in the low-injection regime ($N_D >> \Delta p$), their resistivity at MPP being close to their dark resistivity (close to 1:1 curve in Figure 80 (b)). Oppositely, devices using lowly doped wafers reach high injection regime at MPP, their resistivity being largely reduced compared to dark conditions. In the low-resistivity range, Δp quickly increases when c-Si dark resistivity increases, then we observe a saturation and it does not vary much for higher resistivity values.

5.1.3 Influence of c-Si doping on the electron contact properties

We performed TLM measurements on dedicated samples of this batch to extract the electron contact characteristics. We cut samples of 2*15mm and 1*15mm, and used spacing dimensions from 0.3 to 2.1mm.

First, we compared the c-Si sheet resistance extracted with TLM with the expected value from the 4PP measurements and in-line thickness measurement on as-cut wafers (ρ/t), used as a reference in this study, then we show the corresponding extracted contact resistivity (Figure 81).

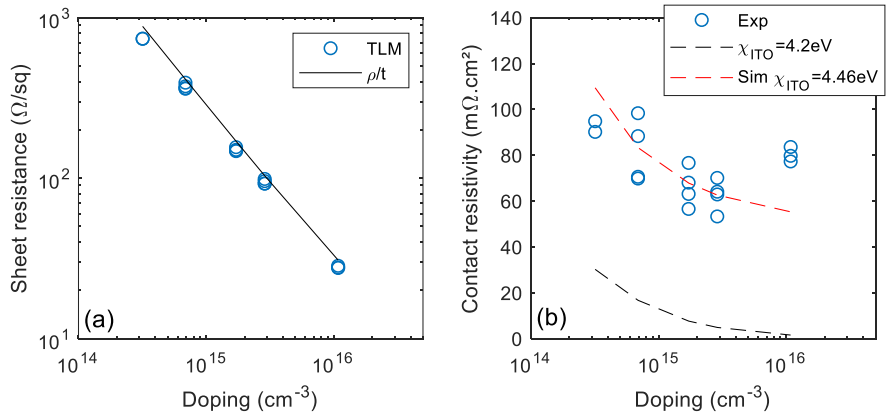

Figure 81: Extracted (a) c-Si sheet resistance and (b) electron contact resistivity as a function of wafer doping. The dashed lines are obtained from modelling as described in text

We observe that all over the doping range, we measure accurately the sheet resistance with the TLM technique; we however slightly underestimate its value (9 to 18 % as compared to our reference).

With this set of samples, all measured contact resistivities are in the range [50-100] $m\Omega.cm^2$, with a mean value of $74.6 m\Omega.cm^2$. $\rho_C(e^-)$ decreases when increasing N_D from $3.18 * 10^{14}$ to $2.88 * 10^{15}\ cm^{-3}$, but increases for $N_D = 1.08 * 10^{16} cm^{-3}$.

Changing the c-Si doping should only impact the c-Si/a-Si:H(i+n) interface. The expression for the electron current from the c-Si to the a-Si:H reads (see §2.5.2.1.1):

$$J_n(c\text{-}Si(n)/\text{a-Si: H(i)}) = (1+\delta)\, A_n^* T^2 \left(\frac{n^{a\text{-}Si:H}}{N_C^{a\text{-}Si:H}} - \frac{n^{c\text{-}Si}}{N_C^{c\text{-}Si}} \exp\left(-\frac{\Delta E_{C,c\text{-}Si/a\text{-}Si:H}}{k_B T} \right) \right) \qquad \text{Eq. 112}$$

In Eq. 112, the term $n^{c\text{-}Si}$ translates the electron density in the c-Si at the interface, which depends both on doping of the c-Si and on band bending, therefore increasing N_D should result in higher $n^{c\text{-}Si}$ at the interface. If $\frac{n^{c\text{-}Si}}{N_C^{c\text{-}Si}} \exp\left(-\frac{\Delta E_C}{k_B T}\right) > \frac{n^{a\text{-}Si:H}}{N_C^{a\text{-}Si:H}}$, then electrons flow from the c-Si to the a-Si:H layer. Considering a constant ΔE_C, then with increasing N_D the contact resistivity should decrease. We confirm this trend by simulations on Silvaco Atlas (Figure 81 (b)), even if simulated absolute values are lower using the standard parameters for the TCO description.

Yang's model can also be applied at the a-Si:H(n)/ITO interface using:

$$J_n(\text{a-Si: H(n)/ITO}) = (1+\delta)\, A_n^* T^2 \left(\frac{n^{a\text{-}Si:H}}{N_C^{a\text{-}Si:H}} - \frac{n^{ITO}}{N_C^{ITO}} \exp\left(-\frac{\Delta E_{C,a\text{-}Si:H/\text{ITO}}}{k_B T} \right) \right) \qquad \text{Eq. 113}$$

In the absence of Fermi level pinning, $\Delta E_{C,a\text{-}Si:H/\text{ITO}}$ can be expressed:

$$\Delta E_{C,a\text{-}Si:H/\text{ITO}} = \chi_{ITO} - \chi_{a\text{-}Si:H} \qquad \text{Eq. 114}$$

Where χ_{ITO} and $\chi_{a\text{-}Si:H}$ are the electron affinities of the two materials. We can fit more adequately the experimental data by adjusting the ITO/a-Si:H contact band offset, changing the ITO electron affinity χ_{ITO} from $4.2eV$ to $4.46eV$ (black and orange dashed line in Figure 81). However, the observed increase of $\rho_C(e^-)$ measured at high doping does not fit this trend, and would require more investigations. We will further explore this topic in §6.2.2.

5.1.4 Analysis of the R_S variation with c-Si doping

We saw (Figure 80 (b)) that under high injection, the c-Si resistivity at 1Sun MPP conditions stays quite low even for high dark resistivity c-Si wafers. Bivour et al. [108] showed that the front effective sheet resistance in rear emitter devices can be expressed as $R_{Sh,eff} = \left(\frac{1}{R_{Sh,ITO}} + \frac{1}{R_{Sh,c-Si}} \right)^{-1}$, c-Si playing a part in lateral conduction. In §4.1.2 we determined $R_{Sh}(ITO) = 210\ \Omega/sq$, using the values for the c-Si resistivity at maximum power point under 1Sun from Figure 80 (b) we can calculate that $R_{Sh,eff} = 26 - 75\ \Omega/\text{sq}$ depending on the wafer doping. Therefore, the sheet resistance of the c-Si under working conditions is much lower than that of the ITO, even for high dark resistivity samples. As the sheet resistance of the c-Si

at 1Sun MPP varies little between batches of 2.72 to 14.12 $\Omega.cm$ (see Figure 80) low variations of R_S are observed. Oppositely, for the low values of c-Si wafer resistivities, i.e. for the 0.49 to 2.72 $\Omega.cm$ batches, R_S varies more substantially due to the resistivity at MPP lowering as higher n is enabled with doping. Variations in $\rho_C(e^-)$ determined at obscurity seem to have little impact on the observed trend in R_S. But as $\rho_C(e^-)$ varies with doping, it may also vary with injected minority or majority carrier density, therefore the behavior of the contact under illumination will be investigated in the following (§6.2.3).

SHJ devices made from highly doped wafers operate at low injection, but already have high wafer conductivity, while devices made from lowly doped wafers operate at high injection, where the photo-conductivity of the c-Si is very important. Both cases allow for substantial lateral current in the c-Si explaining the relatively low observed variations in R_S.

We have discussed that the ITO plays a role both in the lateral transport and in the contact formation of the electron and hole contacts in the SHJ cell. In the following section, we study the influence of the ITO layer properties on series resistance.

5.2 Integrating alternative TCOs

Alternative TCOs have been studied in the literature for integration in SHJ solar cells, either seeking to outperform the ITO (e.g. hydrogenated indium oxide [90] or indium tungsten oxide [149] materials), or to reduce/avoid indium consumption (notably with aluminum doped zinc oxide materials [63]).

At CEA, several TCO materials, targets and recipes have been tested in the past years and it was possible to demonstrate a J_{SC} gain at the cell level in some conditions. However the optical gain was sometimes combined with FF losses, depending on the silver paste used for metallization. To confirm the potential influence of the TCO/metal interface on the FF losses, we propose to study one of these new TCOs integrated at the SHJ rear side with regard to two metallization pastes labelled “paste 1” and “paste 2” in the following.

For this purpose, we fabricated cells with two splits at the PVD step: the front surface was always using our standard ITO, and the rear surface was using either ITO or a new TCO. Then we metallized the cells using BB6 designs with the two different pastes. Note that the two pastes have different standard curing times. Additionally, we tried an alternative curing step, labelled “curing*” for the “paste 1”-”new TCO” combination. The J-V characteristics of the cells are measured using the Chroma IV tester (see §3.5).

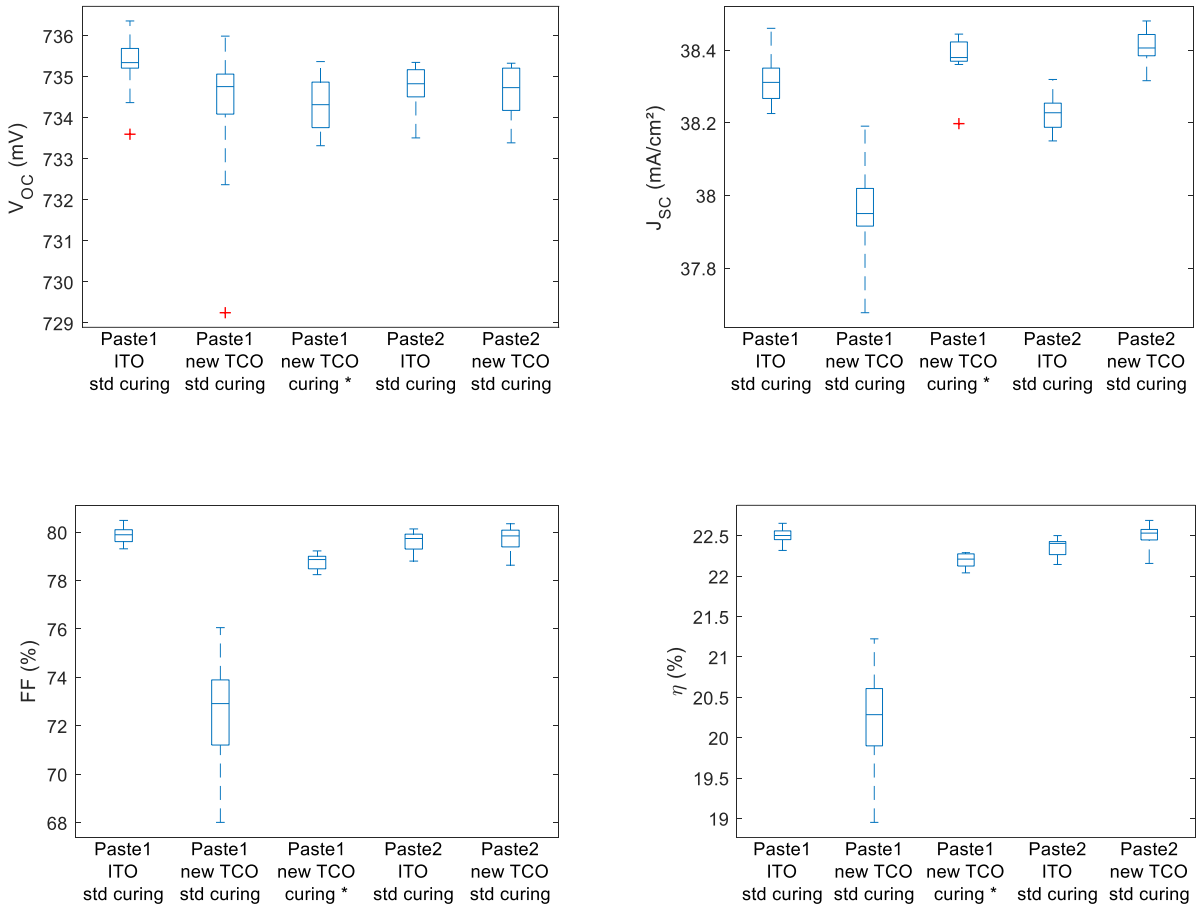

Figure 82: J-V parameters for the different combinations of metallization pastes and TCOs

We observe in Figure 82 that with paste 2, the new TCO is beneficial to cell efficiency compared to the ITO (~+0.13%), due to a better J_{SC} for nearly unchanged V_{OC} and FF. However, with paste 1, we observe that the new TCO makes the FF drop of about 7%abs., while V_{OC} and J_{SC} also decrease, leading to ~-2.2%abs. efficiency loss compared to ITO. In particular, we see no J_{SC} gain. With a different curing step, we can reduce this FF drop significantly, but the new TCO is still not beneficial to cell efficiency (~-0.29%abs), however we do see a J_{SC} gain. This highlights a possible root cause of contact resistance between the paste 1 and the new TCO, especially when using the standard curing process. Finally, we obtain very slight gain in efficiency (+0.03%abs.) with the new TCO combined with paste 2 than with the standard ITO combined to paste 1.

To investigate the compatibility problem of the TCO and pastes, we fabricated p-side TCO/Ag TLM samples to measure the contact resistance between the rear TCO and the metallization for each of these batches. Results are presented in Figure 83.

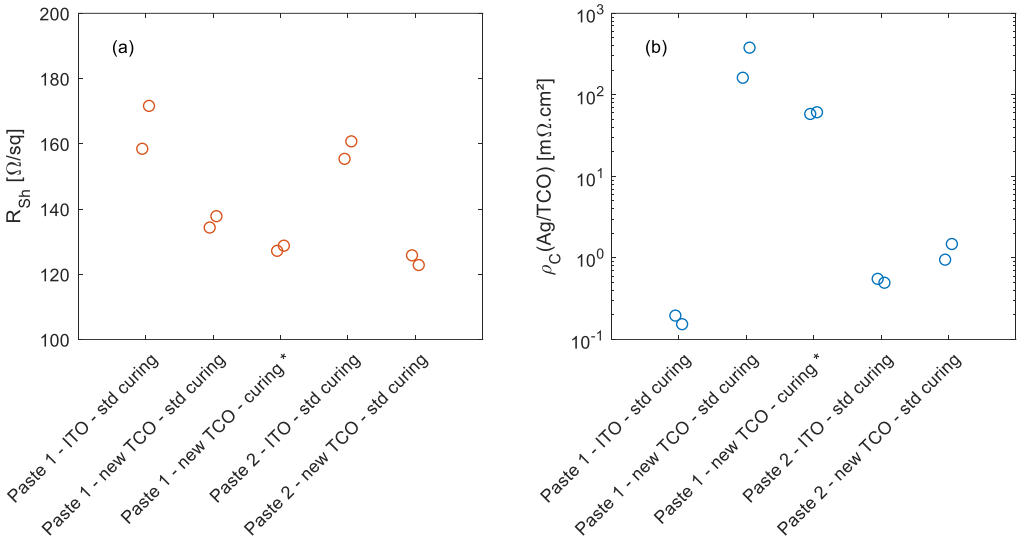

Figure 83: (a) Sheet resistance of the TCO and (b) contact resistivity of the Ag/TCO for each batch

We observe in Figure 83 (a) that the R_{Sh} values of the new TCO are lower than those obtained with ITO, for both pastes and curing conditions. This confirms that the FF loss observed with paste 1 combined to the new TCO does not stem from lateral transport losses.

The contact resistivity between the ITO and the metallization (Figure 83 (b)) is quite low with both pastes ($<1\ m\Omega.cm^2$) while for the new TCO, values for both pastes are increased: we find a relatively low increase with paste 2 ($<2\ m\Omega.cm^2$) but a very high value ($>100\ m\Omega.cm^2$) with paste 1. Modifying the curing step allows decreasing both R_{Sh} and ρ_C, but ρ_C is still very high ($\sim 60 m\Omega.cm^2$). Thus, we confirmed that the new TCO and paste 1 form a contact of high contact resistivity, which is the root cause for the degradation of cell performance. Such high contact resistivities may indicate macroscopic defects, such as problems of adhesion at the metal/TCO interface (e.g. cavities [89]).

Figure 84 illustrates the relation between the measured FF and ρ_C.

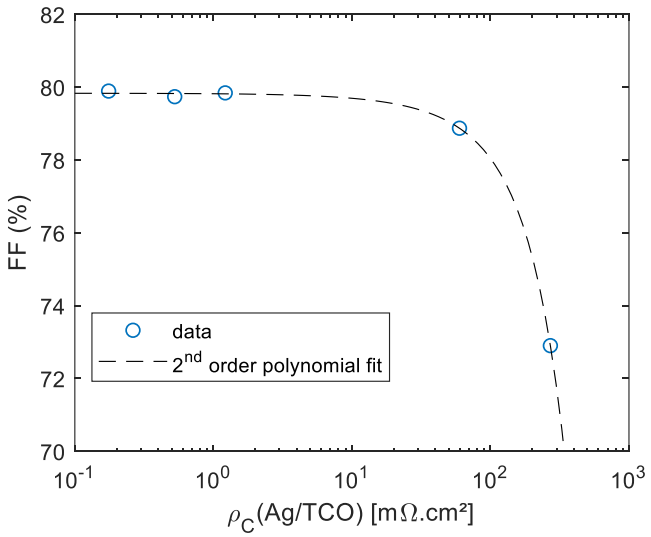

Figure 84: Variation of the FF as a function of $\rho_C(Ag/TCO)$

We observe that FF is very lowly affected when $\rho_C < 1 m\Omega.cm^2$, but starts to decrease very significantly when $\rho_C > 10 m\Omega.cm^2$. This example highlights the importance of measuring the Ag/TCO contact to detect paste/TCO compatibility problems. If generally considered negligible, $\rho_C(Ag/TCO)$ can in some instances lead to very important resistive losses. Further analysis would be required to troubleshoot why the paste 2 to the new TCO contact is so resistive.

5.3 Varying the thickness of the front stack layers

In this section, we propose to study the influence of the thickness of the different layers composing the electron contact on the cell efficiency, the contact properties and the passivation quality. We used c-Si wafers with a dark resistivity of $\rho_{av} = 1.23\ \Omega.cm$, with a final thickness after wet etching of approximately 160µm. For each set of parameters, we fabricated different kind of samples: 5-busbars (BB5) rear emitter cells, un-metallized cured passivation test samples and TLM samples for $\rho_C(Ag/ITO)$ and $\rho_C(e^-)$ determination.

We fabricated samples with different ITO layer thicknesses at the front side, between 0nm and 150nm, by changing the tray speed in the PVD chamber, keeping all the other parameters constant. We varied the thickness (t) of the front a-Si:H layers by changing the deposition duration, keeping all other deposition parameters constant (or by skipping the deposition step for $t = 0nm$). The rear stack is kept constant for all conditions.

We measured the thickness of the layers on single-side polished c-Si samples using ellipsometry. We fitted the curves with the ITO layer parameterized by a double Lorentzian oscillator combined with the Drude model, and a-Si:H layers by a Tauc-Lorentz oscillator. Note that for ITO, 100nm on glass substrates corresponds to approximately 70nm on a textured SHJ cell (see §4.1.1), while for a-Si:H layers the ratio is closer to what is reported in the literature, ((1.66 expected for flat surface to textured surface ratio [150]). Nevertheless, the thicknesses will be referred to as measured with ellipsometry on single-side polished.

5.3.1 ITO thickness

For cell optimization, the thickness of the ITO is not a variable that can easily be varied over wide ranges, especially at the front side, as $t{\sim}75nm$ corresponds to the minimal reflection losses [60]. However, varying the ITO thickness is a nice way to experiment on the role of ITO on passivation, lateral transport and contact formation.

Figure 85 illustrates the J-V parameters measured on each batch.

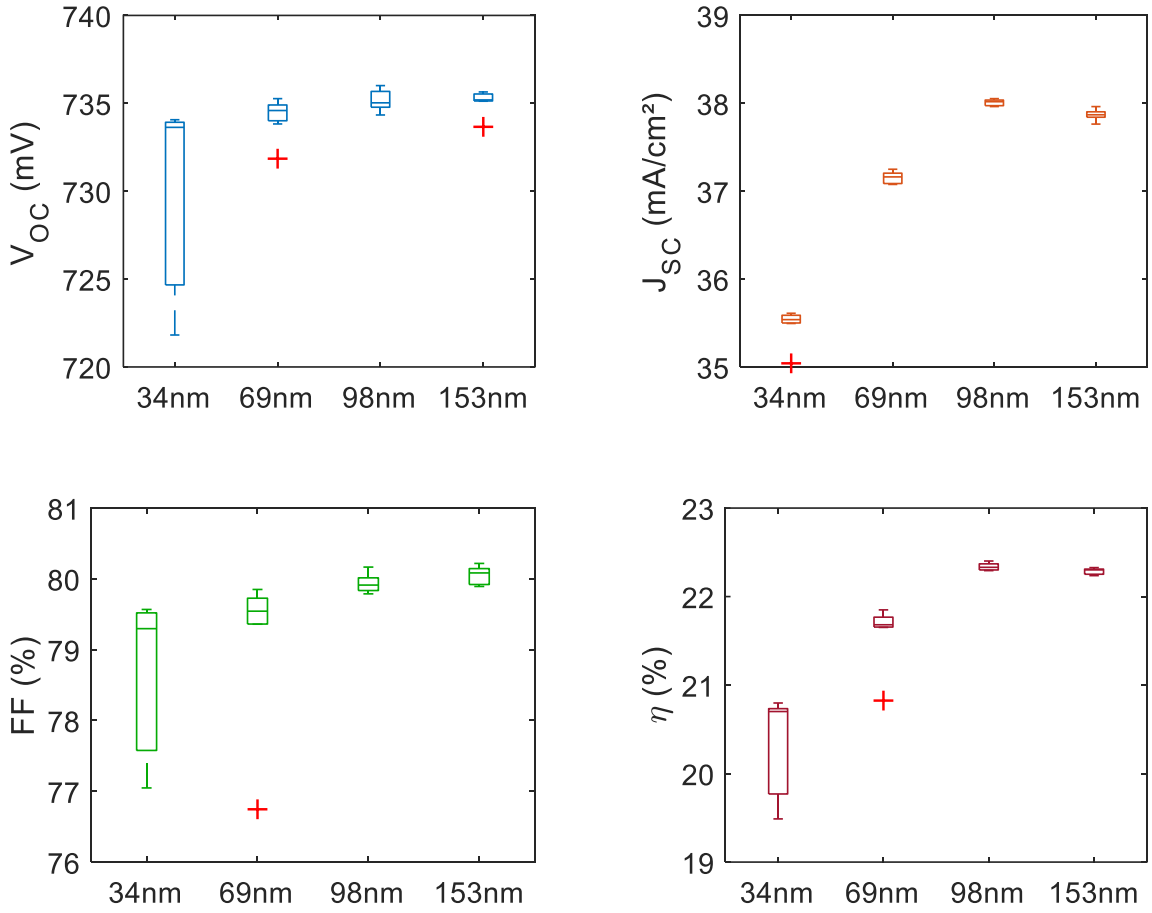

Figure 85: J-V parameters as a function of ITO thickness

As ITO thickness increases, the FF increases, and V_{OC} slightly increases for t in the range of 69 to 153nm. The J_{SC} is maximum for $t = 98nm$. When the ITO thickness is low, we also see that samples are more prone to show low flyer values in V_{OC} and FF, which we attribute to a lower physical protection of the a-Si:H layer by thin ITOs to prevent defectivity during cell fabrication (see §2.5.4). Finally, when $t_{ITO} = 0nm$, we could not obtain any correct J-V curve (efficiency largely below 1%), indicating either a very bad contact between the a-Si:H(n) and metallization paste, or that screen printing strongly harms the underlying a-Si:H layers. Results from the effective lifetime measurements for the different batches of this study are presented in Figure 86.

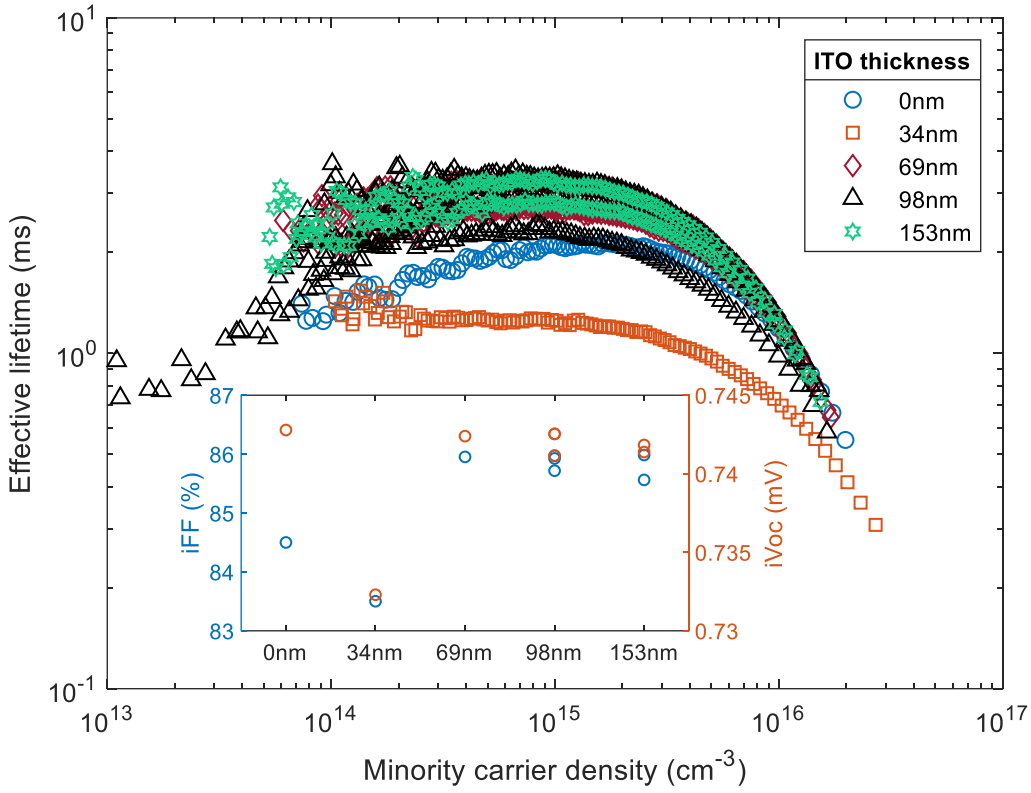

Figure 86: Effective lifetime as a function of minority carrier density for varying ITO thickness

We note that without ITO and after curing, the passivation is quite good, which confirms that the very poor efficiencies obtained without ITO do not come from passivation issues. When a thin ITO of 34nm is added, we see a degradation of the passivation in comparison to no ITO, but thicker ITOs all see an improvement. The degradation at $t = 34nm$ is likely due to defectivity generated for this condition.

In terms of series resistance (Figure 87), we observe that higher ITO thicknesses lead to lower R_S, except for the thickest ITO where this phenomenon seems to saturate.

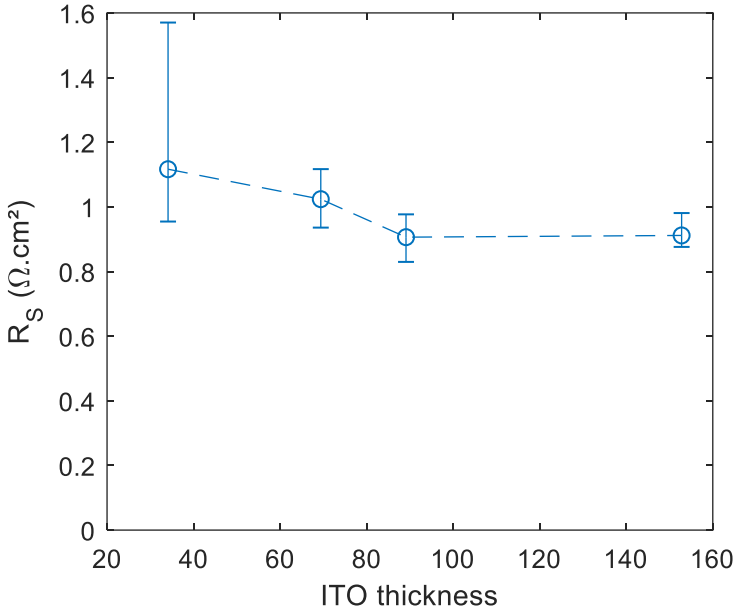

Figure 87: Series resistance as a function of ITO thickness. The blue dots represent the median values and error bars represent the first and third quartiles

We then performed TLM measurements on p-side TLM samples for the different ITO thicknesses:

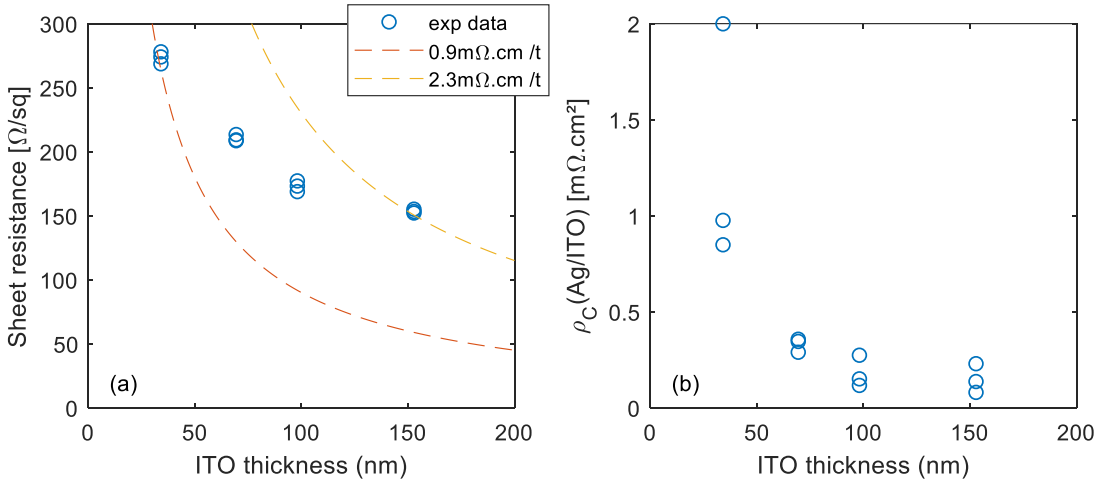

Figure 88: Sheet resistance (a) and contact resistivity (b) extracted with TLM as a function of the ITO thickness. Expected R_{Sh} for two constant values of ITO resistivity are also represented on (a)

We observe that with increasing thickness of the ITO, its sheet resistance decreases, but its resistivity also varies, increasing nearly linearly from 0.9 $m\Omega.cm$ to $2.3m\Omega.cm$ over the studied range. The Ag/ITO contact resistivity decreases from 34nm to 98 nm ITO thickness, then stabilizes. We also measured the electron contact for each thickness (Figure 89).

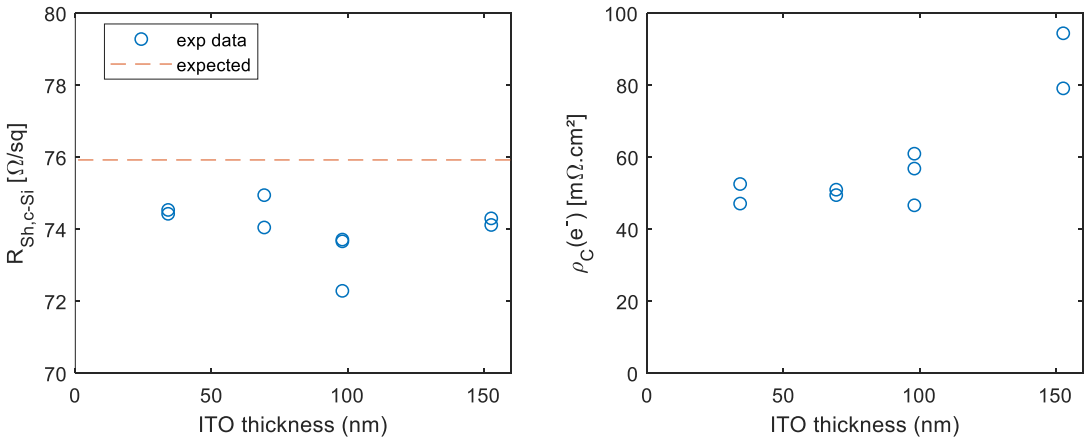

Figure 89: TLM extracted (left) sheet resistance of the c-Si and (right) electron contact resistivity as a function of ITO thickness. The dotted line represents the expected sheet resistance from the inline measurement of the resistivity and thickness of the wafers

We observe that the c-Si sheet resistance is measured correctly, which validates the contact measurement. We find that the electron contact resistivity stays quite constant ($\rho_C = 52 \pm 5 m\Omega.cm^2$) until $t_{ITO} = 98nm$, but increases for $t_{ITO} = 153nm$. We saw that the Ag/ITO contact resistivity is low for $t = 153nm$, and it is unlikely that the ITO thickness influences the electron contact due to bulk transport, as the ITO resistivity is quite low ($< 2.3 m\Omega\,.cm$). Therefore, this increase probably arises from the interface with the a-Si:H layers. This likely explains why the R_S does not further decrease when increasing the thickness to 153nm.

5.3.2 Varying the a-Si:H(i) layer thickness

The intrinsic a-Si:H layer is essential to obtain good passivation properties [60], but is known to increase the electron contact resistivity [135] and lead to parasitic absorption [60] even though some carriers photo-generated within can be collected [151], there should therefore be a tradeoff between R_S losses, passivation and optical losses. J-V results are presented in Figure 90.

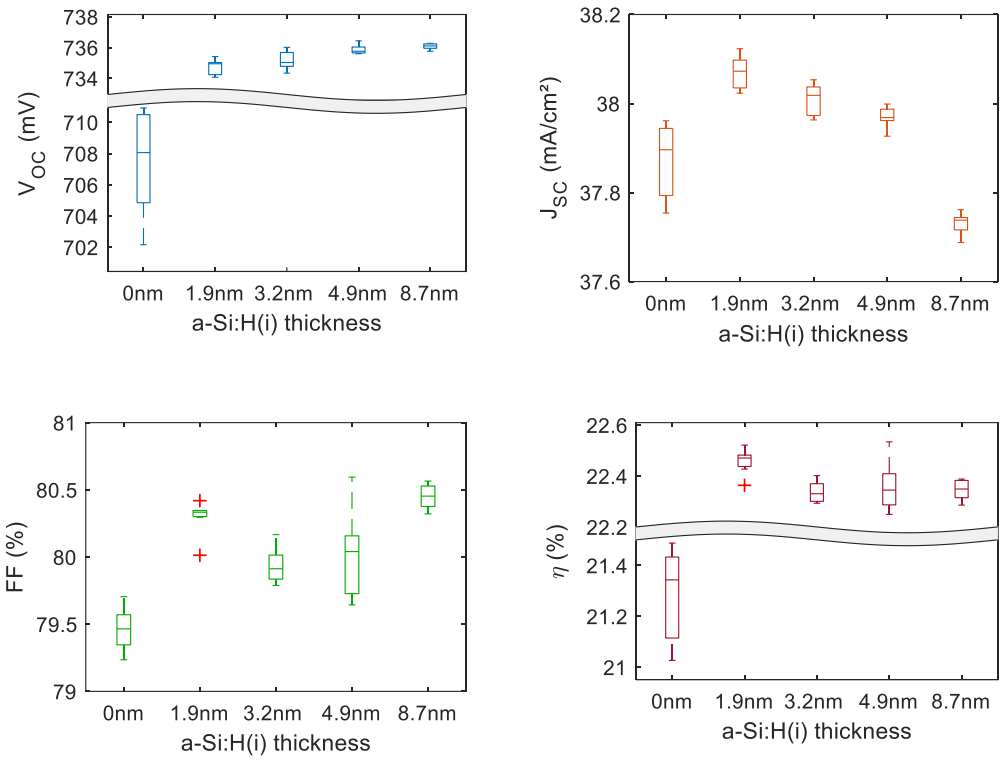

Figure 90: IV parameters for varying a-Si:H(i) layer thicknesses. Red crosses represent outlier values

We see that with no a-Si:H(i) layer, all J-V parameters drop substantially leading to approximately 1%abs. efficiency compared to the other conditions. Increasing a-Si:H(i) thickness leads to higher V_{OC} and lower J_{SC}. The trend for FF is more complex and should be analyzed with regard to the contact and passivation properties. The maximum efficiency is obtained with the thinner a-Si:H(i) layer. Figure 91 illustrates effective lifetime data for these samples.

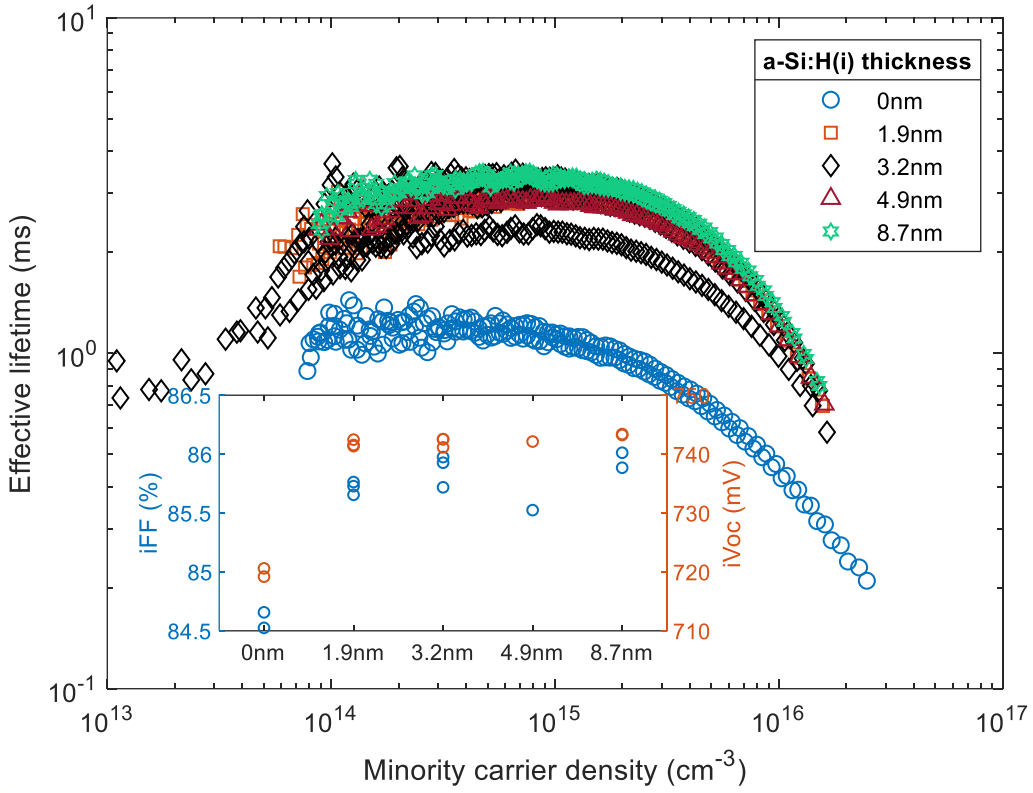

Figure 91: Effective lifetime as a function of minority carrier density for the different a-Si:H(i) thicknesses

We observe that when there is no a-Si:H(i) layer, passivation is way below all other conditions. With a thin layer, we already see a tremendous increase in effective lifetime, and only a slight increase of the passivation level when the a-Si:H thickness increases (mainly through iFF improvement). On Figure 92, we observe that the R_S stays quite constant whatever the a-Si:H(i) thickness.

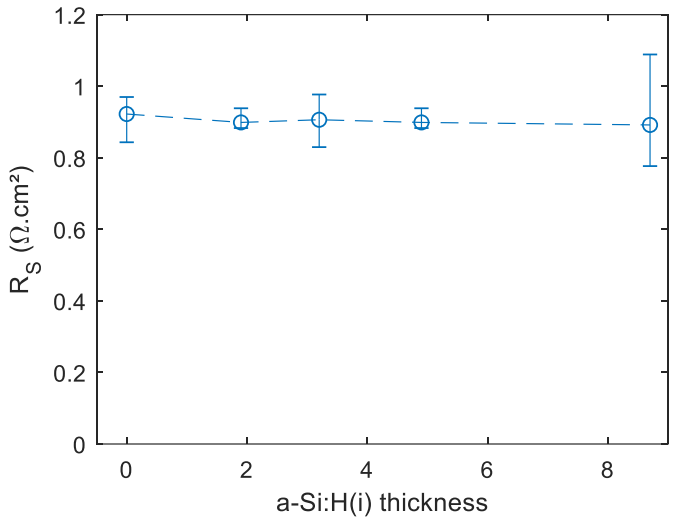

Figure 92: Series resistance as a function of a-Si:H(i) thickness. The blue dots represent the median values and error bars represent the first and third quartiles

We characterized the electron contact with TLM (Figure 93 below). The measured sheet resistances closely match the expected sheet resistance from the doping and thickness measured on wafers before processing, validating the measurement.

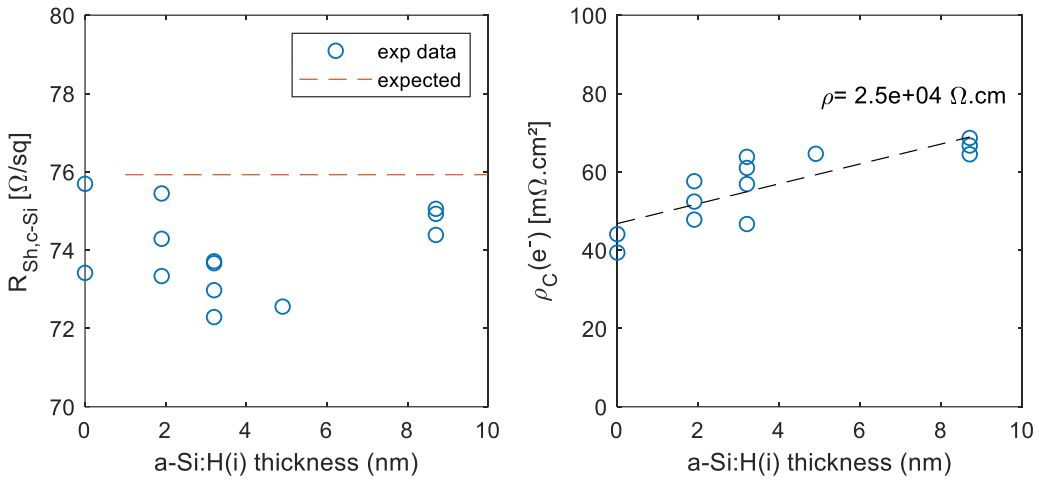

Figure 93: (left) sheet resistance and (right) electron contact resistivity as a function of a-Si:H(i) thickness

We observe an increase of $\rho_C(e^-)$ with increasing a-Si:H(i) thickness, that could be due to bulk a-Si:H(i) transport, to changes at the interfaces, to variations in the band bending or a combination of these effects. Here we make the assumption that it only stems from bulk a-Si:H(i) transport, and extract the resistivity of the layer from a linear regression of our data points. We extract $\rho = 2.5 * 10^4 \Omega.cm$ which may seem low for a single intrinsic layer. However, one has to consider that the a-Si:H(i) layer within the device will be submitted to the high electric field promoted by the doped a-Si:H(n) layer. Simple band diagram calculation gives similar conductivities for both a-Si:H(i) and (n) layers within the stack in the device. The extracted value from the fitting procedure is thus considered realistic.

In conclusion, we observe that a thin a-Si:H(i) layer is sufficient for passivation, while thicker layers increase $\rho_C(e^-)$ and parasitic absorption. The FF and R_S do not directly follow the trend of the electron contact, because the a-Si:H(i) thickness also influences significantly J_{SC} and V_{OC}, which in turns impact FF. Process variability and defectivity may also impede a clear trend in this case.

5.3.3 Varying the a-Si:H(n) layer thickness

The a-Si:H(n) layer is necessary for both field effect passivation and contact formation [101], while it will be the source of parasitic absorption with almost no chance for any contribution to carrier collection [151]. J-V results for each batch are presented in Figure 94.

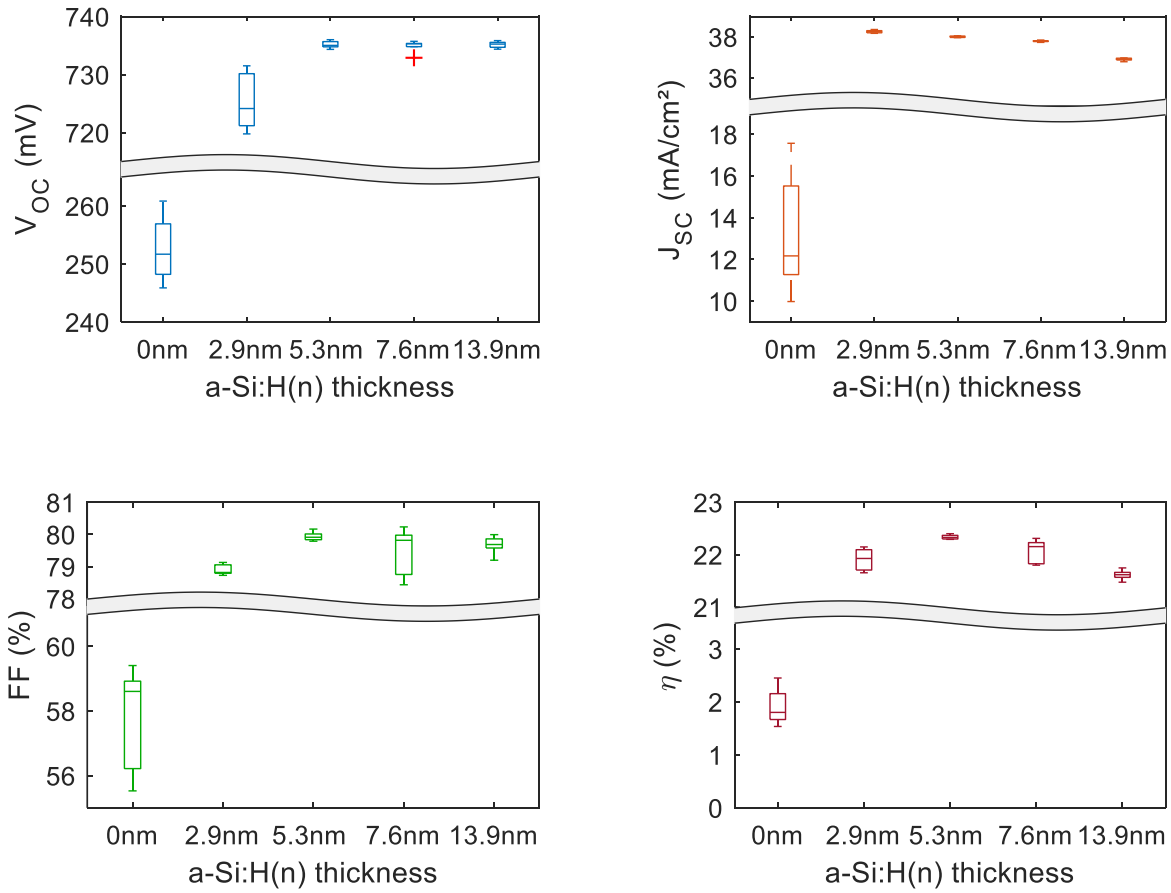

Figure 94: IV parameters for varying a-Si:H(n) layer thickness

We observe that with no a-Si:H(n) layer, we obtain very low cell performance, with all J-V parameters well below the other conditions. A minimum thickness is necessary to obtain a decent V_{OC}, but thicker layers do not improve V_{OC}, but make the J_{SC} drop.

We measured the effective lifetime on passivation test samples (Figure 95), and found that it is very low without (n) layer (<10µs, not shown in Figure 95). It increases for $t = 2.9nm$ but does not change significantly when its thickness is 5.3nm or more. iV_{OC} and iFF follow similar trends.

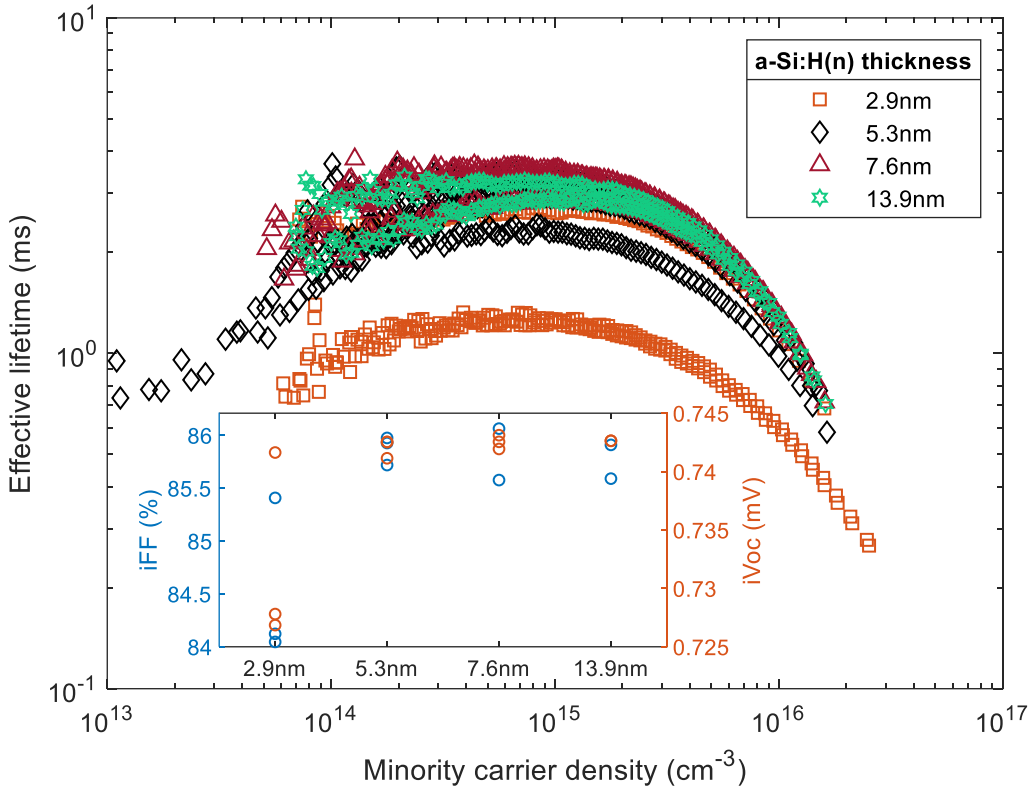

Figure 95: Effective lifetime as a function of minority carrier density for varying a-Si:H(n) thicknesses

We also measured the series resistance of these samples (Figure 96) and found that it slightly decreases when a-Si:H(n) layer thickness increases from 2.9 to 5.3nm. For thicker layers, it tends to saturate (or slightly increase).

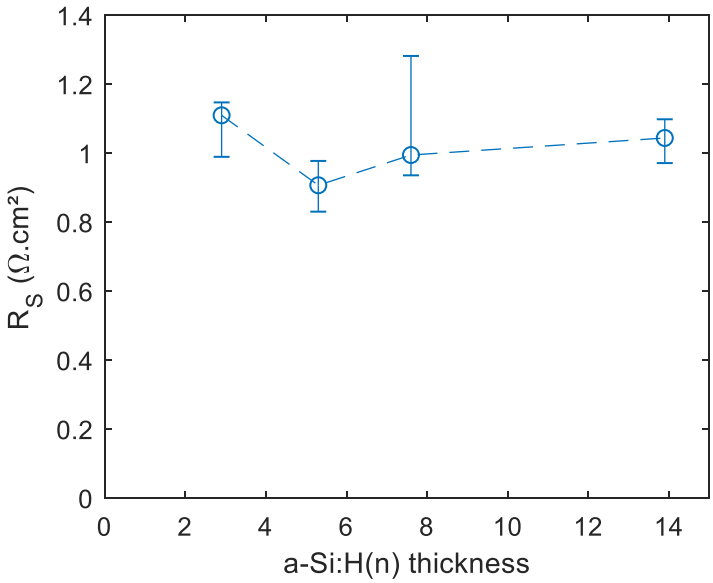

Figure 96: Series resistance as a function of a-Si:H(n) thickness. The blue dots represent the median values and error bars represent the first and third quartiles

Prior to measuring the electron contact resistivity as a function of a-Si:H(n) layer thickness, we verified that we extracted correctly the sheet resistance (Figure 97).

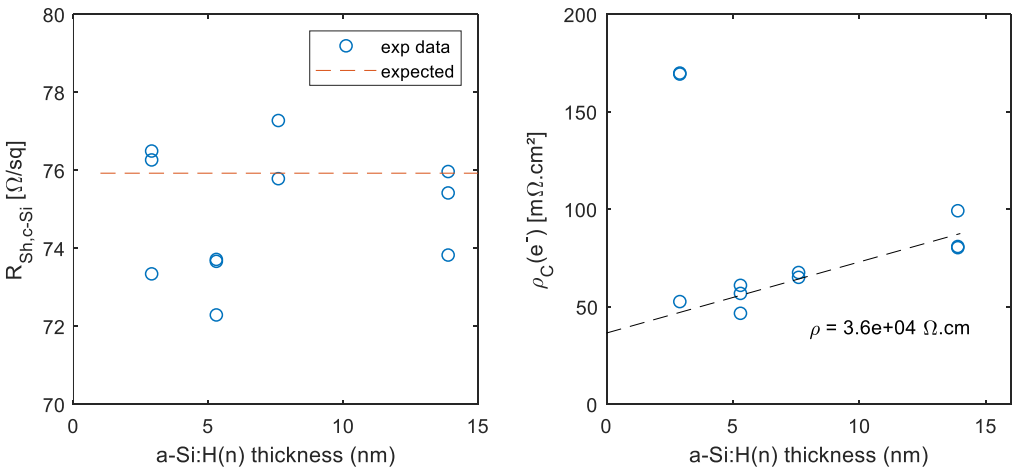

Figure 97: Electron contact resistivity as a function of a-Si:H(n) thickness

$\rho_C(e^-)$ increases linearly with a-Si:H(n) thickness from 5.3 to 13.9 nm. For the lowest thickness value (2.9nm), we note higher values for $\rho_C(e^-)$ determined for two over the three samples measured but it is difficult to conclude on a clear trend. For the case without a-Si:H(n), we obtained non-ohmic I-V characteristic, so the TLM analysis was not performed. It was shown in the literature that if using a too thin a-Si:H(n) layer, it becomes depleted and its conductivity decreases [101], leading to decreased performance and/or non-linear I-V curves in TLM measurements.

Similarly to the undoped layers, we make the assumption that the variation of $\rho_C(e^-)$ with thickness stems from bulk transport in the a-Si:H(n) layer over the range from 5.3 to 13.9 nm, which allows extracting a resistivity of $\rho = 3.6 * 10^4 \Omega.cm$.

5.3.4 Breakdown of the electron contact

We have shown that varying the thickness of the layers forming the electron contact stack, changes its resistivity. From these variations, we can break down $\rho_C(e^-)$ into the different contributions from interfaces and layer transport. The electron contact can be expressed as the sum of the different contributions from the layers and interfaces that compose it:

$$\rho_C(e^-) = \rho_C(Ag/ITO) +) + R_{ITO} + \rho_C\big(ITO/a\text{-}Si{:}\,H(n)\big) + R_{a\text{-}Si:H(i)} + R_{a\text{-}Si:H(n)} + \rho_C\big(a\text{-}Si{:}\,H(i)/c\text{-}Si(n)\big) \quad \text{Eq. 115}$$

Where R_{ITO}, $R_{a\text{-}Si:H(i)}$ and $R_{a\text{-}Si:H(n)}$ are the bulk contributions from ITO and the a-Si:H layers.

We have discussed that the ITO is too conductive to lead to significant resistive losses by bulk transport, and that the Ag/ITO contact resistivity is quite low in most cases, allowing to simplify Eq. 115 to:

$$\rho_C(e^-) = \rho_C(ITO/a\text{-}Si{:}\,H(n)) + R_{a\text{-}Si:H(i)} + R_{a\text{-}Si:H(n)} + \rho_C\big(a\text{-}Si{:}\,H(i)/c\text{-}Si(n)\big) \quad \text{Eq. 116}$$

We also addressed the influence of the a-Si:H layers thickness on the electron contact resistivity. We have proposed that bulk transport in the a-Si:H layers is responsible for most of this impact. Based on these results, we can break down $\rho_C(e^-)$ by extrapolating the contact resistivity such as they would be without bulk conduction in these layers, neglecting interface and band bending effects. We do this using the resistivity of the layers inside the stack

(calculated with Figure 93 and Figure 97). Then, we obtain for a typical front side stack for CEA SHJ cells:

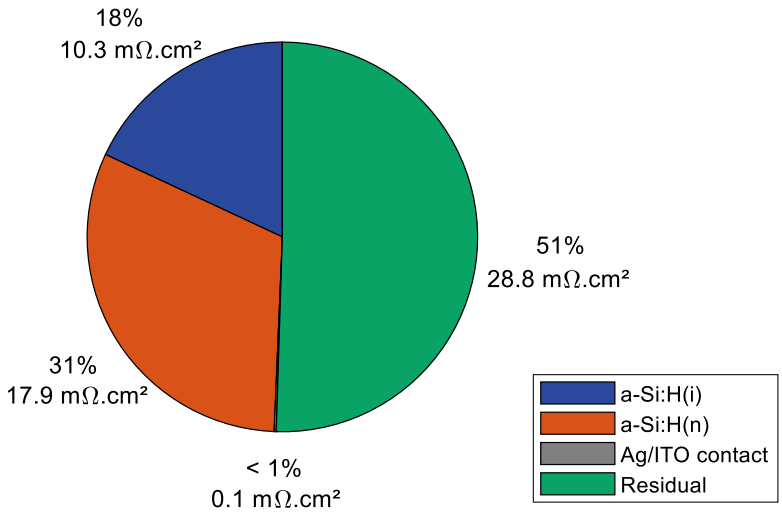

Figure 98: Electron contact resistivity breakdown

In Figure 98, we note that with this method, we can attribute about half of the electron contact resistivity to the a-Si:H layers due to their high resistivity. The residual include notably the a-Si:H(n)/ITO and c-Si(n)/a-Si:H(n) interfaces as well as band bending effect. Increasing the conductivity of the a-Si:H layers is therefore expected to lower the electron contact resistivity.

It is therefore critical to minimize the resistivity and thickness of the a-Si:H layers in order to optimize the electron contact without affecting the passivation properties.

5.4 Chapter outlook

In this chapter, we have discussed that several fabrication process steps influence the series resistance. Varying the bulk doping, we found that efficiency was not affected too much, and have shown that the series resistance is linked to the effective lifetime of the sample, especially for lowly doped samples that operate at high injection level. We also found a non-monotonous variation of the electron contact resistivity with c-Si doping, with minimal values obtained for medium doping range (average $\rho_C(e^-) = 63 m\Omega.cm^2$ obtained for the batch with $N_D \sim 3 * 10^{15} cm^{-3}$).

We have discussed that the integration of a new TCO needs to be studied with regard to the subsequent metallization process, and pointed out that paste/TCO contact measurements are an important tool for identifying compatibility issues. With the new TCO, we found that the contact with some silver pastes ("paste 1" the present example) yielded $\rho_C(Ag/TCO) > 100 m\Omega.cm^2$, leading to large efficiency losses mainly through FF, but that changing the paste, we could obtain very good performance.

By varying the thicknesses of the layers composing the electron contact, we have observed a combined influence on passivation and contact properties that we could link to series resistance. This once again illustrates the multi-functional role of the contact stacks.

Additionally, we have learned some valuable information on the transport phenomena inside the electron contact: we have shown that the substrate resistivity, as well as the thickness of the layers of the stacks, influence the electron contact resistivity. This suggests that the electron contact of CEA SHJ cells presented in this thesis is substantially influenced both by bulk transport inside each layer as well as thermionic emission at the c-Si(n)/a-Si:H(n) interface. In particular, bulk transport in both a-Si:H layers accounts for about half of the contact resistivity. For an a-Si:H(i) thickness of 1.9nm, we obtained an average efficiency of 22.46%, and values for the electron contact as low as $53 m\Omega . cm^2$.

There is a growing interest in the literature for the integration of alternative electron contact layers in SHJ cells, such as micro or nanocrystalline silicon, which generally feature larger conductivities than a-Si:H layers. This also changes the band offsets with ITO and c-Si as these materials also have different bandgaps and electron affinities. Nevertheless, nanocrystalline silicon has already proven that it makes a low resistance electron contact (e.g. [102], [152]).

Finally, the methodologies that we have implemented in this chapter and in Chapter 4 could be utilized to study additional fabrication processes to further investigate the electron contact, and to address the hole contact.

Chapter 6

Influence of measurement conditions on the determination of SHJ cell contact characteristics

In standard test conditions (STC), solar cells operate under 1Sun illumination. However, many characterization techniques are carried out in the dark, which may for some of them overlook some effects exhibited under illumination. In particular, TLM measurements for contact resistance determination are usually carried out in the dark. Additionally, measurements under varying temperature are a common approach to identify the transport mechanisms at play.

In this chapter, we investigate the influence of both illumination and temperature on the determination of SHJ cell contact characteristics using the TLM method. We first study the Ag/ITO contact, and then electron and hole contacts.

6.1 Effect of measurement conditions on the determination of the Ag/ITO contact resistance

6.1.1 Temperature

We realized some p-side ITO/Ag TLM structures such as described in § 4.1: ITO is deposited on a-Si:H(p) layer and the TLM samples edges are cut to avoid lateral transport in c-Si. We used our reference recipe for every deposition process. Inter electrode distances were kept small ($\leq 2mm$) to guarantee proper contact signal, and data points not complying to the rule $\frac{2R_C}{R_{tot}} > 1\%$ were removed (see § 3.8.1.4).

Our TLM samples were measured under varying temperature, from approximately 20°C to 75°C. At each temperature point, heating was stopped, temperature stabilized, then IV measurements in between every inter-electrode spacing carried out.

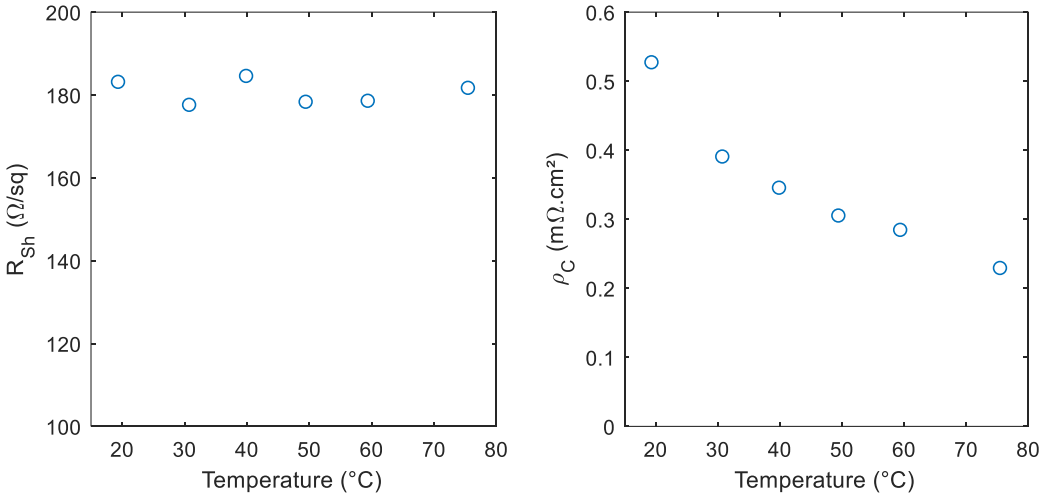

Figure 99: Sheet resistance of the ITO and contact resistivity of the Ag/ITO contact as a function of temperature

We observe in Figure 99 that the sheet resistance of the ITO is quite constant over this range of temperature, which gives additional proof that no current flows laterally in the bulk c-Si, as the latter has a temperature-dependent conductivity. However, ρ_C is temperature-dependent, indicating some non-negligible temperature-activated transport mechanisms exist.

In the literature, it has been proposed based on the high doping level of the ITO that the main transport mechanism is tunneling [89], [90]. We apply the metal/semi-conductor theory (see §2.5.1.1) to this contact considering $WF_{AG} = 4.3\ eV$ [86] corresponding to pure silver, and the ITO parameters of our front ITO such as in §3.7.1, and with an ITO tunnel effective mass of $0.3 * m_e$-[153]. Over the full studied temperature range, we get a characteristic energy E_{00} such that $\frac{k_B T}{E_{00}} > 0.1eV$ indicating that theoretically, we should be in a regime of pure tunneling. Applying Eq. 68, we get $\rho_C = 5.6 * 10^{-7} \Omega.cm^2$ at ambient temperature (similar to [154]) and predict a negligible temperature dependence.

The classical metal/semiconductor theory is therefore not sufficient to explain the measured contact resistivity and its temperature variation. Reasons for this could be that the theory is not adapted for contacts to highly degenerated materials, or the lack of accounting for interfacial

defects or Fermi level pinning. The parameters used in the computation are also not well known, and notably the work function both ITO and silver screen print paste (which is not pure silver) were not characterized and may differ significantly [155], [156]. Other hypotheses such as not completely conformal metal deposition [89], or contact interfacial oxides forming during annealing of the pastes leading to parasitic resistance [90] have been proposed before. We did not push this characterization further as we identified a weak impact of the Ag/ITO contact on the efficiency.

6.1.2 Illumination

Using the same samples than in the previous section, we performed TLM measurements under varying light intensity. Here we make the assumption that because there is no bias applied between the bulk c-Si and the contacts (i.e. open circuit conditions), there is no current flow from the former to the latter. Therefore, the current photogenerated in the bulk should not be collected. Additionally, varying the illumination is not supposed to yield a significant effect on metals or degenerated semi-conductors, so no influence of illumination is expected with these samples.

However, plotting $R_{tot} = f(d)$ yields non-linear TLM curves when illuminated (see Figure 100 (a)). The more the illumination intensity increases, the more pronounced the non-linear effect is. The points measured with big spacing distances are the most affected. The individual IV curves (Figure 100 (b)) change under illumination as compared to dark conditions: their slope changes, but also their y-intercept, indicating that some photo-generated carriers are collected.

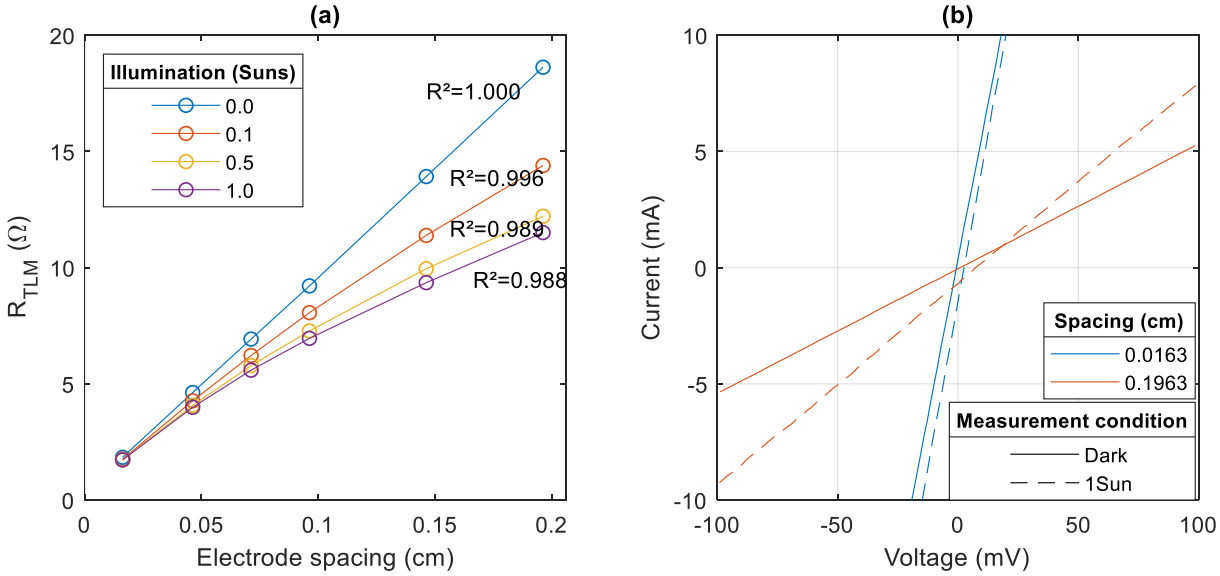

Figure 100: TLM curves for the Ag/ITO contact measured on a sample with a-Si:H(p) insulation

We also tried with thick a-Si:H(i) ITO/Ag samples and observed a very similar behavior under illumination. This makes it impossible to draw conclusions on the effect of light on ITO or the Ag/ITO contact: the TLM method is not valid with this type of test vehicle.

The effect probably stems from the electric insulation of the ITO which is not complete anymore under illumination. In particular, with p-side ITO/Ag samples, this could be the PN junction

blocking the current coming from the contacts to the bulk, but allowing current to flow in the opposite direction. For thick (i) ITO/Ag samples, this may be directly photogenerated current (either in bulk c-Si or directly into the a-Si:H(i)) that make it more conductive and less able to insulate ITO from the c-Si).

We also made some trials with samples insulated from the base using a 100nm thick thermally grown SiO_2, on which ITO was subsequently deposited. This time a very low effect of incident light intensity is observed on the TLM curves, which stay very linear. It allows to extract accurately sheet resistance and contact resistance (Figure 101):

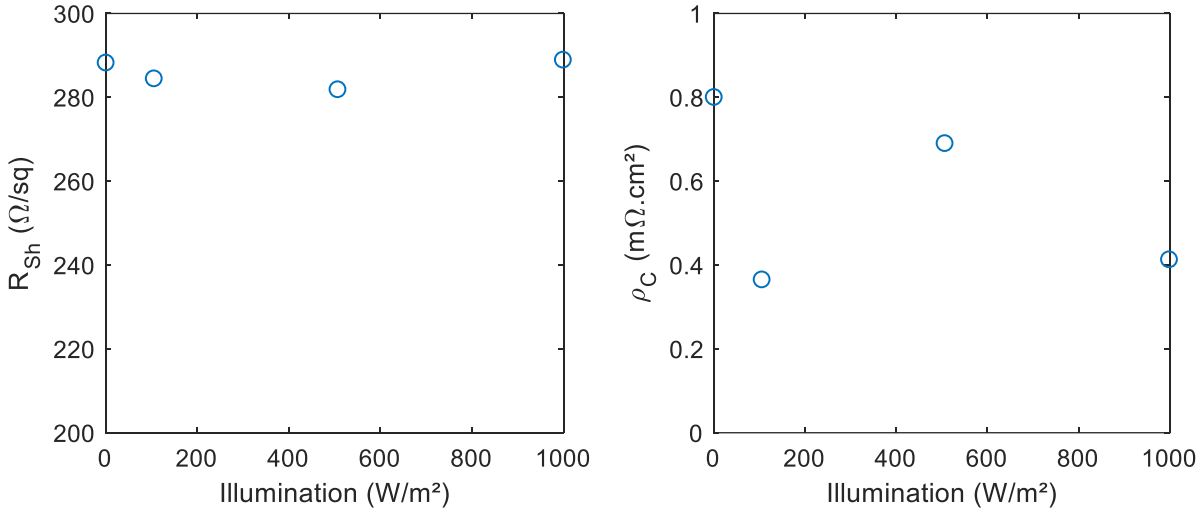

Figure 101: Sheet resistance and contact resistivity extracted with TLM as a function of incident light intensity on samples with thermally grown SiO_2 insulation layer

Here, sheet resistance stays constant with illumination, and contact resistivity varies slightly, but this is probably due to measurement uncertainties. It is worth mentioning that the illumination can induce heating in the material, which adds up to the uncertainty of the measurement. These results seem to confirm that neither ITO nor the Ag/ITO contact are influenced by illumination.

As already mentioned in §2.5.1.3, the growth of the ITO can differ significantly on thermally grown SiO_2 compared to growth on a-Si:H layers [57], [109], which could explain the higher value of sheet resistance determined using these samples.

To conclude, we have seen that in the case p-side Ag/ITO and thick (i) Ag/ITO TLM samples, contact determination with the TLM method performed under illumination was not straightforward in the current development stage, and may not be valid possibly because the insulation in between the c-Si and ITO layers is not complete under illumination. With SiO_2 insulation, we observe no significant trend with illumination.

6.2 Effect of measurement conditions on electron and hole contact resistance

We prepared n and p-stack TLM samples such as described in section §4.2, to study both the electron and the hole contact behaviors.

These samples have been measured as a function of temperature – ranging from 15 to 75°C – and illumination level from 0 to 1000W/m^2. The voltage sweep for the I-V measurements is from -0.1V to 0.1V.

In this section we will first discuss the expected evolution of the c-Si resistivity under varying temperature and illumination. Then we will study the evolution of the electron and hole contacts with temperature and illumination. We will also discuss the validity of our measurement by comparing the measured resistivity of our samples with the expected values from theory.

6.2.1 Dependence of c-Si resistivity versus temperature and illumination

To test if the measurement of resistivity is correct, we modelled its theoretical evolution with temperature and illumination. The relationship linking resistivity to temperature and excess carrier density is well known, and in the case of no trapping where $\Delta n = \Delta p$ reads:

$$\frac{1}{\rho(T,\Delta p)} = q * \left(\mu_n(T,\Delta p) * (n_0(T) + \Delta p) \; + \; \mu_p(T,\Delta p) * (p_0(T,\Delta p) + \Delta p)\right) \qquad \text{Eq. 117}$$

Where μ_n and μ_p are the electron and hole mobilities in the c-Si substrate, and n_0 and p_0 are the density of electrons and holes at thermal equilibrium in bulk c-Si, and can be calculated solving the neutrality equations:

$$n_0(T) + N_A^*(T) = \frac{n_i^2(T)}{n_0(T)} + N_D^*(T) \qquad \text{Eq. 118}$$

Where N_A^* and N_D^* are respectively the densities of ionized dopants of acceptor and donor types, and n_i is the intrinsic carrier density such that:

$$n_i^2(T) = n_0(T)p_0(T) \qquad \text{Eq. 119}$$

Once Eq. 119 is calculated, taking the value of n_i at a given temperature from the literature [157] allows to calculate $p_0(T)$.

From Eq. 117, Eq. 118 and Eq. 119, we can model the temperature evolution of the resistivity.

However, to infer the effect of steady-state illumination, one has to consider both generation and recombination rates. Using Eq. 81 and Eq. 83 (see §3.2) we can link illumination and excess minority carrier density through lifetime. Effective lifetime is then calculated such as:

$$\frac{1}{\tau_{eff}(\Delta p)} = \frac{1}{\tau_{S,front}(\Delta p)} + \frac{1}{\tau_{S,rear}(\Delta p)} + \frac{1}{\tau_{SRH}(\Delta p)} + \frac{1}{\tau_{int}(\Delta p)} \qquad \text{Eq. 120}$$

SRH recombination is considered using the classical modelling approach (see §1.2.3.1.3). Intrinsic recombination can be modelled using Richter's model for p-type samples, and Veith-Wolf reassessment for n-type samples (see §1.2.3.1.2). Surface recombination is modelled using the approach from Garin et al [33].

If all parameters for the defects are known (both at the surface and in the bulk), the relationship between the c-Si resistivity and light intensity can be determined. Typically, we can determine them by fitting of effective lifetime measurements. However, our TLM samples differ from the samples used for effective lifetime measurements in that they have metal electrodes, which shade some parts of the wafer and decrease injection level when the light source is above the sample. For this reason, we propose to add a "shading coefficient" sh in the simulation. Shading

is considered to affect the whole sample homogeneously, so the short-circuit current is such that:

$$J_{SC} = (1 - sh) * J_{max} \qquad \text{Eq. 121}$$

Where J_{max} is the maximum short-circuit current in the case of no shading.

We showed in §4.2.1 that passivation is not significantly affected by the patterning steps, but that edge cutting has an impact, but we did not quantify it.

Figure 102 shows the modelled evolution of the resistivity in open-circuit condition[7] as a function of illumination for different levels of passivation for samples simulated with a dark resistivity of 2.14 $\Omega.cm$.

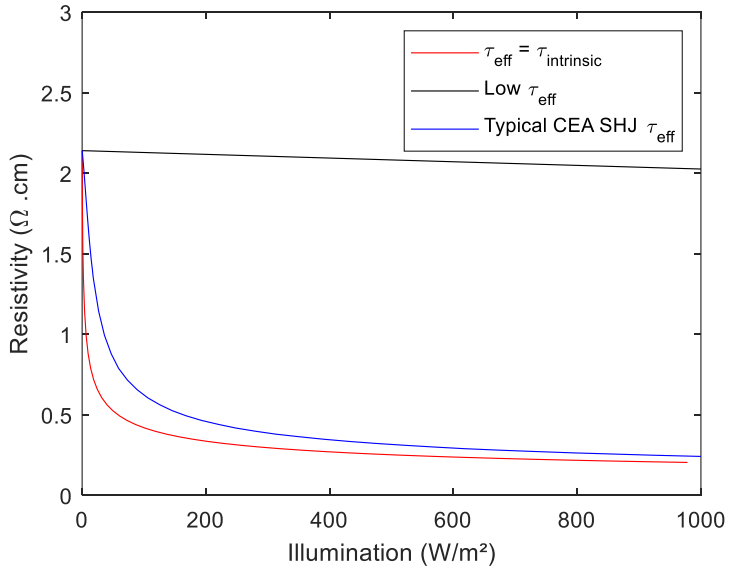

Figure 102: Variation of the resistivity at room temperature with illumination intensity modelled for different passivation properties

In the case of the Auger limited device, the resistivity drops strongly even at low light intensities. Oppositely, with poor effective lifetime – here $\tau_{eff}(\Delta p = 1e15cm^{-3}) = 7.4\mu s$ – the resistivity stays almost constant with light intensity. For effective lifetime levels typically obtained for standard SHJ samples produced at CEA, the silicon wafer resistivity is well influenced by illumination, even at low intensities.

6.2.2 Variation of the electron and hole contact resistance with temperature

TLM measurements were carried out for both n and p-type samples as a function of the temperature. We performed the measurements on the samples from §4.2.2 (p and n stack TLM structures). The wafers are approximately 180µm thick as cut, and around 10µm are removed from each side during the texturing step, resulting in a 160µm thickness for the c-Si base ($t_{c\text{-}Si}$).

[7] Note that all Δp measured from TLM samples should be representative of SHJ cell open-circuit conditions (no polarization in the transverse direction), so the resistivity at a given illumination will be different from the working SHJ device at maximum power point.

To obtain resistivity values, the sheet resistances from the TLM measurements are simply multiplied by the thickness.

The extracted resistivity is given in Figure 103. In the modelling, we used the values obtained at 300K, extrapolated using Eq. 117. The value at ambient temperature determined from the 4PP technique carried out on the same samples at two locations without metallization is also presented.

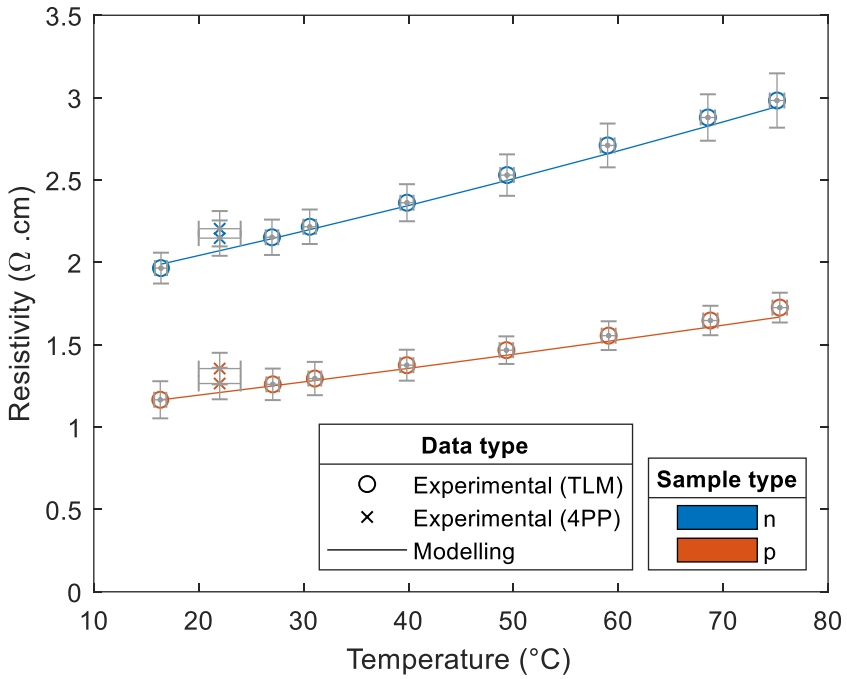

Figure 103: Resistivity of n and p-stack TLM samples as a function of temperature

TLM and 4PP measurements agree to a good degree, and the TLM measurements as a function of temperature match quite closely the expected trend, demonstrating the accuracy of the measurement.

Now Figure 104 shows the corresponding contact resistivities extracted for the same temperature range.

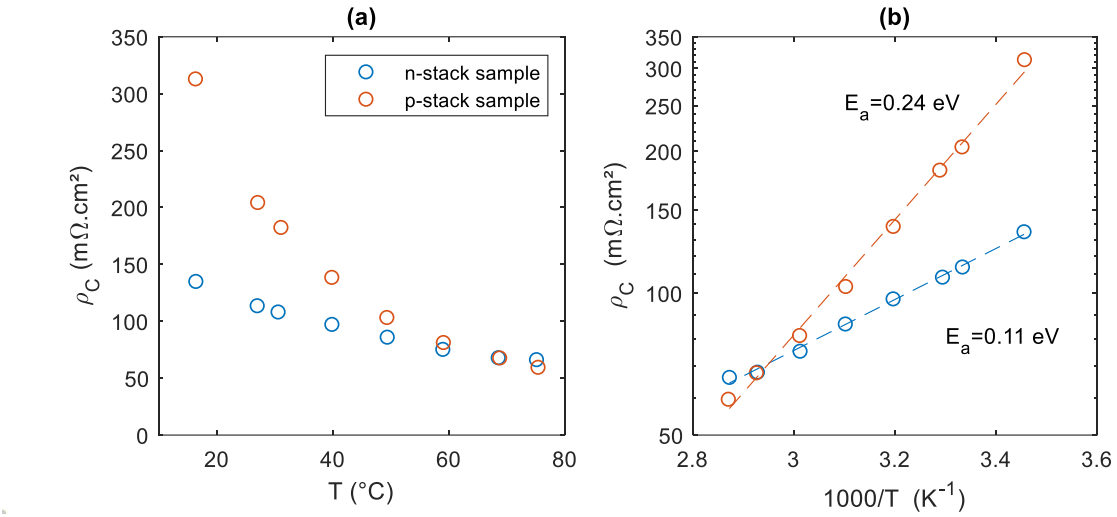

Figure 104: Contact resistivity for n and p-stack TLM samples as a function of temperature plotted in (a) a linear scale and (b) an Arrhenius law with corresponding fit (dashed lines) and activation energies

In Figure 104 (a) we observe that both contacts show a decrease of ρ_C with temperature. The hole contact is more resistive in the low temperature range, however it features a larger variation with temperature, reaching a lower value than the electron contact for T>70°C.

Plotting the same graphic in an Arrhenius law allows extracting an activation energy of the contact resistivity of both contacts (Figure 104 (b)). We extract $E_{a,e^-} = 0.11eV$ and $E_{a,h^+} = 0.24eV$.

We previously discussed (§5.3.4) that the electron contact is the sum of several contributions according to Eq. 115. We also already determined that $\rho_C(Ag/ITO)$ is negligible compared to the whole stack, and we saw that its temperature variation is quite low (see § 6.1.1) and does not explain the magnitude of what we see here. Additionally, neglecting bulk transport in the ITO seems reasonable as its conductivity is high and its thickness low. Therefore, we expect the a-Si:H conductivity and the c-Si/a-Si:H and a-Si:H/ITO interfaces to be responsible for most losses, simplifying the expression to Eq. 117, that we write again here:

$$\rho_C(e^-) = \rho_C(ITO/a\text{-}Si{:}H(n)) + R_{a\text{-}Si:H(i)} + R_{a\text{-}Si:H(n)} + \rho_C\big(a\text{-}Si{:}H(i)/c\text{-}Si(n)\big)$$

To the author's knowledge, there is no analytical formula expressing each of these terms, but under some assumptions we can express the current at each interface, and hypothesizing $\rho_C(e^-) \propto \frac{1}{J_n}$ we expect the activation energy of $\rho_C(e^-)$ to be equal to the opposite of the activation energy of the current due to the dominating process.

Using Yang's model, we already expressed the currents at the c-Si(n)/a-Si:H(i) and a-Si:H(n)/ITO interfaces (see Eq. 112 and Eq. 113). If thermionic emission at the c-Si/a-Si:H(i) interface is the limiting transport mechanism (i.e. $\delta = 0$) we should expect an activation energy of ρ_C equal to $\Delta E_{C,c\text{-}Si/a\text{-}Si:H}$. In the case of pure TE at the ITO/a-Si:H(n) interface, the activation energy would be $\Delta E_{C,a\text{-}Si:H/\mathrm{ITO}}$, corresponding to $0.3eV$ with our numerical simulation parameters. In the presence of tunneling, a second exponential term due to δ arises in the expression of current at both interfaces, which should lower the extracted activation energy.

At the hole contact, the a-Si:H(p)/ITO interface transport is ruled by band-to-band and trap-assisted tunneling (see 2.5.2.1.2). If this is the limiting transport mechanism we expect an activation energy for the current of the form [99]:

$$E_A = \frac{E_{G,p} + E_{G,n}}{2} - \frac{k_B T}{q} \frac{ln\left(\frac{N_{A,p} N_{D,n}}{n_{ip} n_{i,n}}\right)}{1 + \frac{\epsilon_p N_{D,n}}{\epsilon_n N_{A,p}}} + \frac{\Delta E_C + \frac{k_B T}{q} * ln\left(\frac{N_{C,p} n_{in}}{n_{ip} N_{C,n}}\right)}{1 + \frac{\epsilon_n N_{A,p}}{\epsilon_p N_{D,n}}} \qquad \text{Eq. 122}$$

Where the subscripts n and p refer to the n and p type materials in contact, in this case to the ITO and a-Si:H(p) layers. Using the values from our numerical simulation, we expect an activation energy of $E_A \sim 2.1eV$.

Depending on the a-Si:H(n) electron concentration and ITO affinity, the band alignment can create energy barriers leading to a complex expression for the drift-diffusion current [158]. Considering an homogeneous layer without band bending, the drift transport in a-Si:H(n) can be expressed in the dark such as [159]:

$$J_n(a\text{-}Si\text{:}H) = \sigma_n \nabla\varphi = \sigma_0 \exp\left(-\frac{E_C - E_F}{k_B T}\right)\xi \qquad \text{Eq. 123}$$

Where σ_0 is the average conductivity above the mobility edge. Therefore if transport is limited by bulk conduction in the a-Si:H (i+n) bilayer, we can expect an activation energy of the current $E_A = E_C - E_F \sim 0.4eV$ with the parameters used in our numerical simulation (§3.7.1). Eq. 123 is easily transposable to p-type, in which case the activation energy for a-Si:H(p) layers, $E_A = E_F - E_V$ is also of the order of 0.4eV.

In the literature (see § 2.5.2.2) the band offsets at the n and p-type c-Si/a-Si:H interfaces are in the order of $\Delta E_C = 0.15eV$ and $\Delta E_V = 0.36eV$ [100].

- $E_{a,e^-} = 0.11eV$ is not consistent with the activation energy of the a-Si:H layers, but is consistent with $\Delta E_{C,c\text{-}Si/a\text{-}Si:H}$ which may indicate a transport limited by thermionic emission at the c-Si(n)/a-Si:H(i) interface. The $0.04eV$ difference could be explained by a weak tunneling component. But another explanation would be a transport limited by the a-Si:H(p)/TCO interface with a strong tunneling component.
- $E_{a,h^+} = 0.24eV$ is quite different than the expected valence band offset, which indicates that pure thermionic emission over the band offset is not the limiting transport mechanism. The trap-assisted tunneling at the a-Si:H(p)/ITO interface is also very efficient, otherwise we would obtain a much higher activation energy. The limiting transport mechanism could be a strongly mixed tunneling and thermionic emission regime over the c-Si(p)/a-Si:H(p) barrier.

Note that this entire discussion only works if one dominant mechanism is expressed; otherwise we can expect the different current expressions to get mixed up in non-trivial ways. In addition, there is a large experimental error when extracting activation energies using such a short range of temperature. Using a tool equipped with a cryostat or a hot plate enabling higher temperatures would allow a more precise determination of E_A.

6.2.2.1 *Electron contact properties as a function of temperature and c-Si doping*

We conducted the same experiment again, using n-stack TLM samples with varying wafer doping (from §5.1). We model the behavior of resistivity with temperature for all resistivity classes using our reference value at 298K determined from 4PP sheet resistance measurement on as cut wafers and thickness obtained from laser interferometry. We obtain a good match for all samples, with the highest deviation for the least doped sample (Figure 105).

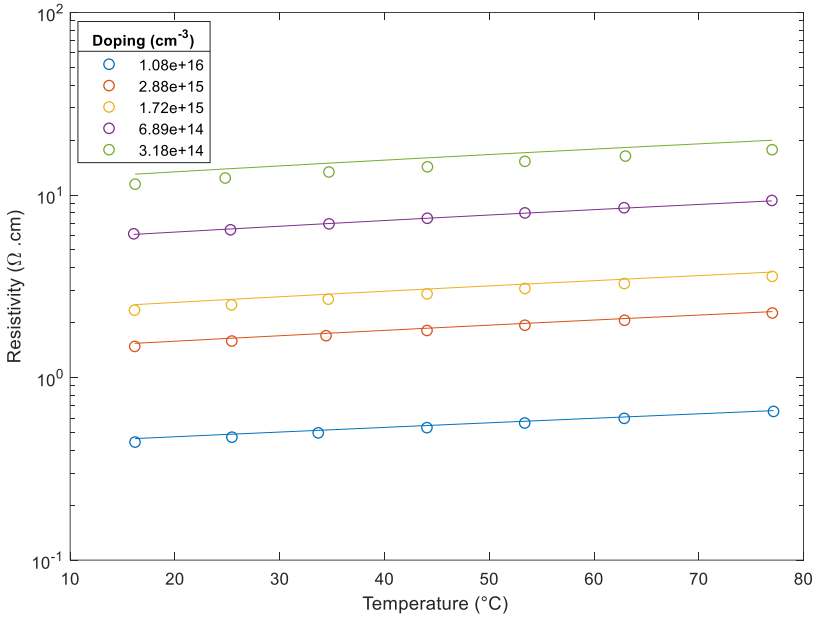

Figure 105: Resistivity as a function of temperature extracted with TLM samples for different wafer resistivities. Dots and lines represent respectively experimental calculated values

The corresponding contact resistivity extracted for each sample is displayed in Figure 106.

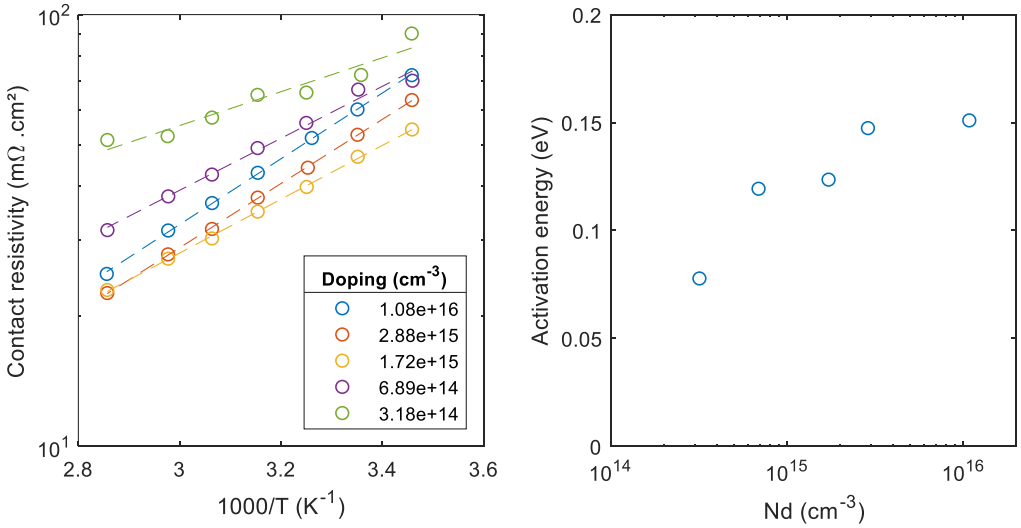

Figure 106: (left) Contact resistivity of the electron contact (left) as a function of temperature and (right) doping and activation energy as a function of doping

We see that whatever the wafer doping level, the contact resistivity decreases with temperature. However, the trend may vary from sample to sample. Lowest values for $\rho_C(e^-)$ are obtained with $N_D = 1.72 * 10^{15} cm^{-3}$ all over the scanned temperature range. We plotted

these graphs into an Arrhenius plot and extracted the activation energies of $\rho_C(e^-)$ as a function of doping (see right graph in Figure 106).

As indicated by the lower slopes obtained for the lower doping levels, we observe that the activation energy increases with increasing doping, and seems to tend towards 0.15eV, which corresponds to the expected ΔE_C. Hypothesizing that ΔE_C does not vary with doping, this hints that the doping level rules the dominant transport mechanism.

Considering Yang's model, tunneling at the c-Si(n)/a-Si:H(n) interface should decrease the obtained activation energy. However, higher c-Si(n) doping should facilitate tunneling, therefore decreasing E_A, but we observe the opposite trend. This indicates that the observed increase in E_A with c-Si doping probably stems from another effect. We can question the application of Yang's model for this contact, and a more thorough description of the transport in a-Si:H layers, and accounting for band bending inside these layers may be pertinent to detail the analysis.

Another possibility for this could be that the activation energy of the contact does not really depend on doping, and that the observed trend is due to a measurement artifact. Current crowding effects are known to affect TLM measurements [160], and to be more severe when the studied layer resistivity is low [161], which could lead to the contact resistivity being more accurately determined at high doping.

6.2.3 Variation of the electron and hole contact resistance with illumination

We have shown in §6.1.2 that in some cases, illumination can bias the TLM measurement and make results non-valid. However, it may be of importance to know the behavior of contacts under illumination, as this is their operating condition. In this paragraph we will try to find experimental conditions allowing to make valid TLM measurements under illumination. Once again, we used the n and p-stack TLM samples from §4.2.2.

First, to be able to determine the relationship between ρ and the illumination intensity, we need to calibrate our model by fitting experimental data with a set of parameters to describe bulk and surface properties. We measured the effective lifetime for an n-type sample that received the patterning treatment (see §4.2.1), and parameters of the simulation models were adapted following the approach previously described (see §6.2.1). Results are shown in Figure 107.

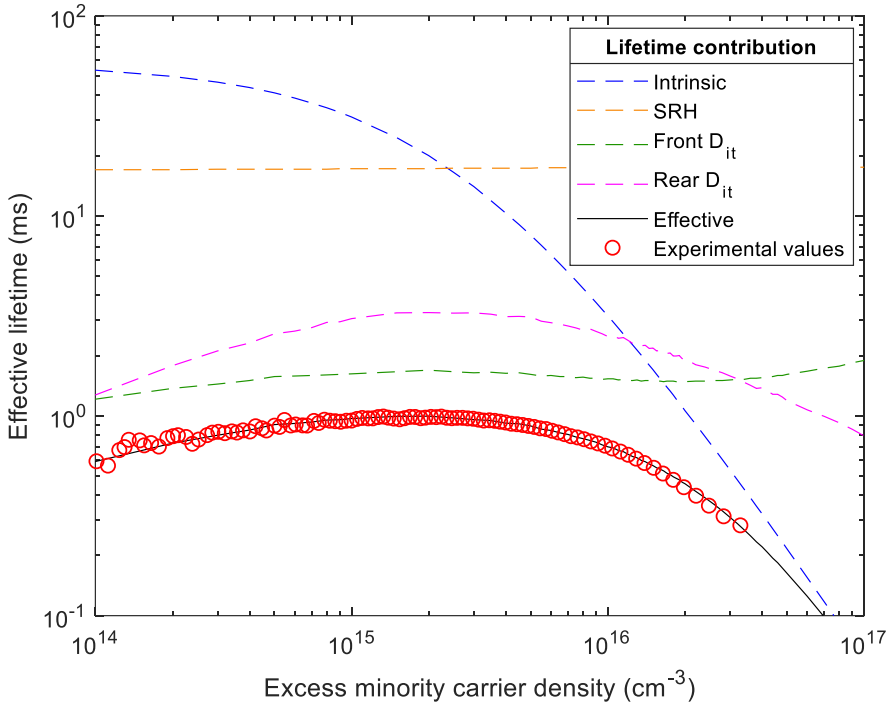

Figure 107: Effective lifetime as a function of excess minority carrier density for experimental values obtained on n-type samples (red dots) and simulated data (solid line). The contributions of the different sources of recombination that affect the effective lifetime are also displayed in dashed lines (simulation data)

Parameters for the lifetime modelling are presented in Table 6.

Table 6: simulation parameters for lifetime modelling

Simulation parameters	**Value**	
Trap energy level ($E_C - E_t$)	$0.74\ eV$	
Trap density (N_t)	$5 * 10^{10} cm^{-3}$	
Hole capture coefficient (σ_p)	$7 * 10^{-17}\ cm^2$	
Electron capture coefficient (σ_n)	$2 * 10^{-15}\ cm^2$	
Wafer thickness	155µm	
	Front	*Rear*
Density of interface traps (D_{it})	$3.65 * 10^{-15}$	$2.3 * 10^{13}\ cm^{-2}.eV^{-1}$
Electron surface recombination velocity (S_{n0})	330	$1000\ cm/s$
Hole surface recombination velocity (S_{p0})	1	$800\ cm/s$

From this set of parameters we can model the variations of resistivity with illumination of the bare n-type wafer. Parameters for surface recombination correspond to $S_{eff,front} = 9.6\ cm/s$ and $S_{eff,rear} = 5.1\ cm/s$.

For p-type samples, effective lifetimes below 100µs were measured after PVD. As the wafers produced in the same batch with n-type wafers showed good lifetime values, we expect bulk lifetime to be the main reason for low effective lifetime values for p-type samples. As already mentioned (see §2.1), standard industrial p-type wafers are generally of lesser bulk quality compared to n-type wafers. Standard products typically have specifications for bulk lifetimes of the order of 200µs, which leads to poor SHJ devices [145], at least if no gettering process or

bulk wafer cleaning is performed prior to cell fabrication [146], [147]. Therefore, the low value that was obtained is not surprising, but will be an issue to study the influence of light intensity with similar injection levels than those present in standard SHJ cells, as high lifetimes are necessary.

TLM measurements were conducted for both n and p-stack samples as a function of the illumination intensity (top illumination). I-V curves are displayed in Figure 108 for the n-stack TLM sample. The measured I-V curves stay fairly linear under illumination, even though we observe a slight rectifying behavior (the p-stack sample is not shown but features better linearity).

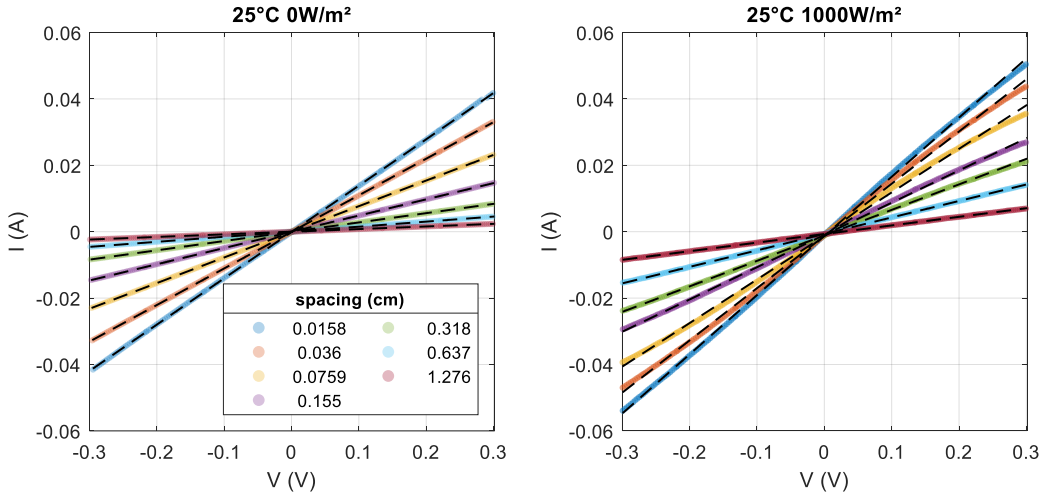

Figure 108: I-V curves for the n-stack sample for each spacing at ambient temperature; (left) under dark conditions and (right) under 1Sun illumination. Experimental data is plotted as transparent colored lines and linear fits are plotted as black lines

To ensure a good linearity, we restrict the TLM analysis to the -0.1V to 0.1V range for all samples in this work. This is also motivated by the definition of contact resistance (Eq. 65), which is defined at voltages close to zero. Another argument was recently proposed [162] relying on the drift of carriers being negligible only at small bias: at high bias, non-negligibly different current densities below the two contacts can arise, making the TLM analysis non-valid.

The TLM plots are also reasonably well represented by lines, but similarly to what we noticed for the Ag/ITO contact, we observe that TLM plots are no more purely linear under illumination, and R^2 diminishes with increasing light intensity. We also observe a very slight shift of the I-V curves (<1mA), suggesting the collection of some photo-generated carriers. However, we get $R^2>0.995$ for all the illumination intensities tested (Figure 109), so we consider the precision satisfying for the analysis.

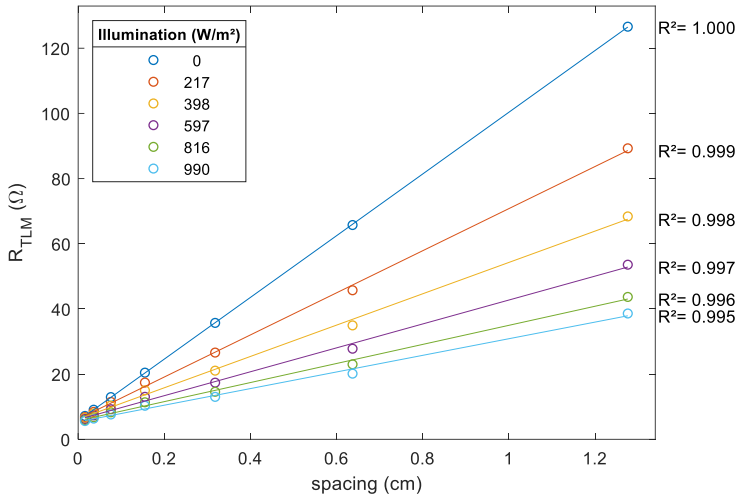

Figure 109: TLM plot for the n-stack sample for different illumination intensities. Experimental data is plotted as dots and linear fits are plotted as lines

Now that we have checked the validity of the measurement, we apply the TLM and the extracted resistivity is shown for both samples n and p-type stack samples in Figure 110.

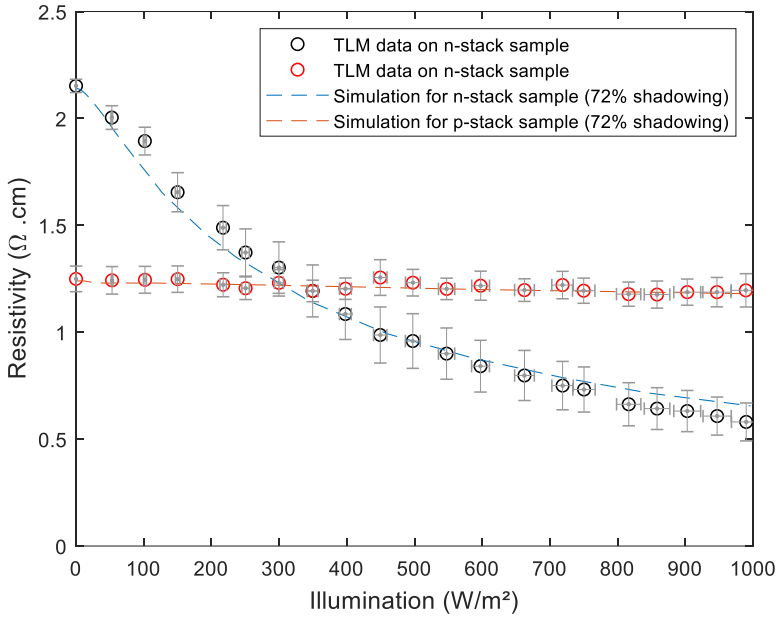

Figure 110: Experimental data of resistivity values measured for the p and n-stack TLM samples as a function of illumination intensity (red and black dots). The dashed lines corresponds to the simulated values with the approach described above

For the p-stack samples, we see no significant effect of light with illumination, as could be predicted from the low lifetimes of the samples. However, for the n-type samples the illumination intensity decreases the measured resistivity.

We applied the modelling approach with the parameters from Table 6. Experimental data can be so reproduced with a decent accuracy, but we need to introduce a high shadowing of $sh = 72\%$ to fit our data (see Eq. 121). As already mentioned, lifetime measurements done after

edge cutting would be more representative of the finished TLM test samples. Here injection level reduction due to damaged passivation from cutting and handling adds up, which introduces some error in the approach. Still, the fact that our modelling can fit data gives credence to the corresponding measurements of contact resistivity, presented in Figure 111.

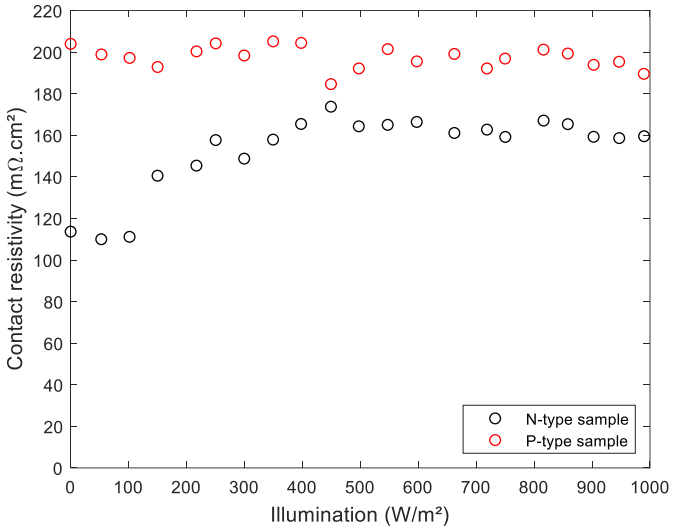

Figure 111: Contact resistivity for electron and hole contacts measured as a function of incident illumination

We can see that the hole contact varies little with illumination, with a slight downward trend, which may only be related to measurement uncertainty. For the n-stack samples, we see an increase in $\rho_C(e^-)$ from 114 to 160 $m\Omega.cm$ with illumination.

This suggests that the electron contact resistivity, under 1Sun V_{OC} in a functioning cell, is actually higher than determined in the dark. Indeed, the junction is not polarized, therefore the TLM samples are in conditions representative of open-circuit, where Δp is higher than at maximum power point, which emphasizes the effect of light. To get values representative of MPP conditions, we need to calculate Δp for each illumination. This can be done e.g. through or modelling approach (§6.2.1). A useful alternative is to use the expression of the conductivity in the dark and under illumination:

$$\sigma_{dark} = \frac{1}{R_{Sh,dark}t} \sim qN_D\mu_n \qquad \text{Eq. 124}$$

$$\sigma(\Delta p) = \frac{1}{R_{Sh}(\Delta p)t} \sim q\left((N_D + \Delta p)\mu_n + \Delta p\mu_p\right) \qquad \text{Eq. 125}$$

From which we can express:

$$\Delta p = \frac{1}{qt(\mu_n + \mu_p)} * \left(\frac{1}{R_{Sh}(\Delta p)} - \frac{1}{R_{Sh,dark}}\right) \qquad \text{Eq. 126}$$

Therefore, we can determine Δp at any illumination from the measurement of R_{Sh} at this illumination level from Eq. 126. Note that a more thorough expression needs to take into account the mobility dependence on Δp, and solve for Δp, but here we used the value from Klaassen et al. in the dark [163], [164].

In this example, hypothesizing $\Delta p_{MPP} = 1e15\, cm^{-3}$, this corresponds to an illumination intensity of about 250 W/cm², and to a contact resistivity of 157 $m\Omega.cm^2$. If this effect is confirmed, it needs to be accounted for on power loss analyses by using the value of the contact resistivity at 1Sun MPP instead of in the dark.

Additionally, we measured the activation energy of the electron contact for three different illuminations (Figure 112).

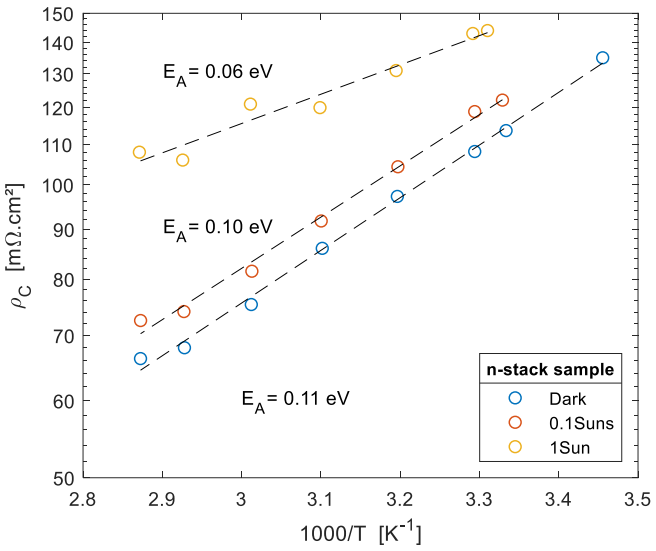

Figure 112: Electron contact resistivity as a function of temperature in the dark and under 0.1 and 1 Sun illuminations

Illumination leads to higher majority carrier density below the contacts, which should have a similar effect than doping of the c-Si, previously investigated in this work (§5.1.3, §6.2.2.1). However, here we see the opposite trend for the activation energy: higher illumination increases $\rho_C(e^-)$ but decreases E_A (0.11eV in the dark versus 0.06eV under 1Sun).

6.2.3.1 Influence of front or rear illumination and of wafer resistivity

An alternative approach could be to measure samples with rear side illumination. This ensures no shading due to the electrodes and more homogeneous photo-generation over the sample. This approach is however less convenient, as the samples need to be placed on a transparent chuck, or contacted from below. When using a glass chuck with illumination from below, the temperature control cannot be enabled, so the samples can heat up a bit during the measurement, which can also bias the analysis.

Using n-type samples of different resistivity (see §5.1.3), we performed a TLM analysis as a function of illumination, with illumination on either front (conventional chuck) or rear (glass chuck) side. We chose electrode spacing varying from 0.3 to 2.1 mm. Figure 113 illustrates results for ρ_C obtained on these samples.

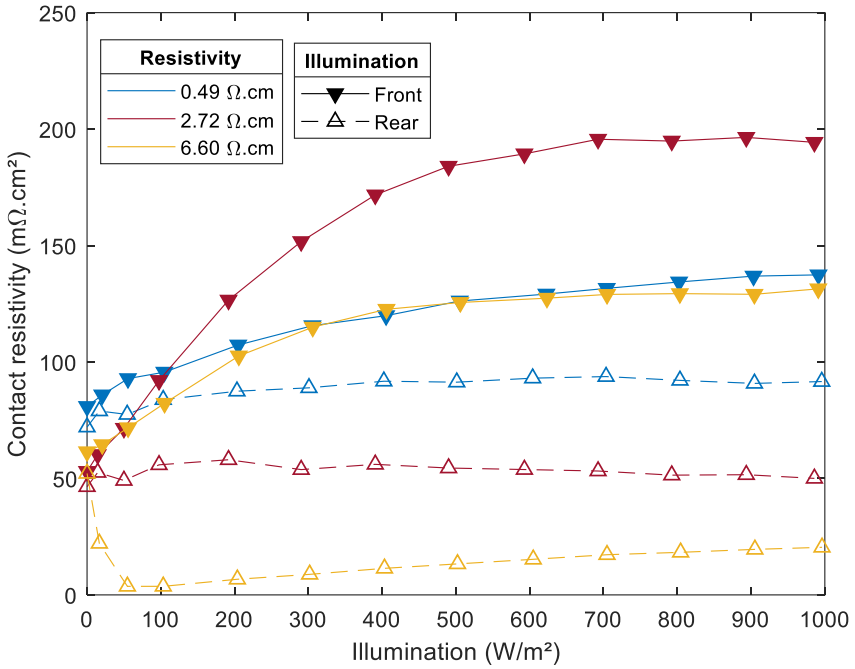

Figure 113: Contact resistivity of the electron contact as a function of illumination for different substrate resistivity, under front and rear illumination conditions

We observe that under front illumination, ρ_C increases with increasing light intensity for all resistivity classes. However, under rear illumination the trend varies with the different resistivities: slightly increasing for the low resistivity sample, mostly constant for the medium resistivity sample, and decreasing then increasing for the highest resistivity sample.

Using the values of Δp_{MPP} from §5.1.2, we can extract the values for $\rho_C(e^-)_{MPP}$ from Eq. 126 (Table 7).

Table 7: Electron contact determined in the dark and under operating conditions

ρ_{dark}	$0.49\ \Omega.cm$	$2.72\ \Omega.cm$	$6.6\ \Omega.cm$
$\Delta p(MPP)$	$2.49 * 10^{14}\ cm^{-3}$	$9.11 * 10^{14}\ cm^{-3}$	$1.39 * 10^{15}\ cm^{-3}$
$\rho_C(e^-)_{dark}$	$72.1\ \Omega.cm^2$	$46.5\ \Omega.cm^2$	$52.2\ \Omega.cm^2$
$\rho_C(e^-)_{MPP}$ (front illumination)	$92.9\ \Omega.cm^2$	$126.6\ \Omega.cm^2$	$115.0\ \Omega.cm^2$
$\rho_C(e^-)_{MPP}$ (rear illumination)	$77.5\ \Omega.cm^2$	$55.8\ \Omega.cm^2$	$6.7\ \Omega.cm^2$

Therefore, with front illumination, we expect higher values of $\rho_C(e^-)$ under operating conditions compared to dark conditions for all samples, but with rear illumination, results depend on doping, with slightly higher values with $0.49\Omega.cm$ and $2.72\Omega.cm$, and a notably lower value with the $6.6\Omega.cm$ sample.

To examine these results in more details, the corresponding R_C and R_{Sh} obtained on these samples are shown in Figure 114.

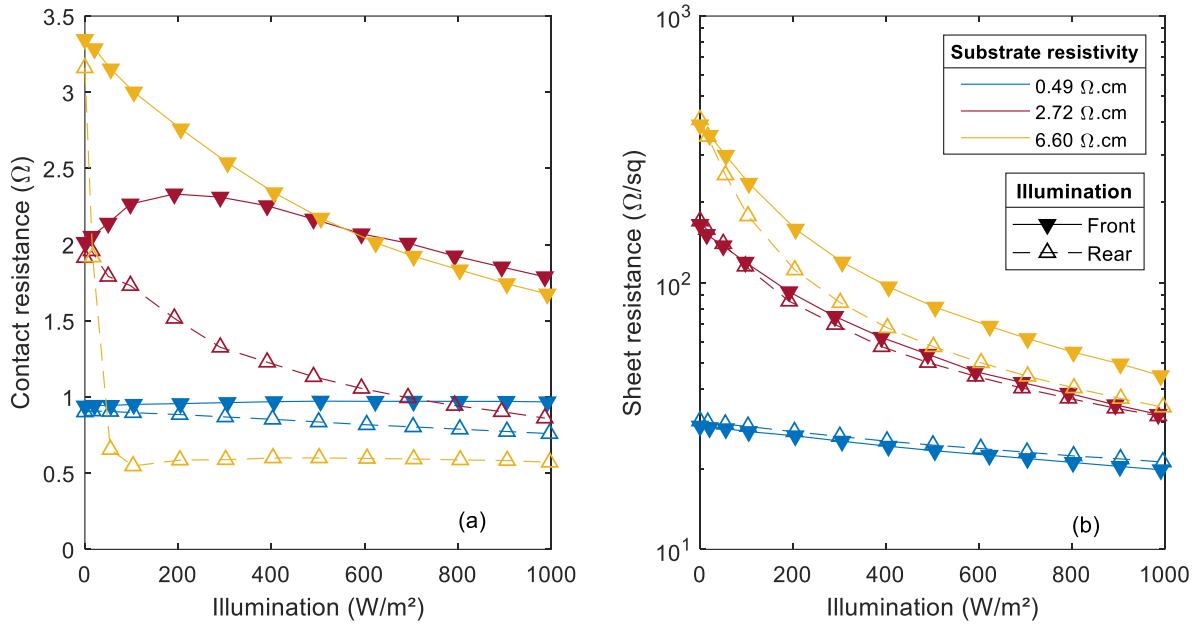

Figure 114: (a) Contact resistance and (b) sheet resistance measured as a function of illumination for varying substrate resistivity, under rear or front illumination

First, we note that the results obtained in dark conditions match with both front and rear illumination setups. We have seen before (§5.1.2) that high resistivity substrates generally achieve higher lifetimes, enabling higher excess minority carrier densities, and therefore they should exhibit higher susceptibility to light, and we do observe this for the R_{Sh}.

We observe that R_{Sh} decreases whichever side the illumination is, with a very similar trend in both cases. We expect lower R_{Sh} with rear illumination, as no shading should allow for higher excess minority carrier densities: we observe this especially with the 6.6 $\Omega.cm$ sample but also slightly for the 2.72 $\Omega.cm$ sample, but not with the 0.49 $\Omega.cm$ sample. We showed before (§5.1.2) that for such low resistivity wafers $\Delta p_{1Sun,MPP}$ does not significantly impact the electron density so that $\rho_{1Sun,MPP} \sim \rho_{dark}$, likely explaining the lack of photo-sensitivity. Additionally, the I-V measurements under rear illumination were made with a fast voltage sweep in order to avoid heating, but still, the absence of temperature control may lead to a slight temperature increase, leading to a resistivity increase (see e.g. §6.2.2), explaining this effect. As the dynamic of the curve is weaker for this sample, it is more prone to experimental uncertainty.

For R_C we see that the trend is different depending on the illumination side:

- With front illumination, the low and high resistivity samples exhibit respectively an increasing and a decreasing curve, as the intermediate class makes a bell shaped curve.
- With rear illumination, the contact resistance decreases whatever the resistivity class is.

With the 2.72$\Omega.cm$ sample, the injection level does not significantly differ under front or rear illumination (as shown by very close R_{Sh} trend) but the dynamics of ρ_C does. This indicates that the carrier density directly below the contact is very important.

Focusing on rear illumination, we observe that when using high resistivity substrates, injecting more carriers has a very important impact on R_C, which drops to well above other conditions

in the dark to well below at 100W/m² illumination, while when working with low resistivity substrates, R_C varies little. This hints that the majority carrier density rules ρ_C, and suggests that doping and illumination have a similar effect.

Figure 115 summarizes the values of $\rho_C(e^-)$ obtained experimentally in the dark and under 1Sun illumination with both approaches as a function of c-Si dark resistivity.

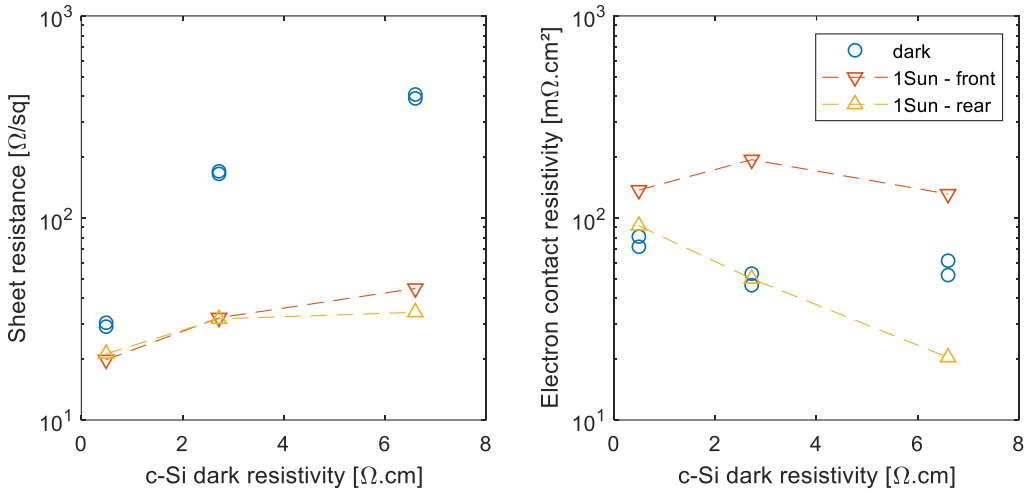

Figure 115: (left) Sheet resistance and (right) $\rho_C(e^-)$ as a function of c-Si dark resistivity for different illumination conditions

We confirmed our results using our TLM numerical simulation with standard parameters (§3.7.1). Note that lifetime values were not adapted to fit experimental data. We simulated the evolution of the sheet resistance and contact resistivity of the electron contact as a function of the c-Si resistivity, in three different conditions (Figure 116):

- dark conditions
- 1 Sun illumination with opaque electrodes (corresponds closely to front illumination)
- 1 Sun illumination with transparent electrodes (corresponds closely to rear illumination)

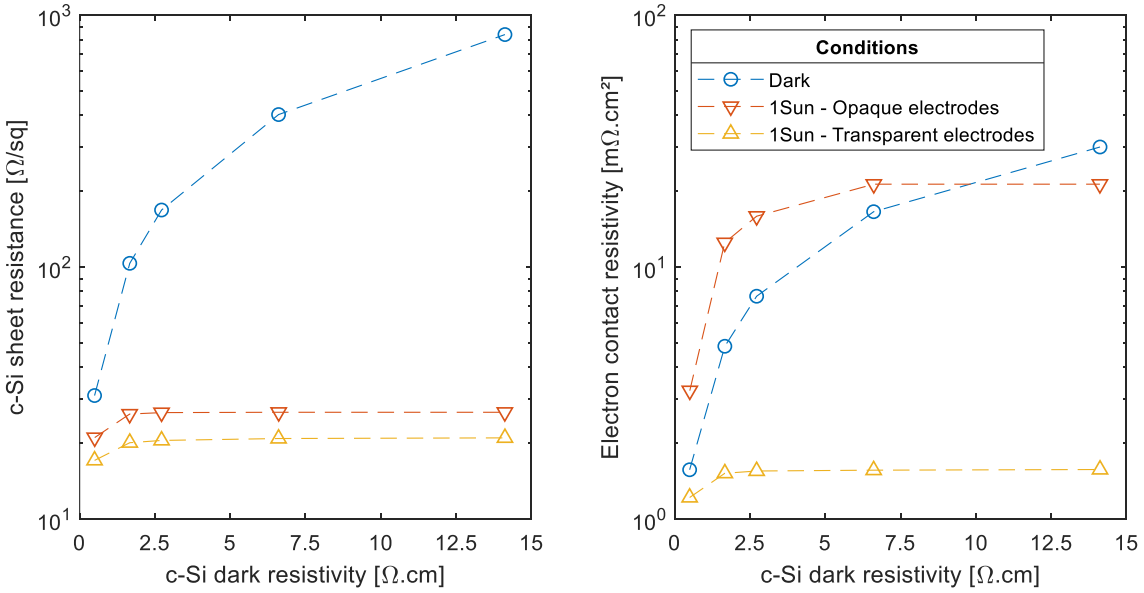

Figure 116: Simulated sheet resistance and electron contact resistivity as a function of c-Si dark resistivity in the dark and under 1 Sun illumination, considering opaque and transparent electrodes

As compared to dark conditions, the sheet resistance extracted under illumination is reduced a lot, especially for high c-Si dark resistivities, and stays quite constant when $\rho \geq 2.72\Omega.cm$, signifying that high injection level is reached. R_{Sh} further decreases when using transparent electrodes as compared to opaque ones. Lifetime parameters in the simulation are less severe than for our experimental samples, explaining why $\rho_C(e^-)$ decreases in the simulation even for $\rho = 0.49\Omega.cm$.

$\rho_C(e^-)$ increases with c-Si wafer resistivity in the dark, and also under illumination but with a different trend. Additionally, it depends on the transparency of the electrodes. With opaque electrodes, $\rho_C(e^-)$ is higher under illumination than in the dark except for $\rho_{c\text{-}Si} = 14.12\Omega.cm$. This could be due to the better diffusion length of minority carriers at low doping mitigating the uneven Δp in front illumination configuration. With transparent electrodes, the electron contact is drastically reduced compared to its value in the dark all over the studied range, but especially for high c-Si dark resistivities where high level injection is reached.

Comparing experimental (Figure 115) and simulation values (Figure 116), we observe similar trends for R_{Sh}, the difference could probably be reduced by calibrating the lifetime parameters of the simulation. For $\rho_C(e^-)$, we observe a significant difference between simulated and experimental absolute values (already pointed out in §5.1.3), and the trends do not match precisely, but we do observe in both cases that the greatest dark/light difference with rear illumination is for the highest resistivities.

6.2.3.2 Discussion of the approach

The TLM measurement assumes that the electronic properties of the samples are homogeneous all over. Even considering that this is true under dark conditions, this is not necessarily true under illumination as local variations of the excess minority carrier can appear due to inhomogeneous shading or passivation quality. Two assumptions need to be verified:

(1) The carrier density below the contacts needs to be the same as in non-shaded areas. With our TLM samples we have significant shading, so to consider that this first assumption is true the diffusion length of electrons (L_{Dn}) and holes (L_{Dp}) must be very large compared to the length of the electrodes L.
Our first criteria is therefore :

$$L_{Dn,p} \gg L \quad \text{Eq. 127}$$

(2) The carrier lifetime must be homogeneous all across the sample to avoid local variations of excess minority carrier density.

- If condition (1) is not respected, then the sheet resistance below the electrodes will not be homogeneous, and will be higher than in between the electrodes. This leads to a wrong evaluation of L_t and ρ_C as both are a function of the sheet resistance underneath the electrodes.
- If condition (2) is not respected, at best, it leads to variability in the measurement, and at worst, it compromises the validity of the TLM method under illumination.

Diffusion lengths can be calculated such as:

$$L_{Dn,p} = \sqrt{\frac{k_B T}{q} \tau_{eff} \mu_{n,p}} \quad \text{Eq. 128}$$

At T=300K, with $N_D = 2.10^{15} cm^{-3}$ and $\Delta n = \Delta p = 1.10^{15} cm^{-3}$, and $\tau_{eff} = 1ms$, we get values of 1.8mm and 1.1mm respectively for L_{Dn} and L_{Dp}.

In the case of the studied samples, $L = 0.5mm$, therefore $L < 3L_{Dn}$ and $L < 2L_{Dp}$, which is not ensured to satisfy our first assumption. Probably the most problematic condition is homogeneous passivation. As we need to cut the outer edges of the TLM samples to avoid parasitic lateral current, we necessarily induce laser damage which are detrimental to the passivation. Note that these could be mitigated by edge passivation such as demonstrated in [165]. Also, the ITO works as a physical protecting barrier for the cells. When etching it away, the samples become much more sensitive to scratches, which makes them hard to manipulate without harming the passivation layers. Figure 117 illustrates front and rear PL images of a TLM sample.

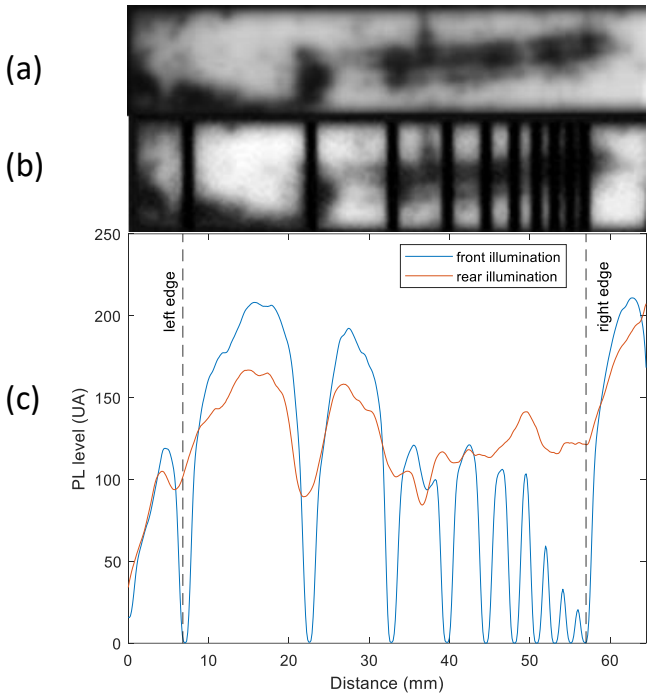

Figure 117: un-calibrated PL images of a TLM sample (a) rear illumination and (b) front illumination. (c) Histogram of PL signal along the sample (averaged across the width)

The outer edges of the sample are visibly black, showing the unpassivated edge, and black marks are present on some regions of the sample, showing damaged passivation layers. We can also notice that when the sample is measured under front illumination, zones in between electrodes show a diminishing PL grey level when spacing decreases (left to right), while the PL level is much more homogeneous when illumination is from the rear side. It is therefore obvious that there is a large inhomogeneity of Δp along this sample, which is a sign that none of the criteria are respected with front illumination. To improve the reliability of the results, rear illumination in addition to a more homogeneous passivation are required.

As the results with rear illumination are more likely to respect condition (1), this implies that that at least part of the variation of ρ_C with illumination when using front illumination is a bias, and that the TLM analysis is not valid with front illumination.

We conclude that the measurement of the electrical characteristics of the contacts illumination should be carried out under rear side illumination.

6.3 Chapter outlook

In this chapter, we investigated the influence of temperature and illumination level on the electrical properties of SHJ cell contacts.

We showed that the Ag/ITO contact is influenced by temperature, indicating a thermally activated transport mechanism, which does not fit with the pure tunneling regime predicted by theory. We also investigated this contact under illumination, and concluded that it is probably unaffected by light, but however found that the TLM method is non-valid with p-side and thick a-Si:H(i) ITO/Ag TLM samples, indicating that in this case TLM measurements under illumination can be troublesome.

We investigated the behavior of the electron and hole contacts under varying temperature, and showed that ρ_C decreases with increasing temperature for both contact types. We could extract the activation energy for the contact resistivity, in order to study the transport phenomena at play. At the electron contact, we extracted an activation energy $E_a = 0.08$ to $0.15eV$ depending on doping, indicating that c-Si doping rules the dominant transport mechanism, which may be a mixed thermionic emission tunneling regime at the c-Si(n)/a-Si:H(i) interface. For the hole contact, we found $E_a = 0.24eV$, which is very unlikely to be ruled by the a-Si:H(p)/ITO interface, but more probably to thermionic field emission over the c-Si(p)/a-Si:H(i) interface.

We studied the impact of illumination on the contact properties since a cell operates under illumination. However, we showed that this measurement procedure (including samples preparation) requires fine tuning to obtain meaningful results. With the help of numerical simulation, we demonstrated that homogeneous carrier injection is necessary within the wafer to obtain non-biased values, which requires rear illumination for our current TLM sample design, as well as a homogeneous passivation quality (not clearly reached for our samples). In particular, activation energy should be measured again as a function of illumination with samples respecting the criteria that we set that are challenging because temperature variation combined with rear illumination are not possible with our current setups.

Chapter 7

Resistive power loss analysis for bifacial SHJ cells

We already mentioned before (e.g. §2.4) that the conventional models to assess power loss due to resistive effects are not appropriate to be used directly for SHJ cells, or more generally on new solar cells concepts providing high passivation levels such as shallow emitter homojunction or passivating contacts devices. The reasons are mainly that they do not account for interface resistance – which is very important in passivating contact cells –, nor for lateral transport in the absorber; which is also very important, notably in cells operating at high-injection level or featuring low resistivity absorbers (see §2.5).

In this chapter, we will propose and discuss a more relevant model for the analysis of resistive power losses in inverted emitter bifacial SHJ cells. Our model needs to account for several aspects of the cell, namely: lateral transport in the absorber, impact of the electron and hole contact resistivities and bifacial operation. Bifacial design is easily accounted for (e.g. [52]), by considering losses using the same equations for the front and rear losses in fingers and busbars. However, lateral transport and contacts are linked through a complex relation that we will investigate in this chapter. Figure 118 illustrates in a simplified way all the current paths in a bifacial rear emitter SHJ cell.

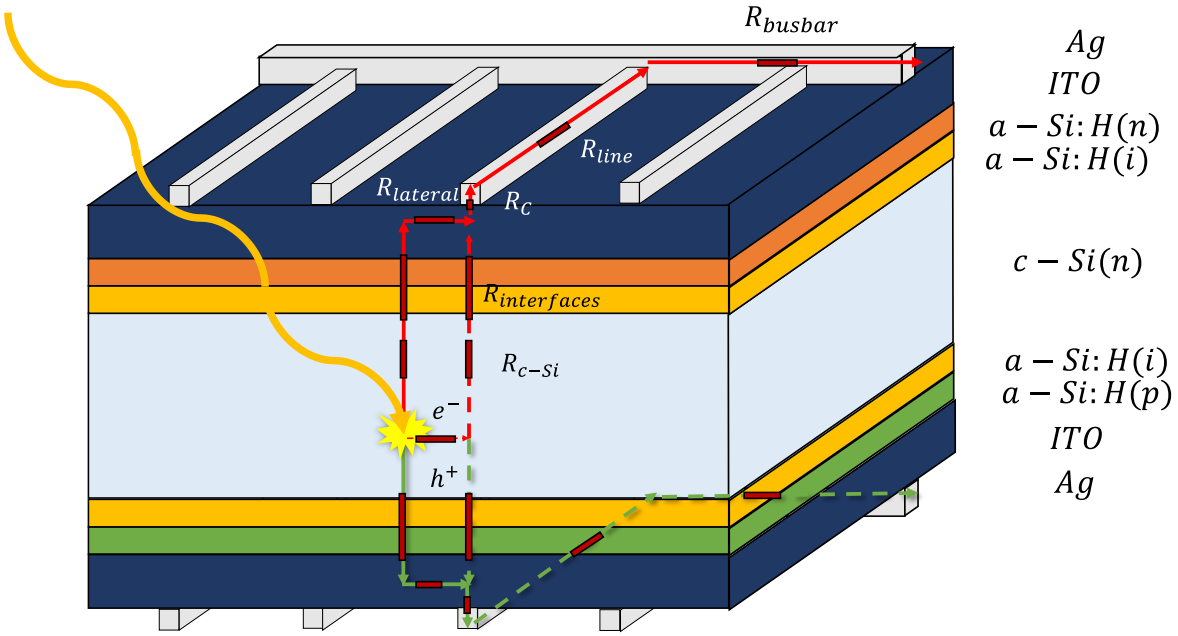

Figure 118: path of electrons (red) and holes (green) from their generation in bulk c-Si to their collection in the external circuit

7.1 Lateral transport in SHJ cells

The impact of the electron and hole contact resistivities can be accounted for a simple way by making the assumption that the current crosses the interface homogeneously. This is what is implicitly done in Lachenal's paper [58]:

$$R_S(e^-) = \rho_C(e^-) \quad \text{Eq. 129}$$

$$R_S(h^+) = \rho_C(h^+) \quad \text{Eq. 130}$$

Using TLM measurements we demonstrated that indeed, at the front side, lateral transport takes place in the absorber in parallel to the TCO layer, and that Eq. 107 models quite efficiently the parallel connection of both layers. Therefore we proposed in [166] to take into account the lateral transport in c-Si in parallel to the TCO for the front side, and only the TCO at the rear:

$$R_S(front\ lateral) = \frac{1}{12} * p_f^2 * \left(\frac{1}{R_{Sh,cSi}} + \frac{1}{R_{Sh,TCO}}\right)^{-1} \quad \text{Eq. 131}$$

$$R_S(rear\ lateral) = \frac{1}{12} * p_r^2 * R_{Sh,TCO} \quad \text{Eq. 132}$$

Where p_f and p_r are the pitches of the front and rear metallization grids. Eq. 129, Eq. 130, Eq. 131, Eq. 132, form an easy way to consider lateral transport and the resistance from electron and hole contacts. Adding the classical expression for losses in metallizations both at the front and at the rear in the fingers, the busbars and the metal contact (Eq. 52, Eq. 53, Eq. 54), as well as the bulk in the transverse direction (Eq. 55) makes a full model for R_S modelling. This model will be referred to as the "Model 1".

However, there are still several neglected effects. In TLM samples, there are only minority carriers flowing, therefore in §4.1.2 we were only concerned about electrons. Now in a working n-type rear-emitter SHJ cells, there are both electrons and holes, but only electrons are

collected at the front contact, therefore we only need to consider the sheet resistance of electrons ($R_{Sh,cSi}(e^-)$) for the front side lateral transport [81].

Moreover, there is an interplay between contact resistance and lateral transport that is neglected using Eq. 129, Eq. 130 and Eq. 131. Considering homogeneous photo-generation, if the photo-generated carriers flow directly through the interface to the TCO layer, then they will cross the electron contact homogeneously and Eq. 129 will be valid. Oppositely, when a significant current goes through the bulk, then there will be current crowding under the contacts, and Eq. 129 will not be valid anymore.

As shown by Bivour et al., lateral transport in the absorber also occurs at the rear, but it is less important [108]. This has been attributed to several effects, mostly high values of hole contact resistivity, and lower mobility of holes [81]. Additionally, we have seen in the literature that Huang et al [76] proposed a two-layer TLM model (see §2.3.2) that takes into account two layers separated by an interface contact resistance.

The objective of this chapter is to propose an adaptation of Huang's model to the frame of a power loss analysis. In TLM samples all current comes from the contacts, while in solar cells, it is photo-generated in the bulk and flows towards the contacts. This changes the boundary conditions in Huang's model and makes it not applicable directly to the case of a solar cell.

In this work, we use a two-fold approach; first we model the TLM structure with a simpler model, and demonstrate that we reach a close agreement with Huang's model. Then, based on the same simplified approach, we adapt it to power loss analysis, and derive a model for the lateral transport in SHJ cells.

Very recently, and during the redaction of this document, Haschke et al. proposed a model inspired by the two-layer TLM model of Huang et al. to account for power losses in SHJ cells [81]. They solved the problem for the case of generation in the bulk instead of current injected from the electrodes such as in TLM samples. This model is detailed in Appendix 4. The solution is however considerably more complicated than Huang's model and cannot be expressed analytically. We will use this model as a reference for our analysis.

In the following, we will derive a simple model for the modelling of the TLM case, using Huang's model as a basis. In a second time, we will use our approach and transpose it to the case of a power loss analysis, and compare it to Haschke's model.

7.1.1 Two-layer TLM with interface and contact resistances

In this section, we will propose and discuss a model for a 2-layer TLM model simpler than Huang's model, more easily transposable to a power loss analysis. Here we apply Huang's model in the hypothesis of no alloying such as described in §2.3.2. Let us consider a two-layer TLM sample representative of the front stack of an SHJ cell (Figure 119):

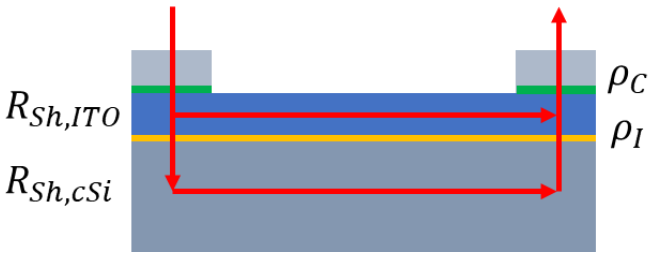

Figure 119: Simple representation of current flow in a two-layer TLM sample. Contact resistance is represented in green and interface resistance in yellow

Where ρ_C represents the Ag/TCO contact resistivity, and ρ_I the interface contact resistivity (either electron contact $\rho_C(e^-)$ or hole contact $\rho_C(h^+)$ depending on the studied structure), defined as:

$$\rho_C = R_{Sh,ITO} * {L_{t,C}}^2 \quad \text{Eq. 133}$$

$$\rho_I = R_{Sh,c\text{-}Si} * {L_{t,I}}^2 \quad \text{Eq. 134}$$

Where $L_{t,C}$ and $L_{t,I}$ are the transfer length of the Ag/TCO and interface contacts respectively.

Now, let us consider three borderline cases:

(1) In the case of infinite interface contact resistance, the system can be simplified to a one-layer TLM sample (see Figure 120 (1)). Thus it can be modeled as:

$$R_{tot} = 2 * \frac{\rho_C}{W L_{t,C}} * coth\left(\frac{L}{L_{t,C}}\right) + R_{Sh,ITO} * \frac{d}{W} \quad \text{Eq. 135}$$

(2) In the case of infinite sheet resistance of the ITO, the system is equivalent to a sample with etched ITO in between contacts (see Figure 120 (2)). Here we hypothesize that contact resistance can just be added, but considering a "short contact" approximation as current is already spread below the contact thanks to the interface. Thus it can be modeled as:

$$R_{tot} = 2 * \frac{\rho_I}{W L_{t,I}} * coth\left(\frac{L}{L_{t,I}}\right) + 2 * \frac{\rho_C}{WL} + R_{Sh,cSi} * \frac{d}{W} \quad \text{Eq. 136}$$

(3) In the case of no contact nor interface, our system simplifies to Figure 120 (3) and reads:

$$R_{tot} = \frac{R_{Sh,ITO} * R_{Sh,cSi}}{R_{Sh,ITO} + R_{Sh,cSi}} * \frac{d}{W} \quad \text{Eq. 137}$$

(1) (2) (3)

Figure 120: Representation of current flow in TLM structures representative of the borderline cases mentioned above

We propose a simple expression based on borderline cases (1) and (2) put in parallel such as:

$$R_{tot} = \left(\frac{1}{2 * \frac{\rho_C}{WL_{t,C}} * coth\left(\frac{L}{L_{t,C}}\right) + R_{Sh,ITO} * \frac{d}{W}} + \frac{1}{2 * \frac{\rho_I}{WL_{t,I}} * coth\left(\frac{L}{L_{t,I}}\right) + 2 * \frac{\rho_C}{WL} + R_{Sh,cSi} * \frac{d}{W}} \right)^{-1} \quad \text{Eq. 138}$$

Now we will apply numerically Huang's model in the different borderline cases and compare with our proposed equation of Eq. 138. We used as baseline values for the different parameters such as in Table 8 while R_{Shc-Si} was varied in between 1 and 1000 Ω/sq. All non specified parameters assume these baseline values. To compare results independently of electrode width (W), values of total resistance are displayed multiplied by W.

Table 8: Baseline parameters for the simulation

Electrode length	L	500µm
Spacing	d	200µm
Electron/hole contact resistivity	ρ_I	$100\ m\Omega.cm^2$
Metal/ITO contact resistivity	ρ_C	$1\ m\Omega.cm^2$
ITO sheet resistance	$R_{Sh,ITO}$	$200\ \Omega/sq$

- In the case of a very strong interface resistivity ($\rho_I = 10^5 \Omega.cm^2$), both Huang's model and the proposed model indeed tend towards a 1-layer TLM model (both models superpose to borderline case (1) in Figure 121).

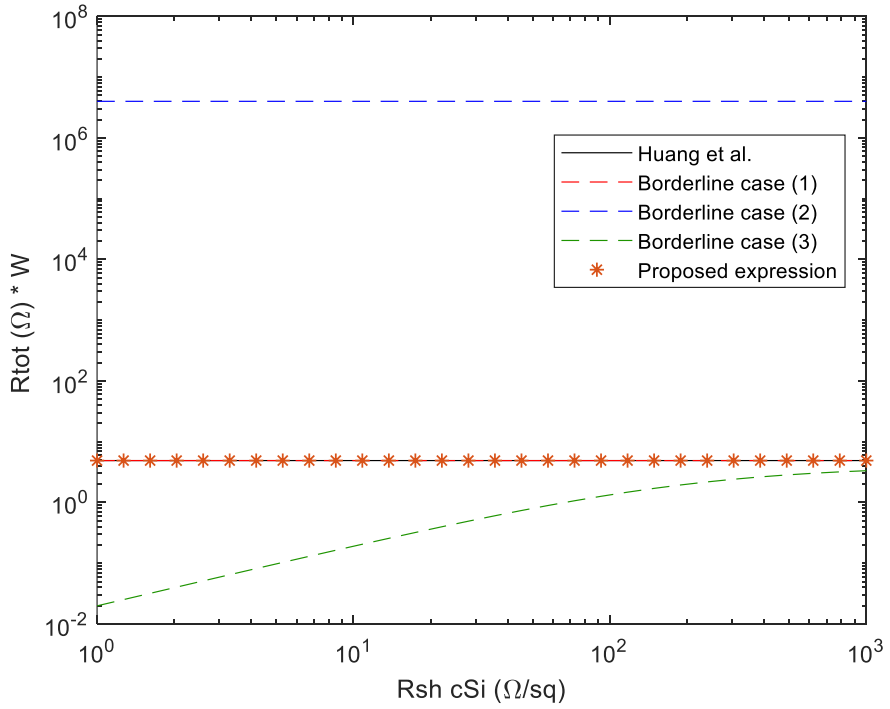

Figure 121: TLM simulation for the double layer model in the case $\rho_I = 10^5\ \Omega.cm^2$

- In the case of a very high sheet resistance of the TCO ($R_{Sh,ITO} = 10^6\ \Omega/sq$, both models also collapse to the borderline case (2) (both models superpose to borderline case (2) in Figure 122).

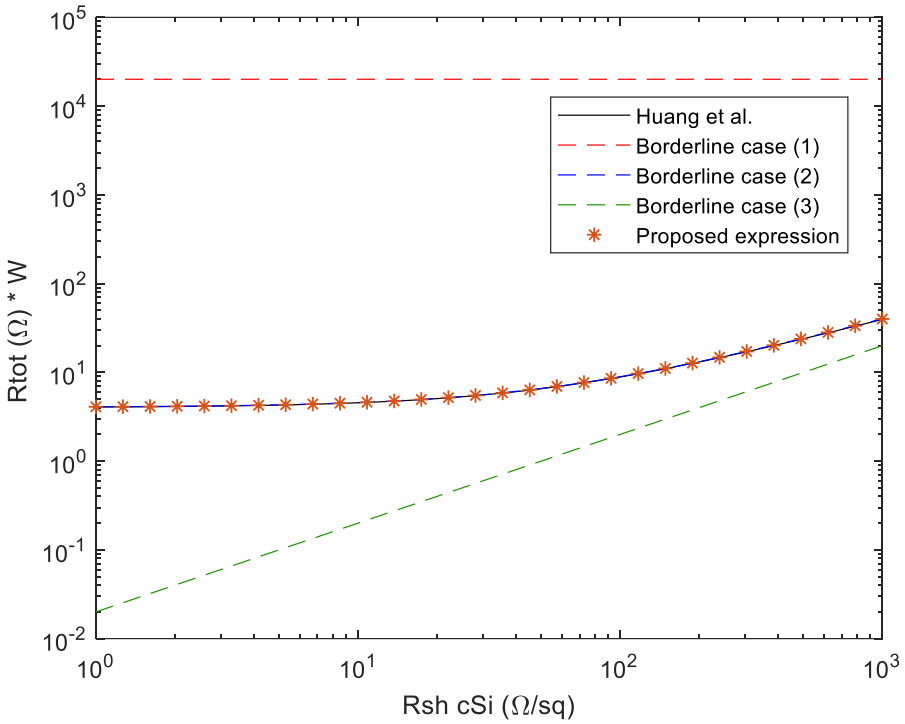

Figure 122: TLM simulation for the double layer model in the case $R_{Sh,ITO} = 10^6\ \Omega/sq$

- And finally, in the case of very weak contact and interface resistance ($\rho_C = \rho_I = 10^{-8}\Omega.cm^2$), again both models collapse to the borderline case (3) (both models superpose to borderline case (3) in Figure 123).

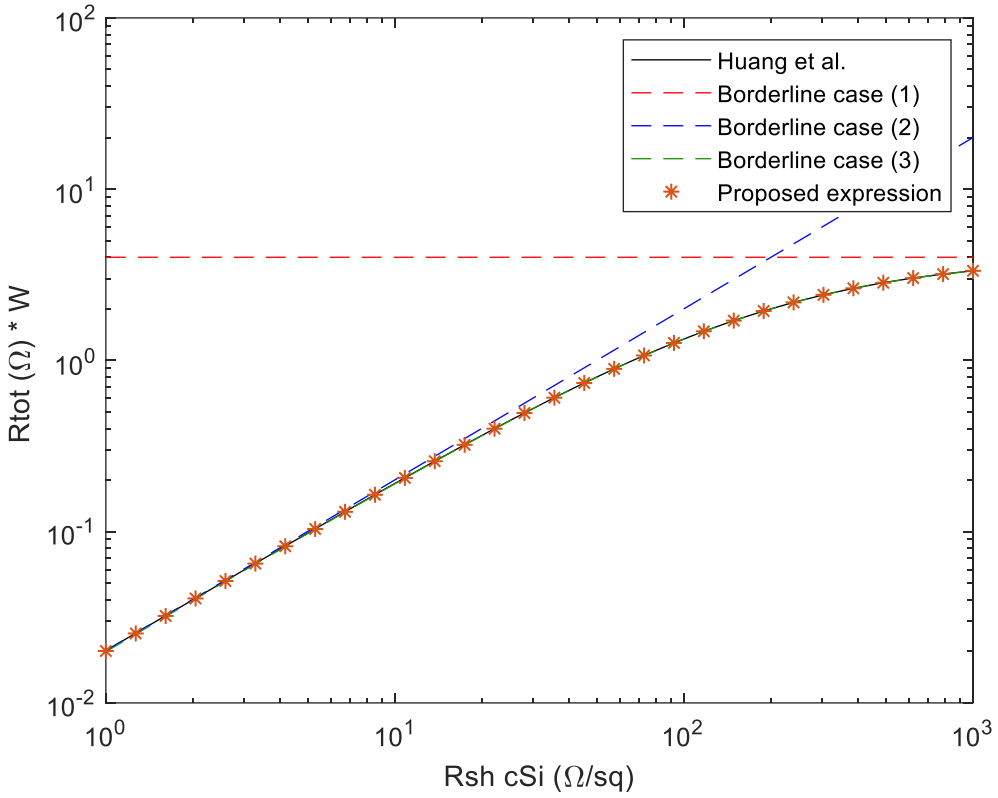

Figure 123: TLM simulation for the double layer model in the case $\rho_C = \rho_I = 10^{-8}\Omega.cm^2$

Now let us consider the case of realistic values. For each value of the variables reported in Table 9, the relative error with respect to Huang's model is always below 20%. The highest values of the error are obtained when all variables are at their minimal values except ρ_C which is at its maximal value. Usually in this thesis we obtained values of $\rho_C \leq 1m\Omega.cm^2$, excluding higher values makes the maximum error drop below 7.5%.

Table 9: Minimum and maximum values for each parameter tested

Variable	Min value	Max value
$\rho_I\ (\Omega.cm^2)$	1e-2	1
$\rho_C(\Omega.cm^2)$	1e-5	1e-2
$R_{Sh,cSi}(\Omega/sq)$	10	1000
$R_{Sh,ITO}(\Omega/sq)$	50	500

We conclude that the agreement between Huang's model and the proposed equation is satisfying for realistic values of each variable.

Earlier in § 4.1.2 experimental values were recorded as $\rho_C(e^-)$~$75\ m\Omega.cm^2$, $\rho_C(Ag/ITO) = 0.2\ m\Omega.cm^2$ and $R_{Sh,ITO} = 210\Omega/sq$. We used these values as inputs in Huang's model and the proposed model of Eq. 138, and compared them with experimental results measured on samples with no insulation (see § 4.1.2) corresponding to a 2-layer TLM with interface and contact resistances.

R_{tot} values measured and simulated for different c-Si sheet resistances are presented in Figure 124. Finger spacing is $d = 334\mu m$, corresponding to the smallest spacing used experimentally.

We conclude that the agreement between Huang's model and the proposed equation is satisfying for realistic values of each variable.

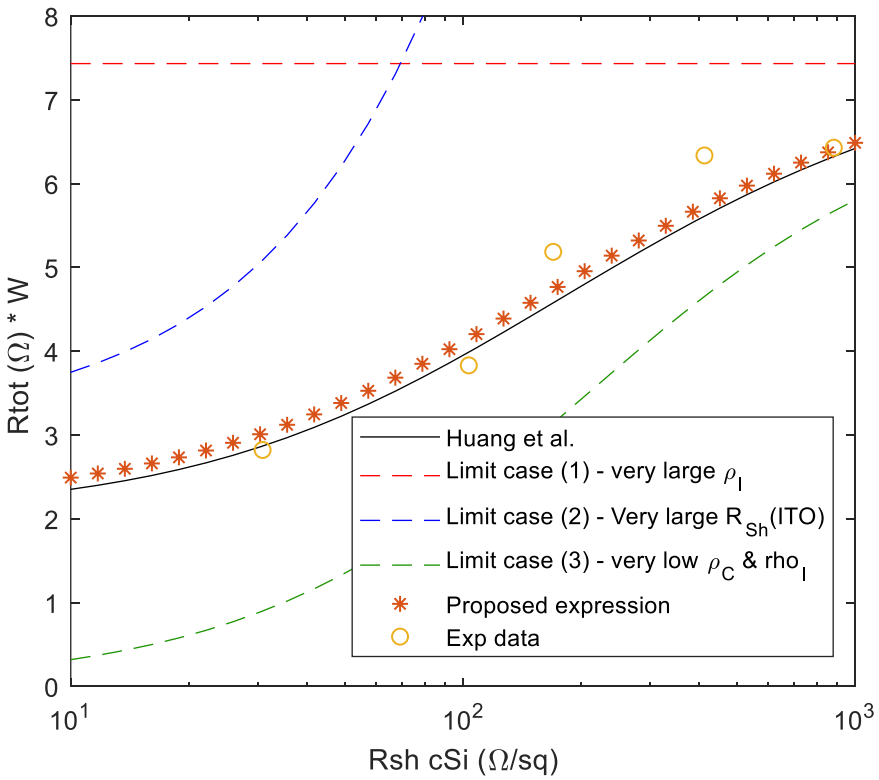

Figure 124: TLM simulation for the double layer model in the case of input values corresponding to experimental measurements. Also shown are experimental data on n-side ITO/Ag TLM samples from §4.1.2

We observe that all simulated values follow a similar trend: our model deviates slightly from Huang's over the whole range of data, but the dynamic of the curves matches very closely. Experimental data are coherent with the modelled trend, even though some deviation is observed, which can be attributed partly to experimental error on n-side ITO/Ag TLM samples. Nevertheless, note that the assumption here is that contact resistivity is constant with doping, which was not really observed for n-stack TLM samples in §5.1.3, which adds up uncertainty in the analysis.

7.1.2 Resistive power loss due to lateral transport

Based on the insights from the previous paragraph, we will reproduce the same approach but for a power loss analysis applicable to the front side of an SHJ cell, comparing Haschke's model with boundary conditions from the proposed model. Our structure is now represented by Figure 125.

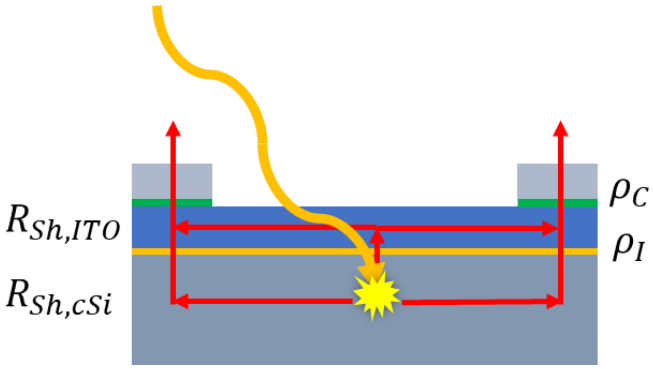

Figure 125: simple drawing of cross section of the front surface of an SHJ cell. Contact resistance is represented in green and interface resistance in yellow

Note that in order to get expressions as close to Haschke's paper we will use the full expressions demonstrated with the same hypothesis that they use, i.e. generation is homogeneous all over the cell even below the grid (see in Appendix 2 (f)). The expression for lateral transport with this hypothesis is:

$$R_S(lateral) = \frac{1}{12} * R_{Sh} * \frac{l_f}{lf + \frac{w_{bus}}{2}} * \frac{(p - w_f)^3}{p} \qquad \text{Eq. 139}$$

As Haschke's model does not involve busbars, we will just hypothesize that $\frac{l_f}{lf+\frac{w_{bus}}{2}} = 1$. Doing the same approximation on the expression of the contact yields:

$$R_S(contact) = \frac{1}{2}\frac{\rho_C}{L_t} * p * \coth\left(\frac{w_f}{2L_t}\right) \qquad \text{Eq. 140}$$

Also note that Haschke's model includes the effect of injection on $R_{Sh,c-Si}$, and interprets both electron and hole $R_{Sh,cSi}$ separately. Indeed, in a TLM configuration only majority carriers are considered, and they flow from one contact to the other. However, at the front surface of an n-type rear-emitter SHJ cell, electrons generated in the bulk are collected at the front electrodes, and only $R_{Sh,cSi(e^-)}$ is considered, as holes are collected at the rear and do not participate in front lateral transport (and oppositely, only holes matter at the rear side).

For these reasons, the borderline cases (represented in Figure 126) become:

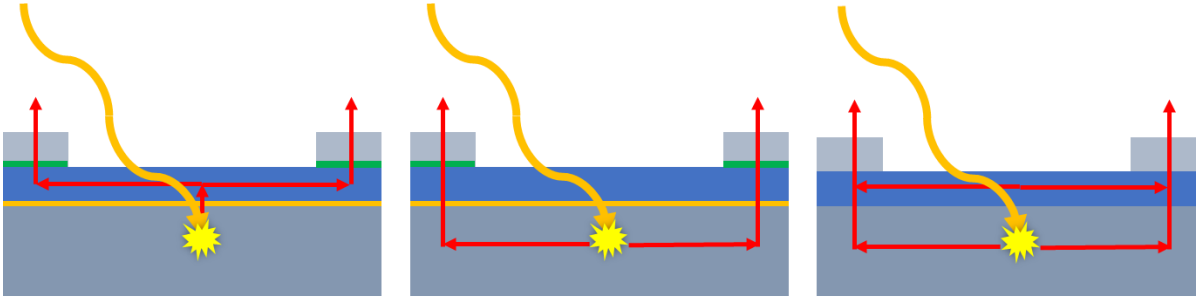

(1) (2) (3)

Figure 126: Borderline cases of Haschke's model

We will label the R_S part stemming from these contributions $R_{S_{front\ lateral}}$. The borderline cases are therefore the following:

(1) No lateral current in wafer (i.e. very resistive c-Si). The interface is crossed homogeneously all across the pitch. In this case the front lateral component of R_S reads:

$$R_{S_{front\ lateral}}(1) = \rho_I + \frac{1}{12} * R_{Sh,ITO} * \frac{(p - w_f)^3}{p} + \frac{1}{2}\rho_C * \frac{p}{L_t} * \coth\left(\frac{w_f}{2L_t}\right) \quad \text{Eq. 141}$$

(2) No lateral transport in ITO (i.e. very resistive ITO). We hypothesize that current at the metal/ITO contact is already spread thanks to the transfer length of the interface, therefore resulting in a short-contact approximation. Now the front lateral component of R_S reads:

$$R_{S_{front\ lateral}}(2) = \frac{1}{12} * R_{Sh,cSi(e^-)} * \frac{(p - w_f)^3}{p} + \frac{1}{2}\rho_I * \frac{p}{L_{t,I}} * \coth\left(\frac{w_f}{2L_{t,I}}\right) + \rho_C * \frac{p}{w_f} \quad \text{Eq. 142}$$

(3) No interface or contact resistivity (i.e. very low values of ρ_C and ρ_I).

$$R_{S_{front\ lateral}}(3) = \frac{1}{12} * \left(\frac{1}{R_{Sh,cSi(e^-)}} + \frac{1}{R_{Sh,ITO}}\right)^{-1} * \frac{(p - w_f)^3}{p} \quad \text{Eq. 143}$$

Note that this expression is very close to what we proposed in [166], but considering homogeneous photo-generation instead of generation only under non-shaded area.

Following the same approach than the previous paragraph, we propose a model of parallel connection of borderline conditions (1) and (2).

$$R_{S_{front\ lateral}}(4) = \left(\frac{1}{R_{S_{front\ lateral}}(1)} + \frac{1}{R_{S_{front\ lateral}}(2)}\right)^{-1} \quad \text{Eq. 144}$$

We label this model "Model 2".

We then proceed to test Haschke's model (see Appendix 4), Model 1 and Model 2 in boundary conditions. We use the baseline parameters from Table 10; all non-specified parameters assume these values. The doping density N_D is varied from 10^{13} to 10^{17} cm^{-3} (i.e. $\rho_{dark} = 440 - 0.09\Omega.cm$).

Table 10: Baseline parameters for the simulation

Finger width	w_f	50µm
Finger length	l_f	1.9cm
Pitch	p	1.8mm
Electron/hole contact resistivity	ρ_I	$100\ m\Omega.cm^2$
Metal/ITO contact resistivity	ρ_C	$1\ m\Omega.cm^2$
ITO sheet resistance	$R_{Sh,ITO}$	$200\ \Omega/sq$
Excess minority carrier density	$\Delta p\ (= \Delta n)$	$1 * 10^{15} cm^{-3}$

We calculate the resistivity of the c-Si using the mobility model from Klaassen et al. [163], [164] with the slight modifications mentioned in PVLighthouse [167]. We consider the bandgap

temperature variations from Thurmond et al. [168], the intrinsic concentration n_i and effective masses for electrons and holes from Couderc et al. [157], and hypothesize 100% ionization of the dopants.

- To reach borderline condition (1) both doping and injection level have to be very low in order to reach very high $R_{Sh,cSi(e^-)}$ and suppress lateral transport in c-Si, therefore Δn is fixed to 0 (this condition is representative of J_{SC} conditions and not MPP). In the left side of Figure 127, we can see that Haschke's model and both proposed models tend toward borderline case (1). For higher doping, model 2 predicts a higher R_S than Haschke's model, and model 1 lower R_S.

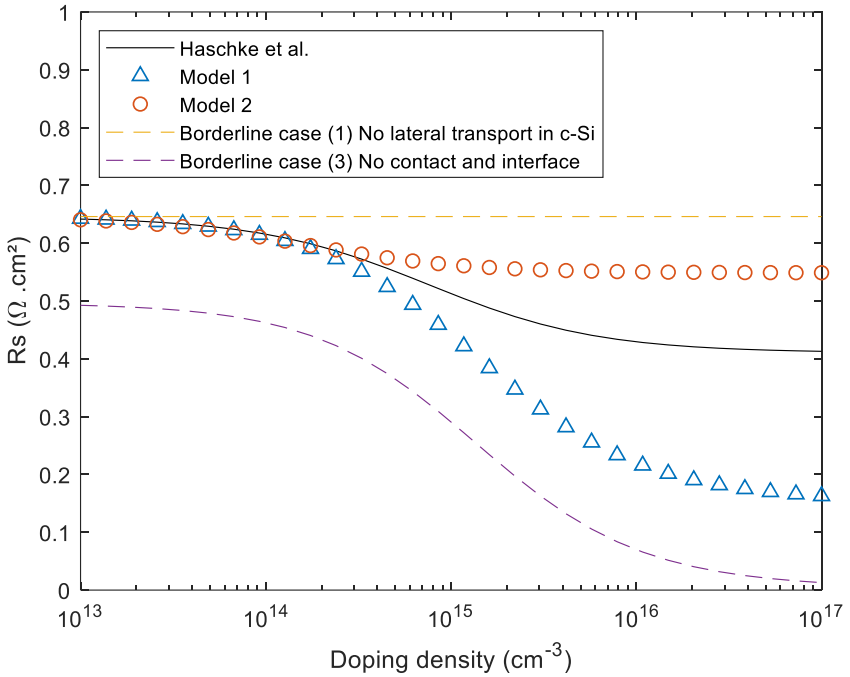

Figure 127: Series resistance as a function of doping density in borderline condition (1)

- To reach borderline condition (2), we set a very high (far from experimental) value of $R_{Sh,ITO} = 10^6\ \Omega/sq$ (see Figure 128). Again, Haschke's model predicts lower values than model 2, and higher values than model 1.

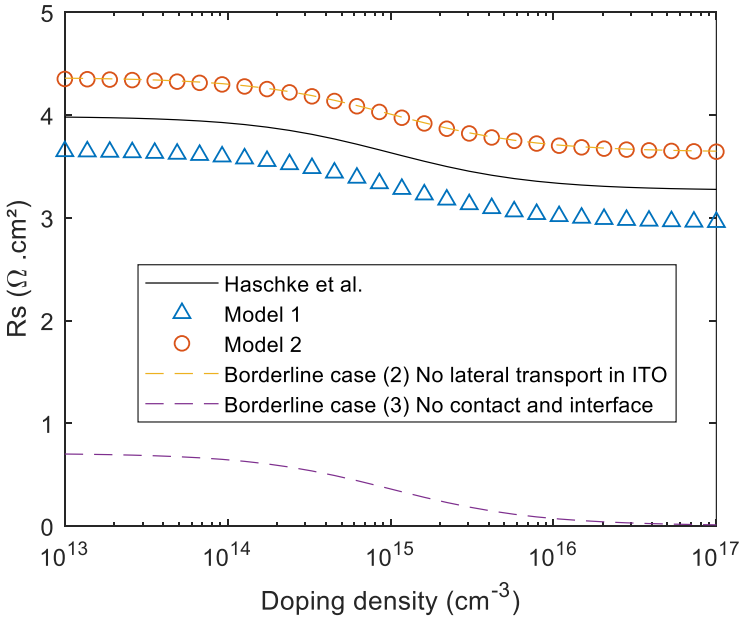

Figure 128: Series resistance as a function of doping density in borderline condition (2)

- To reach borderline case (3), ρ_I and ρ_C were set to $10^{-2} m\,\Omega.cm^2$. In this case, results from all models concur.

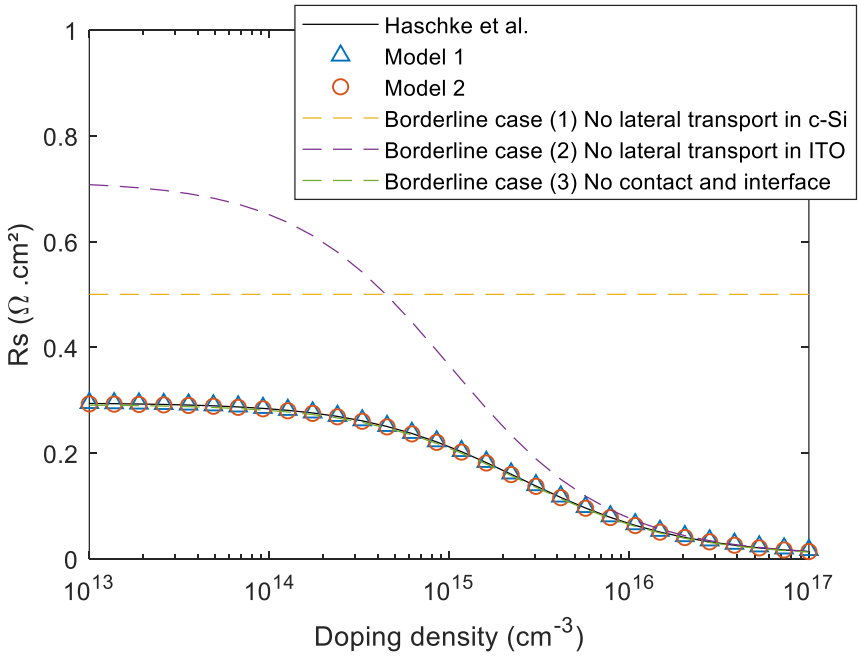

Figure 129: Series resistance as a function of doping density in borderline condition (3)

To conclude, we observe that Haschke's model gives equivalent or in between results when compared to that of the two models proposed in this document. Most of the difference comes from the current crowding effect below the contacts: model 1 and 2 make the assumption that current increases linearly from mid-pitch to the contact in both layers (see Appendix 2 (a)). However, in reality, current can transit to the ITO at the proximity of the contact, without being restrained to the contact size (such as in model 2) leading to non-linear current trends in each

layer. Using Haschke's model, it can be shown that this hypothesis is inaccurate in some cases. Figure 130 illustrates that the total current does evolve linearly from mid-pitch to the contact, but that the individual currents in ITO and c-Si do not. At the vicinity of the contact, a significant part of the current passes from the c-Si to the TCO to avoid current crowding below the electrode. With model 1, we consider a homogeneous current through ρ_I, which underestimates R_S, while model 2 exacerbates the impact of current crowding and leads to overestimate R_S[8].

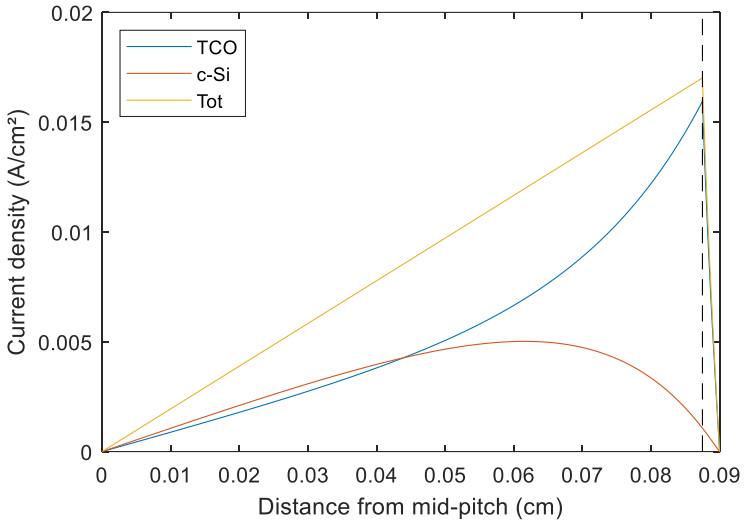

Figure 130: Current density from mid-pitch (left) to mid-electrode (right). The total and individual currents in each layer are displayed, as calculated using Haschke's model. The black dashed line represents the separation in between metallized and un-metallized regions. (baseline parameters from Table 10 are used)

Models 1 and 2 display similar trends, and capture part of the complexity of the lateral transport. Nevertheless, they fail in simulating the coupling between ρ_I and lateral transport in c-Si accurately contrary to the model of Haschke et al.

7.2 Comparison of the models with experimental data

In the previous section, we have discussed models (adapted to SHJ cells) assessing resistive power losses, taking into account interfaces, parallel lateral transport in c-Si and ITO, separate paths of electrons and holes, and the influence of carrier injection.

Now we will compare these models together with experimental results of series resistance obtained in the previous chapters.

To apply models for R_S assessment, we need numerous parameters:

- Metallization paste parameters: R_{line} obtained from electrical measurement between two busbars, and w_f obtained from microscope measurements.

[8] When ρ_I is non-negligible, $w_f/2L_{t,I}$ tends to become small, so that $\coth\left(\frac{w_f}{2L_{t,I}}\right) \rightarrow \frac{2L_{t,I}}{w_f}$: this makes the term $\frac{1}{2}\rho_I * \frac{p}{L_{t,I}} * \coth\left(\frac{w_f}{2L_{t,I}}\right)$ to be high, which makes the current favor the path through the ITO

- Grid geometry parameters: l_f and p known from the chosen screen print stencil or measured with microscopy.
- c-Si bulk parameters: $\rho_{dark}, t_{c\text{-}Si}$ measured with in-line contactless measurements
- ITO properties and contacts properties with the metallization: $R_{Sh,ITO}$ and $\rho_C(Ag/ITO)$ obtained from TLM measurements
- Electron and hole contact properties: $\rho_C(e^-)$ and $\rho_C(h^+)$ obtained from TLM measurements
- Passivation properties: Δn_{MPP} can be obtained from Eq. 110 at $V = V_{MPP}$. Note that if no J-V data are available, we can instead use the implied MPP voltage, iV_{MPP} (obtained by PCD measurement), or the pseudo MPP voltage, pV_{MPP} (obtained by Suns-Voc measurements), but this will tend to overestimate the injection level as series resistance affects the MPP.

From these we can calculate the different contributions of R_S:

- Contributions from grid lines and busbars are calculated with Eq. 53 and Eq. 54
- The contribution from transverse resistance in c-Si is calculated considering the injection level at MPP ($R_{Sh,c\text{-}Si}(MPP)$) using Eq. 55
- Contributions from the lateral transport at the front and rear side and through the interfaces and the metal/TCO contact of the cell are calculated using the three different approaches discussed:
    - Model 1 (simple model presented in §7.1.1 [166])
    - Model 2 (proposed model with parallel current paths in ITO and c-Si (see §7.1.2))
    - Haschke et al.'s model.

We have presented in the previous chapter most of these measurements over several data sets and allowing us to assess the expected trends in R_S and to compare it to the experimental measurements. All measured electrical quantities are regrouped in Table 11 (average of the measurements).

As our studies were more focused on the front side of the cell, we did not systematically evaluate the hole contact, nor the rear ITO sheet resistance and its contact with the rear metallization grid. In the following we will assume that for all the batches we have $R_{Sh}(ITO_{rear}) = 200\ \Omega/sq$ (assumed), $\rho_C(h^+) = 290\ m\Omega.cm^2$ (from values presented in §4.2.2), and $\rho_C(Ag/ITO_{rear}) = 0.2\ m\Omega.cm^2$ (assumed equal to the front Ag/ITO contact for $t_{ITO} = 100nm$ from §5.3.1).

Note that the electron and hole contact resistivities are considered as measured in the dark.

The metallization design is for all cases 5-busbars (BB5), with a finger width $w_f = 57\mu m$ and length $l_f = 1.52cm$ identical for the front and rear grids, the pitch at the front and rear is respectively $p_f = 2.1mm$ and $p_r = 0.6mm$.

Table 11: Model input values (all quantities determined from electrical measurements in previous chapters)

c-Si doping study							
N_D	$\rho_C(Ag/ITO_{front})$	$\rho_C(e^-)$	$R_{Sh}(ITO_{front})$	$\rho_{C\text{-}Si}$	V_{MPP}	$R_{line,front}$	$R_{line,rear}$
cm^{-3}	$m\Omega.cm^2$	$m\Omega.cm^2$	Ω/sq	$\Omega.cm$	mV	Ω/cm	Ω/cm
$1.08*10^{16}$	0.11	81	210	0.49	619	1.12	0.78
$2.88*10^{15}$		63		1.66	621		
$1.72*10^{15}$		66		2.72	615		
$6.89*10^{14}$		82		6.61	620		
$3.18*10^{14}$		92		14.12	620		
ITO thickness study							
t_{ITO}	$\rho_C(Ag/ITO_{front})$	$\rho_C(e^-)$	$R_{Sh}(ITO_{front})$	$\rho_{C\text{-}Si}$	V_{MPP}	$R_{line,front}$	$R_{line,rear}$
nm	$m\Omega.cm^2$	$m\Omega.cm^2$	Ω/sq	$\Omega.cm$	mV	Ω/cm	Ω/cm
34.1	1.27	53	274	1.23	606	1.04	1.02
69.4	0.33	49	230		620		
98.1	0.18	55	173		627		
152.8	0.15	87	154		623		
a-Si :H(i) thickness study							
$t_{a-Si:H(i)}$	$\rho_C(Ag/ITO_{front})$	$\rho_C(e^-)$	$R_{Sh}(ITO_{front})$	$\rho_{C\text{-}Si}$	V_{MPP}	$R_{line,front}$	$R_{line,rear}$
nm	$m\Omega.cm^2$	$m\Omega.cm^2$	Ω/sq	$\Omega.cm$	mV	Ω/cm	Ω/cm
0	0.18	42	173	1.23	598	1.04	1.02
1.9		53			624		
3.2		55			627		
4.9		65			629		
8.7		67			631		
a-Si :H(n) thickness study							
$t_{a-Si:H(n)}$	$\rho_C(Ag/ITO_{front})$	$\rho_C(e^-)$	$R_{Sh}(ITO_{front})$	$\rho_{C\text{-}Si}$	V_{MPP}	$R_{line,front}$	$R_{line,rear}$
nm	$m\Omega.cm^2$	$m\Omega.cm^2$	Ω/sq	$\Omega.cm$	mV	Ω/cm	Ω/cm
2.9	0.18	131	173	1.23	605	1.04	1.02
5.3		55			627		
7.6		66			622		
13.9		87			624		

Figure 131 illustrates all experimental R_S data obtained from Chapter 5, fitted with the three proposed methods using all data presented.

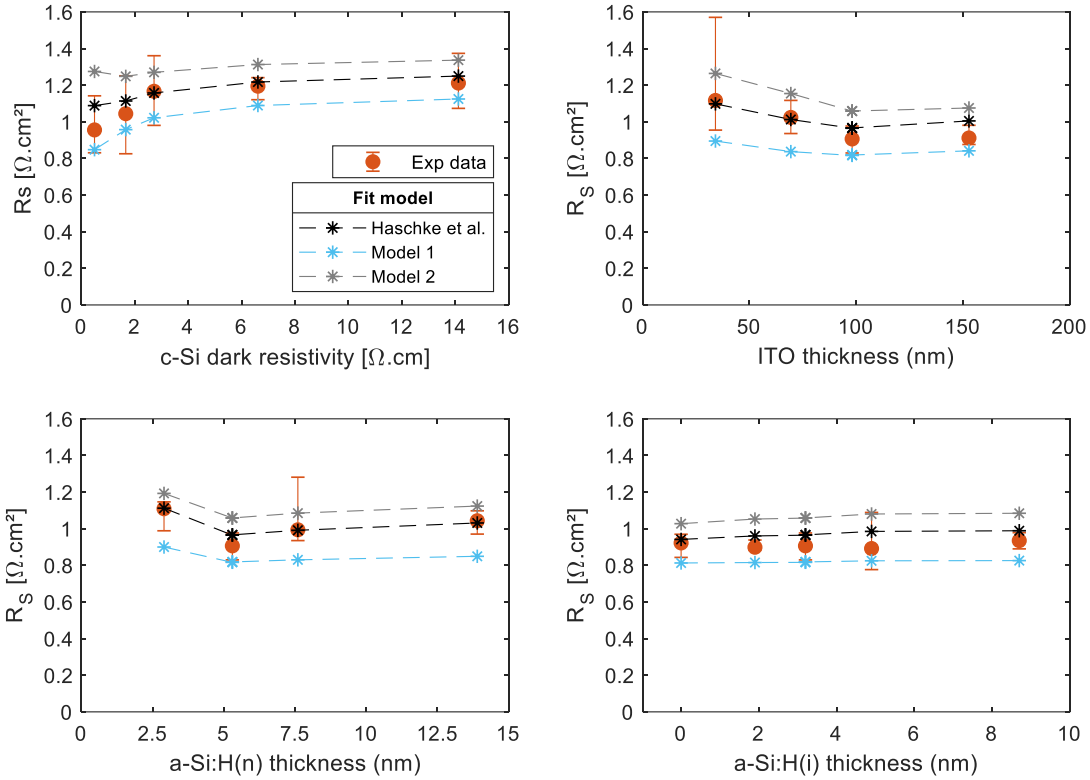

Figure 131: Experimental and fitted data of R_S for different conditions. Dots represent the median value of R_S determined for the condition, and error bars the first and third quartiles

First of all, we observe a very good quantitative agreement of R_S between experimental values and predicted with Haschke's model: for all batches, the value calculated with Haschke's model is within the uncertainty of the R_S measurement (pFF-FF method), or less than $0.01\Omega.cm^2$ appart. Model 2 systematically predicts R_S values higher than Haschke's model, and oppositely the model 1 predicts lower values. All three models show similar trends, indicating that the proposed and simple models are helpful to give qualitative insight on R_S. Additionally, this confirms the interplay in between the passivation and the resistive losses. It also tends to show that the contact resistivity determined in the dark is close to its value in a working device, as everything matches to a good extent without taking the effect of injection on $\rho_C(e^-)$ and $\rho_C(h^+)$ into account.

To examine the effect of the uncertainty in the input parameter on the simulated R_S, we studied in more depth the samples from the varying c-Si resistivity study. We included the determined experimental error as upper and lower bound in the modelling for the following parameters: V_{MPP}, R_{line} (front and rear), $R_{Sh}(ITO)$ (front and rear), $\rho_C(Ag/ITO)$ (front and rear), $\rho_C(e^-)$ and $\rho_C(h^+)$.

For V_{MPP}, R_{line}, $\rho_C(Ag/ITO)$ and $R_{Sh}(ITO)$ values, we use the standard deviation over the data sets as values for the uncertainty. We get $\sigma R_{line,front} = 0.08\Omega/cm$, $\sigma R_{line,rear} = 0.03\Omega/cm$, $\sigma V_{MPP} = 3$ to $8mV$ depending on the condition, $\sigma\rho_C(Ag/ITO) = 0.03m\Omega.cm^2$, $\sigma R_{Sh}(ITO) = 16\Omega/sq$. For $\rho_C(e^-)$ and $\rho_C(h^+)$ we lack statistics so we calculate the systematic error (§3.8.1.1), with geometry and resistance systematic errors as evaluated in §3.8.1.3. We find, $\delta\rho_C(e^-) =$ 13 to 20 $m\Omega.cm^2$ and $\delta\rho_C(h^+) = 28m\Omega.cm^2$.

First, we evaluate the effect of uncertainty on $\rho_C(e^-)$ alone (case (a) in Figure 132), and then on all parameters (case (b) in Figure 132).

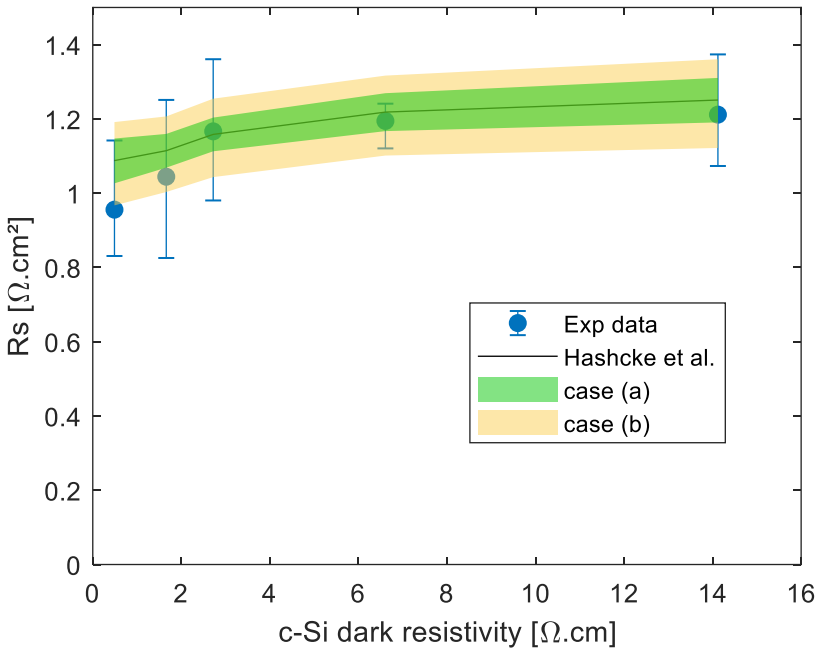

Figure 132: Series resistance Sensitivity to uncertainty of Haschke's model

We observe that the error in the input parameters can be important, for instance considering only the error on $\rho_C(e^-)$, R_S can vary on an approximately $0.1\Omega.cm^2$ range, but we mostly stay within the uncertainty range of the experimental R_S measurement.

7.3 Resistive loss breakdown for a standard CEA SHJ cell

Since Haschke's model closely fits our experimental results, we detail the previous analysis with this model for the condition $t_{ITO} = 98.1nm$ (from the study in §5.3.1). For parameters of the simulation refer to the last section and to Table 11.

For this cell BB5 cell with 22.3% efficiency, we measured $R_S = 0.91 \pm 0.07\ \Omega.cm^2$. The simulation yields $R_S = 0.96\ \Omega.cm^2$, which fits accurately. In Figure 133, we display the different calculated contributions of R_S.

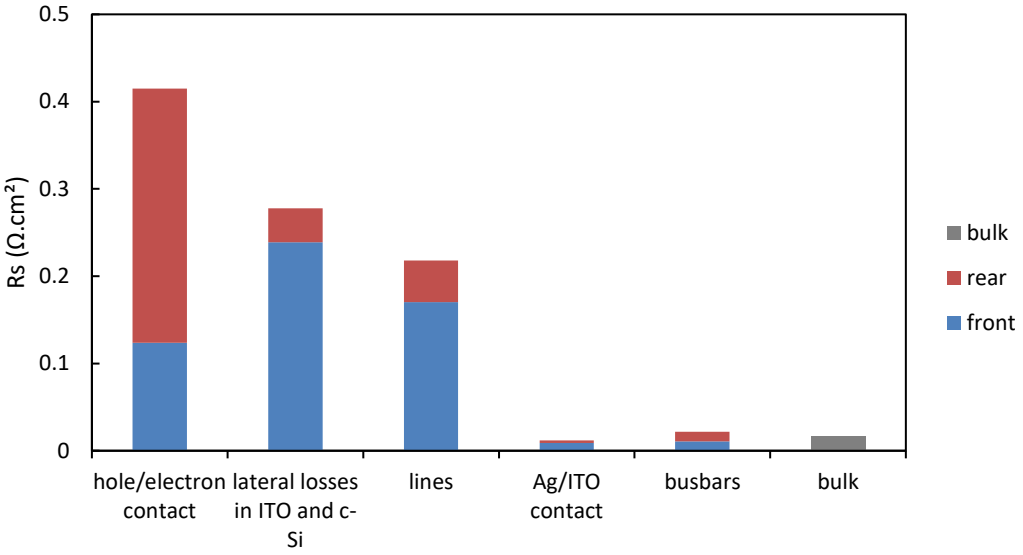

Figure 133: Breakdown of the Rs contributions for the studied cell

These values can be transformed into a cost in FF due to R_S, $\Delta FF(R_S)$, rewriting Eq. 30 such as:

$$\Delta FF(R_S) = R_S * \frac{J_{MPP}^2}{V_{OC}J_{SC}} \qquad \text{Eq. 145}$$

In BB5 cells from the CEA Labfab, R_S costs 4.4%abs. FF. The more limiting contribution are the electron and hole contacts, which together account for approximately 0.41 $\Omega.cm^2$ (-1.9% abs. FF). The second most important contribution is the lateral losses in the ITO and c-Si (~0.28 $\Omega.cm^2$ or -1.3% abs. FF). Third, metallization lines account for 0.22 $\Omega.cm^2$ (-1.0% abs. FF).

At the rear surface, the metallization used in this example is very dense, which mitigates lateral transport losses in the bulk, ITO and lines. However, the hole contact is very resistive and is responsible for the highest contribution to R_S. At the front side, the low c-Si resistivity, further decreased under illumination, coupled to a low $\rho_C(e^-)$ enables a strong lateral transport in the bulk. This alleviates lateral losses that could be high due to the large front pitch. Contributions from the Ag/ITO contact, busbars and bulk transverse transport account for a low percentage of the total.

To lower R_S in such devices, interface engineering is required at both contacts. More conductive front TCOs would also slightly increase lateral transport, and reduce the impact of the electron contact by lowering current spreading at the contacts. Finally, more conductive metallization pastes could non-negligibly decrease R_S.

7.4 Impact of the electron and hole contacts on R_S

In this section, we address the different effect that the electron and hole contacts have on R_S values of n-type rear emitter SHJ cells.

To illustrate the impact of $\rho_C(e^-)$, we performed a simulation using Haschke's model with the standard parameters for the front lateral transport: $R_{Sh}(ITO) = 200\Omega/sq$, $\rho_{c\text{-}Si} = 1\Omega.cm$, $t_{c\text{-}Si} = 160\mu m$, $\Delta p_{MPP} = 10^{15}cm^{-3}$, $w_f = 50\mu m$, $p = 1.8mm$, $\rho_C(Ag/ITO) = 1m\Omega.cm^2$ (Figure 134).

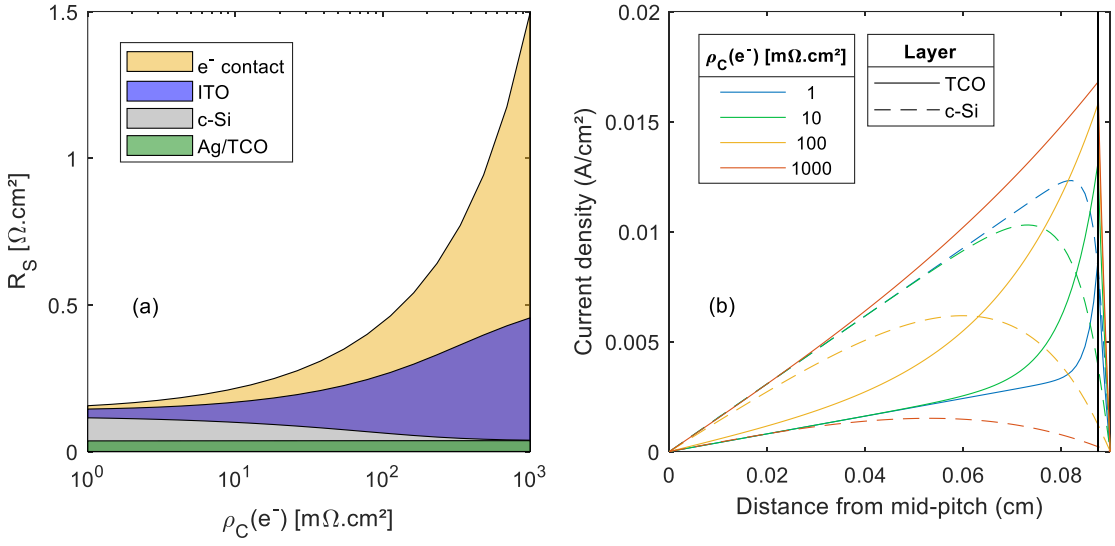

Figure 134: (a) Contribution to series resistance from the front lateral transport as a function of electron contact resistivity (b) front lateral current density in ITO and c-Si and through the electron and Ag/ITO contacts as a function of the electron contact resistivity

We observe in Figure 134 (b) that as electron contact resistivity increases, the current is increasingly shifted from the c-Si to the ITO. Figure 134 (a) illustrates that an increase of $\rho_C(e^-)$ not only leads to higher losses at the contact, but also to higher losses in the ITO, as transport in c-Si is progressively disabled. Overall, excluding the direct impact of the electron contact (yellow area), R_S still increases from approximately 0.15 to 0.46 $\Omega.cm^2$ over the studied range of $\rho_C(e^-)$. This illustrates why reducing the electron contact resistivity is critical to decrease R_S.

We performed a similar simulation at the rear surface, with a denser metallization grid (p=0.6mm) (Figure 135).

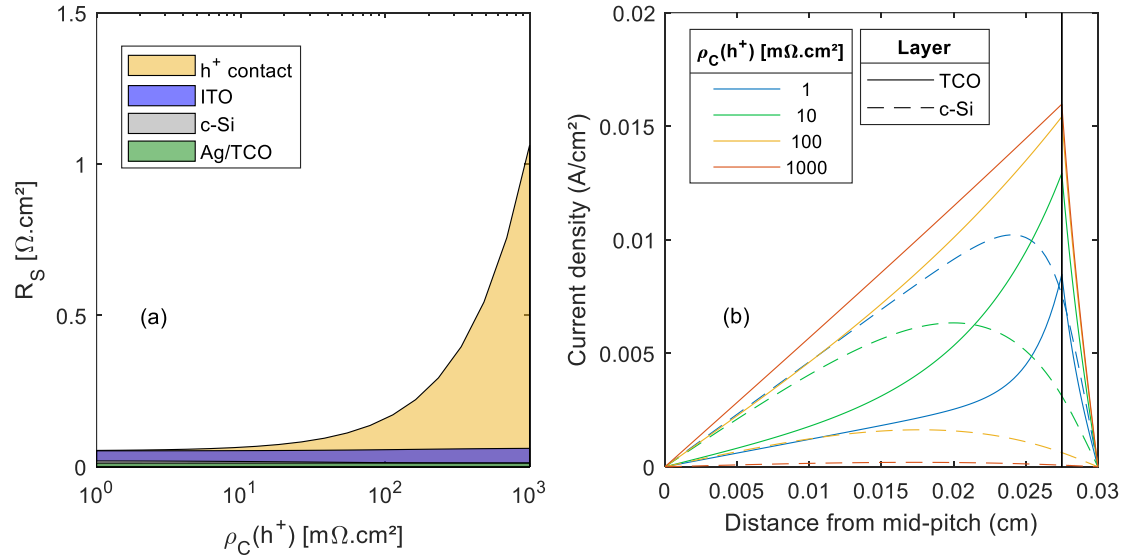

Figure 135: (a) Contribution to series resistance from the rear lateral transport as a function of electron contact resistivity (b) rear lateral current density in ITO and c-Si and through the hole and Ag/ITO contacts as a function of the hole contact resistivity

We observe that for the same ITO and contact properties, lateral losses are lower at the rear than at the front. Due to the small pitch, the lateral losses in ITO and c-Si are reduced, and with high metal coverage, the Ag/ITO contact is less limiting. Despite this, losses are still quite high when $\rho_C(h^+)$ is substantial. Because the c-Si hole mobility is low, and conductivity only relies on photo-generated holes, the ITO and c-Si layers are not efficiently coupled, and $\rho_C(h^+)$ is very critical.

7.5 Chapter outlook

In this chapter we have described the approach undertaken to derive a simple model for the lateral transport in parallel in c-Si and ITO, and through the interfaces and the Ag/ITO contact. We compared this model ('model2') to a simpler model from previous work ('model 1') [166] and to the newly published model from Haschke et al. [81]. We found that theoretically, Haschke's model is superior as it takes into account more accurately the coupling between the c-Si and ITO than both our models. However, model 1 and 2 represent respectively lower and upper bound of R_S, as model 1 underestimates the impact of $\rho_C(e^-)$ and model 2 overestimates current crowding effects. We confronted these models to experimental R_S values from Chapter 5, and found that we best reproduce the experimental R_S values with Hashcke's model, with a very close quantitative values and trends for the different experimental conditions. We therefore consider the methodology developed within this thesis as a good approach to determine R_S and its different components for SHJ devices.

Additionally, we broke down the series resistance contributions for a 22.3% (BB5) SHJ cell produced at the CEA pilot line, and identified its main contributions: hole contact (30% of R_S), front lateral transport in c-Si and ITO (25%), front metallization lines (18%) and electron contact (13%).

Finally, we discussed the impact of electron and hole contact resistivities, and possible gains in R_S by reducing them. A decrease in $\rho_C(e^-)$ not only decreases losses in the contact, but also allows a more efficient coupling of the c-Si and front ITO. A decrease in $\rho_C(h^+)$ almost only reduces losses in the contact because the c-Si and rear ITO are not efficiently coupled, but is nevertheless critical as it is the first source of losses in the cell.

It appears critical to optimize the a-Si:H/ITO/Ag stacks contact properties to obtain lower R_S values, or to develop new heterojunction schemes that would present improved contact properties (higher conductivities, and/or lower energy barriers for electrons and holes).

When a mature TLM technique will allow measuring electron and hole contacts under illumination, the effect of injection level on the electron and hole contacts should also be added to the model to better represent conditions of 1Sun illumination and maximum power point.

Coupling this resistive model with an optical one and including as well recombination losses models would allow the full simulation of J-V curves, and could allow performing e.g. metal grid optimizations, with regard to parameters that influence Haschke's model (i.e. c-Si dark resistivity, injection level, electron and hole contact resistivities).

General conclusion and perspectives

Conclusions

In Chapter 1, we have seen that the photovoltaic energy is an important resource to tackle the complex problem of the decarbonization of the electricity production. Subsequently, we discussed the operating principles of solar cells and the main factors limiting their efficiency. Then we discussed the technologies currently dominating the PV market, the emerging structures based on the passivating contact designs, and introduced the silicon heterojunction technology. Finally, we introduced the objectives of this work: characterize, model and improve the current transport in SHJ cells in order to limit resistive losses in such devices, focusing on the transport through the electron and hole contact stacks.

Chapter 2 was dedicated to the analysis of the state-of-the-art. We addressed the SHJ cell technology, characterization methods for the measurement of series resistance and contact resistance, power loss analysis, and the charge carrier transport in SHJ cells. The SHJ cell employs passivating contacts to passivate the crystalline silicon absorber. At both sides, it is composed of bilayers of undoped and doped hydrogenated amorphous silicon layers, on top of which a transparent conductive oxide layer is deposited, and over which silver pastes are screen-printed to form the metallization grid. It therefore features electron and hole contacts composed of c-Si/a-Si:H(i)/a-Si:H(n,p)/TCO/Ag stacks. Methods for measuring the Ag/TCO as well as electron and hole contact resistivity were reviewed, and the latter were identified as important source of resistive losses in SHJ cells [58], [91], [107]. Furthermore, the details of the transport through these contact stacks is still not completely understood [82], [103]. Additionally, classical models for the resistive power losses were discussed to be non-adapted to SHJ cells devices notably because they do not account for losses through the electron and hole stacks but also because it neglects lateral transport in the c-Si absorber.

In Chapter 3, we described the process of fabrication of the samples, then reviewed the different means of characterization used in the frame of this work, and detailed simulation parameters for TCAD modelling of SHJ devices. We also reported the precautions that have been taken in this work regarding the measurement of contact resistivity with the transfer length method to avoid a certain amount of bias it commonly encounters. We found that to obtain meaningful results we needed to cut the edges of the samples, have sufficiently conducting electrodes (such as screen-printed electrodes), use the complete TLM formula and avoid using too low electrode spacing when studying thick layers. We also showed that uncertainties need to be minimized to realize precise measurements, notably the geometry of the sample needs to be measured and not assumed, and spacing should be selected wisely in order to balance the signal to noise ratio.

In Chapter 4, we first compared different approaches for the measurement of silver to TCO contact resistance with the TLM method. We concluded that the use of the a-Si:H(p) to insulate the TCO from the c-Si(n) substrate (p-side ITO/Ag TLM samples) was the best method, and concluded on values of the Ag/ITO contact of $0.11 \pm 0.03\ m\Omega.cm^2$. We also found that the TLM method is more accurate than the 4PP method to measure the sheet resistance of the TCO, as the metal electrodes provide the TCO a physical protection from the electric probes which can pierce the layer or create stress-induce leakage affecting the measurement. We find for the studied ITO a sheet resistance of $210\Omega/sq$. Secondly, we developed an approach for the fabrication of test vehicles representative of the SHJ structure (i.e. including thermal budget and all SHJ cells layers) to measure the electron and hole contact resistivity, while not degrading the passivation of the samples (n or p-stack TLM samples). We used a patterning approach with the help of inkjet printing of an hot-melt resist and wet etching to selectively remove the ITO in between but not under the electrodes of TLM samples. We showed that with the use of HCl we could remove a standard ITO in about 6 minutes, while keeping the passivation unharmed. We could subsequently etch away the hot-melt resist using a KOH solution, but it was shown to be extremely detrimental to a-Si:H(n) and a-Si:H(i) layers, while keeping the a-Si:H(p) layers unharmed. Nevertheless, we developed a KOH-free approach that demonstrated a complete removal of the hot-melt without significant degradation of the passivation. Finally, we demonstrated that we could determine electron and hole contact resistivity from these test vehicles with screen-printed metal pads.

In Chapter 5, we studied the impact of variations in the fabrication process of SHJ cells on the SHJ cells efficiency, while focusing on the series resistance and on the characterization of the electron contact using the approach developed in Chapter 4. First, we observed that the c-Si absorber resistivity influence relatively little the efficiency, but that cells using low resistivity wafers showed improved FF but degraded V_{OC} and J_{SC} compared to when using higher resistivity wafers. We found that the R_S increased with absorber dark resistivity, but we observed a saturation effect for resistivities above 2.72 $\Omega.cm$. We attributed this to the carrier injection level reached under operating conditions for well passivated devices, were the c-Si resistivity becomes almost independent of its doping. Furthermore, we studied the influence of the thickness of the layers composing the electron contact. We found that over some range of thicknesses for both the (i) and (n) a-Si:H layers, there is a near linear increase of the electron contact resistivity which was found to agree with a resistivity of the both layers in the order of

$10^4 \Omega.cm$. We conclude that this likely indicates that the electron contact is greatly influenced by the bulk transport in a-Si:H layers, in addition to interface phenomena. This may account for approximately half of the determined electron contact resistivity in the studied samples.

In Chapter 6, we focused on the Ag/ITO and the electron and hole contacts as a function of illumination and temperature. Because solar cells operate under illumination, measuring contact resistance in these conditions could be important. Varying the temperature allowed investigating on the charge carrier transport phenomena. We first saw that the Ag/ITO features a temperature dependence, which shows that thermally activated transport phenomena are at play, even though the metal/semiconductor theory indicates that it should operate under a pure tunneling regime. We also found that studying this contact under illumination with the structures discussed in Chapter 4 (p-side ITO/Ag or thick-(i) ITO/Ag TLM samples) does not allow a valid measurement, as the ITO layer is not completely electrically insulated from the underlying c-Si substrate under these conditions. Secondly, we addressed the electron and hole contacts. Using n and p-stack TLM samples we are able to measure the resistivity of the c-Si substrates as a function of the temperature matching very closely the theoretical trend, giving confidence in our measurement. We also showed that with temperature, both electron and hole contact resistivity decreases, and extracted activation energies of these contacts of respectively $0.11eV$ and $0.24eV$. We also found that the electron contact activation energy depends on the resistivity of the c-Si substrate, and varies from 0.08 to $0.15eV$ over the studied range of c-Si doping level. We discussed these values regarding several transport phenomena. For the electron contact the activation energy best fits a thermionic field emission regime over the c-Si/a-Si:H interface with a weak tunneling component. For the hole contact, we showed that the trap-assisted tunneling at the a-Si:H(p)/ITO cannot explain such a low value of activation energy, and a more probable explanation is thermionic field emission regime over the c-Si/a-Si:H interface with a strong tunneling component. Regarding the behavior under illumination, we concluded that it is best to use rear side illumination, in order to avoid parasitic shadowing that induces inhomogeneities of excess carrier density over the sample and bias the TLM measurement. Similarly, a homogeneous passivation is required, and local inhomogeneities bias the measurement. We demonstrated with both experimental and simulation approaches that illumination is susceptible to impact strongly the value of contact resistivity, especially if using high resistivity wafers.

In Chapter 7, we discussed the adaption of classical models to power loss analysis for SHJ solar cells. To address that, it needs to take into account parallel lateral transport in the c-Si and ITO layers, as well as the impact of electron and contact stacks. We derived two models: model 1 takes into account lateral transport in c-Si and ITO in a simple manner and considers homogeneous current through the interfaces. Model 2 considers two paths for the generated current either through the bulk where current then crowds below the contacts, or homogenous current through the c-Si then transport in the ITO towards the contacts. We compared them to the recently proposed model of Haschke et al. [81] and to the experimental results obtained in Chapter 5, and found that the model of Haschke et al. best reproduces our experimental results. Nevertheless, both our proposed models are helpful approximations: model 1 represents a lower bound of R_S as it underestimates the impact of the electron contact, while model 2 represents a higher bound as it overestimates the impact of current crowding below

the electron and hole contacts. Using Haschke's model, we could breakdown the resistive losses in a BB5 cell taken from the study in §5.3.1, and found that R_S costs approximately 4.4%abs. FF with respect to the pFF, with the main contribution coming from the electron and hole contacts resistivity (-1.9%) and from lateral transport in the ITO and c-Si (-1.3%). Finally, we discussed the different impacts of the electron and hole contact resistivity in n-type rear emitter SHJ cells: at the front surface the electron contact resistivity impacts directly R_S but also enables lateral transport in c-Si when ρ_C is low, while at the rear the hole contact mainly impacts directly R_S as the conduction in the c-Si is less important due to the low hole mobility in c-Si.

Perspectives

This work opens up many perspectives. The fabrication process of TLM samples for the evaluation of electron and hole samples should be further optimized, notably the edge cutting process, in order to obtain samples with more homogeneous passivation qualities that would be appropriate for measurement under illumination. To study the hole contact under illumination, p-stack TLM samples should be fabricated using high bulk lifetime wafers, to reach similar passivation properties as currently obtained with the n-type wafers used for SHJ fabrication. Additionally, the fabrication process could be simplified to allow for a more systematic characterization of the electron and hole contacts. Optimizing a masking process to obtain much sharper ITO edges would avoid the use of patterning methods. Beyond that, different techniques and their corresponding test structures could be investigated, such as those proposed by Cox and Strack [169], or close variations recently proposed (e.g. [135]). However, the latter could not be used under illumination due to the sample design.

Regarding the electron contact, there are plenty of possible optimizations. For instance it could be interesting to study the effect of the doping density of the doped a-Si:H layers on contact properties, or to compare alternative materials to the a-Si:H layers. The latter topic is presently extensively studied, notably nanocrystalline or microcrystalline silicon thin layers [102], or less conventional new contact materials (e.g. transition metal oxides such as MoOx [170] or organic materials such as PEDOT:PSS [171]. Nevertheless, we already obtain quite low electron contact resistivity values with the current SHJ structure developed at CEA. As for the hole contact, the contact resistivity of the rear stack is still too high (>$200 m\Omega.cm^2$), and represents the major source of resistive losses. Values as low as $100 m\Omega.cm^2$ were obtained in the literature [133] which shows that there is still some room for improvement. Therefore, this contact should be investigated in more depth in the future.

Another important perspective is to further examine the transport mechanisms in heterojunctions to model the electron and hole contacts more comprehensively, and realize insightful interface engineering. To this end, the activation energy of the contacts is an interesting metric. Therefore doing more TLM measurement under varying temperature for samples of various fabrication recipes is indicated. To investigate into more depth the electron and hole contacts behavior under illumination, we should develop a more practical setup to measure contacts under rear side illumination. Ideally, this setup would also allow temperature control to extract activation energies under varying illumination conditions.

Using the modelling approach for R_S based on the model of Haschke et al. and coupling it to a recombination losses model, and to an optical model, we could obtain a full modelling of SHJ cells. This model would be interesting for example to perform optimization of metallization grid geometry as a function of material and contact properties (e.g. wafer and ITO resistivity, electron and hole contact resistivity, etc.).

Both measurement and modelling approaches could be generalized to similar cell technologies, that face similar problematics (for instance poly-silicon based cells that feature high contact resistivity SiOx/poly-Si contacts and achieve high levels of passivation [172]).

Finally, generalizing the analysis of resistive losses considering operation in conditions representative of a module in external environment (higher temperatures, bifacial illumination, etc.) instead of STC conditions could be of great interest.

Appendices

Appendix 1: Demonstration of the transmission line model of the standard TLM

In this paragraph we will detail the derivation of the TLM equations such as proposed by Berger [75]. Let us represent the structure as below:

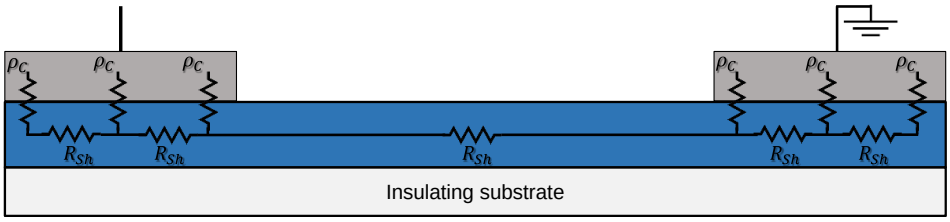

Figure 136: Transmission Line Model representation of coplanar electrodes contacting a layer

To solve the system and demonstrate the method one needs to use the mathematical frame of the transmission line model. A transmission line is an infinite network of elementary components put in parallel/series arrangement. A simple transmission line corresponding to our TLM contact can be depicted such as shown in Figure 137:

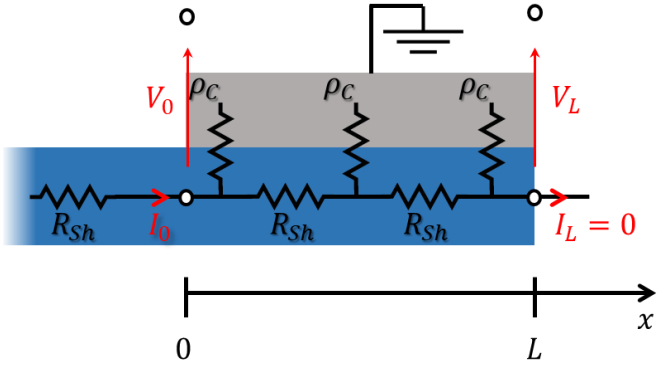

Figure 137 : TLM sample bellow a contact depicted as a transmission line

This is solved using the telegrapher's equations, which in our DC case without inductance and conductance reads:

$$\frac{dV(x)}{dx} = -RI(x)$$
$$\frac{dI(x)}{dx} = -GV(x) \qquad \text{Eq. 146}$$

Where R and G are the elementary elements of resistance and shunt conductance in the TLM.

The solution to these equations is such as [75] :

$$V(x) = V_0 \cosh(\alpha x) - I_0 Z sinh(\alpha x)$$
$$I(x) = I_0 \cosh(\alpha x) - \frac{V_0}{Z} sinh(\alpha x) \qquad \text{Eq. 147}$$

Where Z is the impedance of the circuit, defined as:

$$Z = \sqrt{\frac{\frac{dR}{dx}}{\frac{dG}{dx}}} \qquad \text{Eq. 148}$$

And α the attenuation constant:

$$\alpha = \sqrt{\frac{dR}{dx}\frac{dG}{dx}} \quad \text{Eq. 149}$$

Laterally the current only goes through the studied layer of sheet resistance R_{Sh} so:

$$\frac{dR}{dx} = \frac{R_{Sh}}{W} \quad \text{Eq. 150}$$

And the shunt conductance is linked to contact resistivity through [160]:

$$\frac{dG}{dx} = \frac{W}{\rho_C} \quad \text{Eq. 151}$$

Which in turns gives:

$$Z = \frac{1}{W}\sqrt{R_{Sh}\rho_C} \equiv \frac{1}{W} * R_{Sh} * L_t \equiv \frac{\rho_C}{W L_t} \quad \text{Eq. 152}$$

$$\alpha = \sqrt{\frac{R_{Sh}}{\rho_C}} = \frac{1}{L_t} \quad \text{Eq. 153}$$

Assuming no current crowding (which is not absolutely true and can result in biased results [152], [173]), boundary conditions can be applied as such:

$$I(x = L) = 0$$

It allows to calculate, from Eq. 147 (as $\cosh(0) = 1$ and $\sinh(0) = 0$):

$$I(x = L) = 0 = I_0 \cosh(\alpha L) - \frac{V_0}{Z} sinh(\alpha L) \quad \text{Eq. 154}$$

$$\leftrightarrow \frac{V_0}{I_0} = Z\frac{\cosh(\alpha L)}{\sinh(\alpha L)} = Z \coth(\alpha L) = \frac{1}{W} * R_{Sh} * L_t * \coth\left(\frac{L}{L_t}\right) \quad \text{Eq. 155}$$

Finally, contact resistance can be defined as:

$$R_C = \frac{V_0}{I_0} = \boldsymbol{R_{Sh} * \frac{L_t}{W} * \coth\left(\frac{L}{L_t}\right)} \quad \text{Eq. 156}$$

Appendix 2: Demonstration of resistive power loss

Let us consider the device at a given illumination, under a given load, resulting in an external voltage V and a current density J. Note that neither the current nor the potential is homogeneous over the cell, V and J only represent the characteristics generated when measuring the cell.

As current density is normalized over the whole cell, shaded parts of the cell where no current is generated have a lower current density than illuminated parts. In his demonstration, Mette [67] considers that the photogenerated current under shaded parts is zero, and uniform under non-shaded areas and equal to J_{Gen} such that:

$$J_{Gen} = \frac{J}{1 - sh}$$

Where sh is the shading fraction of the unit cell.

Following his approach, we have:

$$I_{UC} = J * A_{UC} \equiv J_{Gen} * A_{UC,non\ shaded}$$

Where $A_{UC,non\ shaded}$ is the non-shaded area of the unit cell. Therefore we can calculate each contribution as follows.

Appendix 2 (a): Resistive losses from lateral current in the emitter

Unit cell #1 (UC1) can be illustrated such as:

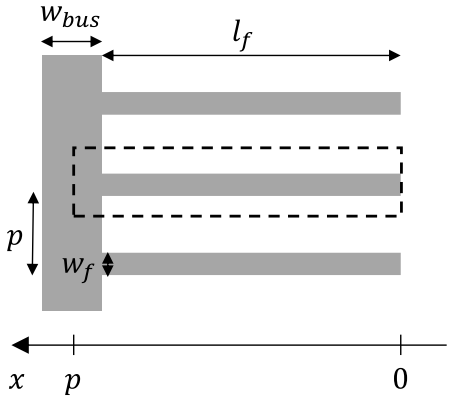

Figure 138 : Top view of the vicinity of UC1. Dashed lines represent the limit of UC1

When the current reaches the emitter, it will be directed to the closest grid line and therefore the closer to the grid, the higher will be the current density, in a linear relation with zero current at half pitch and maximum current I_{UC1} at the edge of the finger:

$$I(x) = \frac{I_{UC1}}{p - wf} * x$$

Because the current is not homogenous, the power loss due to resistive effects in the emitter over unit cell #1 is calculated using an integral expression with current coming from both sides of the finger.

$$P_{loss}(emitter) = 2\int_0^{\frac{p-w_f}{2}} I(x)^2 dR$$

The resistance of a cross section perpendicular to the finger can be expressed as:

$$dR = \frac{R_{Sh}}{l_f} * dx$$

So the power loss in the emitter over a unit cell can be written such as:

$$P_{loss}(emitter) = 2\int_0^{\frac{p-w_f}{2}} \frac{I_{UC1}^2}{l_f^2} * x^2 * \frac{R_{Sh}}{l_f} * dx$$

$$= 2\frac{R_{Sh}}{l_f} * \frac{I_{UC1}^2}{(p - wf)^2}\int_0^{\frac{p-w_f}{2}} x^2 dx$$

$$= 2\frac{R_{Sh}}{l_f} * \frac{I_{UC1}^2}{(p - wf)^2}\left[\frac{x^3}{3}\right]_0^{\frac{p-w_f}{2}}$$

$$= 2\frac{R_{Sh}}{l_f} * \frac{I_{UC1}^2}{(p - wf)^2} * \frac{\left(\frac{(p - w_f)^3}{8}\right)}{3}$$

$$= \frac{1}{12} * \frac{R_{Sh}}{l_f} * I_{UC1}^2 * (p - w_f)$$

The area of unit cell #1 is:

$$A_{UC1} = p * \left(l_f + \frac{w_{bus}}{2}\right)$$

So:

$$r_S(emitter) = \frac{P_{loss}(emitter)}{I_{UC1}^2} * A_{UC1}$$

$$= \frac{1}{12} * R_{Sh} * (p - w_f) * p * \frac{\left(l_f + \frac{w_{bus}}{2}\right)}{l_f}$$

Considering $p \gg w_f$ and $lf \gg w_{bus}$ we get:

$$r_S(emitter) \sim \boldsymbol{\frac{1}{12} * R_{Sh} * p^2} \qquad \text{Eq. 157}$$

Appendix 2 (b): Resistive losses due to the contact:

The TLM model [83] gives the expression for R_C between a metal finger and an underlying semi-conductor such as :

$$R_C = \frac{\rho_C}{l_f * L_t} * \coth\left(\frac{w_f}{L_t}\right)$$

Where ρ_C and L_t are the contact resistivity between the metal and the semi-conductor and L_t is the transfer length of that contact.

In the TLM model, the current is injected from a contact and collected in the other. However, in the case of a solar cell, this expression is not valid as current flows towards the contact from both sides. The equation for this case needs to be derived again from the Telegrapher equation (see Appendix 1):

$$I(x) = I_0 \cosh(\alpha x) - \frac{V_0}{Z} sinh(\alpha x)$$

With the impedance and attenuation constant such as:

$$Z = \frac{\rho_C}{l_f L_t} \quad ; \quad \alpha = \frac{1}{L_t}$$

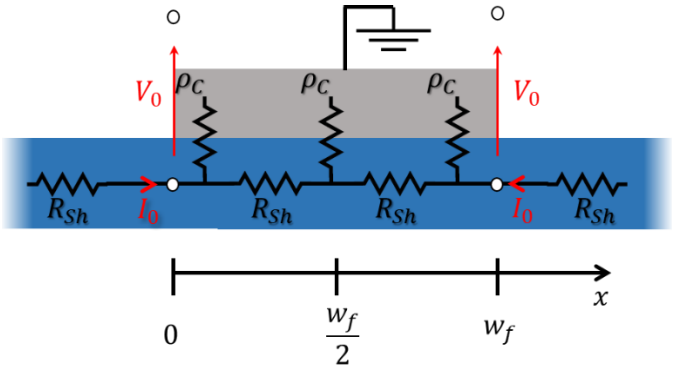

Figure 139: drawing of the equivalent model of a contact on the emitter of a solar cell

Considering symmetry, the boundary conditions become ([78] (see Figure 139):

$$I(x = 0) = -I(x = w_f) = I_0$$

And

$$V(x = 0) = V_0$$

Also, due to symmetry, the x component of current is necessary 0 at $w_f/2$ as both currents cancel out. Thus:

$$I\left(\frac{w_f}{2}\right) = 0$$

$$\leftrightarrow I_0 \cosh\left(\frac{w_f}{2L_t}\right) - \frac{V_0}{\frac{1}{l_f} * R_{Sh} * L_t} sinh\left(\frac{w_f}{2L_t}\right) = 0$$

$$\leftrightarrow R_C = \frac{V_0}{I_0} = R_{Sh} * \frac{L_t}{l_f} * \frac{\cosh\left(\frac{w_f}{2L_t}\right)}{sinh\left(\frac{w_f}{2L_t}\right)}$$

$$\leftrightarrow R_C = R_{Sh} * \frac{L_t}{l_f} * \coth\left(\frac{w_f}{2L_t}\right) = \boldsymbol{\frac{\rho_C}{L_t l_f} * \coth\left(\frac{w_f}{2L_t}\right)}$$

$$r_S(contact) = R_C * A_{UC1}$$

$$= \boldsymbol{\frac{1}{2}\frac{\rho_C}{L_t} * \frac{p\left(l_f + \frac{w_{bus}}{2}\right)}{l_f} * \coth\left(\frac{w_f}{2L_t}\right)}$$

$$\sim \boldsymbol{\frac{1}{2}\frac{\rho_C}{L_t} * p * \coth\left(\frac{w_f}{2L_t}\right)} \qquad \text{Eq. 158}$$

Appendix 2 (c): Resistive losses from the fingers

Still considering unit cell #1, the current also increases linearly along the finger as:

$$I(x) = \frac{I_{UC1}}{l_f} * x$$

Following a similar approach than for the emitter, the power loss can be expressed as:

$$P_{loss}(finger) = \int_0^{l_f} I(x)^2 dR$$

With

$$dR = R_{line} * dx$$

With

$$R_{line} = \frac{\rho}{t_f w_f}$$

Where ρ is the resistivity of the metal, and t_f and w_f are the thickness and width of the finger.

Which gives:

$$P_{loss}(finger) = \int_0^{l_f} R_{line} \frac{I_{UC1}^2}{l_f^2} * x^2 dx$$

$$P_{loss}(finger) = R_{line} \frac{I_{UC1}^2}{l_f^2} * \left[\frac{x^3}{3}\right]_0^{l_f}$$

$$P_{loss}(finger) = \frac{1}{3} R_{line} * I_{UC1}^2 * l_f$$

Then:

$$r_S(finger) = \frac{P_{loss}(finger)}{I_{UC1}^2} A_{UC1}$$

$$= \frac{1}{3} * R_{line} * p * l_f * \left(l_f + \frac{w_{bus}}{2}\right)$$

With $l_f \gg w_{bus}$ we get:

$$r_S(finger) \sim \frac{\mathbf{1}}{\mathbf{3}} * \boldsymbol{R_{line}} * \boldsymbol{p} * \boldsymbol{l_f^2} \qquad \text{Eq. 159}$$

Appendix 2 (d): Resistive losses due to busbars

The busbar losses need to be studied with respect to unit cell #3, centered around the I-V probe, and delimited as depicted in Figure 140.

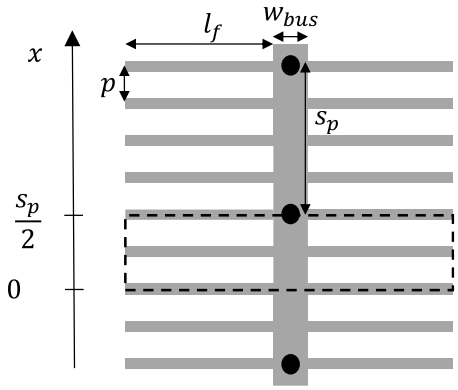

Figure 140 : unit cell #2

Where s_p represents the spacing of the I-V probes.

The area of unit cell #2 is:

$$A_{UC2} = s_p * \left(l_f + \frac{w_{bus}}{2}\right)$$

Following the same approach than for the lines, we will hypothesize that the current along a busbar increases linearly from zero in between two IV probes to a maximum value I_{UC2} at an IV probe:

$$I(x) = \frac{I_{UC2}}{s_p/2} * x$$

And

$$dR = R_{bus}dx$$

With

$$R_{bus} = \frac{\rho}{t_{bus}w_{bus}}$$

Where ρ is the resistivity of the metal, and t_{bus} and w_{bus} are the thickness and width of the busbar.

The power loss in the busbar then reads:

$$P_{loss}(bus) = \int_0^{\frac{s_p}{2}} I(x)^2 R_{bus}dx$$

$$= 4\int_0^{\frac{s_p}{2}} \frac{I_{UC2}^2}{s_p^2} * R_{bus} * x^2 dx$$

$$= 4 * \frac{I_{UC2}^2}{s_p^2} * R_{bus} * \frac{1}{3} * \frac{s_p^3}{8}$$

$$= \frac{1}{6} I_{UC2}^2 * R_{bus} * s_p$$

Then:

$$r_S(busbar) = \frac{P_{loss}(busbar)}{I_{UC2}^2} * A_{UC2}$$

$$= \frac{1}{6} R_{bus} * s_p^2 * \left(l_f + \frac{w_{bus}}{2}\right)$$

Considering $lf \gg w_{bus}$ we get:

$$r_S(busbar) \sim \boldsymbol{\frac{1}{6} * R_{bus} * l_f * s_p^2}$$

Appendix 2 (e): Resistive losses from transverse current in the bulk c-Si

The bulk has to be considered at the level of Unit cell #3. Electrons and holes generated in the absorber flow towards their respective contacts. Considering constant resistivity across the bulk, the resistance stemming from the absorber can be written:

$$r_S(bulk) = \rho * t$$

Where ρ and t are the absorber resistivity and thickness.

Appendix 2 (f): Note on the generation hypothesis

As stated above, we previously took the approximation from Mette et al. of generation only in non-shaded areas. However as stated in [81] another hypothesis is equally pertinent as some effects i.e. texturing can make generation to occur below fingers.

This implies slight changes in the demonstrations and lead to different expressions for the contributions from the emitter and the contact. Mostly what changes is the expressions for the current. These modifications probably have a really low impact on the results, and the aforementioned simplifications of each expression are the same with both hypothesis.

The full formulas in this case are changed for the emitter and for the contact, where they become:

$$r_S(emitter) = \frac{1}{12} * R_{Sh} * \frac{l_f}{lf + \frac{w_{bus}}{2}} * \frac{\left(p - w_f\right)^3}{p} \quad \text{Eq. 160}$$

$$r_S(contact) = \frac{1}{2}\frac{\rho_C}{L_t} * \frac{p\left(l_f + \frac{w_{bus}}{2}\right)}{l_f} * \coth\left(\frac{w_f}{2L_t}\right) \quad \text{Eq. 161}$$

Appendix 3: Demonstration of measurement methods of R_S

This appendix presents the mathematical derivations of several methods to measure R_S. All derivations are based on the 1-diode model for simplicity (Eq. 12).

Appendix 3 (a): Dual light method

The Dual Light Method (DLM) was originally proposed by Wolf and Rauschenbach in 1963 [174]. The 1-diode model neglecting shunt resistance can be written in an alternate form such as:

$$J_0 = \frac{J_L + J}{\exp\left(\frac{V - R_S J}{n\frac{k_B T}{q}}\right) - 1} \quad \text{Eq. 162}$$

Let us consider two J-V curves measured at two illuminations intensities with current densities and voltages denoted as J_1, J_2, V_1 and V_2. With the hypothesis that all the diode parameters do not vary with illumination intensity, equating the J_0 of both curves gives:

$$\frac{J_{L_1} + J_1(V_1)}{\exp\left(\frac{V_1 - R_S J_1(V_1)}{n\frac{k_B T}{q}}\right) - 1} = \frac{J_{L_2} + J_2(V_2)}{\exp\left(\frac{V_2 - R_S J_2(V_2)}{n\frac{k_B T}{q}}\right) - 1} \quad \text{Eq. 163}$$

By taking J_1 and J_2 such that they correspond to a same current difference ΔJ such that $\Delta J = J_{L_1} + J_1 = J_{L_2} + J_2$, this simplifies to:

$$\frac{\Delta J}{\exp\left(\frac{V_1 - R_S J_1}{n\frac{k_B T}{q}}\right) - 1} = \frac{\Delta J}{\exp\left(\frac{V_2 - R_S J_2}{n\frac{k_B T}{q}}\right) - 1}$$

Then:

$$V_1 - R_S J_1 = V_2 - R_S J_2$$

And finally:

$$R_S = \frac{V_2 - V_1}{J_2 - J_1} \quad \text{Eq. 164}$$

From the definition of ΔJ, $J_1 - J_2 = J_{L,2} - J_{L,1}$. With the approximation $J_{SC} = J_L$ it reads:

$$R_S(V) = \frac{V_1 - V_2}{J_{SC2} - J_{SC1}} \quad \text{Eq. 165}$$

Where V is the mean value of V_1 and V_2.

Fixing a ΔJ is equivalent to shifting a curve by ΔJ, so that $J_1 = J_2 = J$ This is useful to illustrate graphically the method, where the difference in voltage at a given J is directly an indicator of R_S (Figure 141).

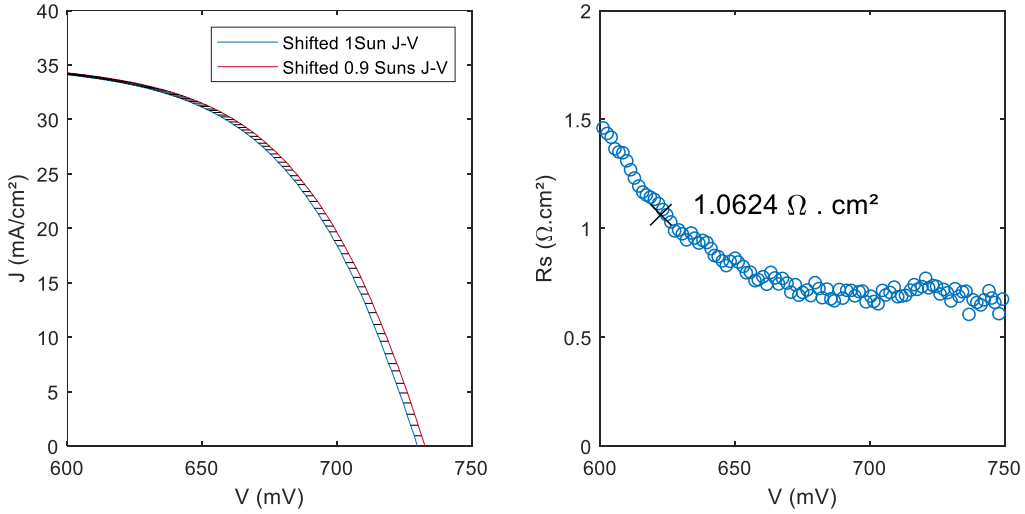

Figure 141 : Graphic illustration of the DLM method centered on 0.95Suns for a SHJ cell of 22.1% efficiency at 1Sun

Appendix 3 (b): Multi-light method

Fong et al. [36] proposed a simple improvement to the DLM, namely the Multi-Light Method (MLM), which is an extension of the formalism to take into account more than two curves. For an odd number N of J-V curves of linearly varying illumination, the R_S for the central curve reads:

$$R_S(J) = \left| \frac{\sum_{i=1}^{i=N}(V_i - \bar{V})^2}{\sum_{i=1}^{i=N}(V_i - \bar{V})(J_i - \bar{J})} \right| \quad \text{Eq. 166}$$

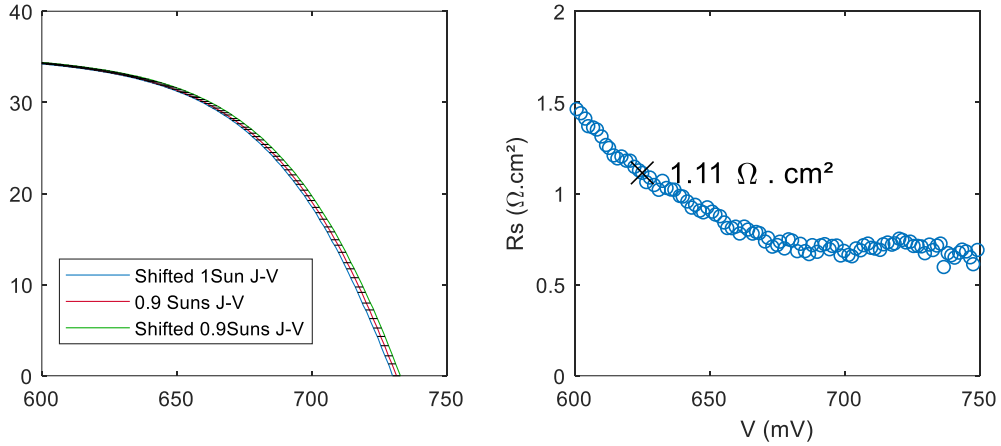

Figure 142: Graphic illustration of the MLM method centered on 0.95Suns for a SHJ cell of 22.1% efficiency at 1Sun

Appendix 3 (c): Dark-light method

The Dark-Light method was originally proposed by Aberle et al. [175]. From the 1 diode model, neglecting shunt resistance we can write:

$$J = -J_L + J_0 * \left(\exp\left(\frac{V - R_S J}{n \frac{kT}{q}} \right) - 1 \right)$$

$$\leftrightarrow \exp\left(\frac{V - R_S J}{\frac{nkT}{q}} \right) = \frac{J + J_L}{J_0} + 1$$

$$\leftrightarrow V = n \frac{kT}{q} \ln\left(\frac{J + J_L}{J_0} + 1 \right) + R_S J \quad \text{Eq. 167}$$

In dark conditions Eq. 172 gives:

$$\leftrightarrow V_{dark} = n \frac{kT}{q} \ln\left(\frac{J_{dark}}{J_0} + 1 \right) + R_{S,dark} J_{dark} \quad \text{Eq. 168}$$

By considering n and J_0constant with illumination level, one can write:

$$V - V_{dark} = R_S J - R_{S,dark} J_{dark} - n \frac{kT}{q} * \ln\left(\frac{\frac{J + J_L}{J_0} + 1}{\frac{J_{dark}}{J_0} + 1} \right)$$

By matching J to $J_{dark} - J_L$ (this can be applied graphically by shifting the dark IV curve by J_L), the difference of voltage between the two curves at the matched currents gives:

$$\mathrm{V} - V_{dark} = (J_{dark} - J_L) * R_S - R_{S,dark} J_{dark} \qquad \text{Eq. 169}$$

This leads to, considering $J_L = J_{SC}$:

$$R_S(V) = \frac{V - V_{dark} + R_{S,dark} J_{dark}}{J_{dark} - J_{SC}} \qquad \text{Eq. 170}$$

Where R_S dark can be assessed from Eq. 174 by the voltage difference at V_{OC} ($J = 0$; $J_{dark} = -J_{SC}$):

$$V_{OC} - V_{dark}(J_{dark} = -J_{SC}) = -R_{S,dark} J_{dark}$$

$$\leftrightarrow V_{OC} - V_{dark}(J_{dark} = -J_{SC}) = R_{S,dark} J_L$$

$$\leftrightarrow R_{S,dark} = \frac{V_{OC} - V_{dark}(J_{dark} = -J_{SC})}{J_{SC}} \qquad \text{Eq. 171}$$

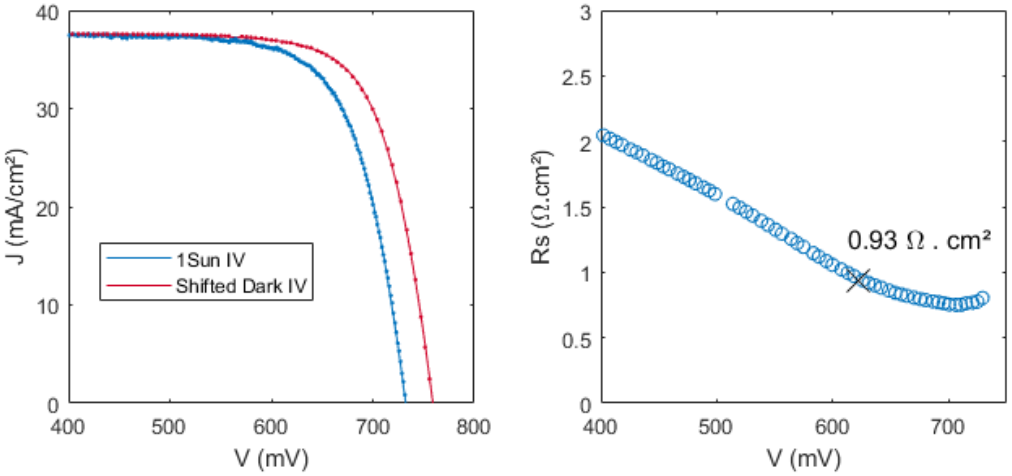

Figure 143 : Graphic illustration of the dark-light method for a 22.1% efficiency SHJ cell

Appendix 3(d): Comparison between Jsc-Voc & J-V curves

Again, the 1D model is the basis of the following discussion:

$$J = -J_L + J_0 * \left(exp\left(\frac{V - J * R_S}{n \frac{k_B T}{q}} \right) - 1 \right) + \frac{V - R_S J}{R_{Sh}} \qquad (1)$$

In the case of a measurement at V_{OC} this reads, and considering $J_{SC} = J_{ph}$:

$$\mathbf{0} = -J_{SC} + J_0 * \left(exp\left(\frac{\boldsymbol{V_{OC}}}{n \frac{k_B T}{q}} \right) - 1 \right) + \frac{V_{OC}}{R_{Sh}} \qquad (2)$$

Even though there is R_S, at $\boldsymbol{V_{OC}}$ the cell is not affected by it as there is no current ($\boldsymbol{J = 0}$).

J_L is proportional to the illumination intensity, therefore as long as the $J_L = J_{SC}$ approximation holds, J_{SC} is proportional to the illumination intensity. Considering R_S,J_0 & R_{Sh} to be constant with illumination intensity, varying the illumination is equivalent to varying the current. Which allows to write:

$$J_{SC}(E) = J_0 * \left(exp\left(\frac{V_{OC}(E)}{n\frac{k_B T}{q}} \right) - 1 \right) + \frac{V_{OC}}{R_{Sh}} \qquad \text{Eq. 172}$$

Varying the illumination to measure $J_{SC}(E)$ and $V_{OC}(E)$, allows the extraction of a $J_{SC} - V_{OC}$ curve. Again, a way to represent graphically is to shift it by J_{SC} of the reference illumination (here 1Sun).

$$J_{SC,shifted}(V_{OC}) = J_{SC}(1Sun) - J_0 * \left(exp\left(\frac{V_{OC}}{n\frac{k_B T}{q}} \right) - 1 \right) - \frac{V_{OC}}{R_{Sh}}$$

It is affected by R_{Sh}, but unaffected by series resistance effects. The shifted Jsc-Voc curve is representative to a J-V curve without the effect of R_S. At a given current, the difference in tension between the Jsc-Voc and J-V curves allows the determination of R_S as follows:

$$R_{S,JscVoc-JV}(J) = \frac{V(J) - V_{OC,shifted}(J)}{J} \qquad \text{Eq. 173}$$

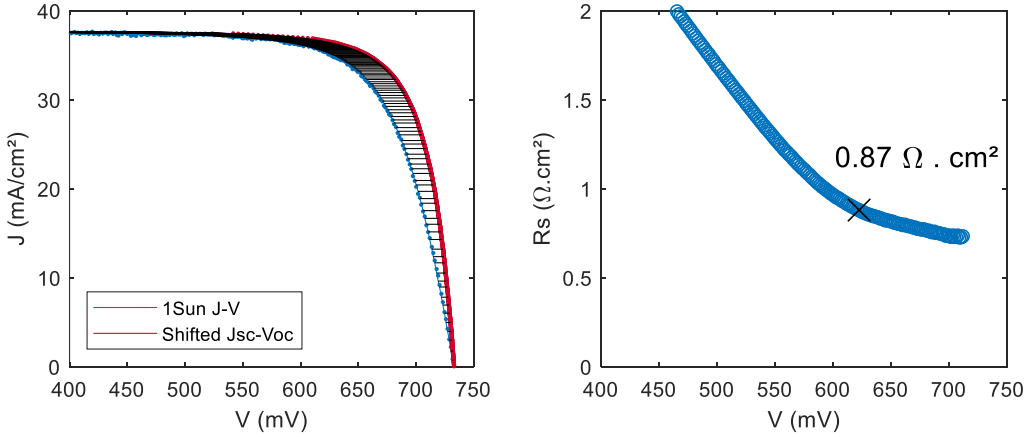

Figure 144 : J-V & shifted Jsc-Voc curves for a 22.1% efficiency SHJ cell

Appendix 4: Haschke et al.'s model for power loss analysis

In [81], the authors describe the lateral transport towards the contacts of SHJ cells using a SPICE-like equivalent circuit of two layers separated with a contact resistivity, with homogeneous photogeneration, such as described in Figure 145.

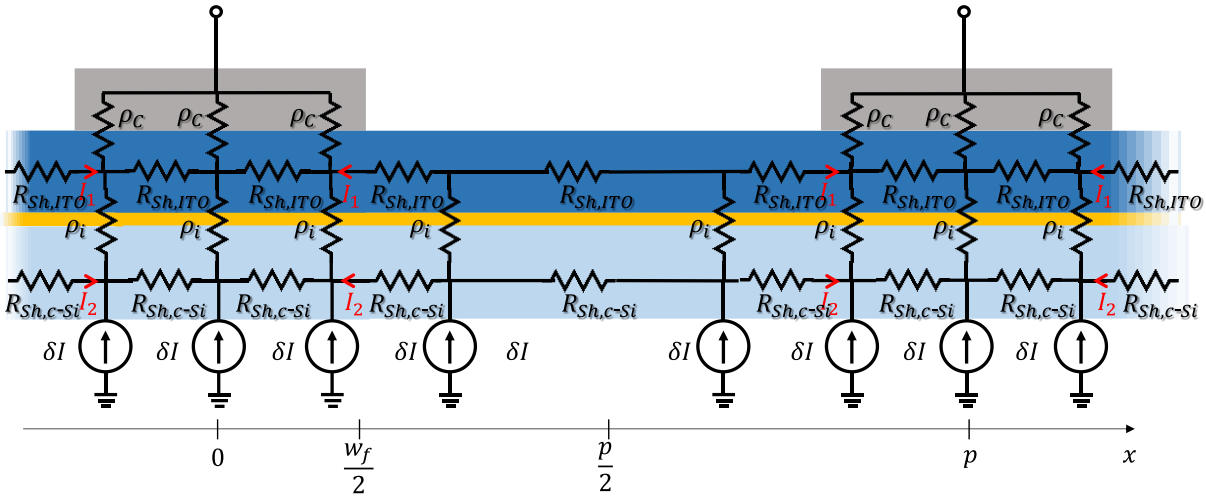

Figure 145: Equivalent circuit of the front side of an SHJ cell

They obtain expressions for the currents in each layer (I_1 in ITO and I_2 in c-Si) in between fingers such as:

$$I_1(x) = -\alpha_1 \sinh(\xi_C x) + \frac{R_{Sh,c\text{-}Si} I_0}{R_{Sh,c\text{-}Si} + R_{Sh,ITO}} * \frac{x}{p} \quad \text{Eq. 174}$$

$$I_2(x) = \alpha_1 \sinh(\xi_C x) + \frac{R_{Sh,ITO} I_0}{R_{Sh,c\text{-}Si} + R_{Sh,ITO}} * \frac{x}{p} \quad \text{Eq. 175}$$

Where I_0 is the photogenerated current, α_1 is a constant and:

$$\xi_C = \sqrt{\frac{R_{Sh,c\text{-}Si} + R_{Sh,ITO}}{\rho_I}} \quad \text{Eq. 176}$$

Below the fingers, the current takes the form:

$$I_{C1}(x') = \alpha_p \sinh(\eta_p x') + \alpha_n \sinh(\eta_n x') \quad \text{Eq. 177}$$

$$I_{C2}(x') = \lambda_p \alpha_p \sinh(\eta_p x') + \lambda_n \alpha_n \sinh(\eta_n x') \quad \text{Eq. 178}$$

Where α_n and α_p are constants, $x' = x - \frac{p}{2'}$ and:

$$\eta_{n,p} = \sqrt{\frac{1}{2} * \left(\frac{R_{Sh,ITO}}{\rho_C} + \xi_C^2 \pm \sqrt{\left(\frac{R_{Sh,ITO}}{\rho_C} + \xi_C^2 \right)^2 - 4 * \left(\frac{R_{Sh,c\text{-}Si} R_{Sh,ITO}}{R_{Sh,c\text{-}Si} + R_{Sh,ITO}} * \frac{\xi_C^2}{\rho_C} \right)} \right)} \quad \text{Eq. 179}$$

Where the subscripts n and p stand for the negative and positive sign of Eq. 179.

Similarly, for the voltages in between fingers:

$$V_1(x) = \frac{R_{Sh,ITO}}{\xi_C l_f} * \alpha_1 \cosh(\xi_C x) - \frac{R_{Sh,c\text{-}Si} R_{Sh,ITO}}{R_{Sh,c\text{-}Si} + R_{Sh,ITO}} * \frac{I_0 x^2}{2 p l_f} + d_3 \quad \text{Eq. 180}$$

$$V_2(x) = \frac{R_{Sh,c\text{-}Si}}{\xi_C l_f} * \alpha_1 \cosh(\xi_C x) - \frac{R_{Sh,c\text{-}Si} R_{Sh,ITO}}{R_{Sh,c\text{-}Si} + R_{Sh,ITO}} * \frac{I_0 x^2}{2 p l_f} + d_4 \quad \text{Eq. 181}$$

And below fingers:

$$V_{C1}(x') = -\frac{R_{Sh,ITO}}{l_f \eta_p} \alpha_p \cosh(\eta_p x') - \frac{R_{Sh,ITO}}{l_f \eta_n} \alpha_n \cosh(\eta_n x') + \frac{\rho_C I_0}{w_f p} \quad \text{Eq. 182}$$

$$V_{C2}(x') = -\frac{R_{Sh,c\text{-}Si}}{l_f\,\eta_p}\lambda_p\alpha_p\cosh(\eta_p x') - \frac{R_{Sh,c\text{-}Si}}{l_f\,\eta_n}\lambda_n\alpha_n\cosh(\eta_n x') + \frac{(\rho_C+\rho_I)I_0}{w_f p} \quad \text{Eq. 183}$$

Where:

$$\lambda_{n,p} = \frac{R_{Sh,ITO}}{R_{Sh,c\text{-}Si} - \rho_I * \eta_{n,p}^2} \quad \text{Eq. 184}$$

Using boundary conditions, the system can be expressed such as:

$$M * \begin{pmatrix} \alpha_1 \\ d_3 \\ d_4 \\ \alpha_p \\ \alpha_n \end{pmatrix} = V \quad \text{Eq. 185}$$

Where:

$$M = \begin{pmatrix} -\sinh\left(\xi_C\frac{p-w_f}{2}\right) & 0 & 0 & -\sinh\left(-\eta_p\frac{w_f}{2}\right) & -\sinh\left(-\eta_n\frac{w_f}{2}\right) \\ \sinh\left(\xi_C\frac{p-w_f}{2}\right) & 0 & 0 & -\lambda_p\sinh\left(-\eta_p\frac{w_f}{2}\right) & -\lambda_n\sinh\left(-\eta_n\frac{w_f}{2}\right) \\ \frac{R_{Sh,ITO}}{\xi_C l_f}\cosh\left(\xi_C\frac{p-w_f}{2}\right) & 1 & 0 & \frac{R_{Sh,ITO}}{\eta_p l_f}\cosh\left(-\eta_p\frac{w_f}{2}\right) & \frac{R_{Sh,ITO}}{\eta_n l_f}\cosh\left(-\eta_n\frac{w_f}{2}\right) \\ \frac{R_{Sh,c\text{-}Si}}{\xi_C l_f}\cosh\left(\xi_C\frac{p-w_f}{2}\right) & 0 & 1 & \frac{R_{Sh,c\text{-}Si}}{\eta_p l_f}\lambda_p\cosh\left(-\eta_p\frac{w_f}{2}\right) & \frac{R_{Sh,c\text{-}Si}}{\eta_n l_f}\lambda_n\cosh\left(-\eta_n\frac{w_f}{2}\right) \\ \xi_C\cosh\left(\xi_C\frac{p-w_f}{2}\right) & 0 & 0 & -\lambda_p\eta_p\cosh\left(-\eta_p\frac{w_f}{2}\right) & -\lambda_n\eta_n\cosh\left(-\eta_n\frac{w_f}{2}\right) \end{pmatrix} \quad \text{Eq. 186}$$

$$V = \begin{pmatrix} -\frac{R_{Sh,c\text{-}Si}I_0}{R_{Sh,c\text{-}Si}+R_{Sh,ITO}} * \frac{p-w_f}{2p} \\ -\frac{R_{Sh,ITO}I_0}{R_{Sh,c\text{-}Si}+R_{Sh,ITO}} * \frac{p-w_f}{2p} \\ \frac{R_{Sh,c\text{-}Si}R_{Sh,c\text{-}Si}}{R_{Sh,c\text{-}Si}+R_{Sh,ITO}}I_0 * \frac{(p-w_f)^2}{8l_f p} + \frac{\rho_C}{l_f} * \frac{I_0}{p} \\ \frac{R_{Sh,c\text{-}Si}R_{Sh,c\text{-}Si}}{R_{Sh,c\text{-}Si}+R_{Sh,ITO}}I_0 * \frac{(p-w_f)^2}{8l_f p} + \frac{\rho_I+\rho_C}{l_f} * \frac{I_0}{p} \\ -\frac{R_{Sh,ITO}}{R_{Sh,c\text{-}Si}+R_{Sh,ITO}} * \frac{I_0}{p} \end{pmatrix} \quad \text{Eq. 187}$$

Solving Eq. 185 allows to determine the constants and to express the current and voltage all across the circuit. Therefore, we can express the power losses in the layers and at the electron and metal/TCO contacts such as:

$$P_{c\text{-}Si} = 2 * \frac{R_{Sh,c\text{-}Si}}{l_f} * \left(\int_0^{\frac{p-w_f}{2}} I_1^2(x)dx + \int_{\frac{-w_f}{2}}^0 I_{C1}^2(x')dx'\right) \quad \text{Eq. 188}$$

$$P_{ITO} = 2 * \frac{R_{Sh,ITO}}{l_f} * \left(\int_0^{\frac{p-w_f}{2}} I_2^2(x)dx + \int_{\frac{-w_f}{2}}^0 I_{C2}^2(x')dx'\right) \quad \text{Eq. 189}$$

$$P_I = \frac{2l_f}{\rho_I} * \left(\int_0^{\frac{p-w_f}{2}} \left(V_1(x) - V_2(x)\right)^2 dx + \int_{\frac{-w_f}{2}}^{0} \left(V_{C1}(x') - V_{C2}(x')\right)^2 dx' \right) \quad \text{Eq. 190}$$

$$P_C = \frac{2l_f}{\rho_C} * \int_{\frac{-w_f}{2}}^{0} {V_{C1}}^2(x') dx' \quad \text{Eq. 191}$$

Which can each be expressed in terms of R_S with:

$$R_{S,i} = \frac{P_i}{I_0^2} * p * l_f \quad \text{Eq. 192}$$

Where the subscript I stands for any of the contributions.

Contributions

Publications

L. Basset, W. Favre, D. Muñoz, and J.-P. Vilcot, "Series Resistance Breakdown of Silicon Heterojunction Solar Cells Produced on CEA-INES Pilot Line," 35th Eur. Photovolt. Sol. Energy Conf. Exhib. 721-724, 2018.

A. Danel, J. Eymard, F. Pernoud, J. Diaz, M. Debourdeau, M. Quemin, A. Bettinelli, L. Basset, L. Sicot, S. Harrison, R. Varache, E. Gerritsen, P.-J. Ribeyron, C. Roux, "Bifaciality optimization of silicon heterojunction solar cells," 36th European Photovoltaic Solar Energy Conference and Exhibition, 2019.

Contributions in conferences

L. Basset, W. Favre, and J.-P. Vilcot, "Analysis of series resistance in silicon heterojunction solar cells produced on cea-ines pilot line," Visual presentation at the European PV solar Energy Conference and Exhibition 2018, 2018.

L. Basset, "The Role of Illumination and Temperature on the Electronic Properties at the Front Surface Field Interface of Silicon Heterojunction Solar Cells," oral presentation at the 28th International Conference on Amorphous and Nanocrystalline Semiconductors, ICANS 2019, 2019.

L. Basset, W. Favre, G. Ménard, and J.-P. Vilcot, "Measurement of silver to ITO contact resistivity in silicon heterojunction solar cells," oral presentation at the Journées nationales du photovoltaïque 2019, 2109.

L. Basset, W. Favre, O. Bonino, A. Puaud, and J.-P. Vilcot, "Influence of injection level and wafer resistivity on series resistance of silicon heterojunction solar cells," Visual presentation at the European PV solar Energy Conference and Exhibition 2020, 2020.

References

[1] M. Allen, "IPCC report 2015-Summary for Policymakers."
[2] "Global Temperature." NASA.
[3] "Carbon Dioxide | Vital Signs – Climate Change: Vital Signs of the Planet." [Online]. Available: https://climate.nasa.gov/vital-signs/carbon-dioxide/. [Accessed: 15-Jun-2020].
[4] J. Rogelj and D. Shindell, "Mitigation Pathways Compatible with 1.5°C in the Context of Sustainable Development," 2018.
[5] C. Breyer *et al.*, "On the role of solar photovoltaics in global energy transition scenarios: On the role of solar photovoltaics in global energy transition scenarios," *Prog. Photovolt. Res. Appl.*, vol. 25, no. 8, pp. 727–745, Aug. 2017.
[6] A. Jäger-Waldau, European Commission, and Joint Research Centre, *Pv status report 2019*. 2019.
[7] "International Technology Roadmap for Photovoltaic 2020." VDMA-PV, Avril-2020.
[8] "Trends in photovoltaic applications 2019." IEA PVPS, 2019.
[9] C. S. Lai and M. D. McCulloch, "Levelized cost of electricity for solar photovoltaic and electrical energy storage," *Appl. Energy*, vol. 190, pp. 191–203, Mar. 2017.
[10] J. A. Short, D. G. Infield, and L. L. Freris, "Stabilization of Grid Frequency Through Dynamic Demand Control," *IEEE Trans. Power Syst.*, vol. 22, no. 3, pp. 1284–1293, Aug. 2007.
[11] K. Hund, D. La Porta, T. P.Fabregas, T. Laing, and J. Drexhage, "Minerals for climate action: the mineral intensity of the clean energy transition." 2020.
[12] J. V. Paatero and P. D. Lund, "Effects of large-scale photovoltaic power integration on electricity distribution networks," *Renew. Energy*, vol. 32, no. 2, pp. 216–234, Feb. 2007.
[13] "Best Research-Cell Efficiency Chart | Photovoltaic Research | NREL." [Online]. Available: https://www.nrel.gov/pv/cell-efficiency.html. [Accessed: 28-Jun-2020].
[14] "Hi-MO3 bifacial module Longi Solar product sheet." .
[15] "Vertex TSM-DE18M(II) product sheet." Trina Solar.
[16] M. Bivour, *Silicon heterojunction solar cells: Analysis and basic understanding*. Stuttgart: Fraunhofer Verlag, 2017.
[17] U. Wurfel, A. Cuevas, and P. Wurfel, "Charge Carrier Separation in Solar Cells," *IEEE J. Photovolt.*, vol. 5, no. 1, pp. 461–469, Jan. 2015.

[18] A. Cuevas and D. Yan, "Misconceptions and Misnomers in Solar Cells," *IEEE J. Photovolt.*, vol. 3, no. 2, pp. 916–923, Apr. 2013.
[19] J. P. Mailoa *et al.*, "A 2-terminal perovskite/silicon multijunction solar cell enabled by a silicon tunnel junction," *Appl. Phys. Lett.*, vol. 106, no. 12, p. 121105, Mar. 2015.
[20] A. Jain and A. Kapoor, "A new method to determine the diode ideality factor of real solar cell using Lambert W-function," *Sol. Energy Mater. Sol. Cells*, vol. 85, no. 3, pp. 391–396, Jan. 2005.
[21] M. A. Green and S. P. Bremner, "Energy conversion approaches and materials for high-efficiency photovoltaics," *Nat. Mater.*, vol. 16, no. 1, pp. 23–34, Jan. 2017.
[22] A. Richter, M. Hermle, and S. W. Glunz, "Reassessment of the Limiting Efficiency for Crystalline Silicon Solar Cells," *IEEE J. Photovolt.*, vol. 3, no. 4, pp. 1184–1191, Oct. 2013.
[23] P. Würfel, *Physics of solar cells: from principles to new concepts*. 2005.
[24] M. J. Kerr, A. Cuevas, and R. A. Sinton, "Generalized analysis of quasi-steady-state and transient decay open circuit voltage measurements," *J. Appl. Phys.*, vol. 91, no. 1, p. 399, 2002.
[25] B. Hallam *et al.*, "The role of hydrogenation and gettering in enhancing the efficiency of next-generation Si solar cells: An industrial perspective," *Phys. Status Solidi A*, vol. 214, no. 7, p. 1700305, Jul. 2017.
[26] T. Trupke *et al.*, "Temperature dependence of the radiative recombination coefficient of intrinsic crystalline silicon," *J. Appl. Phys.*, vol. 94, no. 8, p. 4930, 2003.
[27] A. Richter, F. Werner, A. Cuevas, J. Schmidt, and S. W. Glunz, "Improved Parameterization of Auger Recombination in Silicon," *Energy Procedia*, vol. 27, pp. 88–94, 2012.
[28] B. A. Veith-Wolf, S. Schäfer, R. Brendel, and J. Schmidt, "Reassessment of intrinsic lifetime limit in n-type crystalline silicon and implication on maximum solar cell efficiency," *Sol. Energy Mater. Sol. Cells*, vol. 186, pp. 194–199, Nov. 2018.
[29] W. Shockley and W. T. Read Jr, "Statistics of the recombinations of holes and electrons," *Phys. Rev.*, vol. 87, no. 5, p. 835, 1952.
[30] R. N. Hall, "Electron-hole recombination in germanium," *Phys. Rev.*, vol. 87, no. 2, p. 387, 1952.
[31] S. Rein, *Lifetime spectroscopy: a method of defect characterization in silicon for photovoltaic applications*. Berlin: Springer, 2005.
[32] A. G. Aberle, "Surface passivation of crystalline silicon solar cells: a review," *Prog. Photovolt. Res. Appl.*, vol. 8, no. 5, pp. 473–487, 2000.
[33] M. Garín, U. Rau, W. Brendle, I. Martín, and R. Alcubilla, "Characterization of a-Si:H/c-Si interfaces by effective-lifetime measurements," *J. Appl. Phys.*, vol. 98, no. 9, p. 093711, Nov. 2005.
[34] C. Leendertz, R. Stangl, T. F. Schulze, M. Schmidt, and L. Korte, "A recombination model for a-Si:H/c-Si heterostructures," *Phys. Status Solidi C*, p. NA–NA, Jan. 2010.
[35] S. Olibet, E. Vallat-Sauvain, and C. Ballif, "Model for a-Si:H/c-Si interface recombination based on the amphoteric nature of silicon dangling bonds," *Phys. Rev. B*, vol. 76, no. 3, Jul. 2007.
[36] K. C. Fong, K. R. McIntosh, and A. W. Blakers, "Accurate series resistance measurement of solar cells," *Prog. Photovolt. Res. Appl.*, p. n/a–n/a, Nov. 2011.
[37] D. Kray, S. Hopman, A. Spiegel, B. Richerzhagen, and G. P. Willeke, "Study on the edge isolation of industrial silicon solar cells with waterjet-guided laser," *Sol. Energy Mater. Sol. Cells*, vol. 91, no. 17, pp. 1638–1644, Oct. 2007.

[38] M. A. Green, "Accurate expressions for solar cell fill factors including series and shunt resistances," *Appl. Phys. Lett.*, vol. 108, no. 8, p. 081111, Feb. 2016.
[39] Y. Alajlani, A. Alaswad, F. Placido, D. Gibson, and A. Diyaf, "Inorganic Thin Film Materials for Solar Cell Applications," in *Reference Module in Materials Science and Materials Engineering*, Elsevier, 2018.
[40] "International Technology Roadmap for Photovoltaic Results 2017." ITRPV, 2018.
[41] A. W. Blakers, A. Wang, A. M. Milne, J. Zhao, and M. A. Green, "22.8% efficient silicon solar cell," *Appl. Phys. Lett.*, vol. 55, no. 13, pp. 1363–1365, Sep. 1989.
[42] Y. Chen *et al.*, "From Laboratory to Production: Learning Models of Efficiency and Manufacturing Cost of Industrial Crystalline Silicon and Thin-Film Photovoltaic Technologies," *IEEE J. Photovolt.*, vol. 8, no. 6, pp. 1531–1538, Nov. 2018.
[43] Y. Wang, T. Xie, L. Green, and X. City, "Supply of low-cost and high-efficiency multi-GW mono wafers," *Photovolt. Int.*, vol. 36, pp. 38–42, 2017.
[44] J. Melskens, B. W. H. van de Loo, B. Macco, L. E. Black, S. Smit, and W. M. M. Kessels, "Passivating Contacts for Crystalline Silicon Solar Cells: From Concepts and Materials to Prospects," *IEEE J. Photovolt.*, vol. 8, no. 2, pp. 373–388, Mar. 2018.
[45] A. Richter, J. Benick, F. Feldmann, A. Fell, M. Hermle, and S. W. Glunz, "n-Type Si solar cells with passivating electron contact: Identifying sources for efficiency limitations by wafer thickness and resistivity variation," *Sol. Energy Mater. Sol. Cells*, vol. 173, pp. 96–105, Dec. 2017.
[46] C. Hollemann, F. Haase, S. Schäfer, J. Krügener, R. Brendel, and R. Peibst, "26.1%-efficient POLO-IBC cells: Quantification of electrical and optical loss mechanisms," *Prog. Photovolt. Res. Appl.*, vol. 27, no. 11, pp. 950–958, Nov. 2019.
[47] F. Feldmann, M. Bivour, C. Reichel, M. Hermle, and S. W. Glunz, "Passivated rear contacts for high-efficiency n-type Si solar cells providing high interface passivation quality and excellent transport characteristics," *Sol. Energy Mater. Sol. Cells*, vol. 120, pp. 270–274, Jan. 2014.
[48] S. W. Glunz and F. Feldmann, "SiO2 surface passivation layers – a key technology for silicon solar cells," *Sol. Energy Mater. Sol. Cells*, vol. 185, pp. 260–269, Oct. 2018.
[49] M. Hermle, F. Feldmann, M. Bivour, J. C. Goldschmidt, and S. W. Glunz, "Passivating contacts and tandem concepts: Approaches for the highest silicon-based solar cell efficiencies," *Appl. Phys. Rev.*, vol. 7, no. 2, p. 021305, Jun. 2020.
[50] K. Yoshikawa *et al.*, "Exceeding conversion efficiency of 26% by heterojunction interdigitated back contact solar cell with thin film Si technology," *Sol. Energy Mater. Sol. Cells*, vol. 173, pp. 37–42, Dec. 2017.
[51] K. Yamamoto, K. Yoshikawa, H. Uzu, and D. Adachi, "High-efficiency heterojunction crystalline Si solar cells," *Jpn. J. Appl. Phys.*, vol. 57, no. 8S3, p. 08RB20, Aug. 2018.
[52] X. Ru *et al.*, "25.11% efficiency silicon heterojunction solar cell with low deposition rate intrinsic amorphous silicon buffer layers," *Sol. Energy Mater. Sol. Cells*, vol. 215, Sep. 2020.
[53] W. Favre, D. Munoz, and C. Roux, "First European 25% Efficient Large Area Silicon Solar Cell: Path for European Premium PV Manufacturing is Open."
[54] M. Tanaka *et al.*, "Development of New a-Si/c-Si Heterojunction Solar Cells: ACJ-HIT (Artificially Constructed Junction-Heterojunction with Intrinsic Thin-Layer)," *Jpn. J. Appl. Phys.*, vol. 31, no. Part 1, No. 11, pp. 3518–3522, Nov. 1992.
[55] T. Kamioka, Y. Isogai, Y. Hayashi, Y. Ohshita, and A. Ogura, "Effects of damages induced by indium-tin-oxide reactive plasma deposition on minority carrier lifetime in silicon crystal," *AIP Adv.*, vol. 9, no. 10, p. 105219, Oct. 2019.

[56] E. Kobayashi, Y. Watabe, T. Yamamoto, and Y. Yamada, "Cerium oxide and hydrogen co-doped indium oxide films for high-efficiency silicon heterojunction solar cells," *Sol. Energy Mater. Sol. Cells*, vol. 149, pp. 75–80, May 2016.
[57] A. Cruz *et al.*, "Influence of Silicon Layers on the Growth of ITO and AZO in Silicon Heterojunction Solar Cells," *IEEE J. Photovolt.*, pp. 1–7, 2019.
[58] D. Lachenal *et al.*, "Heterojunction and Passivated Contacts: A Simple Method to Extract Both n/tco and p/tco Contacts Resistivity," *Energy Procedia*, vol. 92, pp. 932–938, Aug. 2016.
[59] A. Danel *et al.*, "Silicon Heterojunction Solar Cells with Open-Circuit-Voltage above 750mV," presented at the 35th European Photovoltaic Solar Energy Conference, Brussels, Belgium, 2018.
[60] S. De Wolf, A. Descoeudres, Z. C. Holman, and C. Ballif, "High-efficiency Silicon Heterojunction Solar Cells: A Review," *green*, vol. 2, no. 1, Jan. 2012.
[61] A. Louwen, W. van Sark, R. Schropp, and A. Faaij, "A cost roadmap for silicon heterojunction solar cells," *Sol. Energy Mater. Sol. Cells*, vol. 147, pp. 295–314, Apr. 2016.
[62] A. D. Rose, T. Geipel, D. Eberlein, A. Kraft, and M. Nowottnick, "Interconnection of silicon heterojunction solar cells by infrared soldering–Solder joint analysis and temperature study," in *2019 European Photovoltaic Solar Energy Conference and Exhibition*, 2019, pp. 229–234.
[63] L.-L. Senaud *et al.*, "Aluminium-Doped Zinc Oxide Rear Reflectors for High-Efficiency Silicon Heterojunction Solar Cells," *IEEE J. Photovolt.*, vol. 9, no. 5, pp. 1217–1224, Sep. 2019.
[64] C. Messmer, M. Bivour, J. Schön, and M. Hermle, "Requirements for efficient hole extraction in transition metal oxide-based silicon heterojunction solar cells," *J. Appl. Phys.*, vol. 124, no. 8, p. 085702, Aug. 2018.
[65] A. Danel *et al.*, "Bifaciality optimization of silicon heterojunction solar cells," presented at the 36th European Photovoltaic Solar Energy Conference and Exhibition, 2019.
[66] S. K. Chunduri and M. Schmela, "Heterojunction solar cell technology: 2019 edition." TaiYang News, 2019.
[67] D. Pysch, A. Mette, and S. W. Glunz, "A review and comparison of different methods to determine the series resistance of solar cells," *Sol. Energy Mater. Sol. Cells*, vol. 91, no. 18, pp. 1698–1706, Nov. 2007.
[68] G. M. M. W. Bissels *et al.*, "Experimental review of series resistance determination methods for III–V concentrator solar cells," *Sol. Energy Mater. Sol. Cells*, vol. 130, pp. 364–374, Nov. 2014.
[69] G. L. Araujo and E. Sanchez, "A new method for experimental determination of the series resistance of a solar cell," *IEEE Trans. Electron Devices*, vol. 29, no. 10, pp. 1511–1513, 1982.
[70] M. Warashina and A. Ushirokawa, "Simple method for the determination of series resistance and maximum power of solar cell," 1980.
[71] S. Bowden and A. Rohatgi, "Rapid and accurate determination of series resistance and fill factor losses in industrial silicon solar cells," 2001.
[72] G. M. M. W. Bissels *et al.*, "Theoretical review of series resistance determination methods for solar cells," *Sol. Energy Mater. Sol. Cells*, vol. 130, pp. 605–614, Nov. 2014.
[73] A. Khanna, T. Mueller, R. A. Stangl, B. Hoex, P. K. Basu, and A. G. Aberle, "A Fill Factor Loss Analysis Method for Silicon Wafer Solar Cells," *IEEE J. Photovolt.*, vol. 3, no. 4, pp. 1170–1177, Oct. 2013.
[74] A. Goetzberger and R. M. Scarlett, "Research and investigation of inverse epitaxial UHF power transistors," Clevite Transistor Palo Alto CA Shockley Transistor DIV, 1964.

[75] H. Berger, "Contact resistance on diffused resistors," in *Solid-State Circuits Conference. Digest of Technical Papers. 1969 IEEE Internationa*, 1969, vol. 12, pp. 160–161.
[76] K.-C. Huang, D. B. Janes, K. J. Webb, and M. R. Melloch, "A transfer length model for contact resistance of two-layer systems with arbitrary interlayer coupling under the contacts," *IEEE Trans. Electron Devices*, vol. 43, no. 5, pp. 676–684, 1996.
[77] D. L. Meier and D. K. Schroder, "Contact resistance: Its measurement and relative importance to power loss in a solar cell," *IEEE Trans. Electron Devices*, vol. 31, no. 5, pp. 647–653, May 1984.
[78] A. Mette, "New Concepts for Front Side Metallization of Industrial Silicon Solar Cells." 2007.
[79] C. D. Rodríguez-Gallegos *et al.*, "PV-GO: A multiobjective and robust optimization approach for the grid metallization design of Si-based solar cells and modules," *Prog. Photovolt. Res. Appl.*, Aug. 2018.
[80] D. Meier *et al.*, "Determining Components of Series Resistance from Measurements on a Finished Cell," 2006, pp. 1315–1318.
[81] J. Haschke, G. Christmann, C. Messmer, M. Bivour, M. Boccard, and C. Ballif, "Lateral transport in silicon solar cells," *J. Appl. Phys.*, vol. 127, no. 11, p. 114501, Mar. 2020.
[82] T. F. Schulze, L. Korte, E. Conrad, M. Schmidt, and B. Rech, "Electrical transport mechanisms in a-Si:H/c-Si heterojunction solar cells," *J. Appl. Phys.*, vol. 107, no. 2, p. 023711, Jan. 2010.
[83] D. K. Schroder, *Semiconductor material and device characterization*, 3rd ed. [Piscataway, NJ] : Hoboken, N.J: IEEE Press ; Wiley, 2006.
[84] K.-U. Ritzau *et al.*, "TCO work function related transport losses at the a-Si:H/TCO-contact in SHJ solar cells," *Sol. Energy Mater. Sol. Cells*, vol. 131, pp. 9–13, Dec. 2014.
[85] J. Robertson, "Band offsets, Schottky barrier heights, and their effects on electronic devices," *J. Vac. Sci. Technol. Vac. Surf. Films*, vol. 31, no. 5, p. 050821, Sep. 2013.
[86] S. M. Sze and K. K. Ng, *Physics of Semiconductor Devices: Sze/Physics*. Hoboken, NJ, USA: John Wiley & Sons, Inc., 2006.
[87] D. K. Schroder and D. L. Meier, "Solar cell contact resistance—a review," *IEEE Trans. Electron Devices*, vol. 31, no. 5, pp. 637–647, 1984.
[88] A. Y. C. Yu, "Electron tunneling and contact resistance of metal-silicon contact barriers," *Solid-State Electron.*, vol. 13, no. 2, pp. 239–247, Feb. 1970.
[89] J. Schube, "Low-Resistivity Screen-Printed Contacts on Indium Tin Oxide Layers for Silicon Solar Cells With Passivating Contacts," *IEEE J. Photovolt.*, pp. 1–7, 2018.
[90] L. Barraud *et al.*, "Hydrogen-doped indium oxide/indium tin oxide bilayers for high-efficiency silicon heterojunction solar cells," *Sol. Energy Mater. Sol. Cells*, vol. 115, pp. 151–156, Aug. 2013.
[91] S.-Y. Lee *et al.*, "Analysis of a-Si:H/TCO contact resistance for the Si heterojunction back-contact solar cell," *Sol. Energy Mater. Sol. Cells*, vol. 120, pp. 412–416, Jan. 2014.
[92] J. Geissbuhler *et al.*, "Silicon Heterojunction Solar Cells With Copper-Plated Grid Electrodes: Status and Comparison With Silver Thick-Film Techniques," *IEEE J. Photovolt.*, vol. 4, no. 4, pp. 1055–1062, Jul. 2014.
[93] P. A. Anderson, "The Contact Difference of Potential Between Tungsten and Barium. The External Work Function of Barium," *Phys. Rev.*, vol. 47, no. 12, pp. 958–964, Jun. 1935.
[94] J. Tersoff, "Theory of semiconductor heterojunctions: The role of quantum dipoles," in *Electronic Structure of Semiconductor Heterojunctions*, Springer, 1988, pp. 218–221.
[95] G. A. M. Hurkx, D. B. M. Klaassen, and M. P. G. Knuvers, "A new recombination model for device simulation including tunneling," *IEEE Trans. Electron Devices*, vol. 39, no. 2, pp. 331–338, 1992.

[96] K. Yang, J. R. East, and G. I. Haddad, "Numerical modeling of abrupt heterojunctions using a thermionic-field emission boundary condition," *Solid-State Electron.*, vol. 36, no. 3, pp. 321–330, 1993.
[97] D. Schroeder, *Modelling of Interface Carrier Transport for Device Simulation*. Vienna: Springer Vienna, 1994.
[98] "Notice Silvaco Atlas." .
[99] E. Danielsson, C.-M. Zetterling, M. Östling, D. Tsvetkov, and V. A. Dmitriev, "Characterization of heterojunction diodes with hydride vapor phase epitaxy grown AlGaN on 4H–SiC," *J. Appl. Phys.*, vol. 91, no. 4, pp. 2372–2379, Feb. 2002.
[100] R. Varache, J. P. Kleider, W. Favre, and L. Korte, "Band bending and determination of band offsets in amorphous/crystalline silicon heterostructures from planar conductance measurements," *J. Appl. Phys.*, vol. 112, no. 12, p. 123717, Dec. 2012.
[101] R. Varache, O. N. Aguila, A. Valla, N. Nguyen, and D. Munoz, "Role of the Front Electron Collector in Rear Emitter Silicon Heterojunction Solar Cells," *IEEE J. Photovolt.*, vol. 5, no. 3, pp. 711–717, May 2015.
[102] G. Nogay *et al.*, "Nanocrystalline Silicon Carrier Collectors for Silicon Heterojunction Solar Cells and Impact on Low-Temperature Device Characteristics," *IEEE J. Photovolt.*, vol. 6, no. 6, pp. 1654–1662, Nov. 2016.
[103] A. Kanevce and W. K. Metzger, "The role of amorphous silicon and tunneling in heterojunction with intrinsic thin layer (HIT) solar cells," *J. Appl. Phys.*, vol. 105, no. 9, p. 094507, May 2009.
[104] R. S. Crandall, E. Iwaniczko, J. V. Li, and M. R. Page, "A comprehensive study of hole collection in heterojunction solar cells," *J. Appl. Phys.*, vol. 112, no. 9, p. 093713, Nov. 2012.
[105] R. Lachaume *et al.*, "Influence of a-Si:H/ITO Interface Properties on Performance of Heterojunction Solar Cells," *Energy Procedia*, vol. 38, pp. 770–776, 2013.
[106] R. Varache, J. P. Kleider, M. E. Gueunier-Farret, and L. Korte, "Silicon heterojunction solar cells: Optimization of emitter and contact properties from analytical calculation and numerical simulation," *Mater. Sci. Eng. B*, vol. 178, no. 9, pp. 593–598, May 2013.
[107] R. Gogolin *et al.*, "Analysis of Series Resistance Losses in a-Si:H/c-Si Heterojunction Solar Cells," *IEEE J. Photovolt.*, vol. 4, no. 5, pp. 1169–1176, Sep. 2014.
[108] M. Bivour, S. Schröer, M. Hermle, and S. W. Glunz, "Silicon heterojunction rear emitter solar cells: Less restrictions on the optoelectrical properties of front side TCOs," *Sol. Energy Mater. Sol. Cells*, vol. 122, pp. 120–129, Mar. 2014.
[109] J. Haschke, C. Messmer, J. Cattin, M. Bivour, M. Boccard, and C. Ballif, "Injection-dependent lateral resistance in front-junction solar cells with nc-Si: H and a-Si: H hole selective contact," in *Proceedings of the 46th IEEE Photovoltaic Specialists Conference*, 2019.
[110] J. Kleider, J. Alvarez, R. Brüggemann, and M. Gueunier-Farret, "Recent Progress in Understanding the Properties of the Amorphous Silicon/Crystalline Silicon Interface," *Phys. Status Solidi A*, p. 1800877, May 2019.
[111] M. Filipič, Z. C. Holman, F. Smole, S. De Wolf, C. Ballif, and M. Topič, "Analysis of lateral transport through the inversion layer in amorphous silicon/crystalline silicon heterojunction solar cells," *J. Appl. Phys.*, vol. 114, no. 7, p. 074504, Aug. 2013.
[112] R. Varache, N. Nguyen, and D. Muñoz, "2D p-FF Simulations for the Interpretation of Junction Isolation's Influence on Silicon Heterojunction Solar Cells," *Energy Procedia*, vol. 55, pp. 149–154, 2014.

[113] O. Nos *et al.*, "Quality control method based on photoluminescence imaging for the performance prediction of c-Si/a-Si:H heterojunction solar cells in industrial production lines," *Sol. Energy Mater. Sol. Cells*, vol. 144, pp. 210–220, Jan. 2016.
[114] A. Danel *et al.*, "Versatile pilot line to support the heterojunction solar cell industrial development: busbar and busbar-less configurations," 2017.
[115] N. Bassi *et al.*, "GridTouch: innovative solution for accurate IV measurement of busbarless cells in production and laboratory environments," in *Proc. of 29th European Photovoltaic Solar Energy Conference and Exhibition*, 2014, pp. 1180–1185.
[116] R. A. Sinton, A. Cuevas, and M. stuckings, "Quasi-steady-state photoconductance, a new method for solar cell material and device characterization," 1996.
[117] J. A. Giesecke, M. C. Schubert, B. Michl, F. Schindler, and W. Warta, "Minority carrier lifetime imaging of silicon wafers calibrated by quasi-steady-state photoluminescence," *Sol. Energy Mater. Sol. Cells*, vol. 95, no. 3, pp. 1011–1018, Mar. 2011.
[118] E. Letty, "Identification and neutralization of lifetime-limiting defects in Czochralski silicon for high efficiency photovoltaic applications," 2017.
[119] T. Trupke, E. Pink, R. A. Bardos, and M. D. Abbott, "Spatially resolved series resistance of silicon solar cells obtained from luminescence imaging," *Appl. Phys. Lett.*, vol. 90, no. 9, p. 093506, Feb. 2007.
[120] M. Losurdo *et al.*, "Spectroscopic ellipsometry and polarimetry for materials and systems analysis at the nanometer scale: state-of-the-art, potential, and perspectives," *J. Nanoparticle Res.*, vol. 11, no. 7, pp. 1521–1554, Oct. 2009.
[121] M. Losurdo *et al.*, "Parametrization of optical properties of indium–tin–oxide thin films by spectroscopic ellipsometry: Substrate interfacial reactivity," *J. Vac. Sci. Technol. Vac. Surf. Films*, vol. 20, no. 1, pp. 37–42, Jan. 2002.
[122] J. Coignus, M. Baudrit, J. Singer, R. Lachaume, D. Muñoz, and P. Thony, "Key issues for accurate simulation of a-Si:H / c-Si heterojunction solar cells," *Energy Procedia*, vol. 8, pp. 174–179, 2011.
[123] V. Giglia, J. Veirman, R. Varache, and E. Fourmond, "Understanding of the Influence of the Surface Defectivity on Silicon Heterojunction Cell Performance," 2019.
[124] M. J. Powell and S. C. Deane, "Improved defect-pool model for charged defects in amorphous silicon," *Phys. Rev. B*, vol. 48, no. 15, p. 10815, 1993.
[125] H.-J. Ueng, D. B. Janes, and K. J. Webb, "Error analysis leading to design criteria for transmission line model characterization of ohmic contacts," *IEEE Trans. Electron Devices*, vol. 48, no. 4, pp. 758–766, 2001.
[126] W. Wang *et al.*, "An Expanded Cox and Strack Method for Precise Extraction of Specific Contact Resistance of Transition Metal Oxide/ *n*- Silicon Heterojunction," *IEEE J. Photovolt.*, vol. 9, no. 4, pp. 1113–1120, Jul. 2019.
[127] M. P. Patkar, T. P. Chin, J. M. Woodall, M. S. Lundstrom, and M. R. Melloch, "Very low resistance nonalloyed ohmic contacts using low-temperature molecular beam epitaxy of GaAs," *Appl. Phys. Lett.*, vol. 66, no. 11, pp. 1412–1414, 1995.
[128] H. H. Berger, "Contact resistance and contact resistivity," *J. Electrochem. Soc.*, vol. 119, no. 4, pp. 507–514, 1972.
[129] G. S. Marlow and M. B. Das, "The effects of contact size and non-zero metal resistance on the determination of specific contact resistance," *Solid-State Electron.*, vol. 25, no. 2, pp. 91–94, 1982.

[130] A. M. Gabor *et al.*, "Dependence of solar cell contact resistivity measurements on sample preparation methods," in *Photovoltaic Specialists Conference (PVSC), 2016 IEEE 43rd*, 2016, pp. 3033–3036.
[131] S. Guo, G. Gregory, A. M. Gabor, W. V. Schoenfeld, and K. O. Davis, "Detailed investigation of TLM contact resistance measurements on crystalline silicon solar cells," *Sol. Energy*, vol. 151, pp. 163–172, Jul. 2017.
[132] jochen Hohl-Ebinger, D. Grote, B. Hund, A. Mette, and W. Warta, "Contacting bare solar cells for STC measurements," 2008.
[133] M. Leilaeioun, W. Weigand, M. Boccard, Z. J. Yu, K. Fisher, and Z. C. Holman, "Contact Resistivity of the p-Type Amorphous Silicon Hole Contact in Silicon Heterojunction Solar Cells," *IEEE J. Photovolt.*, pp. 1–9, 2019.
[134] S. Eidelloth and R. Brendel, "Analytical Theory for Extracting Specific Contact Resistances of Thick Samples From the Transmission Line Method," *IEEE Electron Device Lett.*, vol. 35, no. 1, pp. 9–11, Jan. 2014.
[135] C. Luderer, C. Messmer, M. Hermle, and M. Bivour, "Transport Losses at the TCO/a-Si:H/c-Si Heterojunction: Influence of Different Layers and Annealing," *IEEE J. Photovolt.*, pp. 1–7, 2020.
[136] C. Yu *et al.*, "Development of silicon heterojunction solar cell technology for manufacturing," *Jpn. J. Appl. Phys.*, vol. 57, no. 8S3, p. 08RB15, Aug. 2018.
[137] L. Yang *et al.*, "Study and development of rear-emitter Si heterojunction solar cells and application of direct copper metallization," *Prog. Photovolt. Res. Appl.*, vol. 26, no. 6, pp. 385–396, Jun. 2018.
[138] F. Korsós, P. Tüttő, I. Saegh, K. Kis-Szabó, and A. Tóth, "Accurate contact and contactless methods for emitter sheet resistance testing of PV wafers," 2019, p. 020006.
[139] J.-H. Lan, J. Kanicki, A. Catalano, J. Keane, W. Den Boer, and T. Gu, "Patterning of transparent conducting oxide thin films by wet etching for a-Si: H TFT-LCDs," *J. Electron. Mater.*, vol. 25, no. 12, pp. 1806–1817, 1996.
[140] "WCT 120 product note." Sinton Instruments, 2013.
[141] W. Favre, J. Coignus, N. Nguyen, R. Lachaume, R. Cabal, and D. Muñoz, "Influence of the transparent conductive oxide layer deposition step on electrical properties of silicon heterojunction solar cells," *Appl. Phys. Lett.*, vol. 102, no. 18, p. 181118, May 2013.
[142] M. Bivour, C. Reichel, M. Hermle, and S. W. Glunz, "Improving the a-Si:H(p) rear emitter contact of n-type silicon solar cells," *Sol. Energy Mater. Sol. Cells*, vol. 106, pp. 11–16, Nov. 2012.
[143] I. Haller, Y. H. Lee, J. J. Nocera Jr, and M. A. Jaso, "Selective wet and dry etching of hydrogenated amorphous silicon and related materials," *J. Electrochem. Soc.*, vol. 135, no. 8, p. 2042, 1988.
[144] D. Macdonald and L. J. Geerligs, "Recombination activity of interstitial iron and other transition metal point defects in p- and n-type crystalline silicon," *Appl. Phys. Lett.*, vol. 85, no. 18, pp. 4061–4063, Nov. 2004.
[145] H. Steinkemper, M. Hermle, and S. W. Glunz, "Comprehensive simulation study of industrially relevant silicon solar cell architectures for an optimal material parameter choice: Study on silicon solar cell architectures," *Prog. Photovolt. Res. Appl.*, vol. 24, no. 10, pp. 1319–1331, Oct. 2016.
[146] A. Descoeudres *et al.*, "The versatility of passivating carrier-selective silicon thin films for diverse high-efficiency screen-printed heterojunction-based solar cells," *Prog. Photovolt. Res. Appl.*, vol. 28, no. 6, pp. 569–577, Jun. 2020.

[147] B. Vicari Stefani *et al.*, "Large-Area Boron-Doped 1.6 Ω cm p-Type Czochralski Silicon Heterojunction Solar Cells with a Stable Open-Circuit Voltage of 736 mV and Efficiency of 22.0%," *Sol. RRL*, p. 2000134, Jun. 2020.
[148] "Resistivity calculator - PV Lighthouse." [Online]. Available: https://www.pvlighthouse.com.au/resistivity. [Accessed: 16-Jan-2019].
[149] F. Meng, J. Shi, Z. Liu, Y. Cui, Z. Lu, and Z. Feng, "High mobility transparent conductive W-doped In2O3 thin films prepared at low substrate temperature and its application to solar cells," *Sol. Energy Mater. Sol. Cells*, vol. 122, pp. 70–74, Mar. 2014.
[150] Y. Komatsu *et al.*, "Calibration of Electrochemical Capacitance-voltage Method on Pyramid Texture Surface Using Scanning Electron Microscopy," *Energy Procedia*, vol. 38, pp. 94–100, 2013.
[151] Z. C. Holman *et al.*, "Current Losses at the Front of Silicon Heterojunction Solar Cells," *IEEE J. Photovolt.*, vol. 2, no. 1, pp. 7–15, Jan. 2012.
[152] D. Lachenal *et al.*, "Optimization of tunnel-junction IBC solar cells based on a series resistance model," *Sol. Energy Mater. Sol. Cells*, vol. 200, p. 110036, Sep. 2019.
[153] C. Coutal, A. Azema, and J.-C. Roustan, "Fabrication and characterization of ITO thin films deposited by excimer laser evaporation," *Thin Solid Films*, vol. 288, no. 1–2, pp. 248–253, 1996.
[154] A. C. Rastogi and S. T. Lakshmikumar, "Indium-tin-oxide-metal interfacial resistance and its implication for solar cells," *Sol. Cells*, vol. 26, no. 4, pp. 323–328, 1989.
[155] D. Mitra, K. Y. Mitra, V. Dzhagan, N. Pillai, D. R. T. Zahn, and R. R. Baumann, "Work Function and Conductivity of Inkjet-Printed Silver Layers: Effect of Inks and Post-treatments," *J. Electron. Mater.*, vol. 47, no. 3, pp. 2135–2142, Mar. 2018.
[156] R. Lachaume, "Contribution à la caractérisation électrique et à la simulation numérique des cellules photovoltaïques silicium à hétérojonction," Grenoble, 2014.
[157] R. Couderc, M. Amara, and M. Lemiti, "Reassessment of the intrinsic carrier density temperature dependence in crystalline silicon," *J. Appl. Phys.*, vol. 115, no. 9, p. 093705, Mar. 2014.
[158] M. S. Lundstrom and R. J. Schuelke, "Numerical analysis of heterostructure semiconductor devices," *IEEE Trans. Electron Devices*, vol. 30, no. 9, pp. 1151–1159, 1983.
[159] R. A. Street, *Hydrogenated Amorphous Silicon*, 1st ed. Cambridge University Press, 1991.
[160] H. H. Berger, "Models for contacts to planar devices," *Solid-State Electron.*, vol. 15, no. 2, pp. 145–158, 1972.
[161] P. Zhang, Y. Y. Lau, and R. M. Gilgenbach, "Analysis of current crowding in thin film contacts from exact field solution," *J. Phys. Appl. Phys.*, vol. 48, no. 47, p. 475501, Dec. 2015.
[162] L.-L. Senaud, "Illuminated Contact Resistance Measurements to Investigate the Properties of Contact Stacks in Silicon Heterojunction Solar Cells," presented at the EU PVSEC 2020, 2020.
[163] D. B. M. Klaassen, "A unified mobility model for device simulation? I. Model equations and concentration dependence," *Solid-State Electron.*, vol. 35, no. 7, pp. 953–959, 1992.
[164] D. B. M. Klaassen, "A unified mobility model for device simulation—II. Temperature dependence of carrier mobility and lifetime," *Solid-State Electron.*, vol. 35, no. 7, pp. 961–967, 1992.
[165] S. Schäfer *et al.*, "26%-efficient and 2 cm narrow interdigitated back contact silicon solar cells with passivated slits on two edges," *Sol. Energy Mater. Sol. Cells*, vol. 200, p. 110021, Sep. 2019.

[166] L. Basset, W. Favre, D. Muñoz, and J.-P. Vilcot, "Series Resistance Breakdown of Silicon Heterojunction Solar Cells Produced on CEA-INES Pilot Line," *35th Eur. Photovolt. Sol. Energy Conf. Exhib. 721-724*, 2018.
[167] "MOBILITY CALCULATOR - PVLighthouse." .
[168] C. D. Thurmond, "The standard thermodynamic functions for the formation of electrons and holes in Ge, Si, GaAs, and GaP," *J. Electrochem. Soc.*, vol. 122, no. 8, pp. 1133–1141, 1975.
[169] R. H. Cox and H. Strack, "Ohmic contacts for GaAs devices," *Solid-State Electron.*, vol. 10, no. 12, pp. 1213–1218, 1967.
[170] S. Zhong *et al.*, "Mitigating Plasmonic Absorption Losses at Rear Electrodes in High-Efficiency Silicon Solar Cells Using Dopant-Free Contact Stacks," *Adv. Funct. Mater.*, vol. 30, no. 5, p. 1907840, Jan. 2020.
[171] M.-U. Halbich, D. Zielke, R. Gogolin, R. Sauer-Stieglitz, W. Lövenich, and J. Schmidt, "Improved surface passivation and reduced parasitic absorption in PEDOT:PSS/c-Si heterojunction solar cells through the admixture of sorbitol," *Sci. Rep.*, vol. 9, no. 1, Dec. 2019.
[172] C. Luderer, C. Reichel, F. Feldmann, M. Bivour, and M. Hermle, "Passivating and low-resistive poly-Si tunneling junction enabling high-efficiency monolithic perovskite/silicon tandem solar cells," *Appl. Phys. Lett.*, vol. 115, no. 18, p. 182105, Oct. 2019.
[173] C.-Y. Ting and C. Y. Chen, "A study of the contacts of a diffused resistor," *Solid-State Electron.*, vol. 14, no. 6, pp. 433–438, 1971.
[174] M. Wolf and H. Rauschenbach, "Series resistance effects on solar cell measurements," *Sol. Cells*, pp. 146–170, 1963.
[175] A. G. Aberle, S. R. Wenham, and M. A. Green, "A new method for accurate measurements of the lumped series resistance of solar cells," 1993, pp. 133–139.